Title	Tidal stream energy assessment with and without a shock capture scheme - Incorporating a non-constant thrust force coefficient
Author(s)	Flores Mateos, Lilia Margarita
Publication Date	2019-04-23
Publisher	NUI Galway
Item record	http://hdl.handle.net/10379/15136

Tidal Stream Energy Assessment with and without a Shock Capture Scheme - Incorporating a Non-constant Thrust Force Coefficient

NUI Galway
OÉ Gaillimh

Thesis submitted to the College of Engineering and Informatics, National University of Ireland, Galway in fulfilment of the requirements for the degree of

Doctor of Philosophy

Lilia Margarita Flores Mateos, MSc P.O., BPhys

Supervisor: Professor Michael Hartnett

April 2019

Declaration

I, the undersigned, declare that this work has not previously been submitted to this or any other University, and that unless otherwise stated, it is entirely my own work. I agree that NUI Galway "James Hardiman" Library may lend or copy this thesis upon request.

_____

Lilia Margarita Flores Mateos

Dated: April 2, 2019

A mi familia en México...

A la familia que me ha acogido en España ...

To the Irish family who have embraced me here in the Emerald Isle......

Acknowledgements

ration and reassurance.

- To Maximo for showing me a more graceful Galway and making my life more amusing.

- To Mary, Leonie, Maximo, Ruth, Marina, Ariel, Shejin, Mykhaylo, Kieran, Ryan, and Richard for reviewing and improving the different versions of this thesis.

- To Maximo, Mykhaylo & Nadia, Leonie, and family for being my *mecenas* and providing me with financial stability when I need it the most.

- To Grazia, Kieran & baby Hanna, Leonie & Shejin, Mykhaylo & Nadia, Piort, Alessandra & Ryan, Janna, Leone & Jacqui, Lei & Sussane, Ariel & Eammon, Sinead, Maria-Vittoria, Jinhee, Kirsten, Ronnan, Nurul, Joe, Joanne, Boxing group, and Women Rugby society for making of Ireland such as special place.

- To the friends that I have met in Santo-Angél, Ensenada, and Puebla for making every return to feel like home.

Lilia Margarita Flores Mateos

National University of Ireland, Galway

April 2019

Abstract

Tidal currents provide a significant energy source in many locations worldwide, particularly at coastal areas where bathymetric conditions intensify their magnitudes. Potential sites for tidal-stream energy resource harvesting require realistic assessments and reliable simulations of effects of turbine arrays on tidal dynamics. Accuracy of the analysis has direct implications on economic and technical aspects of tidal energy project developments.

An alternative approach for simulating turbine array energy capture, momentum sink-TOC, was developed to improve conventional methodologies for assessing tidal-stream energy resource. The method uses a non-constant thrust force coefficient calculated based on turbines operating-conditions, and relates turbine near-field changes produced by power extraction to turbine thrust forces. Sink-TOC combines linear momentum actuator disc in open channel flows theory with the momentum sink method.

Momentum sink-TOC was implemented in two depth-average complex hydrodynamic models to simulate different marine turbine configurations and to perform tidal-stream energy resource assessments. The first model solves smooth and slow flows (SSF) with an alternating direction implicit scheme. The second model solves rapidly varying flows (RVF) combining MacCormack and total variation diminishing schemes. The RVF solver incorporates a computational less expensive approach for simulating sharp gradients produced by power extraction than existing techniques. Benchmarking of numerical results against analytical solutions indicates that both models correctly

compute momentum extracted by turbines.

Calculation of turbine velocity coefficients and head drops across turbine arrays enabled the calculation of turbine efficiency, total power extracted, power dissipated by turbine wake-mixing, and power available for electricity generation. These metrics represent an advantage over traditional methodologies used to assess resources. Assessment of bounded flow scenarios through a full fence configuration performed better using the SSF solver, because head drop was more accurately simulated. However, this scheme underestimates velocity reductions due to power extraction. Evaluation of un-bounded flow scenarios through a partial-fence was better performed by the RVF solver as the head drop was more correctly approximated by this scheme. The free-surface flow simulations led to identification of non-uniform upstream conditions for the partial-fence configuration. Computational performance comparisons indicated that the RVF solver requires higher computational cost independently of domain-size, and whether energy extraction procedure is incorporated or not.

Tidal-stream energy resource evaluations with fence and partial-fence configurations indicate that a computationally economical pre-assessment can be adequately performed using an SSF solver. However, more accurate evaluation requires solution of the discontinuities produced in the tidal-stream by power extraction. The methodology and numerical models obtained in this research could be use to determine realistic upper limits of available power with turbine arrays in farm format in real-world coastal environments.

Contents

List of Figures

xiv

xvii

xviii

xix

List of Tables

xxi

Nomenclature

Nomenclature introduced in Chapter 1

RVF	Rapidly varying flows
SSF	Slow and smooth flows

Nomenclature introduced in Chapter 2

c	Shallow water wave speed ($c = \sqrt{gH}$),
g	Acceleration due to gravity
H	Mean water depth
M_2	Principal lunar semidiurnal component, its period is 12.42 hr
S_2	Principal solar semidiurnal component, its period is 12 hr
L_*	Characteristic length
L_R	Barotropic Rossby radius
f	Coriolis parameter ($f = 2\Omega sin\Psi$)
Ω	Angular speed of the earth
Ψ	Latitude on the earth
ζ	Surface elevation
h_n	Amplitude of the n-harmonic
g_n	Phase lag of the n-harmonic
ω_n	Temporal frequency of the n-constituent
t	Time
SFI	Significant impact factor
h	Total water depth
F_r	Froude number $F_r = u/\sqrt{gh}$
LMAD-OCH	Linear momentum actuator disc in open channel flow theory
U_{b4}	Turbine bypass flow at station 4

B	Blockage ratio
A	Turbine cross-sectional area
A_c	Channel cross-sectional area
P_{max}	Maximum power extracted
a	Tidal head difference across the channel
ρ	Density of the sea water
γ	Factor that accounts for the tidal dynamics in the channel at the natural state
Q_{max}	Peak volume flux in the natural state
$LMADT$	Linear momentum actuator disc theory
C_T'	Localised thrust force coefficient
w	Characteristic vertical velocity
u	Characteristic horizontal velocity (x-component)

Nomenclature introduced in Chapter 3

ε	Eddy viscosity
2D-SWEs	Two-dimensional version of the shallow water equations

The description of the terms of 2D-SWEs are described in Table 3.1.

$\overrightarrow{F_T}$	Thrust force, which presents two components $F_T(F_{Tx}, F_{Ty})$
C_T	Thrust coefficient
$\overrightarrow{U}$	Depth-average velocity, which presents two components (U, V)
C_r	Courant number
C_{rl}	Local Courant number
ψ	Flux limiter function used in TVD-M
HLLC	Harten-Lax-van Leer-Contact Riemann solver
S_*	Contact wave speed
CPU	Central Processing Unit
OpenMP	Open Multi-Processing, common shared-memory application program interface
C_d	Drag coefficient
HFDT	Half time-step
DIVAST	Depth Integrated Velocity And Solute Transport numerical model

ADI	Alternating Direction Implicit method
TVD	Symmetric Total Variation diminishing method
ADI-M	DIVAST ADI
TVD-M	DIVAST TVD-MacCormack
ADI-TOC	Numerical model that solves smooth flows and incorporates the LMAD-OCH theory. This model was developed in this thesis.
TVD-TOC	Numerical model that solves rapidly varying flows and incorporates the LMAD-OCH theory. This model was developed in this thesis.

Nomenclature introduced in Chapter 4

L_v	Length referred to as near-field extent
d	Turbine diameter
$(\;\;)_t$	Denotes turbine flow (core flow)
$(\;\;)_b$	Denotes turbine bypass flow
$(\;\;)_{1,2,3,4,5}$	Denotes location (station) within the flow field
α_2	Turbine velocity coefficient
α_4	Wake induction factor
β_4	Bypass induction factor
T	Thrust exerted by the turbine to the flow
P	Power removed by the turbine
dp	Pressure drop due to momentum extraction
Bhb	Turbine area defined as $A = Bhb$
b	Inter-turbine spacing
C_T	Thrust coefficient
C_P	Power coefficient
$\Delta h/h$	Relative head drop due to power extraction
P_W	Power dissipated by the turbine wake mixing
η	Turbine efficiency
P_*	Power removed by the turbine in terms of turbine efficiency
P_T	Total power extracted by the turbine
$\mathbf{I}$	Internal state

E	External state
$F_{\mathbf{I}}(F_{\mathbf{E}})$	Internal mass flux (External mass flux)
$(\quad)_*$	Solution to one of the 1D- Riemann problem
θ	Angle that the turbine axis makes with an axis parallel to the y-direction.
α	Angle that the turbine makes with the incident current
T	Thrust Force computed by DIVAST-ADI
$\Delta X(\Delta Y)$	Grid size on the $X-$direction ($Y-$direction)
Momentum sink-TOC	Momentum sink method which undertakes the turbine operating conditions prescribed by the blockage ratio and wake induction factor
N	Number of turbines per grid cell
A_t	Area of an individual turbine
ITS	Inter-turbine spacing

Nomenclature introduced in Chapter 5

$C0$	Simple channel domain
W/L	Aspect ratio, where L-length and W-width
T_{M2}	Tidal period of the M_2 constituent
Δt	Numerical model time step
Q	Flow rate
U	Velocity magnitude ($\mathbf{U} = \sqrt{U^2 + V^2}$)
$I_{max}(J_{max})$	Maximum number of grids in the $X-$ ($Y-$ direction)
T	Turbines inclusion
NoT	Turbines omission
P_{MP}	Maximum power extracted

Nomenclature introduced in Chapter 6

C-CTE	Momentum sink calculation strategy based on a pre-define thrust coefficient
C-TOC	Momentum sink calculation strategy based on LMAD-OCH theory
C_T^{CTE}	Pre-define constant thrust coefficient
C_P^{CTE}	Pre-define constant power coefficient

C_T^{TOC}	Thrust coefficient based on LMAD-OCH theory
C_P^{TOC}	Power coefficient based on LMAD-OCH theory
$\overline{(\ \ )}$	Temporal average
$(\ \ )_{grid}$	Average per grid-cell
Δh_e	Head drop below mean water
L_h	Length referred to as far field extent
B_l	Local blockage ratio
B_a	Array blockage ratio
B_g	Global blockage ratio
Bl_{grid}	Local blockage ratio per grid-cell
Ba_{grid}	Array blockage ratio per grid-cell
Bg_{grid}	Global blockage ratio per grid-cell
N_c	Number of cell-grids that constitute the partial-fence
$(\ \ )_{array}$	Average over the cells that constitute the array
N_g	Number of turbines per grid-cell
N_{pf}	Number of individual turbines within the partial-fence

Nomenclature introduced in Appendix A.2

G	Polynomial with real coefficients and degree m
M	Companion matrix

Chapter 1

Introduction

1.1 Research Background

Modern societies have become highly dependant on energy. However, with clear scientific evidence linking mass consumption of fossil fuels to global warming, governments have been forced to seek more eco-friendly alternatives of producing energy. Scientific research shows that alternative sources of energy have strong potential. In particular, high predictability of tidal currents makes them an attractive source of energy, especially in sites where the geographic and bathymetric features enhance their speeds, such as Ireland.

Hydrodynamics of Irish coastal sites are dominated by semidiurnal tidal constituents. Around 92% of tidal energy within the Irish Sea is due to Atlantic Ocean dynamics. Semidiurnal tidal currents and amplitudes are particularly strong on the east and west coasts of Ireland. Eleven potential locations for tidal-stream energy harvesting had been identified in these areas. A general tidal-current energy resource assessment in Ireland indicates a resource of 2.633 TWh/y (SEI, 2006; O'Rourke *et al.*, 2010). This estimation represents 6.27 % of Ireland's total electricity consumption in 2010 (Heavey *et al.*, 2017). An assessment based on measured data from two lo-

cations of the west side of Ireland: Bulls Mouth (County Mayo) and the Shannon Estuary (south of Galway Bay), indicate an annual energy output of 137.39 MWh for the Shannon Estuary and 2.16 MWh for the Bulls Mouth (O'Rourke *et al.*, 2014). A more sophisticated strategy to perform numerical assessment was implemented in the Shannon Estuary. The use of an array optimisation algorithm on the Shannon Estuary indicates that 18 staggered turbines of 21 m diameter, can extract $\approx$ 1000 kw per tidal cycle (Phoenix, 2017).

Tidal energy represents a promising sector for Irish energetic independence in a sustainable way. This alternative is particularly relevant for the island for two main reasons: firstly, Ireland is strongly dependent on fossil fuels such as oil, coal, peat, and natural gas; and secondly, except for peat all other fossil fuels are imported. Ireland is considered to be the most dependent fossil fuel importer in the European Union.

An initial task for any tidal energy project is site characterisation of tidal-streams. This aspect is important for the design, plan, and development of the project. A reliable assessment of the tidal-stream resource enables realistic estimations of the amount of electricity that can be produced. It can also assess the hydrodynamic conditions in which the turbines should perform. An initial tidal resource assessment can be successfully performed with hydrodynamic depth-average numerical models. These numerical schemes are suitable tools for studying far-field depth-average velocities and water depth of tidal-streams. Examples of potential coastal sites for tidal current energy extraction are tidal basins, tidal channels, estuaries, and coastal headlands. Importantly, numerical modelling enables the analysis of long-term time series of the flow properties and their response to scenarios such as tidal energy extraction, extreme events, and climate change. Another advantage of modelling is the possibility of estimating extractable power for tidal-stream energy harvesting. Analytical models describe the basic mechanism involved in the performance of tidal arrays in ideal scenarios. As a result, models can be used to identify the optimal layout of turbine arrays and turbine

sizes to be deployed.

The modelling of tidal-stream turbines and the estimation of the extractable power is a complicated task. The various scales involved in the modelling of these devices increase the complexity of the problem. Processes interact in tidal-stream turbine modelling at the level of blades, turbine diameter, turbine arrays, site, and regional scale. To simplify the analysis of a turbine energy extraction the concept of an actuator disc was incorporated. The actuator disc implies that the resistance offered by the turbine is considered to be uniform and normal to the flow direction. The inclusion of actuator disc in tidal flow analysis provides a simplified but adequate description of a marine turbine power extraction.

Initial analysis of turbine performance considered an actuator disc within a flow of infinite extent. The analysis of this scenario provided information on wind turbine performance. By relating disc resistance to flow, and to momentum lost by the flow, it is possible to use the conservation of mass and energy at upstream and downstream regions of a turbine to quantify the diversion of the flow around the disc. Thus, the power extracted by the device could be estimated. This analysis led to the determination of Lanchester-Bez limit, which indicates that in optimal conditions turbines can convert up to 59% of kinetic energy into mechanical energy. This limit has been useful in the design of wind turbines.

A scenario more representative of a marine turbine in a marine environment considers an actuator disc within a flow of finite extent. This flow is limited by a bottom constraint, a rigid-lid surface, and the presence of neighbouring turbines on the sides or channel's walls. This scenario indicates that the maximum extractable power would increase with respect to the infinite flow by a factor which is a function of the turbine blockage ratio. The blockage ratio indicates the fraction of a channel cross-section occupied by turbines. Therefore, the finite flow scenario indicates the relevance of blockage ratio effect of turbines within the water column.

Furthermore, the analysis of finite flow was expanded to include flows with deformable surfaces. It is reported that maximum power extraction increases when water elevation changes produced by power extraction of a turbine are considered. A more realistic analysis of marine turbine performance was obtained by including the turbine wake mixing region to the free-surface flow. The inclusion of the mixing region allows the power dissipated due to turbine wake mixing to be accounted for. Such a scenario is known as actuator disc within open channel flow. This analytical model of a device's power extraction illustrates the importance of considering natural constraints of the stream in coastal areas to the turbine performance.

Considering the numerical representation of marine turbines in far-field simulations, it is important to consider a methodology that accounts for flow directionality and turbine inter-spacing. Two methodologies exist which satisfy these requirements: (a) line sink of momentum and (b) momentum sink. The line sink of momentum method is based on the actuator disc in open channel flow analytical model. This methodology calculates the depth and velocity disturbance produced by power extraction via the modification of mass flux passing through a turbine array where the devices are arranged as a fence. This method constrains the relative change of the water elevation across the turbine array, simulating a power extraction scenario less representative of real conditions. In addition, the simulation of the disturbances produced by power extraction on the depth and velocity of the flow uses a scheme, which solves rapidly varying flows (RVF). This scheme requires high computational costs. Ideally, a numerical model should accurately simulate the flow, and be computationally affordable. In those terms, it is important to evaluate the relevance of simulating RVF on the tidal-stream assessment.

The momentum sink method is based on the addition of a sink term to the momentum equations. The sink term accounts for the flow momentum extracted by the axial component of the turbine's thrust force. The disadvantage of this method refers to the

incapacity to consider the influence of the turbine blockage ratio and the tidal-stream constraints into the sink term calculation.

Summarising, tidal currents are a prominent resource worldwide, which become particularly important in coastal areas where tidal-streams intensify in magnitude. The development of any tidal energy project requires the assessment of the tidal-stream resource. The accuracy of this analysis has direct implications on the economic and technical aspects of tidal energy development. Consequently, it is important to develop a robust numerical methodology to perform tidal-stream resource assessment. This method should numerically represent marine turbine momentum extraction in conditions as realistic as possible. The actuator disc in open channel flow analytical model provides a realistic description of the power extraction due to marine turbines. However, its numerical implementation required the extra-constraint of the flow free-surface and also solves the power extraction problem treating the depth-average velocity and depth changes as discontinuities of the flow. This solution procedure requires high computational costs.

In this research, a method to simulate marine turbine arrays based on the actuator disc in open channel flow theory is developed. This method is implemented in two numerical schemes: one solves RVF and the other solves flows that are slow and smooth (SSF) i.e. flows with a Froude number much less than unity. The relevance of the schemes' solution procedure to simulate the energy captured by the turbines is investigated. It is necessary also to determine, whether a scheme, which solves RVF is necessary in order to accurately assess the tidal-stream resource. Thus, the use of two numerical schemes used in this research enable the evaluation and comparison of their computational performance.

1.2 Aims of the Research

The primary aim of this research is to assess tidal-stream power resources and far-field hydrodynamic effects of tidal-stream turbine arrays. The research has the following main objectives:

1. To simulate the energy captured by marine turbines based on their operating conditions. This is possible by implementing linear momentum actuator disc in open channel flow theory.

2. To determine changes in the water elevation across an array due to power extraction.

3. To implement the turbine mechanics in two depth-average hydrodynamic models. The first numerical scheme simulates SSF, the second solves RVF.

4. To validate the numerical representation of marine turbine arrays.

5. To determine the role of the models' solution procedure in order to solve spatial gradients produced in the flow's depth and velocity due to power extraction, and to identify the numerical scheme that assesses the tidal-stream resource more accurately.

6. To evaluate and compare the computational performance of the two numerical schemes proposed here.

7. To assess tidal-stream resources considering changes in the flow in the near-field extent produced by power extraction. The parameterisation of these changes allows for the inclusion of turbine velocity coefficient, head drop across the array, and the turbine efficiency into the resource evaluation.

1.3   Thesis Outline

The layout of the thesis is as follows:

The context of the research within this thesis is presented in **Chapter 2**. Here, the nature of the tidal currents, tidal-stream turbine technology developments, and analytical and numerical methodologies to perform the tidal assessment are reviewed.

The derivation of the governing equations which describe marine turbine power extraction at a regional scale is presented in **Chapter 3**. Assumptions and limitations of the modelling of two-dimensional shallow water flows are also discussed. Two existing numerical models used to solve SSF and RVF are introduced.

Marine turbine array representations developed in this thesis, together with the procedure proposed to perform resource assessments, are described in **Chapter 4**. Here, the assumptions and implications of the Linear Momentum Actuator Disc Theory in open channel flow are presented. Additionally, the extended versions of the models that solve SSF, and RVF proposed in this thesis are described. These models simulate momentum extracted by turbines, based on the operating conditions of the turbine and considering free-surface flows.

Validation of the method used to represent marine turbines, in addition to a state-of-the-art procedure to evaluate the tidal-stream resource, are presented in **Chapter 5**. To benchmark the two models in terms of performance and computational cost, comparison of the solutions obtained with schemes that solve SSF and RVF are presented. An ideal turbine configuration: tidal fence, was used to benchmark the method and the models.

In **Chapter 6**, the proposed strategy in this thesis to represent marine turbines and to evaluate the resource was compared with conventional methodology. The traditional methodology is based on turbine thrust force which used a constant power and thrust coefficient. Additionally, the performance of a realistic configuration: partial-fence, is evaluated and compared to a fence layout. The analysis considers scenarios

with more realistic blockage ratios. The numerical results obtained from both models are benchmarked with analytical solutions that consider the head drop across the array as the solution of a cubic polynomial. This equation was reported by linear momentum actuator disc in open channel flow theory.

Finally, a summary and discussion of the main findings reached in this thesis are presented in **Chapter 7**. The main conclusions derived from the discussion and suggestions for potential further research following from this study are lastly presented.

Chapter 2

Literature Review

2.1 Introduction

Tidal-stream resource is a promising energy source due to its regular pattern and its high predictability. The development of the tidal energy sector could help to substitute conventional energy sources and contribute to the reduction of greenhouse gas emission. However, tidal-stream energy harvesting requires the assessment of the resource as an initial step. The certainty of this evaluation has implications on the economic and technical aspects of a tidal energy project development. Tidal-resource assessment can be performed with hydrodynamic depth-average numerical models. However, the accuracy of the evaluation depends on the simulation of the momentum extracted by the marine turbines and on the metrics used to assess the resource. Conventionally, the tidal-stream was considered not to be influenced by natural constraints such as the submarine floor and free-surface. Also, typically, the momentum extracted by a turbine is computed without considering near-field changes produced by power extraction on flows that bypass and pass through turbines. Finally, the resource characterisation is usually provided without specifying the amount of power loss by turbine wake mixing. This metric is relevant to evaluate the efficiency of a turbine.

To improve the conventional strategy of evaluating resources, it is required to incorporate the natural constraints which the stream is subject to in the coastal areas (shallow water). Better estimations would be obtained if turbine operating conditions were related to near-field changes produced by the energy captured by turbines. Additionally, the calculation of the turbine efficiency would provide a more accurate description of the resource by differentiating the total power extracted from the available power for electrical generation. The linear momentum actuator disc in open channel flow theory provides the basis to implement the improvement previously mentioned. However, its numerical implementation has been restricted to a discontinuous Galerkin model. This scheme uses a computationally expensive approach to simulate energy capture. Additionally, this method constraints the head drop produced by power extraction. A computationally less expensive, as well as less restrictive method to simulate the energy capture, is investigated in two numerical models in this thesis. This method is implemented in a scheme which solves gradually varying flows and another that solves RVF. The use of two models with different solution procedure enables the possibility of evaluating the RVF solution capability to the simulation of power extraction by marine turbines.

In the Introduction, a context for the research developed in this thesis along with the main objectives are provided. In the present chapter, a more detailed literature review is presented. Firstly, a review of the mechanism responsible for tidal currents generation are described in Section 2.2; then, a review of tidal energy resource and its advantages are described. Additionally, an overview of up-to-date technology in terms of the tidal-stream marine turbines is presented in Section 2.3. Then, a review of tidal energy resource assessment methodologies are reported in Section 2.4; this section presents the analytical and numerical approaches used to represent energy extraction due to marine turbines. In Section 2.5 a summary of the chapter is provided, where the contributions of the thesis are presented.

2.2   Tidal Currents

Tidal currents are driven by head differences as tides pass through coastal regions (Borthwick, 2016). The study of tides has a long history. The first description of tides generating forces was given by Newton in his theory of gravitation. He showed that tides are generated by the gravitational forces of the sun and moon acting on the rotating earth. He explained the effect of their variations on an earth fully covered by water with the *equilibrium theory of tides*. The theory assumes that the shape of the sea's surface is always in equilibrium with the gravitational forces of the celestial bodies (referred to as forcings). If the earth and moon are on the same axis, the shape of the sea surface will deform, stretching out in both directions along the Earth-Moon axis (See Figure 2.1).
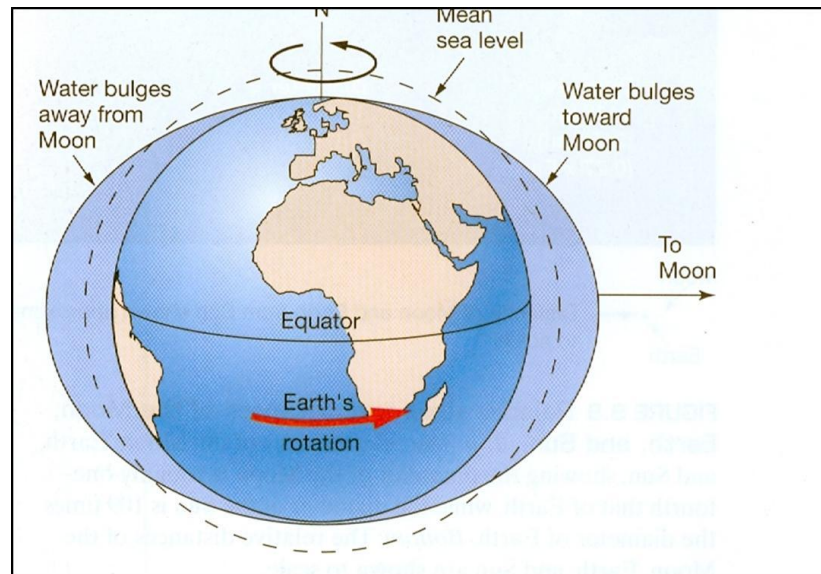
Fig. 2.1: Tidal bulge. Figure taken from http://news-sciences-10.blogspot.com/2018/01/.

In order for the ocean to maintain equilibrium with the forcing, the sea surface bulges, which represent the tides, needs to move laterally through the ocean. The propagation of the signal is described as a surface gravity wave. The speed of propa-

gation is limited by the shallow water wave speed c ($c = \sqrt{gH}$), where g represents the acceleration due to gravity and H the mean water depth (Thompson *et al.*, 2005).

The equilibrium theory of tides explains the fundamental periodicity of the tides on the semidiurnal frequency, i.e. two high tides and two low tides occur per lunar day (24 hr and 50 min). The semidiurnal tidal constituents are M_2 and S_2. The principal lunar semidiurnal component (M_2) has a period of 12.42 hr. Meanwhile, the principal solar semidiurnal component (S_2) presents a period of 12 hr. Additionally, the equilibrium theory correctly explains the spring and neap tides. When the moon and the sun are aligned with the earth, their semidiurnal components interfere constructively, producing tides of higher amplitude (spring tides). If they are in quadrature, the interference is destructive, giving rise to lower amplitudes (neap tides). However, the equilibrium theory does not account for the rotation of the earth about its own axis, the existence of continents, and the inability of the tidal wave to move at the same rate of the earth's rotation (Godin, 1988; Brown *et al.*, 1999).

The dynamic theory was developed by scientists and mathematicians that included Bernoulli, Euler, and Laplace (Brown *et al.*, 1999). Their analysis of tides took into consideration depths, configurations of the ocean basins, the Coriolis force, the inertia of the ocean, and frictional forces. One result of the dynamic theory is the prediction of amphidromic systems in the ocean. Such a system is constituted by amphidromic points, co-range lines, and co-tidal lines of a specific tidal component. By identifying the location with zero amplitude range (amphidromic points), lines of same amplitude (co-range lines), and lines of the same phase (co-tidal lines), it is possible to describe the propagation of tidal waves. Examples of amphidromic systems and tide propagation in an idealised broad and narrow basin, as well as the Gulf of St. Lawrence and the Bay of Fundy in Canada, are presented in Figure 2.2. It illustrates the co-tidal lines (continuous line) and co-range lines (dash lines) on each amphidromic system.

Tides along the edge of an ocean's basin and the coastline tend to propagate
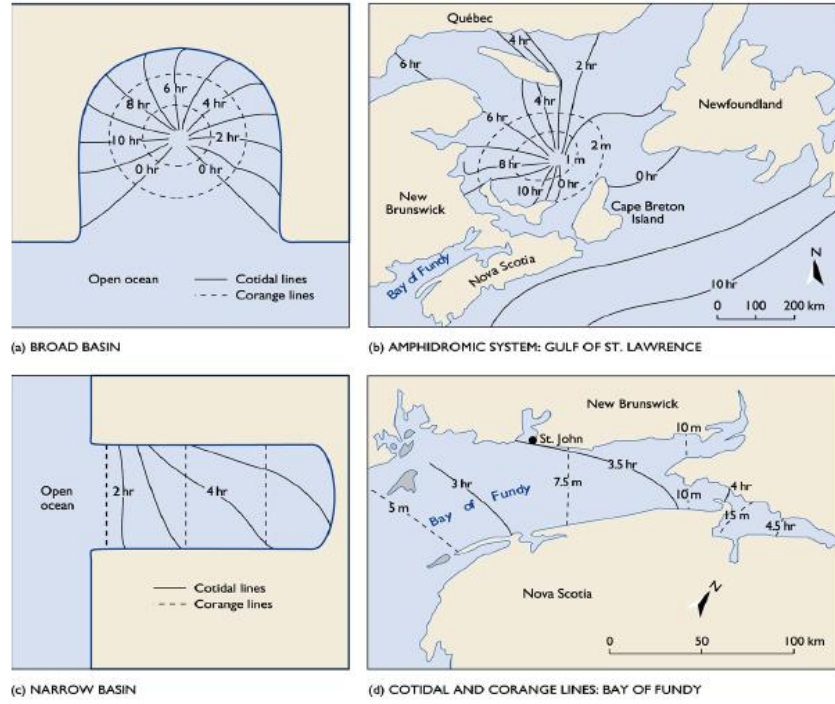
Fig. 2.2: Examples of amphidromic systems at idealised and realistic basins: broad basin (a), narrow basin (c), Gulf of St. Lawrence (b) and the Bay of Fundy (d) in Canada. Figure taken from http://ffden-2.phys.uaf.edu/645fall2003_web.dir/ Ellie_Boyce/cotidal%20corange%20fig.jpg

as a progressive Kelvin wave, this is large-scale wave motion, affected by the earth's rotation. The propagation of a Kelvin wave along a coast produces a higher tidal range on the right side of the wave direction of propagation (on the Northern Hemisphere) (Wang, 2002). The propagation of tides provides information about the tidal currents. Also, the propagation of a tide along a coast leads to interactions with bays or inlets, which are characterised by a length scale L_*. The response of these coastal features to the tide depends on whether L_* represent a wide or narrow bay (Thompson *et al.*, 2005). Tides will propagate around the boundaries of a wide bay. A wide bay implies that its characteristic length L_* is two times larger than the barotropic Rossby radius

L_R ($L_* > 2L_R$):

$$L_R = \frac{\sqrt{gH}}{f} \tag{2.1}$$

where f represents the Coriolis parameter ($f = 2\Omega sin\Psi$), where Ω indicates the angular speed of the earth and Ψ is the latitude. L_R is an indicator of the distance that a wave can travel before being significantly affected by the earth's rotation (Cushman-Roisin and Beckers, 2007). In the case of waves travelling at mid-latitudes, the Rossby radius is $\approx 200km$. Conversely, a narrow bay (or inlet) indicates that L_* is small with respect to the Rossby radius. Under these circumstances, as the tide passes the opening of a inlet, the sea level will rise and lower uniformly. As the wave propagates into the inlet, it encounters reflections from previous wave cycles, then interference of the waves take place. This situation may lead to standing waves (Thompson *et al.*, 2005). A standing wave produces two extreme situations: antinode and node. An antinode is a location where the standing wave has a maximum amplitude, it is a consequence of constructive interference. In this situation, tidal currents present maximum vertical velocities. A node refers to a position where the standing wave has zero amplitude, as a result of destructive interference. Here, maximum tidal currents velocities are horizontal. The location of the nodes and antinodes depend on basin geometry and tidal components (Brown *et al.*, 1999). There are situations in which a water body is forced at its natural period; in this circumstance resonance occurs and extremely large amplitudes take place (Neill and Hashemi, 2018).

Real tidal motion is complicated. The relative movement of the sun and moon with respect to the earth, the interaction of amphidromic points, the ocean irregular shapes and depths and the bottom frictional retardation are factors that increase the complexity of tidal propagation (von Arx, 1962). Nevertheless, it is possible to predict accurately tides propagation and to some extent tidal currents (Adcock *et al.*, 2015). The prediction of the oceanic response to astronomical forcings comes from the consideration that the observed tide is the superposition of tidal frequencies, termed

harmonics or tidal constituents. In this context, the prediction of the surface elevation ζ can be obtained, assuming that the signal is constituted by n finite number of harmonics, in the following way:

$$\zeta_n = h_n cos(\omega_n t - g_n) \tag{2.2}$$

where h_n is the amplitude, g_n the phase lag (e.g. relative to Greenwich), and ω_n is the temporal frequency of the n-constituent. The amplitudes and phases of the harmonics are affected by coastal boundaries and bathymetry (Foreman and Henry, 1989). The harmonic method is used for tidal analysis and prediction (Godin, 1988). The prediction of real tides at a particular point is important, allowing the determination of tidal heights and tidal currents. In the latter case, due to two-dimensional spatial variation, tidal currents are commonly analysed with tidal ellipses. Obtaining suitable measurements of tidal currents for analysis is a complicated task. Ideally, these measurements are obtained from the deployment of current-meters such as ADCP (Acoustic Doppler Current Profiler) (Neill and Hashemi, 2018); however, during initial stages of a tidal project, currents data calculated by numerical simulations are suitable alternatives.

Particularly strong currents can be produced by local geographical constrictions such as narrow straits, channels, off headlands, between islands and landmasses or basins. On these sites, tidal currents are intensified by hydraulic pressure gradients caused by differences in sea-level. These locations may be attractive for exploiting tidal-stream resources.

2.3 Extracting Energy from Tidal Currents

2.3.1 Tidal Energy Resource

Renewable sources of energy have motivated the development of technologies that aims to substitute conventional energy sources such as oil, natural gas, and coal. Con-

ventional energy resources are predicted to be exhausted in the medium-term future (Sleiti, 2017). Additional interest in the development of renewable energy includes the concern for global warming. Since 1850, the global use of fossil fuels has increased to dominate energy supply, leading to a rapid growth in carbon dioxide (CO_2) emissions (IPCC, 2012). In 2017, carbon emissions increased by more than 1.5% from 2016 (BP, 2018). Energy from tides can play a role in the reduction of greenhouse gas emissions (Denny, 2009) and in the mitigation of climate change. Additionally, an appropriate implementation of renewable energy could provide further benefits such as social and economic development, energy access, secure energy supply and reduction of negative impacts on the environment and health (IPCC, 2012).

Tidal energy generation presents a significant advantage over other forms of renewable energy as tides can be predicted over long time periods. In addition, the characterisation of tidal currents at specific potential sites enables the possibility to quantify energy outputs at specific times with high accuracy.

An initial estimation of tidal resources was quantified in terms of tidal energy dissipation by bottom friction (Charlier, 2003). However, it is understood that this represents an upper limit and that a smaller fraction of the global dissipation rate is realistically able to be extracted (Garret and Cummins, 2013). Nevertheless, the global tidal-stream power potential reported is at least 120 GW (Selin, 2018; SIMEC, 2018). Larger estimations of up to 337 GW of wave and tidal energy is the worldwide potential by 2050 (EY, 2013). These numbers would represent a significant percentage of global energy consumption. In Europe, the tidal current technical potential is calculated in 48 TWh/yr (Lewis *et al.*, 2011).

In addition to the large tidal-stream resource potential, implementation of national strategies and the investment of the private sector has accelerated the development of alternative technologies to extract energy from tidal currents. Such is the case with tidal-stream energy conversion systems. The potential of tidal current technologies is

greater than for tidal range (Kempener and Neumann, 2014); the latter is used in tidal barrage structures and tidal lagoons. Tidal current devices have expanded the number of suitable locations for deployment (Nash and Phoenix, 2017; IPCC, 2012). In this way, the design of devices is adapting to the regional and local sites specific needs.

Despite the high cost involved in developing of tidal-stream technology, the final product would provide a sustainable, reliable, and long-term supply of energy.

2.3.2 Tidal-Stream Turbines

The tidal-stream turbine concept represents a less obstructive configuration than tidal barrage structures and tidal lagoons. The latter two alternatives rely on trapping water at high tide and releasing it when there is a sufficient hydrostatic head difference across the barrage (Rourke *et al.*, 2009). Conversely, marine turbines allow flow to pass through the turbine. The current and the pressure difference across the turbine generates power (Garrett and Cummins, 2004). The investigation of an array of tidal-stream turbines distributed at the entrance of a bay indicates that power extraction is as productive as the tidal barrage structures (Garrett and Cummins, 2004). Additionally, it is reported that tidal ranges inside the bay are not strongly affected by power extraction.

The design of marine turbines has been inspired by wind turbines; nevertheless, marine turbines must perform in more challenging conditions. Potential areas for turbine deployment include shallow water areas. Constraints due to sea bottom friction and free-surface are particularly important in shallow water areas. Additionally, water is about 800 times denser than air, thus the loading on the marine turbine blades is higher. Other factors to be considered in the design of marine turbines are reversing tidal currents, erosion due to cavitation, corrosion due to salty water, and biofouling due to an accumulation of organisms on wetted surfaces (Sleiti, 2017).

Broadly, the design of turbines is based on four principles:

- **Flow that passes through a turbine rotates blades:** This concept is referred to as axial-flow turbines (Borthwick, 2016), and is applied to horizontal- and vertical-axis turbines. Horizontal-axis turbines perform better in rectilinear flows and an example of this design is Seagen marine turbine (Douglas *et al.*, 2008) (2.3(a)). A variation of this type of turbine consists of acceleration of the flow by incorporating a constricted section of a duct, which produces a Venturi effect on the flow (Figure 2.3(b)). As the rotor blades rotate, they sweep out a circle, whose area can be used to estimate the blockage ratio, a parameter that influences the thrust of the turbine on the flow, and consequently, the available power. This type of turbine requires significant clearance for the rotor to operate. Additionally, they present a strong swirl component immediately behind the turbine blades.

  Vertical-axis turbines perform better in regions where the tidal current presents higher spatial variations. An example of the concept is the vertical-axis turbine with a spiral blade (Heavey *et al.*, 2017) presented in Figure 2.3(d). This kind of device performs well in relatively shallow flow fields and because they do not need to adjust the turbine blades, the operating system is simpler and maintenance cost is lower. A variation of this kind of turbine is GKinetic (Mannion *et al.*, 2018), which introduces a bluff body between two vertical-axis turbines (Figure 2.3(g)). The bluff body accelerates the upstream flow to the turbines. This modification enables the device to be used in areas of low tidal speeds, expanding the locations where tidal-stream can be extracted.

- **Flow passes across blades:** This type of device seeks to achieve a high flow blockage ratio, and consequently to increase the power extracted. An example of this principle is the Gorlov-type multiple cross flow turbines (Figure 2.3(c)).

- **Flow generates a lift force acting on a hydrofoil:** This idea uses the oscillation of the arm by the stream to drive the hydraulic system that generates the

electricity. An example of this principle is the Biostream Oscillating hydrofoil (Figure 2.3(e)), where the lift force drives rotatory motion of the tail structure. Shallow water environments are suitable locations for oscillating hydrofoils (Neill and Hashemi, 2018).

- **Flow moves a device that flies underwater:** The device is anchored to the sea-bottom and follows an eight-number trajectory by a rudder (Figure 2.3(f)). Following this pattern enables the device (also referred to as a kite) to reach a speed higher than the current speed. As a result, the relative speed of the flow that passes through the turbine is accelerated.
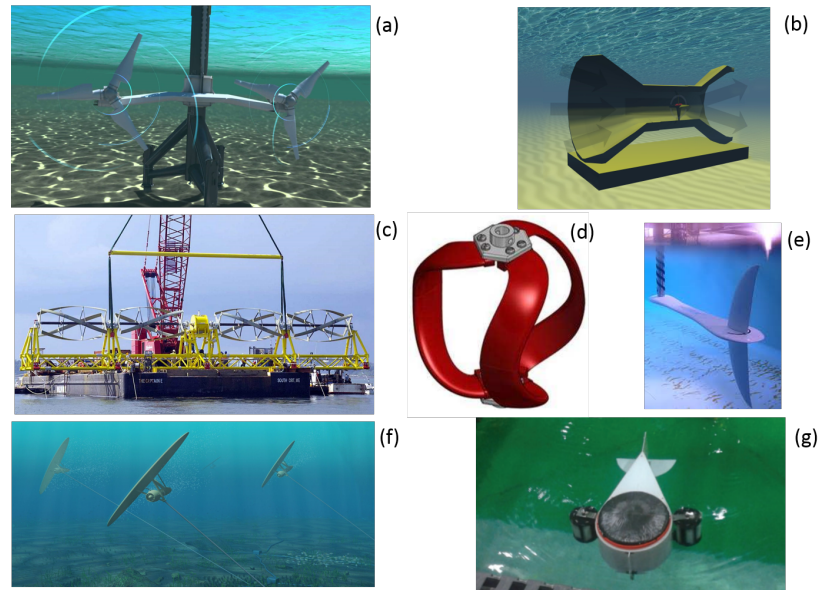
Fig. 2.3: Examples of tidal-stream energy conversion systems. (a) Horizontal-axis, (b) Venturi effect turbine concept (From www.Aquaret.com), (c) Gorlov-type cross flow turbine (From www.orpc.com), (d) Vertical-axis turbine with spiral blade, (e) Biostream Oscillating hydrofoil (From http://bps.energy/biostream), (f) Sea tidal kite (From https://minesto.com), (g) GKinetic tidal turbine.

In the last few years, great effort has been made in the development of turbine technology to bring it from proof of concept stage to demonstration of technical feasibility. Axial turbines with horizontal axis are at the most advanced stage. Turbines

such as Atlantis AK1000 and Atlantis solon-k ducted turbine are designed to extract 1MW (Borthwick, 2016). Another example is the 12 MW twin rotor Marine Current Turbine developed by SeaGen (Neill and Hashemi, 2018). In terms of devices for the low-velocity ocean and tidal currents, a quarter-scale model of the tidal kite developed by Minesto has been tested. It is intended to develop a 1.5 MW deep green small array of full-scale devices in 2017 (Borthwick, 2016; Neill and Hashemi, 2018).

A large number of devices are necessary to extract a significant level of electricity generation i.e. an array format. Additional advantages of the array configuration include the sharing of infrastructure and maintenance cost (Neill and Hashemi, 2018). Suggested configurations imply the covering of a large cross-section of the tidal-stream (Nash *et al.*, 2015; Divett *et al.*, 2013; Draper and Nishino, 2013); however, the turbines' layout needs to consider that the presence of neighbouring turbines alters the flow field. This situation in turn affects the power availability and could also impact the environment negatively (Nash and Phoenix, 2017).

2.4 Tidal Energy Resource Assessment Methodologies

2.4.1 Analytical Approaches

Models have been developed to allow the analysis of the basic mechanism involved in the performance of marine turbines in certain ideal scenarios. These models describe the understanding of the power extraction process and enable the evaluation of tidal-stream energy resources. These theories provide guidance for the identification of optimum turbine arrangements, which maximises energy capture.

In this section, the analytical approaches described in Figure 2.4 are reviewed. Each approach considers a specific type of flow and a turbine configuration. Three types of

flow were considered (i) infinite flow, (ii) finite flow with rigid lid surface, and (iii) finite flow with free-surface, referred to as open channel flow. Here, the actuator disc concept is used to represent the energy captured by a turbine. Three turbine configurations were considered (1) an isolated turbine, (2) full fence configuration, and (3) partial-fence configuration. The constraint complexity increases from an infinite flow (Figure 2.5(a)), to a finite flow (Figure 2.5(b)), and finally to open channel flow (Figure 2.5(c)). Specifications of these analytical models and their contribution to the understanding of the power extraction process by marine turbines are described below.
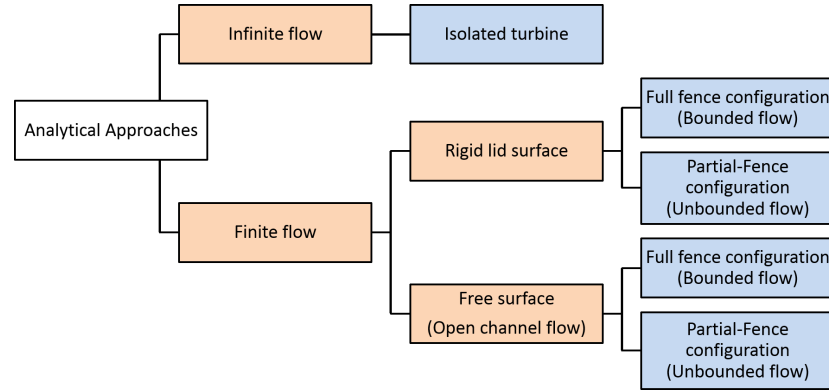
Fig. 2.4: Scheme of the analytical approaches reviewed.

Power extraction using a marine turbine is difficult to estimate due to the resistance offered by the turbine, this resistance causes flow to divert around the turbine. This situation is further complicated to analyse because different length scales are involved, such as the turbine blade, the turbine diameter, and turbine wake length (Draper *et al.*, 2014b). Nevertheless, it is possible to simplify the analysis of the flow structure around the device by representing the turbine as a porous actuator disc. It is considered that the actuator disc, with diameter equivalent to the turbine diameter, exerts uniform resistance, normal to the flow direction. The implementation of the actuator disc requires some assumptions of the flow (Burton *et al.*, 2001). Firstly, flow is considered to be one-dimensional; consequently, the actuator is used to represent

power extraction in symmetric flows. Secondly, the uniform flow entering the stream is considered to be inviscid and steady. In this way, viscous losses are neglected, and vorticity is not generated at the disc. The steady consideration indicates that the flow does not change in time. Additionally, the pressure discontinuity produced by the momentum sink is assumed to be localised, i.e. after momentum extraction pressure equalises across the flow. Finally, the actuator disc approximation enables the use of mass, energy and momentum conservation at specific regions of the flow, to estimate the diversion of flow around the actuator disc, and ultimately, quantify the power extracted (Burton *et al.*, 2001; Draper *et al.*, 2014b).

Initial power extraction estimations represented an isolated turbine as an actuator disc within an infinite flow; this scenario is presented in Figure 2.5(a). This situation better represents wind-turbine operating conditions, but it has been applied to marine turbines. The application is possible if the cross-section of the turbine is small in comparison with the channel cross-section area. The analysis of the actuator disc within an infinite flow leads to the determination of the Lanchester-Betz-Joukowsky limit, which indicates that at most 59% of the upstream kinetic flux (passing through the actuator disc area) can be extracted by the disc and transformed into mechanical energy (van Kuik, 2007). This value indicates a limit to the power generation from wind turbines, and its derivation provided the theory for the design and operation of wind turbines (Ragheb and Ragheb, 2011; Huleihil and Mazor, 2012).

Initial tidal-stream resource assessment was determined based on incoming kinetic energy flux across the undisturbed state (Blunden and Bahaj, 2006). The estimation was constrained by introducing secondary parameters such as the significant impact factor (SFI), or shape parameters. The SFI indicates the percentage of the total resource that can be extracted without causing significant changes to flow momentum, or significant environmental impact to the site (Ltd, 2005). The shape parameters account for velocity availability and the neap/spring variation (Fraenkel, 2002). In UK
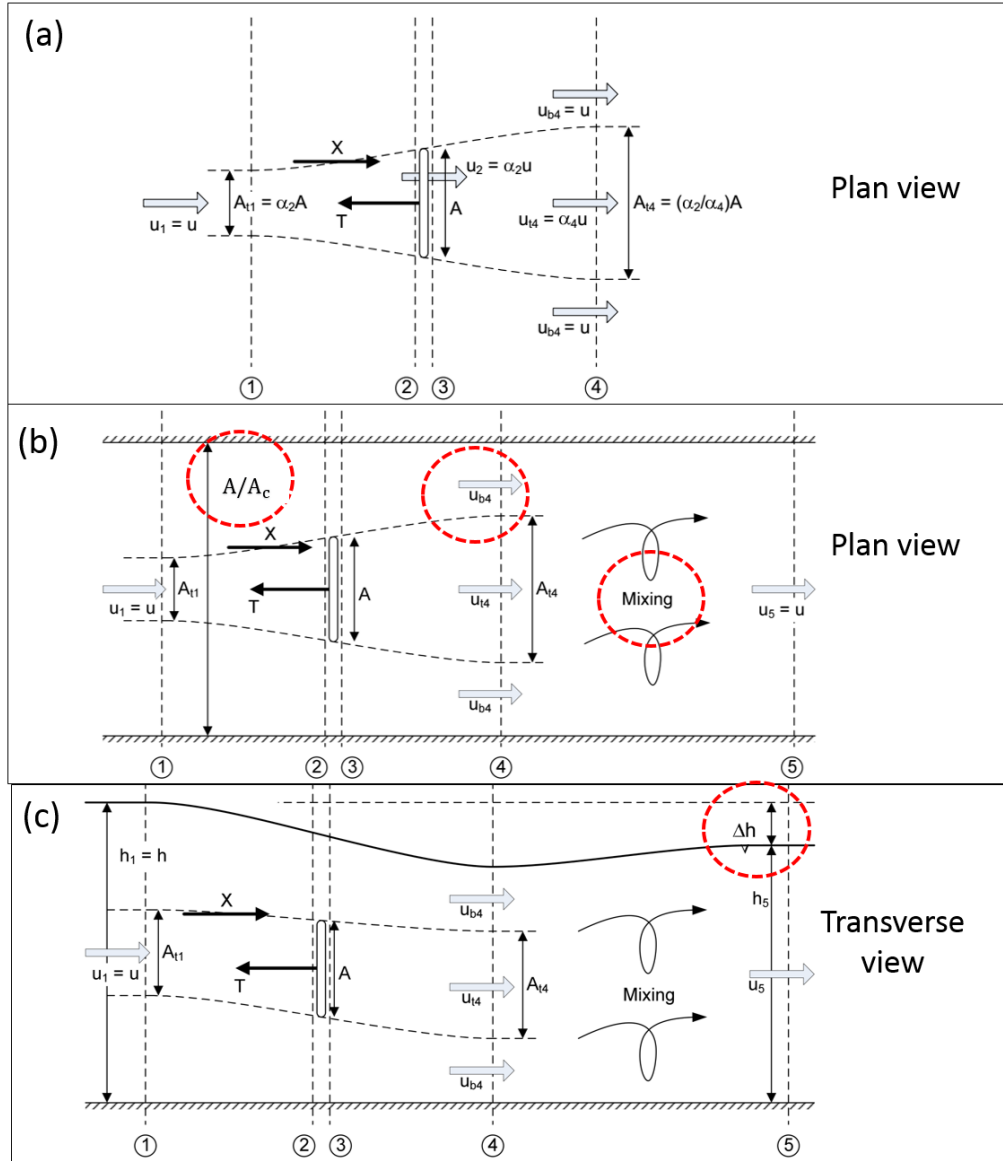
Fig. 2.5: Analytical schemes of tidal-stream power extraction with an actuator disc: infinite flow (a), finite flow (b), and open channel flow (c). Main contributions introduced by each approach are denoted by red dashed-line circle. Figures taken from Draper (2011).

sites an upper limit for the available resource was defined using 20% SIF factor (Ltd, 2005). Meanwhile, in Irish sites a mean power output available was obtained (Fraenkel, 2002). However, the approaches failed to represent the true potential of the sites as

the maximum extractable power is related to the mean kinetic energy flux only for particular channels (Draper, 2011; Adcock *et al.*, 2015). In addition, the kinetic energy flux through a channel does not account for the *back effect* of turbines on the current (Blunden and Bahaj, 2006; Garrett and Cummins, 2008). This effect refers to the free stream flow reduction throughout the channel due to the power extraction by an array of turbines. The operation of devices increases the total drag in a channel resulting in a flow rate reduction.

To study a flow with features representative of the marine environment it is necessary to include constraints which the tidal-stream is subject to on the bottom of the sea and at the surface. A flow with finite extents limited by a bottom constraint and a rigid lid surface was proposed by (Garrett and Cummins, 2005); this scenario is presented in Figure 2.5(b). Analysis of the actuator disc within a finite flow incorporates turbine bypass flow (U_{b4}), turbine blockage ratio $B = A/A_c$, and a turbine-downstream mixing region. B indicates the fraction of the channel cross-sectional area occupied by the turbine, where A and A_c indicate the cross-sectional area of the turbine and the channel, respectively. Analysis of tidal flow considers a core-flow, which experiences velocity reduction when passing through the turbine due to the momentum loss, and a bypass flow that experiences velocity intensification when circumventing the turbine. The downstream mixing region represents the location where the reduced velocity turbine's wake merges with the faster bypass flow.

An ideal scenario to study the performance of a marine turbine is a bounded inviscid flow (Nishino and Willden, 2012a). This situation is obtained within a channel where regularly spacing turbines are deployed in the middle of the channel. Here, the turbines are placed in a row that fully occupy the channel cross section. This turbine configuration is referred to as a fence. This configuration forces the flow through the turbine array, producing uniform tidal current across the channel. The implementation of a fence allows uniform conditions of power extraction along the cross section of the

channel. As a result, the power extracted by a single turbine describes the power extraction conditions within a fence.

The analysis of maximum average power extracted by a fence of turbines led to an analytical model that related power extracted to flow reduction. Garrett and Cummins (2005) identified that power extraction rate tends to increase as more turbines are added to a fence; however, after reaching a maximum value e power decreases as the flow become choked. The maximum power that can be extracted is represented by:

$$P_{max} = \gamma \rho g a Q_{max} \tag{2.3}$$

P_{max} is a function of tidal head difference across the channel a, acceleration due to gravity g, peak volume flux at the undisturbed state Q_{max}, and a factor γ accounting for tidal dynamics during the channel at the natural state. The latter factor varies within the range $0.20 < \gamma < 0.24$ depending on whether the flow is dominated by acceleration or dominated by friction and flow separation at the channel exit and entrance. This analytical model has been corroborated numerically (Sutherland *et al.*, 2007; Draper *et al.*, 2010).

A flow of finite extent subjected to power extraction by a turbine fence provides an understanding of the blockage ratio B effect of a turbine within the water column (Garrett and Cummins, 2007). Considering a turbine operating at optimum conditions, Garrett and Cummins (2007) identified that the maximum power extracted by a turbine placed in a channel is proportional to the factor $(1-B)^{-2}$. This result indicates that the presence of the boundaries increase the Lanchester-Betz limit by a factor of $(1-B)^{-2}$ i.e. in optimal conditions the turbines can convert a larger amount of kinetic energy into mechanical energy due consideration of the boundaries. Additionally, the consideration of the turbine wake mixing region in the analysis of the bounded flow with rigid surface enables the calculation of turbine efficiency. The efficiency is defined as the ratio of power available to the turbine to the total power extracted from the stream, where the total power includes power dissipated due to wake mixing and bottom friction.

The analysis of bounded finite flow was refined by Whelan *et al.* (2007) who introduced free-surface flow. This type of boundary is justified by the fact that turbines will operate in relatively shallow water and the proximity of free-surface will influence flow evolution and momentum extraction (Whelan *et al.*, 2009). The free-surface consideration enables the quantification of pressure changes due to power extraction, occurring at the region of the turbine. Contrary to the rigid lid flow, where the F_r number is considered to be zero, the finite flow with free-surface implies $F_r > 0$. This property enables the characterisation of free-surface deformation across an array; the head drop consideration is consistent with observations that report a water drop immediately behind an operating rotor (Myers and Bahaj, 2007). An expression for the turbine's power and thrust coefficients was derived by Whelan *et al.* (2009). The coefficients are functions of flow conditions, defined by the upstream Froude number, and the operating conditions of the turbine, defined by its blockage ratio and porosity. Turbine porosity reflects velocity reduction at a turbine. The solution for free-surface finite flow is valid for sub-critical flows. This restriction limits the upstream Froude number and the operating conditions of the turbine. This analytical model has been validated with experimental tests and numerical simulations (Whelan *et al.*, 2009).

The analysis of a bounded flow with deformable surface was extended by Houlsby *et al.* (2008), who included a turbine-wake mixing region. This scenario is referred to as an actuator disc in open channel flow, and it is described by the sketch presented in Figure 2.5(c). The consideration of the free-surface scenario together with the mixing region provides a better description of turbine operating conditions (Draper *et al.*, 2010). The identification of power dissipation provides a measure of turbine efficiency. As the power extracted from a tidal site is finite, estimation of turbine efficiency in addition to the power coefficient becomes important in the design of turbines (Draper, 2011). Furthermore, the inclusion of a mixing region in the analysis enables the determination of a relationship between flow conditions at the turbine's upstream and down-

stream locations. This relationship is a function of the turbine operating conditions, which are determined by the size of the turbines and their inter-spacing (characteristics represented by the blockage ratio) and the porosity of the devices (Draper, 2011). The relationship between the upstream and downstream conditions of flow reported by Houlsby *et al.* (2008) refers to the relative change of water elevation across a turbine. The water elevation change due to power extraction provides the basis to enable the simulation of turbines as a line sink of momentum in a depth-average model (Draper, 2011; Serhadlioglu, 2014).

In the case of a partial-fence configuration i.e. a row of turbines arrayed across only a part of the channel cross-section, it is reported that this configuration separates the flow in two: one stream passes through the array (array core flow), and the other stream flows past it (array bypass flow). This situation is referred to as laterally unbounded flow. Further discussion of this scenario is presented in Section 6.3. Two main analytical models have been developed to describe the power extraction for laterally unbounded flows (i) LMAD-OCH and (ii) Two scales approaches:
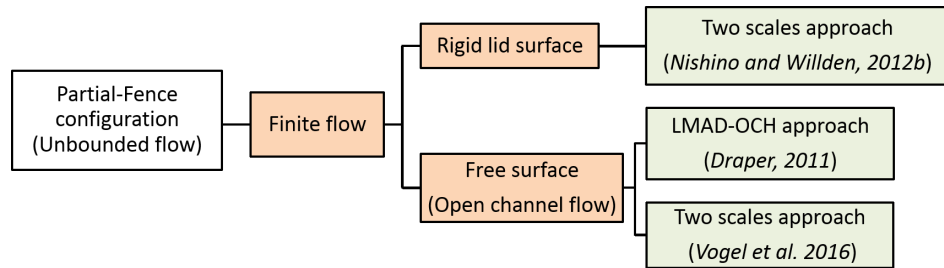
Fig. 2.6: Scheme of the analytical approaches reviewed for a partial-fence configuration.

The LMAD-OCH theory studies a partial-fence as a long row (Draper *et al.*, 2010), in this way, upstream conditions can be assumed to be uniform, and marine turbines within the array can be represented by actuator discs. This approach focusses on the estimation of the momentum extracted by a partial-fence and provides information on energy lost by turbine-wake mixing. However, the analysis does not include array-wake

mixing that takes place at a larger scale (Draper, 2011).

The second approach studies laterally unbounded flows produced by the deployment of the partial-fence as the coupling of the turbine- and array-scale. Initially, a long row was considered, and in this way the two scales were analysed independently. A long row allows for the consideration that the flow around a turbine occurs much faster than the horizontal expansion of the flow around an entire array (Nishino and Willden, 2012b). In addition, the partial-fence scenario is described with two different types of blockages, referred to as the local and global blockage ratio (Nishino and Willden, 2012b). The two-scale approach originally considered a rigid lid approximation. Later, this approach became less restrictive with respect to the row length extent; a better allowance for the interaction of the device- and array-scale flow events enabled the analytical study of short rows (Nishino and Willden, 2013b). Recently, Vogel *et al.* (2016) included a deformable free-surface in the two-scale approach. This assumption enables the consideration of finite Froude numbers, where increasing Froude number led to larger power extraction coefficients.

Analytical models provide an understanding of the physics involved in tidal-stream power extraction. However, a more complete analysis of the tidal resource requires (i) the simulation of tidal-streams through tidal channels and coastal features, and (ii) estimation of energy capture by turbines. Numerical models have the capability to perform these tasks, enabling the analysis of the power extraction process and its implications on the regional hydrodynamics. Additionally, numerical schemes represent economic alternatives to perform resource characterisation. In-situ measurement campaigns are expensive, especially at locations where strong tidal currents are present. Therefore, numerical tidal-stream resource assessment is useful particularly at early stages of a tidal energy project, prior to site selection and investment in costly field campaigns (Neill and Hashemi, 2018). In the following section, a brief description of the main methodologies used to perform numerical tidal resource assessment are presented.

2.4.2 Numerical Approaches

Power generation from tidal-streams involves the interaction of different scale problems. Five scales can be identified: blade scale, turbine scale, array scale, site scale and regional scale (Adcock *et al.*, 2015). Numerical methods have proven to be valuable tools to provide understanding of the different scales involved in the development of tidal power extraction technology.

In particular, herein the regional scale is analysed; it considers the large-scale effects of tidal-stream turbines on tidal dynamics. The characteristic length of this scale is $10^1 < L_* < 10^6$ m. The assessment of tidal resources at regional scale requires the specification of three aspects: a numerical model approach, the tidal energy extraction representation, and domain size (Adcock *et al.*, 2015). Depth-average models are suitable tools for studying far-field velocities and elevations and consequently, useful to simulate the effects of turbine arrays.

Marine turbine numerical representation is based on quantification of the momentum extracted by turbines. Three main approaches have been implemented to simulate energy extracted from tidal-streams. They are based on the approximation of: (i) drag effects of turbines (bed roughness), (ii) axial component of thrust force produced by turbines on flow (momentum sink), and (iii) the modification of mass flux passing through turbine-fence (line sink of momentum) approach implemented in models which use a shock fitting method to simulate RVF.

The bottom roughness approach accounts for the momentum extracted by the turbine with the addition of a quadratic bottom friction term in the region where turbine arrays are located (Bryden *et al.*, 2004; Bryden and Couch, 2007; Blanchfield *et al.*, 2008). Garrett and Cummins (2005) identified that in a finite flow, the depth-average drag force imparted by the device on the flow is proportional to the square of the flow rate. This result encouraged the implementation of the bottom roughness

approach to represent turbines as a first approximation. However, this method is not able to simulate array configurations such as rows of turbines (Serhadlioglu, 2014) and neither does it account for flow directionality (Nash and Phoenix, 2017). Also, the total power simulated does not differentiate between the power available to the turbine and the power lost due to wake mixing and frictional forces (Draper, 2011).

The bottom roughness approach has been used to assess the maximum tidal power potential in the Johnstone Strait, BC, Canada (Sutherland *et al.*, 2007), and the Minas Passage in Canada (Karsten *et al.*, 2008). In both situations, the flow reduction and the estimated maximum power extraction is consistent with the analytic theory described by Garrett and Cummins (2005). In the case of the Minas Passage, Karsten *et al.* (2008) reported that extracting maximum power produces significant changes to the tidal amplitudes; however, a large percentage of power (35%) can be extracted with a maximum 5% change in the tidal range in the Minas passage and the Bay of Fundy–Gulf of Maine system. The increase of bed friction to represent marine turbines in small passages has been criticised by Serhadlioglu (2014), who indicates that this implementation emulates the effect of constructing a barrage across the Minas passage.

The momentum sink approach was developed to improve the numerical representation of marine turbines. This method accounts for flow directionality and is a widely used technique. The sink term accounts for the flow momentum extracted by the axial component of a turbine's thrust force. This is accomplished by adding a sink term to the momentum equations (the turbine's numerical representation used in the present thesis is based on the sink term approach). In the case of simulations of far-field flows, the spatial resolution is coarse, and a single grid-cell contains a cluster of turbines. Therefore, the thrust force simulation corresponds to the resultant effect of the turbine's cluster. Further description of the momentum sink is presented in Section 4.3.2.

The sink term has been used to study the hydrodynamical impact of power extraction from turbine-arrays in two-dimensions for different turbine-array layouts (Ahmadian *et al.*, 2012a; Ahmadian and Falconer, 2012). The sink term produced by power extraction was further refined by the specification of turbine-area components on $x-$ and $y-$ directions (Fallon, 2012; O'Brien, 2013). The turbine area quantification within the grid, based on the turbine inter-spacing specification, enables the study of hydrodynamical effects of the inter-turbine spacing and far field hydro-environmental impacts of tidal turbine arrays (Hartnett *et al.*, 2012; Fallon *et al.*, 2014; Nash *et al.*, 2014). The sink term has also been implemented in nested models to study higher resolution domains with a depth-average model at cheaper computational cost (O'Brien, 2013). The sink term and a nested capability have been used to simulate far-field hydrodynamic effects of turbine arrays, where turbines were simulated at the resolution of a turbine diameter (Nash *et al.*, 2015; Phoenix, 2017). The simulation at this spatial scale provides information on the turbine interactions and consequently, the hydrodynamic impacts of individual turbines.

In terms of three dimensional simulations, the momentum sink method has also been adopted in nested models, to investigate the turbine-scale hydrodynamics (Coppinger, 2016). The method has also been used in models such as FLUENT, to study energy extraction effects on the local-flow in two and three dimensions from within the water column in a tidal flow (Sun *et al.*, 2008). Additionally, the approach was used to study far-field impacts of tidal power extraction via turbine arrays, such as the effect on the large-scale sediment dynamics, through an idealised headland sand bank formation (Neill *et al.*, 2012); the effect on tidal currents in the Tory Channel, New Zealand (Plew and Stevens, 2013); and the influence on the hydrodynamics of Ria de Ribadeo (NW Spain) (Ramos *et al.*, 2013). Finally, the momentum sink has also been implemented in ocean circulation models (Sheng *et al.*, 2012), to investigate the far-field effect of tidal energy extraction on tidal, wind-driven, and density-driven

currents, as well as the effects on the temperature/salinity fields in the Bay of Fundy, the adjacent Gulf of Maine, and the western Scotian Shelf.

A drawback of this conventional methodology is that the momentum sink computation does not consider natural boundaries of the tidal-streams. In coastal areas, tidal-streams are subject to seabed and free-surface. The consideration of these boundaries is relevant because they can significantly increase the power that can be extracted from the flow. Additionally, the resource characterisation does not discriminate between the power available to the turbine and the power lost by dissipation. This is a consequence of the way the momentum extracted by the turbine is calculated. The momentum sink approach calculates the momentum extracted by a disc, without considering the operating conditions of the turbine (given by the size, inter-turbine spacing, and porosity). The porosity of a turbine indicates the rate of reduction experienced by the velocity at the turbine with respect to the upstream velocity (Draper, 2011; Johnson *et al.*, 2014). A disc with low porosity will exert a larger force on the fluid, as less fluid will pass through the turbine and consequently, the flow will present a strong magnitude reduction at the turbine. Meanwhile, a disc with high porosity will exert a smaller force on the fluid, the flow velocity through the disc will be high, and the velocity reduction will be lower.

The operating conditions of the turbine are important for the correct simulation of the force exerted by the turbine on flow. Their inclusion allows a more realistic assessment of the power extracted by the device (where the power corresponds to the force exerted by the disc times the velocity of the fluid passing through the disc). A final disadvantage of momentum sink method described above is that it is used only to solve SSF; this type of flow does not experience strong spatial gradients. According to the linear momentum actuator disc in an open channel flow (LMAD-OCH) theory, the capability to solve RVF is important in the simulation of the power extracted by arrays of turbines.

32

The line sink of momentum was developed to account for the turbine operating conditions in the simulation of momentum extracted by a turbine (Draper *et al.*, 2010). This approach is based on the numerical application of the LMAD-OCH theory. This analytical model develops a relationship between upstream and downstream depth-average velocities and depths as a function of turbine operating conditions. This relationship refers to relative change of water elevation across an array of turbines (Houlsby *et al.*, 2008). A numerical scheme that solves rapidly varying flow is required to solve the depth-average velocity and depth discontinuity produced by power extraction due to the array. The line sink of momentum was implemented numerically by Draper *et al.* (2010); Draper (2011) in a discontinuous Galerkin finite element method. This model is a Gudonov type, and treats the discontinuities in the flow as an internal boundary. The implementation of the line sink of momentum sets the relative change of the water elevation as the internal boundary. This change in the elevation due to power extraction is derived from the LMAD-OCH theory. Further description of the line sink of momentum is presented in Section 4.3.1.

This method has been used to assess the tidal-stream potential of turbines configured as a fence that completely traverses a cross-section of an idealised channel (Draper *et al.*, 2010). Such a configuration has also been used in the Pentland Firth to estimate the maximum power extracted: 4.2 GW (Draper *et al.*, 2014c). Estimations of the extractable power of sub-channels was also investigated, but the power varies according to the device operating conditions within the fences. A further refinement estimation of the Pentland Firth potential is given by Adcock *et al.* (2013). They estimated an upper limit for the tidal-stream power resource based on a large, but viable blockage ratio of 0.4; this estimation is more conservative at 1.9 GW.

The line sink of momentum has also been used to assess the tidal resource with partial-fences. The method has been used to numerically estimate the force applied

by a porous disc in scale experiments (Draper *et al.*, 2013b). They studied the momentum extracted by porous discs arranged in two configurations: firstly, as a fence in the middle of the channel, and secondly, as a partial-fence near a headland. They compared measurements of the force applied by the porous disc on the flow with numerical predictions of the thrust force. The comparison indicates a notable agreement (within 10 %), except for the porous disc closest to the headland. The performance of a partial-fence has also been studied at an idealised coastal headland (Draper *et al.*, 2013a). In this case, the line sink was used to identify the power available (defined as the total extracted power, less the power lost by vertical mixing in the immediate wake of the devices).

Draper *et al.* (2013a) identified that the flow bypassing partial-fences reduces the mass flux passing through the devices, a situation that results in a decrease of power extracted. This effect was intensified when larger blockage ratios were used, as they produce a larger thrust force on the flow. Finally, the method has been used to investigate a farm composed of partial-fences in the Anglesey Skerries, off the Welsh coast (Serhadlıoğlu *et al.*, 2013). They investigated the roles of turbine operating conditions, array connectivity, and location of partial-fences in the estimation of the power available.

A limitation of this recent approach is the use of an expensive computational technique which constraint the head drop produced by power extraction. This modern methodology use a rapidly varying flows solver and Shock fitting technique. Pre-specification of relative change of the water elevation across an array required by the numerical scheme reduce the possibility to represent realistic scenarios. Additionally, the changes in velocity and depth produced by power extraction at the region of the array may have to be solved using a rapidly varying flow scheme. This last point is particularly important in terms of computational requirements, because RVF simulations present high computational cost (Liang *et al.*, 2006).

Consequently, it was considered worthwhile if a RVF solution procedure is required for correct numerical assessment of tidal-stream resources in this research.

2.5   Summary

An overview of the literature review performed and the main points discussed are shown schematically in Figure 2.7. Highlighted in blue are the areas where this research has contributed to.
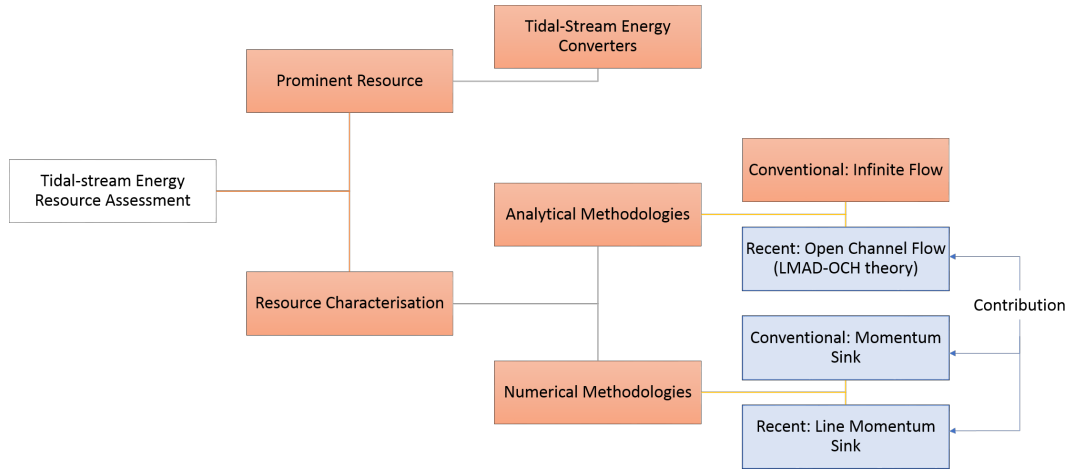
Fig. 2.7: Literature review scheme.

Tidal currents are a prominent energy resource in many locations worldwide, particularly at coastal areas where bathymetric constraints enhance the magnitude of the current velocities. In Ireland, there are eleven potential sites for tidal current energy extraction. The main areas are located on the East, West and North coast of Ireland, where the elevation amplitudes of the semidiurnal frequencies are significant.

Potential sites for tidal resource harvesting require a realistic assessment of the resource and a reliable simulation of the large-scale effects of turbine arrays on tidal dynamics. The simulation of marine turbines at the regional scale, characterised by its length scale, allows for the analysis of the performance of arrays of turbines. Depth-

average models are appropriate numerical tools to simulate turbine arrays and to assess tidal-stream resources at the regional scale.

Tidal stream resource assessment at regional scales requires the numerical representation of marine turbine arrays. The conventional momentum sink approach and the recent line sink of momentum methodology compute the momentum extracted by arrays accounting for flow directionality and inter-turbine spacing.

The line sink of momentum is based on the LMAD-OCH theory. This analytical model includes tidal-streams natural constraints in the power extraction analysis and enables the determination of a relationship between upstream and downstream conditions of the flow to the turbine operating conditions. The flow conditions are prescribed by the depth-averaged velocities and depths. This relationship is given by a predetermined difference of the water elevation across the turbine. A line sink of momentum takes into account that the changes in velocity and depth produced by power extraction can be considered as a discontinuity in the velocity and depth field. The changes produced by power extraction at the turbine near-field had been solved with a expensive shock fitting technique and RVF solver. The line sink of momentum was introduced in a Godunov-type scheme that treats the discontinuity of variables as an internal boundary. The scheme sets this internal boundary as a change in water elevation across a turbine array.

A method that enables the consideration of the turbine operating conditions in the numerical representation of the array, which additionally does not constrain the water elevation would provide a representation of the turbine closer to realistic scenarios. This method can be developed from the momentum sink. This method computes the axial component of the thrust force exerted by the turbines on the flow. An additional advantage of the simulation of the momentum sink extracted by a turbine, based on the operating conditions of the marine turbine, is the possibility of investigating the role of numerical solution schemes.

The present research improves the conventional methodology to assess the tidal-stream resource by accomplishing the following points:

- Incorporation of natural constraints of tidal-streams in coastal areas in the evaluation of the resource.

- Inclusion of turbine operating conditions into the energy capture computations.

- Incorporation of turbine near-field changes produced in depth-average velocities and depths due to power captured into energy capture simulations.

- Development of a method to numerically represent marine turbines, which does not constrain the head drop across a turbine array produced by power extraction.

- Investigation of the solution procedure relevance to simulating energy capture by turbines, by implementing the method mentioned above in two numerical models: one solves SSF and the other solves RVF.

The turbine representation developed in this thesis is different from previous research which concerns two-dimensional tidal flow modelling for tidal resource assessment. The novel method proposed in this research, together with the tidal-stream resource assessment procedure implemented, enables the estimation of the turbine efficiency. The calculation of this parameter together with the head drop across turbine arrays enable the differentiation of total power extracted from available electrical power. This property, in addition to the calculation of further power metrics specified in Section 4.2, provides a more complete analysis of the resource than conventional evaluation of tidal-streams. Additionally, the turbine representation is incorporated in hydrodynamic models, which are able to simulate flooding and drying process. This feature is particularly important for assessment of complex sites such as estuaries where mudflats can represent a significant percentage of the site. Finally, the models developed enable the analysis of configurations such farms of arrays, which is an important aspect as it

is accepted that a large number of turbines is needed to produce a significant amount of power.

The methodology proposed in this thesis (i) represents marine turbine arrays in depth-average models and (ii) evaluates the tidal-stream resource, it is described in **Chapter 4**. The numerical representation of the turbines was incorporated into two schemes, the first solves SSF and the second solves RVF. The resultant models are referred to as ADI-TOC, and TVD-TOC, respectively.

The validation of the method proposed in this thesis to numerically represent the turbine array is presented in **Chapter 5**. Here, an ideal turbine configuration; tidal fence, is used to evaluate how accurately models compute changes produced by power extraction in the flow, within the turbine near-field extent. An assessment of this method is completed with a benchmarking of the energy captured by turbines computed by both models. Additionally, the computational performance of the scheme that solves SSF and RVF are compared.

In **Chapter 6**, the methodology proposed by this thesis to numerically represent turbines and to assess tidal-streams is compared to a conventional strategy, which simulates turbines and evaluates the resource. The methodology proposed is then used to evaluate the performance of a more realistic turbine configuration; a partial-fence. In addition, the influence of a fence and partial-fence on hydrodynamics of a tidal channel is investigated. Finally, the performance of both configurations in terms of power extraction is studied for a range of realistic blockage ratios.

Chapter 3

Numerical Solution of Depth-average Flow

3.1 Introduction

Numerical solutions of the depth average flow fields, simulated at the regional scale, are presented in this chapter. Section 3.2 provides an overview of the general equations that describe the evolution of two-dimensional shallow water flows and the limitations of the depth-average approach. Section 3.3 introduces the governing equations of a tidal stream that passes through a tidal channel, experiencing momentum loss due to power extraction; the non-conservative and conservative form of the governing equations are presented. Section 3.4 describes the numerical methods used to discretise the governing equations; also, this section provides an overview of numerical methods for shock problems used to solve RVF. Additionally, an introduction to parallel computing is given. Section 3.5 describes the numerical models used in this research study, in their original form. Finally, Section 3.6 summarises this chapter.

3.2   Two-Dimensional Shallow Water Equations

In coastal and estuarine flows where vertical accelerations are small in compari-
son with horizontal accelerations, and the flow is well-mixed vertically, flows can be
described with a two-dimensional depth integrated version of the shallow water equa-
tions (2D-SWEs) (Falconer, 1993).

The two-dimensional SWEs are derived from the depth-average Navier-Stokes equa-
tions. Their derivation required certain assumptions to be made with respect to (i)
density variation, (ii) Reynolds' stresses, which represent time and spatial fluctuations
of velocity, (iii) the relationship between the horizontal and vertical characteristic spa-
tial scales, and (iv) the behaviour of flows at boundaries (Weiyan, 1992; Kundu and
Cohen, 2002).

The first assumption refers to the consideration of small density variations along
a fluid path. In this case, density can be assumed to be constant in all terms of
the continuity and momentum equations, except the gravitational term (Boussinesq
approximation) (Vallis, 2005). The second assumption considers that the Reynolds'
stresses depend on the deformation of the mean flow, introducing an eddy viscosity
concept (Stewart, 2004). The third consideration refers to the shallow flow, which
satisfies two relations: (a) the characteristic horizontal scale L, which is much larger
than the characteristic vertical length scale h, and (b) the characteristic vertical velocity
w is small in comparison with the characteristic horizontal velocity u. Further, the
flow is considered to be constrained at the boundaries: at the bottom flow is subject to
roughness and at the surface flow may present a deformable surface affected by wind
stress.

To treat turbulent motion in the equations, the Boussinesq approximation is used.
It allows the omission of the turbulent components of the velocity and introduces
the eddy viscosity ε (Cushman-Roisin and Beckers, 2007). When applying the afore-
mentioned assumptions to the Navier-Stokes and continuity equation, it is possible to

obtain a flow with a hydrostatic pressure distribution from the vertical momentum equation (Vallis, 2005). To obtain the depth-average continuity equation and the $x-$ and $y-$ components of the momentum equations, the continuity and momentum equation have to be integrated with respect to depth. This depth integration also applies to eddy viscosity and shear stress terms of the bed. The limits of integration consider the following boundary conditions: a no-slip boundary at the base, and a kinematic boundary at the free surface. The final expressions of the 2D-SWEs for the continuity equation, $x-$component and $y-$component of the momentum equation are given by equations 3.1, 3.2, and 3.3.

$$\frac{\partial \zeta}{\partial t} + \frac{\partial q_x}{\partial x} + \frac{\partial q_y}{\partial y} = 0 \tag{3.1}$$

$$\overbrace{\frac{\partial q_x}{\partial t}}^{\text{Local acceleration}} + \overbrace{\beta \left(\frac{\partial U q_x}{\partial x} + \frac{\partial U q_y}{\partial y} \right)}^{\text{Advective accelerations}} = \underbrace{f\, q_y}_{\text{Coriolis force}} - \underbrace{gH \frac{\partial \zeta}{\partial x}}_{\text{Pressure gradient}}$$
$$+ \underbrace{\frac{\tau_{xw}}{\rho}}_{\text{Wind shear force}} - \underbrace{\frac{\tau_{xb}}{\rho}}_{\text{Bed shear resistance}} + \tag{3.2}$$
$$\underbrace{2\frac{\partial}{\partial x}\left(\bar{\varepsilon} H \frac{\partial U}{\partial x} \right) + \frac{\partial}{\partial y}\left(\bar{\varepsilon} H \left(\frac{\partial U}{\partial y} + \frac{\partial V}{\partial x} \right) \right)}_{\text{Turbulent diffusion term}}$$

$$\frac{\partial q_y}{\partial t} + \beta \left(\frac{\partial V q_x}{\partial x} + \frac{\partial V q_y}{\partial y} \right) = fq_x - gH \frac{\partial \zeta}{\partial y} + \frac{\tau_{yw}}{\rho}$$
$$-\frac{\tau_{yb}}{\rho} + 2\frac{\partial}{\partial y}\left(\bar{\varepsilon} H \frac{\partial V}{\partial y} \right) + \frac{\partial}{\partial y}\left(\bar{\varepsilon} H \left(\frac{\partial V}{\partial x} + \frac{\partial U}{\partial y} \right) \right) \tag{3.3}$$

The momentum equations describe source and sink terms in the flow description. These terms are given by the local acceleration, advective accelerations, Coriolis force,

41

pressure force, wind shear force, bed shear resistance, and the turbulent diffusion term. The terms presented in the equations are defined in Table 3.1.

3.2.1 Limitations of the Depth-Average Representation

The two-dimensional SWEs describe flow phenomena at a regional scale. This scale can consider the large-scale effects of tidal stream turbines on tidal dynamics. The characteristic length of this scale is of the order of $10^1 < L < 10^6$ m (Adcock *et al.*, 2015). At the regional scale, tidal elevations can be modelled correctly, in a computationally efficient way, using depth-averaged numerical models (Stelling *et al.*, 1986; Rodenhuis, 1994). Thus depth-average models can simulate bulk flow through tidal channels and around coastal features. This is an advantage when analysing regional scales, as the assessment of tidal streams for large arrays of turbines is based on bulk flow (Adcock *et al.*, 2015). Nevertheless, depth-average models provide poor spatial reproduction of currents locally within the tidal channel or near coastal features. This is attributed to the incapacity of the models to correctly capture the dynamics of turbulent mixing generated by coastal features. In shallow environments coastal features such as islands and headlands, behave as obstacles to the flow. Behind the obstacle, turbulent flows are generated these are referred to as shallow wakes (Ghidaoui *et al.*, 2006). The presence of shallow wakes indicate that the flow is sheared significantly in the horizontal plane (Stansby, 2006; Serhadlioglu, 2014). These wakes are usually defined by a stability parameter. Stansby (2006) reported that depth-averaged simulations are not able to estimate the mixing length of shallow wakes correctly.

It is suggested that modelling of regional hydrodynamics scale is unlikely to be affected by the three-dimensional flow structure (Draper, 2011). Nevertheless, the limitation of depth-average modelling to capture vertical velocity variations, due to secondary flows produced by vertical shear and bathymetric features, restricts the scheme. For instance, depth-average models are not able to reproduce smaller scale

Term	Expression (units)	Specification
Depth-average velocity flux component in the x-direction	q_x (m^2/s)	$q_x = UH$
Depth-average velocity flux component in the y-direction	q_y (m^2/s)	$q_y = VH$
Time	t (s)	
Momentum correction factor for non-uniform vertical velocity profile	β	$\beta = 1 + \frac{g}{C^2\kappa^2}$ κ: von Karman's constant $= 0.4$ C_e: Chezy roughness coefficient (m^2/s)
Depth-average component of the velocity along the x-direction	U (m/s)	
Depth-average component of the velocity along the y-direction	V (m/s)	
Coriolis parameter	f $(1/s)$	$f = \omega \sin\phi$ ω: Earth's rotational angular velocity ϕ: Latitude of the site
Gravitational acceleration	g (m/s^2)	
Total water depth	H (m)	$H = h + \zeta$ h: Mean water depth ζ: Surface elevation change with respect to h
Density of the flow	ρ (kg/m^3)	
x-direction surface shear stress due to wind	$\frac{\tau_{xw}}{\rho}$ (m^2/s^2)	$\frac{\tau_{xw}}{\rho} = \rho_a C^* W_x \left(W_x^2 + W_y^2\right)^{\frac{1}{2}}$ ρ_a: density of air $(\sim 1.292\ kg/m^3)$ ρ : density of fluid C^*: air/fluid resistance coefficient assumed to be 2.6×10^{-3} W_x: x-component of wind W_y: y-component of wind
x-direction bed shear stress	$\frac{\tau_{xb}}{\rho}$ (m^2/s^2)	$\frac{\tau_{xb}}{\rho} = -\frac{gU\left(U^2+V^2\right)^{\frac{1}{2}}}{C_e^2}$ C_e: Chezy roughness coefficient (m^2/s)
depth-averaged turbulent eddy viscosity	$\overline{\varepsilon}$ (m^2/s)	

Table 3.1: Terms description of the two-dimensional version of the shallow water equations.

variations in the flows current produced from power extraction (Adcock *et al.*, 2015).

However, the investigation of the tidal-stream resource for large arrays of turbines is based on the bulk flow role, rather than smaller spatial gradients (Vogel *et al.*, 2013). Consequently, this thesis uses depth-average simulations to investigate and improve the strategy of assessing tidal resource.

3.3   Tidal Channel

Two-dimensional SWEs are used herein to describe the evolution of a tidal-stream through a channel. Flow is forced by the Semi-diurnal (M_2) tidal component and driven by the head difference between the entrance and exit of a channel. For simplicity, the Coriolis force and wind stress are omitted in this research. The Coriolis effect can be neglected because the characteristic length of the channel is small enough not to be significantly influenced by the Coriolis force; nevertheless, in larger domains the consideration of the Coriolis force can lead to a 10% increase of maximum power extraction (Draper *et al.*, 2013a).

An additional consideration is the viscous terms omission in the momentum equation. This allows direct comparison of the numerical implementation of the LMAD-OCH performed in this research with results that numerically implement bounded flows with a rigid lid (Sutherland *et al.*, 2007) and LMAD-OCH (Draper *et al.*, 2010) analytical models. The viscous terms omission is justified if bottom friction prevails over viscosity effects (Kvočka, 2017). Also, a scaling analysis indicates that viscous terms can be disregarded if the horizontal scale of the domain is large and tidal currents change smoothly over the length of the domain (Draper, 2011). The inviscid character of the equations allows us to neglect the generation of vortical structures associated with the turbine's blade root and tip. The neglection of viscous terms has been considered in far-field extent tidal energy extraction numerical simulation by many researchers

(Draper *et al.*, 2010; Adcock *et al.*, 2013).

The flow being simulated herein has a free-surface this allows investigation of water elevation changes produced by the power extracted from the array. Despite idealisation of the flow, this situation enables the possibility to incorporate and corroborate a new strategy of numerical power extraction quantification. In the following section, the governing equations are extended to represent the momentum loss due to marine turbine power extraction.

3.3.1 Turbine Representation in the Governing Equations

The 2D-SWEs are used to investigate tidal-stream power extraction at regional scale. The study case herein is a tidal channel, where two depth-average models were used to simulate energy extracted by an array of turbines. The first scheme solves RVF, using a shock-capturing scheme. The second scheme solves SSF i.e. flows whose properties do not experience strong gradients, and consequently their simulation does not require a method to solve shock problems.

The mathematical representation of the momentum sink due to tidal-stream power extraction is introduced as the sink term $\overrightarrow{F_T}$. This term represents the turbine thrust force T, responsible for tidal stream momentum loss in a channel.

In the case of smooth flow solution, the governing equations for tidal power extraction in a channel are given by the continuity equation (Eq. 3.1) and momentum equations (Eqs. 3.4 and 3.5). These equations neglect the Coriolis force, the wind stress, and the viscous terms in the momentum equations. Additionally, the flow simulated presents a free-surface.

$$\frac{\partial q_x}{\partial t} + \frac{\partial(\frac{\beta q_x^2}{H})}{\partial x} + \frac{\partial(\frac{\beta q_x q_y}{H})}{\partial y} = -gH\frac{\partial \zeta}{\partial x} - \frac{gq_x\sqrt{q_x^2 + q_y^2}}{H^2 C_e^2} - F_{Tx} \tag{3.4}$$

$$\frac{\partial q_y}{\partial t} + \frac{\partial(\frac{\beta q_x q_y}{H})}{\partial x} + \frac{\partial(\frac{\beta q_y^2}{H})}{\partial y} = -gH\frac{\partial \zeta}{\partial y} - \frac{gq_y\sqrt{q_x^2 + q_y^2}}{H^2 C_e^2} - F_{Ty} \tag{3.5}$$

$$T = \frac{1}{2}\rho\overrightarrow{U}^2 A C_T \tag{3.6}$$

The thrust force is a function of the turbine cross-sectional area A, a thrust coefficient C_T, and the depth-average velocity $\overrightarrow{U}$. The thrust force applied by the turbine to the stream was incorporated into the momentum equations, as an external force $\overrightarrow{F_T}$ Figure 3.1 illustrates the cross section of the turbine area A, indicated by a dotted-red line, and the thrust force exerted on the flow. F_{Tx} corresponds to the $x-$ component of the axial thrust induced by the turbines and F_{Ty} corresponds to the $y-$component (Ahmadian *et al.*, 2012a; Fallon *et al.*, 2014). The other terms in the equations are presented in Table 3.1. The components of the thrust force are given by

$$F_{Tx} = T|sin\theta| \tag{3.7}$$

$$F_{Ty} = T|cos\theta| \tag{3.8}$$

where it is assumed that the thrust force makes an angle θ with the y-axis.
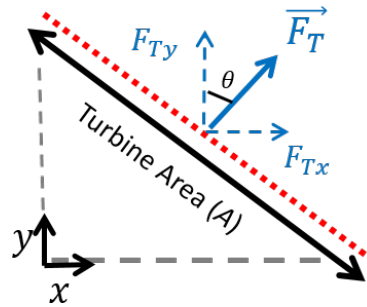
Fig. 3.1: Cross-sectional scheme of the two-dimensional representation of the thrust force exerted on the flow by the turbine $\overrightarrow{F_T}$.

3.3.2 Turbine Representation in the Conservative Form of the Governing Equations

According to the numerical implementation of the LMAD-OCH theory reported by Draper (2011), the power extracted by an array of turbines produce rapid changes in the water depth and velocity field across the array, which are considered as discontinuities. The simulation of sharp gradients within the flow requires a scheme that solves RVF. In turn, the scheme depends upon the solution of the conservative form of the 2D-SWEs for the tidal channel. This representation of the equations ensures conservation of mass and momentum after discretisation. This form of the equations is necessary for the numerical method to preserve the correct solution of the strong gradients (shocks) presented in the velocity and elevation fields (Ming and Chu, 2000; Liang *et al.*, 2006). Conservative form of 2D-SWE is obtained by treating H, q_x, and q_y as independent functions. This requires splitting the pressure gradient term into the flux gradients and source terms (Rogers *et al.*, 2003)

In the case of the $x-$component of the momentum equation, the conservative form of the equations is obtained by splitting the pressure gradient term $gH\frac{\partial \zeta}{\partial x}$ between the flux quantities gradients and the source terms (Rogers *et al.*, 2003) as follows:

$$gH\frac{\partial \zeta}{\partial x} = \frac{\partial}{\partial x}\left(\frac{1}{2}gH^2\right) + gH\frac{\partial h}{\partial x} \qquad (3.9)$$

A similar procedure is used for the y-direction term:

$$gH\frac{\partial \zeta}{\partial y} = \frac{\partial}{\partial y}\left(\frac{1}{2}gH^2\right) + gH\frac{\partial h}{\partial y} \qquad (3.10)$$

Additionally, the local acceleration term of the continuity equation is expressed in the following form because the temporal variation of the mean water depth (h) is null:

$$\frac{\partial \zeta}{\partial t} = \frac{\partial H}{\partial t} - \frac{\partial h}{\partial t} = \frac{\partial H}{\partial t} \qquad (3.11)$$

The tidal channel governing equations (Equations 3.1, 3.4, and 3.5) can be re-arranged into the following conservative form, suitable for the simulation of RVF:

$$\frac{\partial \vec{D}}{\partial t} + \frac{\partial \vec{E}}{\partial x} + \frac{\partial \vec{G}}{\partial y} = \vec{S} + \vec{T} \tag{3.12}$$

where

$$\vec{D} = \begin{bmatrix} H \\ q_x \\ q_y \end{bmatrix}, \ \vec{E} = \begin{bmatrix} q_x \\ \frac{\beta q_x^2}{H} + \frac{gH^2}{2} \\ \frac{\beta q_x q_y}{H} \end{bmatrix}, \ \vec{G} = \begin{bmatrix} q_y \\ \frac{\beta q_x q_y}{H} \\ \frac{\beta q_y^2}{H} + \frac{gH^2}{2} \end{bmatrix}, \tag{3.13}$$

$$\vec{S} = \begin{bmatrix} 0 \\ -gH\frac{\partial h}{\partial x} - \frac{gq_x\sqrt{q_x^2+q_y^2}}{H^2 C_e^2} - F_{Tx} \\ 0 \end{bmatrix}, \ \vec{T} = \begin{bmatrix} 0 \\ 0 \\ -gH\frac{\partial h}{\partial y} - \frac{gq_y\sqrt{q_x^2+q_y^2}}{H^2 C_e^2} - F_{Ty} \end{bmatrix} \tag{3.14}$$

The description of the terms is presented in Table 3.1. In the case of F_{Tx} and F_{Ty}, they are defined by Equations 3.7 and 3.8. Using the operator splitting technique it is possible to solve Equation 3.12 by finding the solution of the following two one-dimensional hyperbolic equations (Liang *et al.*, 2006; Kvocka, 2015):

$$\frac{\partial \vec{D}}{\partial t} + \frac{\partial \vec{E}}{\partial x} = \vec{S} \tag{3.15}$$

$$\frac{\partial \vec{D}}{\partial t} + \frac{\partial \vec{G}}{\partial y} = \vec{T} \tag{3.16}$$

3.4 Numerical Methods

Solutions for the hyperbolic shallow water equations have been approximated numerically using different numerical schemes (Weiyan, 1992). In the case of the tidal-stream power extraction problem at the regional scale, two systems of governing equations were described, one for SSF (Section 3.3.1) and another one for RVF (Section 3.3.2). The numerical solution of these systems were approximated with two depth-average hydrodynamic models; these schemes are two versions of the Depth

Integrated Velocity And Solute Transport (DIVAST) model (Falconer, 1984). The smooth flow problem was solved with an Alternating Direction Implicit (ADI) methodology (DIVAST ADI). The rapidly varying flow problem was solved with a Standard MacCormack scheme and Symmetric Total Variation diminishing (TVD) method (DIVAST TVD-MacCormack). For practical purposes, DIVAST ADI and DIVAST TVD-MacCormack models will be referred to henceforth as ADI-M and TVD-M.

Before introducing the numerical models, the basic principles and strategies used by the models to approximate the solution of the two systems of governing equations are summarised.

3.4.1 Finite Difference Method

ADI-M and TVD-M use finite difference spatial discretisation to approximate the differential operators of the governing equations, and to approximate a solution of the equations. The models discretise the governing equations onto a square structured grid, where the edges of the grid cells are oriented parallel to the Cartesian coordinates (Falconer and Lin, 2001; Kvocka, 2015). The finite difference method was one of the first methodologies applied to the numerical solution of differential equations; it uses a Taylor series expansion to discretise the derivatives of the flow variables (Pozrikidis, 2009). The advantage of this method is the potential to obtain high order approximations, and consequently, to get high order accuracy of spatial discretisations (Blazek, 2001). The disadvantage of the finite difference method and the structured grid is the range of applications is restricted, as it is difficult to generate structured grids for complex geometries. Within the finite difference method there exists various numerical schemes to perform the spatial discretisation that satisfy specific requirements of the problem, such upwind differencing methods. In the case of the ADI-M model, to avoid instabilities in the solution of the non-linear terms of the momentum equations, the cross product advective acceleration terms are solved using a first-order upwind method

(Falconer and Lin, 2001). Meanwhile, TVD-M uses a combination of first-order and second-order upwind type.

Upwind methods are advanced spatial discretisation schemes, which are constructed by considering the physical properties of the governing equation; the name refers to the capacity to distinguish between upstream and downstream influences (e.g. wave propagation direction) (Blazek, 2001). The principle of the upwind method is to obtain information for each variable, based on the direction from which the information of the variable comes from (LeVeque, 2002). Central schemes tend to provide excessive damping if numerical discontinuities are not solved correctly (Chung, 2010). Upwind methods rectify that problem.

First-order upwind methods are more stable and present faster convergence, but they are less accurate, as the schemes are based only on the first-order terms of the Taylor series. In addition, the scheme produces erroneous results, known as false diffusion, if the flow direction is not aligned with the grid lines (Versteeg and Malalasekera, 2007). The first-order upwind schemes are divided into two groups: flux vector splitting schemes and Godunov schemes (Chung, 2010).

Instead, second-order upwind methods involve more neighbour points and reduce discretisation errors, giving higher accuracy, larger convergence time and less dissipative properties (Versteeg and Malalasekera, 2007). Second-order upwind schemes can be divided into low and high resolution. There are two approaches for the second-order upwind schemes with low resolution: variable extrapolation and flux extrapolation (Chung, 2010). The most important development in computational fluid dynamics may be the second-order upwind schemes with high resolution, known as total variation diminishing (TVD) schemes (Chung, 2010). TVD schemes are based on the following physical properties: avoid unrealistic entropy decrease (entropy condition), prevent oscillatory behaviour in the numerical scheme (monotonicity condition), not to allow the total variation of a physical admissible solution to increase in time (total variation

diminishing) (Chung, 2010; Wesseling, 2001). Further specifications are be given in Section 3.4.3.

After specifying the spatial discretisation methodology, the next aspect to introduce is the temporal discretisation method of the models; TVD-M uses an explicit scheme and ADI-M uses a semi-implicit scheme.

3.4.2 Explicit and Implicit Methods

Explicit methods approximate the solution of the governing equations at the current time level only based on known flow quantities (Blazek, 2001). Consequently, it is necessary to calculate all the values of the variable at a given time level before advancing to the next time-step (Carnahan *et al.*, 1969; Chung, 2010). The finite difference approximation to the solution of the governing equations at any grid point is not exact, as there is only a finite number of digits that the computer can retain. The departure of the finite difference approximation from the solution is known as the local discretisation error. In explicit methods, the convergence to a solution is conditioned by a maximum time-step. To provide stability to the explicit schemes, the Courant-Fredrichs-Lewy (CFL) condition, given by Equation 3.17, must be met (Courant *et al.*, 1928).

$$\frac{v\Delta t}{\Delta x} \leq C_r \tag{3.17}$$

where v is the characteristic velocity of the flow, Δt is the time-step size, Δx is the length of the grid spatial resolution, and C_r is the dimensionless Courant number. The time-step constraint represents a serious limitation of the scheme, as it becomes expensive in terms of the excessively large number of time-steps that may be required for high spatial resolution or long-time simulations (Versteeg and Malalasekera, 2007).

Implicit models present an advantage in comparison to explicit ones, with the possibility of using significantly larger time-steps without affecting the time integration

process (Blazek, 2001). Larger time-steps are particularly important for problems that extend over large time periods. An implicit scheme indicates that dependent variables are calculated based on quantities computed at the previous time-step, and quantities to be calculated at the current time. This solution procedure requires the representation of a large system of linear equations, which has to be solved in order to update the variable at each time-step, at the expense of a more complicated calculation procedure (Carnahan *et al.*, 1969). This task can be accomplished using a direct or an iterative method. The implicit methods have no restriction regarding converge of the solution of the governing equations; however, an accurate solution requires a time-step limitation. In the case of ADI-M, the time-step and spatial resolution need to satisfy a maximum of eight times the Courant number (Equation 3.18) in order to compute a reasonable accurate solution (Falconer and Lin, 2001):

$$C_r = 2\Delta t \sqrt{gH\left(\frac{1}{\Delta x^2} + \frac{1}{\Delta y^2}\right)} \approx \frac{\Delta t}{\Delta x}\sqrt{gH} \leq 4\sqrt{2} \tag{3.18}$$

where H, g, and Δx stand for average water depth, gravity and grid-size, respectively. As the grid-cell is regular, $\Delta y = \Delta x$ a further reduction can obtained (right-side of the Equation 3.18).

Finally, the main target of any numerical scheme is the convergence to the exact solution as the grid size is reduced, the accuracy of the solution will depend on consistency, stability and convergence of the model (Chung, 2010)

3.4.3 Numerical Methods for Solution of Shock Problems

In general, numerical methods for solving shock problems can be divided into two main families (i) shock capturing methods (or a combination of first-order and second-order upwind schemes) and (ii) shock fitting methods (or Godunov type) (Gustafsson, 2011; Liang *et al.*, 2006). In terms of marine power extraction, the LMAD-OCH theory considers the generation of rapid changes in flow across an array of turbines as a result

of power extracted by an array (Houlsby *et al.*, 2008). The analytical model has been studied with a two-dimensional model, which solves the sharp gradients generated in the flow with a shock-fitting method (Draper *et al.*, 2010). Sharp gradients can also be solved with shock-capturing methods. These types of schemes are useful for modelling RVF such as hydraulic jumps, flood waves, tidal bores, dam breaks and shock waves (LeVeque, 2002; Weiyan, 1992). A shock-capturing method can produce the correct solution of the conservative form of the governing equations (introduced in Section 3.3.2). This representation of the equations describes the strong gradients presented in the flow, and thus captures the discontinuities or shocks described by the equations (Blazek, 2001; Gustafsson, 2011; Vreugdenhil, 1994). A description of the shock fitting and shock capturing methods follows.

Shock capturing Method

The shock-capturing method uses an algebraic combination of first-order and second-order upwind schemes. The scheme uses a solution procedure to solve the equations of the entire domain and a special procedure near the shock (Gustafsson, 2011). A second-order upwind scheme is implemented on the entire domain. Typical methods are: Lax-Wendroff, MacCormack, and Beam-Warming. Near the shock, where spurious numerical solutions are likely to appear, a first-order upwind scheme is implemented; this scheme adds a kind of artificial viscosity to smooth the solution (Gustafsson, 2011). Total variation diminishing (TVD) methods varies the dissipation amount from grid point to another based on the flow solution. TVD methods produce highly accurate numerical solutions of flows presenting strong shock waves. As the shock-capturing method reported in this thesis corresponds to a combination of MacCormack and TVD, the principles of these two schemes are described.

MacCormack Predictor-Corrector scheme: Two 1D-hyperbolic equations were obtained in Section 3.3.2 (Equations 3.15 and 3.16). The MacCormack algorithm solves 1D-hyperbolic partial differential equations obtained after applying an operator splitting technique (Kvocka, 2015). The 1D-hyperbolic partial differential equation is solved following two steps: a predictor and a corrector step (Chung, 2010). The use of this algorithm can be illustrated with the following 1D advection equation:

$$\frac{\partial \phi}{\partial t} + c\frac{\partial F}{\partial x} = 0 \tag{3.19}$$

where ϕ represents a property of the flow such as velocity, free-surface elevation or flow mass rate. The flux source is denoted by F and no source term is considered.

The predictor-step solution for Equation 3.19 is given by Equation 3.20. The solution of ϕ^n is known, but ϕ^{n+1} is unknown, the predictor step uses a provisional value of ϕ^n at a time level $n+1$ denoted by $\overline{\phi_i^{n+1}}$; where the super-scripts and sub-scripts refer to temporal and spatial indices, respectively.

$$\overline{\phi_i^{n+1}} = \phi_i^n - c\frac{\Delta t}{\Delta x}\left(F_i^n - F_{i-1}^n\right) \tag{3.20}$$

The time-step is Δt and the grid spacing is denoted by Δx. The finite difference calculation of the derivative is backward in space (in yellow). On the other hand, the corrector step, corrects the predicted value $\overline{\phi_i^{n+1}}$ in the following way:

$$\phi_i^{n+1} = \frac{1}{2}\left[\phi_i^n + \overline{\phi_i^{n+1}} - c\frac{\Delta t}{\Delta x}\left(\overline{F_{i+1}^{n+1}} - \overline{F_i^{n+1}}\right)\right] \tag{3.21}$$

now the time-step used is $\Delta t/2$ and the finite difference calculation of the derivative is forward in space (in yellow). The use of two steps to calculate ϕ_i^{n+1} allows a second-order accuracy in time and space $O(\Delta t^2, \Delta x^2)$. Equation 3.21 can be re-written as Equation 3.22 considering $\phi_i^p = \overline{\phi_i^{n+1}}$, and $\phi_i^c = \phi_i^n + -c\frac{\Delta t}{\Delta x}\left(\overline{F_{i+1}^{n+1}} - \overline{F_i^{n+1}}\right)$, where p and c super-script refer to predictor and corrector steps.

$$\phi_i^{n+1} = \frac{1}{2}[\phi_i^p + \phi_i^c] \tag{3.22}$$

Total Variation Diminishing (TVD): The aim of the TVD scheme is to avoid the generation of new extrema in the flow solution (Harten, 1982). New extrema refers to unrealistic, grid-scale scale oscillations their generation can be measured by the total variation TV. The total variation of the function ϕ^n is given by Equation 3.23, it indicates the sum of the magnitude's difference of ϕ^n at the adjacent grid points. The quantity TV monitors the generation of spurious numerical oscillations in the presence of sharp gradients, which can lead into breakdown of the numerical solution (Kvočka, 2017).

$$TV(\phi_i^n) \equiv \sum_i |\phi_{i+1}^n - \phi_i^n| \qquad (3.23)$$

To prevent the generation of spurious oscillations, the TVD scheme diminishes the total variation of the flow solution. This property of the scheme is referred to as monotonicity preserving (Blazek, 2001):

$$TV(\phi_i^{n+1}) \leq TV(\phi_i^n) \qquad (3.24)$$

Equation 3.24 indicates that the TVD scheme must have a total variation at time level $n+1$ less than or equal to the total variation of time level n (Harten, 1982). Thus, a discretisation methodology with TVD properties solves sharp gradients without any spurious oscillations of the solution (Blazek, 2001).

The TVD schemes are implemented as a combination of second-order and first-order schemes. The solution is first-order near discontinuities and higher-order in smooth regions; the transition from low to higher-order is accomplished by implementing slope limiters or flux limiter functions. In the case of the TVD-M model used in this thesis, the MacCormack scheme is the higher-order scheme used in the smooth region; meanwhile, a symmetric five-point TVD term is the first-order scheme used to remove the numerical oscillations near sharp gradients (Liang *et al.*, 2007). The TVD term acts as a dissipation term, therefore, it is used to adjust numerical diffusion introduced (Kvocka, 2015). A symmetric TVD scheme indicates that the dissipation term

depends on the sign of the characteristic speeds of the flow solution (Blazek, 2001). A five-point TVD term refers to the number of grid points involved in the computation of the gradient; in two-dimensions the control volume is a five-point.

In the TVD-M model, the TVD term is added to the corrector step, so Equation 3.22 can be re-written as:

$$\phi_i^{n+1} = \frac{1}{2}[\phi_i^p + \phi_i^c] + TVD_i \tag{3.25}$$

The TVD_i (blue) term refers to the following discretisation (Kvocka, 2015):

$$TVD_i = \left[G(r_i^+) + G(r_{i+1}^-)\right] \cdot \Delta\phi_{i+1/2}^n - \left[G(r_{i-1}^+) + G(r_i^-)\right] \cdot \Delta\phi_{i-1/2}^n \tag{3.26}$$

where

$$\Delta\phi_{i+1/2}^n = \phi_{i+1}^n - \phi_i^n \tag{3.27}$$

$$\Delta\phi_{i-1/2}^n = \phi_i^n - \phi_{i-1}^n \tag{3.28}$$

and

$$r_i^+ = \frac{\left\langle \Delta\phi_{i-1/2}^n, \Delta\phi_{i+1/2}^n \right\rangle}{\left\langle \Delta\phi_{i+1/2}^n, \Delta\phi_{i+1/2}^n \right\rangle} \tag{3.29}$$

$$r_i^- = \frac{\left\langle \Delta\phi_{i-1/2}^n, \Delta\phi_{i+1/2}^n \right\rangle}{\left\langle \Delta\phi_{i-1/2}^n, \Delta\phi_{i-1+1/2}^n \right\rangle} \tag{3.30}$$

The point brackets in the numerator and denominator of Equations 3.29 and 3.30 indicate the scalar product of the vectors within the brackets (Kvocka, 2015). The function G is defined as (Liang *et al.*, 2007):

$$G(x) = 0.5 \times C \times [1 - \psi(x)] \tag{3.31}$$

G depends on the flux limiter function ψ, defined as:

$$\psi(x) = max(0, min(2x, 1)) \tag{3.32}$$

The flux limiter function helps to change from a low to higher-order scheme by (i) supplying artificial dissipation when there is a spurious oscillation near high gradients zones, and (ii) adding very little or no dissipation in regions of smooth variation (Ming and Chu, 2000). The value of variable C (Equation 3.33) depends on the magnitude of the local Courant number C_{rl} (Equation 3.34) as follows:

$$
C = \begin{cases} C_{rl} \times (1 - C_{rl}), & C_{rl} \leq 0.5 \\ 0.25, & C_{rl} > 0.5 \end{cases} \tag{3.33}
$$

$$
C_{rl} = \left(\left| \frac{q_x}{H} \right| + \sqrt{gH} \right) \frac{\Delta t}{\Delta x} \tag{3.34}
$$

where q_x is the depth-average velocity flux component in the x-direction and H is the total water depth (See Table 3.1). The TVD term (Equation 3.26) indicates that the limiter function acts on the characteristic property of the flow denoted by ϕ. In regions with high gradients, the limiter function becomes zero, which leads to the first-order scheme. Meanwhile, in regions of smooth flow, the second-order scheme is retained (Blazek, 2001).

Shock fitting Method

The shock-fitting method is characterised by treating the flow variable's discontinuity as an internal boundary, where the discontinuity is assumed to occur at an interface (Liang *et al.*, 2006). On each side of the shock, the differential equation is solved by some method that does not use any grid points from the opposite side (Gustafsson, 2011). The shock-fitting method (or Godunov method) is characterised by using the solution of a local Riemann problem to provide the mass flux across the interface (Sleigh, 2006). The solution of the Riemann problem can be exact or approximate. A complex form of the hyperbolic equations will be solved more efficiently with an approximate solution of the Riemann problem (Sleigh, 2006). Common Riemann

solvers are Roe's average flux, Lax-Friedrich flux, Harten-Lax-Van Leer flux (HLL), and Harten-Lax-van Leer-Contact (HLLC) flux.

The implementation of the LMAD-OCH theory has been carried out in a discontinuousGalerkin depth-average model (Draper *et al.*, 2010). This model uses a shock-fitting scheme based on the HLLC Riemann solver; therefore, the HLLC solver is described.

HLLC Riemann Solver: The main purpose of this solver is to approximate a solution to the Riemann problem. The Riemann problem is an initial value problem (IVP), when the initial data consist of two constant states, right (R) and left (L), separated by a jump discontinuity at $x = 0$. Using as an example the conservative form of the Euler equation in Cartesian coordinates, the Riemann problem in the domain $-\infty < x < \infty$, $t > 0$ is given by (Toro *et al.*, 1994):

$$\mathbf{U}_t + \mathbf{F}(\mathbf{U})_x = 0 \tag{3.35}$$

$$\mathbf{U}(x, t = 0) = \mathbf{U}_0(x) \tag{3.36}$$

where

$$\mathbf{U}_0(x) = \begin{cases} \mathbf{U}_L, & x < 0 \\ \mathbf{U}_R, & x > 0 \end{cases} \tag{3.37}$$

the vectors of conserved variables and fluxes are:

$$\mathbf{U} = \begin{bmatrix} h \\ h\overline{u} \\ h\overline{v} \end{bmatrix}, \mathbf{F}(\mathbf{U}) = \begin{bmatrix} h\overline{u} \\ h\overline{u}^2 + \frac{1}{2}gh^2 \\ h\overline{uv} \end{bmatrix} \tag{3.38}$$

it is assumed that the coordinate system is rotated so $\overline{u}$ indicate normal velocity to the interface, and $\overline{v}$ is the tangential velocity.

The Riemann problem for the shallow water equations is a generalisation of the dam-break problem (Toro, 2001). Considering a horizontal channel of uniform, rectangular cross section, it is assumed that the channel has two uniform water levels, both
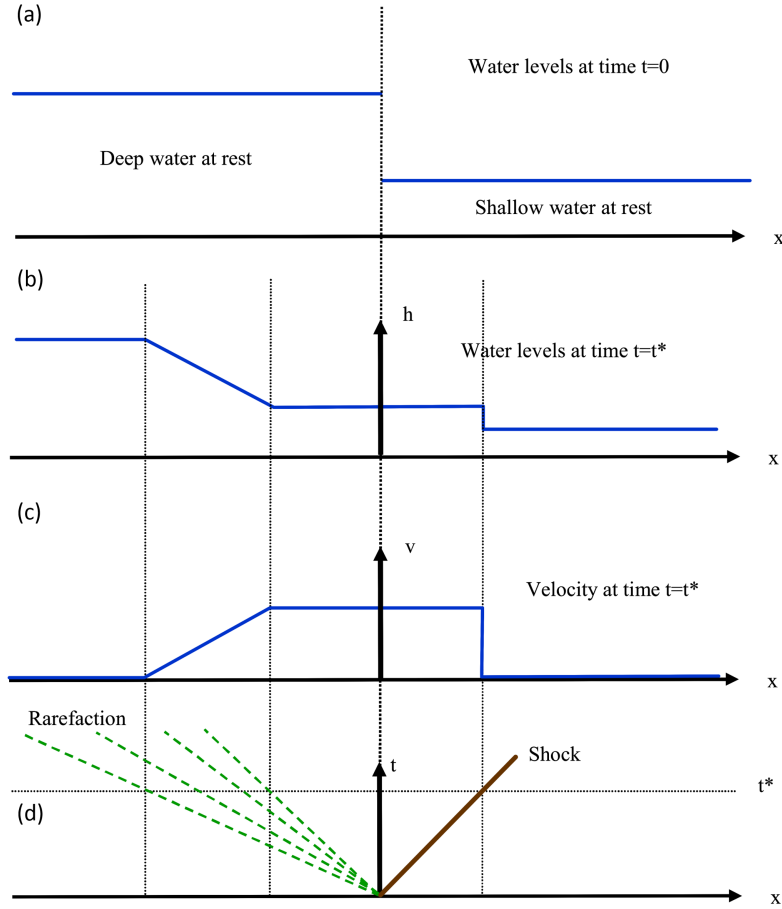
Fig. 3.2: Time evolution of the dam-break problem: initial depth (a), depth at a later time (b) and corresponding velocity distribution (c). Wave diagram of the full process on the $x - t$ plane (d). Figure from Sleigh (2006).

at rest, separated by a wall at a position $x=0$ (Figure 3.2(a)). If the dam is instantly removed, the problem is the determination of free surface evolution with time. The dam removal produces a wake pattern, which consists of two dominant features: (i) a right-facing wave that travels into the shallow water, referred to as a shock wake; (ii) a left-facing wave that travels into the deep water and reduce the free-surface height; referred to as a rarefaction wave. If the wake phenomenon is governed by the shallow water equations, the water depth profile and the corresponding velocity at a later time t_* are described by Figures 3.2(b) and (c). Figure 3.2(d) summarises the two type

of waves generated in the dam problem as a function of space and time. The right wave is a shock (a discontinuous wave), and the left wave is a rarefaction (a smooth wave) (Toro, 2001). The profiles presented in Figure 3.2(d) correspond to *characteristic curves* of the IVP given by Equation 3.36. These curves indicate the solutions to the ordinary differential equation posed and describe basic features of wave propagation phenomena, where a wave is a recognisable feature of a disturbance that travels at a finite speed (Toro, 2009). The rarefaction and shock wave are two types of solutions for the Riemann problem these solutions separate the R and L constant states of the flow (Sleigh, 2006). The rarefaction wave exemplified in Figure 3.2(d) indicates that the two states are separated by a smooth wave i.e. as the wave travels at any fixed time the flow varies smoothly across the wave, the smooth variation is represented by the four green-dashed lines. Meanwhile, the shock wave presented in Figure 3.2(d) indicates that R and L states are connected via a single discontinuity. Hereafter, the shock wave is used to exemplify the Riemann problem solution.

The solution of the Riemann problem consists of finding an approximation to mass flux $\mathbf{F}(\mathbf{U})$, which flows through the interface that separates the L and R states. The HLLC solver describes the Riemann problem structure as three waves (Figure 3.3): a middle wave with wave speed S_* (which is a contact discontinuity), a left wave with speed S_L, and a right wave with speed S_R.

The right and left waves are called non-linear waves and can be either shocks or rarefactions (Toro *et al.*, 1994). Additionally, S_L and S_R represent the smallest and largest signal velocities in the solution of the Riemann problem with data $\mathbf{U}_L$ and $\mathbf{U}_R$, and the corresponding fluxes are $\mathbf{F}_L$ and $\mathbf{F}_R$. The region between the non-linear waves is called *start*, and it has two distinct fluxes $\mathbf{F}_{*L}$ and $\mathbf{F}_{*R}$. Assuming all wave speed estimates
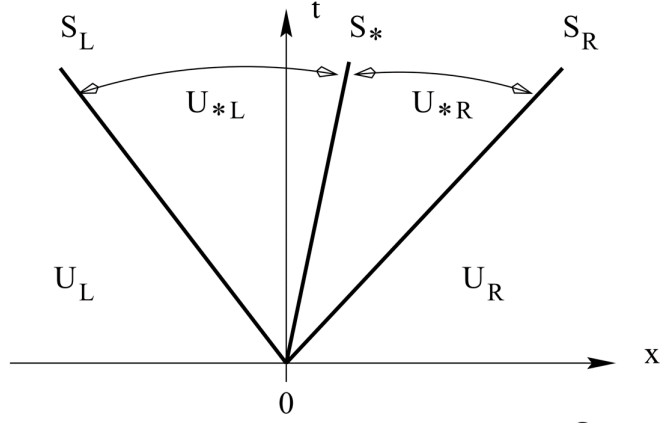
Fig. 3.3: HLLC Riemann solver wave structure. Figure taken from (Toro, 2009)

are available, the HLLC numerical flux is defined as follows (Toro, 2009):

$$\tilde{\mathbf{F}}_{i+1/2}^{hllc} \begin{cases} \mathbf{F}_L, \text{ if } 0 \leq S_L \\[2mm] \mathbf{F}_{*L}, \text{ if } S_L \leq 0 \leq S_* \\[2mm] \mathbf{F}_{*R}, \text{ if } S_* \leq 0 \leq S_R \\[2mm] \mathbf{F}_R, \text{ if } 0 \geq S_R \end{cases} \tag{3.39}$$

where

$$\mathbf{F}_{*L} = \mathbf{F}_L + S_L(\mathbf{U}_{*L} - \mathbf{U}_L) \tag{3.40}$$

$$\mathbf{F}_{*R} = \mathbf{F}_R + S_R(\mathbf{U}_{*R} - \mathbf{U}_R) \tag{3.41}$$

The states $\mathbf{U}_{*L}$ and $\mathbf{U}_{*R}$ are given by

$$\mathbf{U}_{*K} = h_K \left(\frac{S_K - \overline{u}_K}{S_K - S_*} \right) \begin{bmatrix} 1 \\ S_* \\ \overline{v}_K \end{bmatrix}, \ K = L, R \tag{3.42}$$

The mass flux determination requires the estimation of S_L, S_R, and S_* wave speeds. Toro (2001) indicates that the following choice of wave speeds lead to a robust scheme:

$$S_K = u_K - a_K f_K \tag{3.43}$$

$$S_* = \frac{S_L h_R(U_R - S_R) - S_R h_L(U_L - S_L)}{h_R(U_R - S_R) - h_L(U_L - S_L)} \tag{3.44}$$

where $a_K = \sqrt{gh_K}$ is the celerity of a gravity wave ($K = L, R$), and f_K is a factor function of h_* (Equation 3.45). If $h_* > h_K$, a shock wave is obtained; meanwhile if $h_* \leq h_K$, a rarefaction wave is obtained (Sleigh, 2006).

$$f_k = \begin{cases} \sqrt{\frac{1}{2}\left(\frac{(h_* + h_K)h_*}{h_K^2}\right)}, \text{ if } h_* > h_K \\ \\ 1, \text{ if } h_* \leq h_K \end{cases} \tag{3.45}$$

where h_* is an estimate for the exact solution of h in the start region:

$$h_* = \frac{1}{g}\left(\frac{1}{2}\left(\sqrt{gh_L} + \sqrt{gh_R}\right) + \frac{1}{4}(\overline{u}_L - \overline{u}_R)\right)^2 \tag{3.46}$$

3.4.4 Parallel Computing

The higher computational expense required to simulate RVF has motivated the search for strategies to optimise the performance of shock-capturing models. In the case of TVD-M, the model has been optimised by introducing parallel processing on multiple cores on the same Central Processing Unit (CPU), using shared memory (Whittaker, 2014). To provide a context to the TVD-M parallel model, some basic concepts of parallel computing are introduced.

Parallel computing is a form of computation that allows many instructions in a program to run simultaneously (Kiessling, 2009). This way of computing provides a solution to a bottle neck, an issue presented in uni-processor computer architecture as a consequence of lack of resources such as memory and disk space, which results in longer computational times (Ravela, 2010). The main purpose of parallel systems is to support high execution speeds and more efficient memory (Ravela, 2010). The main reason for the overall runtime reduction, in comparison to a serial application, is task sharing. High performance computers (HPCs) contain large number of processors, which in turn may have several cores and each core is fed data from separate threads (Gustafsson, 2011); a thread represents a single sequential flow of control within a program.

In order to parallelise a program, it is necessary to identify sections to be run in parallel. These sections correspond to multiple tasks of the same kind e.g. loops. A loop, when run in parallel, will divide its iteration between multiple threads. However, to make a loop run in parallel, all the iterations should be independent (Kiessling, 2009). The existence of numerical methods that are easier to develop in parallel architectures, such as the Jacobi iterative method for solving systems of equations, will influence the selection of numerical models (Gustafsson, 2011). In reality, programs are rarely able to be run completely in parallel (Kiessling, 2009).

The modification of a model to divide its work into threads and execute them in parallel is done via a third-party Application Program Interface (API). In the case of TVD-M the common shared-memory API implemented is Open Multi-Processing (OpenMP) (Whittaker, 2014). This application was first released in 1997 and is a standard interface for writing shared memory parallel applications in C, C++ and Fortran code. OpenMP hides and implements processes such as work load partitioning, work management, communication and synchronisation among the threads (Ravela, 2010). In addition, the interface allows the programmer to parallelise individual sections of the code, such as loops, one at a time. OpenMP operates on a Fork and Join model of parallel execution. This procedure indicates that the master thread executes instructions sequentially until a parallel region is encountered. At this point, the master thread 'forks' into a number of parallel worker threads. The instructions in the parallel region are then executed by this team of worker threads. At the end of the parallel region, the threads synchronise and join to become a single master thread again (Kiessling, 2009).

Shared memory models assume that all parallel activities can access all the memory. This configuration allows multiple processors to operate independently, while still having access to all the same memory resources. (Ravela, 2010; Kiessling, 2009). An advantage is the reduction of messaging between threads (Chung, 2010). The amount

of time the processors spend messaging or communicating with each other is an aspect to be considered. A larger number of processors does not necessarily imply better performance, on the contrary, the increase in the number of processors can decrease the performance of the parallelised code due to overhead, which refers to the greater amount of time the processors spend communicating with each other (Kiessling, 2009).

3.5 Numerical Models

3.5.1 ADI-M Model

The tidal-stream power extraction problem at the regional scale for SSF (derived in Section 3.3.1) was solved by implementing the LMAD-OCH theory. The numerical scheme developed in this thesis to solve the smooth flow problem is a numerical extension of ADI-M. The resultant scheme is called the ADI-TOC model. To provide a basis for the model developed in this thesis, the description of the ADI-M is presented.

The model ADI-M was developed to simulate hydrodynamic, solute and sediment transport processes in rivers, estuaries and coastal waters. It was originally developed by Falconer (1984) and since then, it has been validated and extended extensively to solve hydro-environmental engineering problems (Falconer and Asce, 1986; Liang *et al.*, 2006; Nash, 2010; Olbert, 2006; Kvočka *et al.*, 2015). ADI-M is a depth-average serial hydrodynamical model that uses an Alternating Direction Implicit (ADI) technique to approximate the solution of the governing differential equations. The ADI version used by ADI-M was proposed by Stelling *et al.* (1986); Liang *et al.* (2006). This technique uses centred finite differences for time and space derivatives. The ADI scheme is computationally efficient to model SSF with typical Froude values ≪1 (Liang *et al.*, 2007). In addition, the ADI's semi-implicit finite difference scheme implies the splitting of a single time-step solution into two time-steps (Chung, 2010). As the computation of the solution considers only one-dimension for each half time-step, the solution of

a two-dimensional matrix is avoided. The final finite difference equations for each half time-step (HFDT) are solved using the method of Gaussian elimination and back substitution (Falconer and Lin, 2001). The numerical scheme for the hydrodynamics is second-order and accurate in both time and space, with no stability constraints. This is due to the time-centred implicit character of the ADI scheme (Stelling *et al.*, 1986).

ADI-M incorporates a flooding and drying capability, which consists of the specification of a minimum depth, in order for the cell grid to be considered in the hydrodynamic calculations. This feature is particularly relevant in the modelling of coastal areas.

The numerical solution of the depth-average momentum Equations 3.4 and 3.5, and the continuity Equation 3.1 (obtained in Section 3.3.1) requires a strategy solution for: local acceleration, advective acceleration, bed shear resistance, and turbulence. A brief description of the strategy implemented by ADI-M is outlined below.

Bottom friction: Bed roughness is calculated based on the Chezy coefficient (C_e), which is a semi-empirical bottom friction coefficient developed to describe uniform flow in open channels (Falconer and Lin, 2001). If the flow is rough turbulent with a typical Reynols number $Re \gg 1000$, a logarithmic velocity-depth profile is assumed. Consequently, C_e is independent of the flow and varies with the relative roughness of the bottom surface (Falconer and Lin, 2001). In this situation C_e is calculated using Manning's equation. In the case of transitional flows ($2000 < Re < 4000$), the Chezy coefficient varies with the flow conditions; under these circumstances, the Chezy coefficient is calculated with the Colebrook-White equation, which depends on the Darcy Weisbach resistance coefficient and the channel Reynols number is calculated in the simulation (Falconer and Lin, 2001). Rough turbulent flow is assumed for the work developed in this thesis, and a drag coefficient C_d is used instead of relative roughness. The Chezy coefficient implemented in this research is $C_e = \sqrt{g/C_d}$.

Turbulence: In ADI-M the depth-integrated turbulence model considers only the effects of the bed shear stress (Falconer and Lin, 2001). The flow velocity reduction due to bed friction is related to the bed characteristics, fluid characteristics and flow features such as shear stress (Kvocka, 2015). In the case of a depth-average model, the turbulent shear stress is dominated by the turbulence near the bottom. Consequently, the turbulence model indicates the impact of bed generated turbulent momentum exchange on the depth-averaged flow profile. Two-dimensional features such as horizontal vorticity can be simulated; however, three-dimensional phenomena such as a turbulent wake behind the object are not captured by the turbulent model of ADI-M.

In terms of variable storage and computation ADI-M uses a space-staggered orthogonal computational grid (Falconer and Lin, 2001; Nash, 2010). Elevation and solute concentration are discretised at the centre of the grid cell, meanwhile velocity components are discretised at the centre of grid cells. Further detail is provided in Appendix A.5.

ADI-M is a well-documented model, a detailed description of the hydrodynamic solution procedure has been reported by Nash (2010), Boye (2014), and Phoenix (2017). ADI-M has been successfully used to quantify hydrodynamics effects due to marine turbine energy extraction, by incorporating the momentum loss as a sink term in the momentum equations in a simplified manner. Important results such as changes in tidal regime and the effects of turbine spacing and environmental impact of an array's configuration have been investigated (Nash *et al.*, 2015; Fallon *et al.*, 2014; Hartnett *et al.*, 2012; Ahmadian and Falconer, 2012).

3.5.2 TVD-M Model

The tidal-stream power extraction problem at the regional scale for RVF (derived in Section 3.3.2) was solved numerically by implementing the LMAD-OCH theory. The numerical scheme developed in this thesis to solve the RVF problem is a numer-

ical extension of TVD-M, the resultant scheme is called the TVD-TOC model. To provide a numerical background to the shock-capturing model developed in this thesis, a summary description of the original version TVD-M is provided.

TVD-M was developed to simulate hydrodynamic processes subject to strong spatial gradients in rivers and coastal waters. This efficient shock-capturing model (Liang et al., 2006, 2007) has been improved by optimising processes on a single central processing unit, and by introducing parallel processing on multiple CPU cores using shared memory (Whittaker, 2014; Kvočka, 2017).

This numerical scheme is useful to model RVF such as hydraulic jumps, flood waves, tidal bores, dam breaks and shock waves. This is possible because the scheme can produce the correct weak solutions of the equations that describe these phenomena and thus capture the discontinuities of the equations (Ming and Chu, 2000; Liang et al., 2006). This model belongs to the shock-capturing type, which consists of the algebraic combination of the first-order and second-order upwind schemes, where a kind of artificial viscosity is included to smooth the solution close to the shock (Gustafsson, 2011; Liang et al., 2006). The proportion of the contribution of each scheme is adjusted depending on the nature of the flow. If the solution is sub-critical (smooth), the second-order scheme is implemented; if the solution is trans- or super-critical, the lower-order scheme is implemented (Liang et al., 2006). TVD-M solves the shallow water equations using a combination of the standard MacCormack scheme and the symmetric total variation diminishing (TVD) term (Kvocka, 2015). Importantly, the shock-capturing method used by TVD-M allow the computation of discontinuities likely to appear in RVF simulation, without requiring treating the discontinuity as an internal boundary.

TVD-M also incorporates a flooding and drying capability, which consists of the specification of a minimum depth, in order for the cell grid to be considered for hydrodynamic calculations. This feature is important for modelling real world coastal areas where flooding/drying processes are present. The numerical solution to the conserva-

tive form of the governing Equations 3.14 and 3.13 use a solution strategy for local acceleration, advective acceleration, bed shear resistance, and turbulence consistent with ADI-M.

In terms of variable storage and computation TVD-M uses a cell-centered ortogonal computational grid to store and compute variables at the same location (Liang *et al.*, 2006), further detail is provided in Appendix A.5.

The TVD-MacCormack scheme was used to study a 1-D open channel flow (García-Navarro *et al.*, 1992), two-dimensional shallow water flow (Ming and Chu, 2000), wave propagation over the shoreline (Vincent and Caltagirone, 2001), the dam-break problem (Liang *et al.*, 2007), and shallow water flows over an irregular bathymetry (Liang *et al.*, 2006). However, the scheme has not been used to compute the discontinuities produced by marine turbines. The full incorporation of the thrust force due to a marine turbine array forms part of the novelty of this thesis.

3.6   Summary

Numerical models are useful tools to perform tidal stream energy resource assessments. At a regional scale coastal tidal streams can be considered as two-dimensional flows with low Froude numbers. Under this circumstance, marine turbine power extraction can be approximated by depth-average shallow water equations. The numerical efficiency of the finite difference methods, in addition to depth-average approach, provide a practical numerical tool to perform tidal resource assessment and evaluate the hydrodynamical impacts of power extraction.

The study case is a tidal stream in a channel. The momentum loss associated with marine turbine power extraction is introduced as a sink term in the momentum equations. To compute the strong spatial gradient produced by power extraction in the flows' velocity and depth, at a turbine-array, it was necessary to use the conservative

form of the governing equations.

Two numerical approaches are undertaken to evaluate tidal stream resource assessment. The first one uses a numerical model based on the ADI method, which has been used previously on many occasions to study the far-field hydrodynamical impacts of marine turbine arrays. In this thesis, the method used by this model to simulate the turbine's energy capture is further improved by employing a non-constant thrust coefficient. The second one is a model with shock-capturing capability, which uses a combination of the first-order and second-order upwind methods: TVD and Mac-Cormack. In contrast with the shock-fitting method proposed by Draper (2011), the shock-capturing method proposed in TVD-M has not previously been used to simulate marine turbines. The shock-capturing method allows the simulation of discontinuities produced in the flow due to power extraction, without treating the discontinuity as an internal boundary. In this thesis, the incorporation of marine turbine energy extraction computations are introduced.

A common feature between ADI-M and TVD-M is the use of a two-stage scheme to solve 2D problems as two 1D problems. However, the models differ in terms of variable storage and computation. TVD-M stores and computes variables at the same location, while ADI-M use a staggered computation grid, where the variables are located at different grid locations (as the solution of a variable depends on the neighbouring variables). Additionally, the semi-implicit character of ADI-M allows more accurate solutions with larger time-steps than TVD-M. The latter uses an explicit scheme, where numerical accuracy requires a further constraint on the computational time-step.

The next stage of development is the description of the marine turbine array representation proposed by this thesis, and the specification of the extended numerical models developed as part of this thesis. This is presented in Chapter 4.

Chapter 4

Marine Turbine Array Representation

4.1 Introduction

In the previous chapter, the 2D-SWE equations that describe a tidal-stream subject to power extraction were described; two scenarios were considered: SSF and RVF. In this way, it is possible to investigate the importance of solving the rapid changes produced in the stream (depth-average velocity and depth) due to power extraction. The solutions to these two scenarios were approximated numerically.

The marine turbine array representation developed in this thesis, as well as the procedure followed to perform the tidal-stream resource assessment, is presented here. Furthermore, the extended numerical models developed in this thesis, ADI-TOC and TVD-TOC, are also presented.

Section 4.2 describes the LMAD-OCH theory. The equations derived from this theory to calculate the momentum sink due to the array of turbines, and to perform tidal-stream resource assessment are developed. Section 4.3 describes two current approaches to numerically represent marine turbine arrays in depth-average models. The advan-

70

tages and disadvantages of these strategies are discussed. Section 4.4 describes the method developed in this thesis to simulate marine turbines. This numerical representation addresses the drawbacks found in current approaches to numerically represent marine turbines in depth-average models. Additionally, this section presents the procedure followed to perform tidal-stream resource assessment. Section 4.5 and Section 4.6 describe the improvements performed in the ADI-M and TVD-M schemes. The extended versions of the models simulate the momentum extracted by the turbine based on the operating conditions of the turbine, incorporating free-surface flow. This was possible by numerically implementing the LMAD-OCH theory and using the momentum sink approach.

4.2   Linear Momentum Actuator Disk in an Open Channel Flow

LMAD-OCH theory provides a more comprehensive investigation of the tidal-stream power extraction in shallow waters than the infinite flow and finite extent flow with rigid lid analytical approaches. The LMAD-OCH analytical model considers a finite extent flow with a deformable surface, including a turbine-wake mixing region (Houlsby *et al.*, 2008; Houlsby and Vogel, 2017). A finite flow is obtained when considering that the tidal-stream is subjected to the sea bed and atmospheric pressure boundary constraints. In this way, gravitational effects play an important role in defining the free-surface of the flow. The power extraction under this scenario can be applied to a single turbine in a channel with parallel sides, or to a turbine located within a long fence of regularly placed devices.

The assumptions of the analytical theory are: uniform spacing and parallel location of the turbines, the dominance of the turbine thrust force over the other source terms (such as bed friction, viscous, and inertial forces), slowly varying characteristics of the

fence and basin (such as blockage ratio and water depth), and finally the consideration of a turbine-wake mixing length (L_v) (Draper, 2011). A description of the energy extraction within the length L_v according to LMAD-OCH is shown in Figure 4.1. The implementation of LMADT for a tidal fence scenario assumes that the upstream flow passes through the fence, mixes, and returns to a vertical profile similar to that upstream over a length L_v; this length is referred to as the near-field extent (Draper *et al.*, 2010). Within this length, it is considered that a faster flow bypasses the turbine and mixes energetically with the slower flow that passes through the turbine. As a result, the flow structure over L_v is three-dimensional (Draper *et al.*, 2010). The turbine-wake mixing length is justified by the estimations of the turbine-wake downstream recovery length. The mean axial velocities recover to about 80% within $10d$ downstream (Stallard *et al.*, 2013), where d indicates turbine diameter. Longer downstream lengths such as $40d$ allow a 98% recovery (Nash *et al.*, 2015).
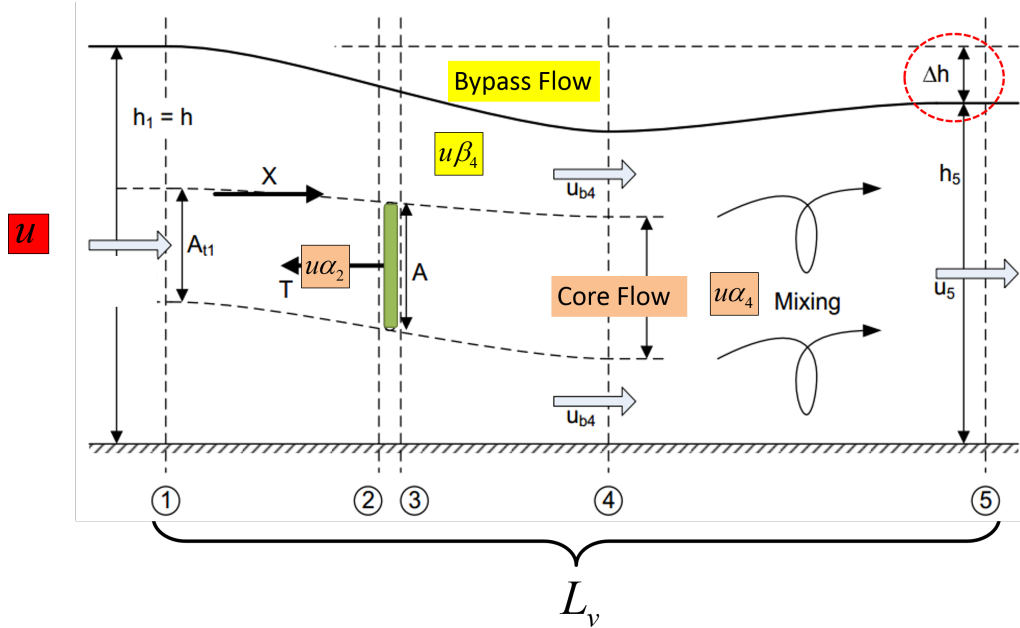
Fig. 4.1: Sketch of tidal-stream power extraction with an actuator disc in an open channel flow. Figure taken from Draper (2011).

The momentum extracted by a marine turbine is studied in a sub-critical tidal-

stream; a water elevation reduction in the downstream depth is developed as a consequence of power extracted. This scenario is analysed in an open channel flow using LMADT by considering five individual stations (see Figure 4.1); the tidal flow also considers core-flow and bypass-flow components. The core-flow refers to the stream that passes through the turbine and is denoted by the subscript t. The bypass-flow corresponds to the flow that circumvents the turbine and is denoted by the subscript b. Stations (1) and (2) are located upstream of the turbine, which is characterised by an area A (see Figure 4.1). The first station is far upstream; at this location the flow is considered to be uniform i.e. the flow is undisturbed by the presence of the turbine and has velocity u and depth h. The second station is immediately upstream of the turbine; here the momentum loss produces a decrease in velocity, represented by the turbine velocity coefficient α_2. Station (3) is immediately downstream of the turbine; station (4) is located further downstream.

At station (4), the core flow velocity experiences a larger velocity reduction due to momentum extraction denoted by a wake induction factor α_4. Meanwhile, the turbine bypass flow presents a velocity magnitude increase characterised by a bypass induction factor β_4. The water depth associated with station 4 is h_4.

The analysis of the tidal-stream assumes that $1.0 > \alpha_2 > \alpha_4 > 0$; consequently, the flow deceleration produced by power extraction is described by: $u > u\alpha_2 > u\alpha_4$. Finally, at station (5), a head drop is shown and this loss of potential energy across the turbine is accompanied by an increase in kinetic energy downstream in the turbine (Houlsby *et al.*, 2008; Bryden *et al.*, 2007). This result indicates that the turbine extracts potential energy instead of kinetic energy, and this is the opposite to a wind turbine energy extraction scenario (Houlsby *et al.*, 2008; Serhadlioglu, 2014).

The analysis of the actuator disc in open channel flow leads to three main results: (1) the derivation of the thrust exerted by the turbine on the flow and the power removed by the turbine, (2) the estimation of the relative head drop and the deter-

mination of the power loss by the turbine wake mixing, and (3) the deduction of the turbine efficiency, which allows the definition of available power. These results are derived in the following sections.

4.2.1 Thrust Force and Power Removed by the Turbine

The momentum extracted by a turbine produces an increase in the pressure over the actuator disc, to ensure continuity of mass and momentum in the flow (Burton *et al.*, 2001). This pressure jump acts as an external force, referred to as thrust (T), and this force is responsible for axial momentum extraction. The derivation of thrust, power (P), and implications of a turbine downstream mixing region in the flow analysis are described below.

Bernoulli's equation is used to quantify pressure changes. As the pressure is discontinuous across the actuator disk, Bernoulli's equation is applied, where the variation of pressure from point to point occurs in a continuous way. Bernoulli's equation is applied to the following sections (see Figure 4.1): bypass-flow (Equation 4.1), turbine-core flow in stations 1-2 (Equation 4.2), and turbine-core in stations 3-4 (Equation 4.3). This leads to the following expressions:

$$h + \frac{u^2}{2g} = h_4 + \frac{u^2 \beta_4^2}{2g} \tag{4.1}$$

$$h + \frac{u^2}{2g} = h_{t2} + \frac{u^2 \alpha_2^2}{2g} \tag{4.2}$$

$$h_{t3} + \frac{u^2 \alpha_2^2}{2g} = h_4 + \frac{u^2 \alpha_4^2}{2g} \tag{4.3}$$

From Equations 4.2 and 4.3, where h_4 is obtained from Equation 4.1, it is possible to define the head drop across the turbine as follows:

$$h_{t2} - h_{t3} = \frac{u^2}{2g}(\beta_4{}^2 - \alpha_4{}^2) \tag{4.4}$$

In the case of open channel flows, thrust force is defined in terms of the elevation

change across the disc in the following way:

$$T = Adp \tag{4.5}$$

$$dp = \rho g(h_{t2} - h_{t3}) \tag{4.6}$$

If it is considered that the actuator disc is located within a tidal fence of regularly spaced actuator discs. The turbine area is defined as $A = Bhb$, where h is the upstream depth (station 1), b the inter-turbine spacing, and B the turbine blockage ratio. Note that the study of a single turbine implies $b = 1$, in such case as it is obtained $B = A/h$. The blockage ratio varies in the range $0 < B < 1$, where $B = 0$ indicates the turbine's non-existence and a free flow of the tidal-stream; on the contrary, $B = 1.0$ implies a turbine that covers the channel cross-section completely and hence the flow is choked. The limiting situations of $B=0$ and $B=1$ imply null power extraction (Sutherland *et al.*, 2007; Garrett and Cummins, 2007).

Substituting Equation 4.4 into Equations 4.6 and 4.5, it is possible to define the thrust force and the thrust coefficient C_T as follows:

$$T = Bbh\rho\frac{u^2}{2}(\beta_4{}^2 - \alpha_4{}^2) = \frac{1}{2}\rho u^2 BbhC_T; \tag{4.7}$$

$$C_T = \beta_4{}^2 - \alpha_4{}^2 \tag{4.8}$$

The power removed by the turbine and the power coefficient, C_P, are defined in terms of the turbine velocity coefficient α_2 in the following way:

$$P = Tu\alpha_2 = \frac{1}{2}\rho u^3 BbhC_P; \tag{4.9}$$

$$C_P = \alpha_2(\beta_4{}^2 - \alpha_4{}^2) \tag{4.10}$$

The turbine velocity coefficient indicates the reduction rate of the flow when passing through a device. It can be derived from an alternative calculation of the thrust force with the momentum and continuity equation. Applying the momentum conservation equation between stations 1-4, it is possible to obtain another expression in terms of

thrust (Houlsby *et al.*, 2008):

$$\frac{1}{2}\rho g b(h_2^2 - h_4^2) - T = \rho u^2 Bbh\alpha_2(\alpha_4 - 1) + \rho u^2 hb(1 - B\alpha_2)(\beta_4 - 1) \tag{4.11}$$

The T term can be eliminated from Equation 4.11 by introducing Equation 4.7:

$$\frac{1}{2}g(h_2^2 - h_4^2) - Bh\frac{u^2}{2}(\beta_4{}^2 - \alpha_4{}^2) = u^2 Bh\alpha_2(\alpha_4 - 1) + u^2 h(1 - B\alpha_2)(\beta_4 - 1) \tag{4.12}$$

An expression for the free-surface at station 4 (h_4) can be derived from the application of the momentum conservation equation across stations 1-4 (Houlsby *et al.*, 2008):

$$h_4 = Bh\frac{\alpha_2}{\alpha_4} + h\frac{1 - B\alpha_2}{\beta_4} \tag{4.13}$$

From Equation 4.13, it is possible to obtain the following expression for α_2 (Houlsby *et al.*, 2008):

$$\alpha_2 = \frac{\alpha_4\left(h(1 - \beta_4) + \beta_4(h - h_4)\right)}{Bh(\alpha_4 - \beta_4)} \tag{4.14}$$

In turn, Equation 4.14 can be re-written to eliminate h_4 by considering Equations 4.1, 4.12, and 4.13; the following expression for α_2 is obtained (Houlsby *et al.*, 2008):

$$\alpha_2 = \frac{2(\beta_4 + \alpha_4) - (\beta_4 - 1)^3(B\beta_4{}^2 - B\beta_4\alpha_4)^{-1}}{4 + (\beta_4{}^2 - 1)(\alpha_4\beta_4)^{-1}}. \tag{4.15}$$

Equation 4.15 indicates that the power extraction dynamics in an open channel flow is a function of three parameters sets: $0 < B < 1.0$; $\beta_4 > 1$, and α_2 or α_4. Additionally, α_2 indicates the inter-relation of the bypass and core flow across the turbine, this relation is prescribed by the parameters B, β_4, and α_4 (Serhadlioglu, 2014). Finally, the solution of Equation 4.15 allows the calculation of the power removed by the turbine through Equation 4.9.

However, an additional equation that defines β_4 is missing. This expression is obtained by eliminating α_2 and h_4 from Equation 4.12 by applying Equations 4.1, 4.13, and 4.15. The result is a quartic polynomial with β_4 coefficients (Houlsby *et al.*,

$$\frac{Fr^2}{2}\beta_4{}^4 + 2\alpha_4 Fr^2\beta_4{}^3 - (2 - 2B + Fr^2)\beta_4{}^2 - (4\alpha_4 + 2\alpha_4 Fr^2 - 4)\beta_4$$
$$+ \left(\frac{Fr^2}{2} + 4\alpha_4 - 2B\alpha_4{}^2 - 2\right) = 0 \tag{4.16}$$

Equation 4.16 is a function of the upstream Froude number, the wake induction fac-
tor α_4, and the turbine blockage ratio B. The solution of the quartic polynomial is
restricted to the physical solution of the bypass flow, and this is given by a bypass
sub-critical flow (Whelan *et al.*, 2009; Houlsby *et al.*, 2008). The roots of Equation
4.16 provide the solution of the bypass induction factor β_4. In turn, this solution is
used to calculate the thrust force coefficient (Equation 4.8) and the power coefficient
(Equation 4.10). Finally, it is possible to calculate the thrust exerted by the turbine
on the flow, and the power extracted by the turbine.

4.2.2   Relative Head Drop and Power Loss by Turbine Wake Mixing

An additional result of the LMAD-OCH theory is the analysis of the turbine-wake
mixing region, which leads to the relative head drop $\Delta h/h$ and the turbine efficiency η
determination. The relative head drop refers to the dimensionless head loss obtained
from stations 1-5 ($\Delta h/h = (h - h_5)/h$). The derivation of parameters η and $\Delta h/h$ are
described below.

The application of the momentum conservation equation between stations 1-5 leads to
the following expression in terms of the headloss Δh (Houlsby *et al.*, 2008):

$$\frac{1}{2}\rho g b(h^2 - (h - \Delta h) - T = \rho b h u^2 \left(\frac{h}{h - \Delta h} - 1\right) \tag{4.17}$$

Equation 4.17 can be re-written using the thrust coefficient definition derived in Equa-
tion 4.7 to eliminate the thrust. As a result, a cubic polynomial with relative head

drop coefficients is obtained (Houlsby *et al.*, 2008):

$$\frac{1}{2}\left(\frac{\Delta h}{h}\right)^3 - \frac{3}{2}\left(\frac{\Delta h}{h}\right)^2 + \left(1 - Fr^2 + \frac{C_T B Fr^2}{2}\right)\frac{\Delta h}{h} - \frac{C_T B Fr^2}{2} = 0 \qquad (4.18)$$

The solution of Equation 4.18 is also restricted to sub-critical upstream flows (prescribed by the Froude number) and it is a function of the turbine operating conditions given by B and α_4.

The analysis of shallow water flows with a free-surface indicates that the momentum lost by the stream generates a head drop. In turn, the head drop enhances the velocity of the flow downstream of the turbine; this feature is evident in the stream velocity at station 5 (u_5) obtained by (Houlsby *et al.*, 2008):

$$u_5 = u\left(\frac{h}{h - \Delta h}\right) \qquad (4.19)$$

The increase of the downstream velocity comes as a consequence of mass conservation to compensate for the head drop (Serhadlioglu, 2014). The head drop consideration in the tidal-stream power extraction indicates that marine turbine extracts potential energy from the flow, rather than kinetic energy.

The identification of the head drop change enables the estimation of the power lost by the turbine wake mixing, P_W. This is obtained from the evaluation of the changes in kinetic and potential energy between stations 4-5, and it has the following form (Houlsby *et al.*, 2008):

$$P_W = \frac{1}{2}\rho u^3 B b h \alpha_2 \alpha_4{}^2 + \frac{1}{2}\rho u^3 b h (1 - B\alpha_2)\beta 4^2 - \frac{1}{2}\rho u^3 b h \left(\frac{h}{h - \Delta h}\right)^2 + h b u (h_4 - h_5)\rho g \qquad (4.20)$$

Combining the power lost in the turbine wake P_W with the power removed by the turbine P (Equation 4.9), it is possible to identify the total power extracted by the turbine P_T:

$$P_T = P + P_W = \rho g u b h \Delta h \left(1 - Fr^2 \frac{1 - \Delta h/2h}{(1 - \Delta h/h)^2}\right) \qquad (4.21)$$

Equation 4.21 indicates that the total power extracted in the channel is a function of the rate at which the potential energy is being lost in the channel (Draper, 2011).

4.2.3 Turbine Efficiency and Power Available

A measure of the effectiveness of turbine performance at extracting energy from the tidal-stream is given by the turbine efficiency, η. This parameter is defined as the ratio of power removed by the turbine, to the total power extracted from the tidal-stream:

$$\eta = \frac{P}{P + P_W} = \frac{P}{\rho g u b h \Delta h}\left(1 - Fr^2 \frac{1 - \Delta h/2h}{(1 - \Delta h/h)^2}\right)^{-1}. \tag{4.22}$$

In the case of finite and small Froude numbers, η can be approximated as:

$$\eta = \frac{P}{\rho g u b h \Delta h} \tag{4.23}$$

Additionally, Draper (2011) shows that the influence of the depth changes on η are better appreciated by re-arranging Equation 4.23 in terms of the turbine velocity coefficient α_2. To accomplish this, the alternative definition of P is used (Burton et al., 2001; Houlsby et al., 2008):

$$P = T(\alpha_2 u) \tag{4.24}$$

Equation 4.24 is re-written by obtaining T from Equation 4.17 and multiplying by $\alpha_2 u$:

$$T\alpha_2 u = \rho g b h u \alpha_2 \left(\Delta h - \frac{\Delta h}{2}\frac{\Delta h}{h} - Fr^2\left(\frac{h\Delta h}{h - \Delta h}\right)\right) \tag{4.25}$$

Using Equation 4.25 in Equation 4.23, it is obtained:

$$\eta = \alpha_2 \left(1 - \frac{\Delta h}{2h} - Fr^2\left(\frac{1}{1 - \Delta h/h}\right)\right) \tag{4.26}$$

In the case of small Froude numbers: $Fr^2(1 - \Delta h/h) \ll 1$, therefore a satisfactory approximation of the efficiency is given by the following expression, which is suitable for many tidal flows expected in real conditions (Draper, 2011):

$$\eta \approx \alpha_2 \left(1 - \frac{1}{2}\frac{\Delta h}{h}\right) \tag{4.27}$$

Expression 4.27 indicates that for negligible head drops $\eta \to \alpha_2$. This result illustrates the importance of considering the inter-relationship of the velocities across the turbine, which in turn are functions of the turbine operating conditions: B and α_4. This relationship is specified by the turbine velocity coefficient α_2 defined in Equation 4.15.

In addition, from the efficiency (either Equation 4.27 or 4.22) and the total power extracted (Equation 4.21), it is possible to obtain another expression for the power removed by the turbine (Equation 4.9) in terms of the efficiency:

$$P_* = \eta P_T \tag{4.28}$$

Equations 4.9 and 4.28 show that the power removed by the turbine represents the available power that would be used for electricity generation. Although P and P_* indicate the same metric, both terms are kept to facilitate the identification of differences reported by the models solutions.

Finally, an alternative representation of power loss by turbine wake mixing can be obtained in terms of total power extracted and turbine efficiency:

$$P_W = P_T - P_* = P_T(1 - \eta) \tag{4.29}$$

4.3 Numerical Implementation of Marine Turbines

The simulation of power extraction by marine turbines in numerical models requires the computation of the momentum extracted by the turbine from the tidal-stream. The methodology adopted in this thesis to numerically represent marine turbines is based on two current approaches used to simulate tidal-stream energy extraction in depth-average models. These two approaches are (a) line sink of momentum and (b) momentum sink. These methodologies consider inter-turbine spacing and flow directionality; they are indifferent to turbine geometry.

The first approach represents turbines as a line sink of momentum by modifying the

mass flux passing through a turbine-fence, and it has been implemented in a discontinuous Galerkin model. This approach applies the LMAD-OCH theory, however, the discontinuous Galerkin model requires the specification of the head drop across the array. This condition adds a constraint to the simulation of the energy captured by turbines.

The second approach represents the turbines as a sink term in the momentum equations. The sink term accounts for the momentum extracted by the axial component of the turbine's thrust force. This method has been previously introduced in ADI-M. A drawback of this approach is that the turbine's operating conditions are ignored when calculating the momentum extracted and turbine wake losses are not accounted for.

Descriptions of the line sink of momentum and momentum sink implementations are presented in the following sections.

4.3.1 Line Sink of Momentum Approach

The line sink of momentum has been used to simulate regularly spaced turbines arranged in a single row; this configuration is referred to as a tidal fence. The study of this configuration enables the satisfactory calculation of power extraction using the LMAD-OCH theory (Houlsby *et al.*, 2008). This analytical model provides the basis for relating turbine operational conditions to momentum extracted by turbines. The line sink of momentum was used to numerically implement the LMAD-OCH theory in a depth-average discontinuous Galerkin hydrodynamic model (Draper *et al.*, 2010). This is a finite volume model that uses an HLLC Riemann solver (Draper, 2011). The momentum extracted by turbines is simulated by computing the modification of the mass fluxes across the line sink of momentum. The region occupied by a turbine array acts as an interface between upstream and downstream conditions of the flow. This interface represents the elevation and velocity discontinuities produced by power extraction. The line sink approach is justified by considering that the length scale of

the turbine wake is much smaller than the mesh size. To complete the line sink of momentum numerical representation, a condition on the head drop across the array is required (Draper, 2011). This condition is given by the relative change of the head drop provided by the LMAD-OCH (Equation 4.18).

Below, a brief description of the procedure followed by the discontinuous Galerkin model to calculate the momentum extracted by the tidal turbine array via the line sink of momentum is presented. The numerical representation of the momentum sink assumes that flows at the location of the fence remain sub-critical. The array is represented by an interface, which acts as an internal boundary and divides the flow into two states: internal and external, referred to as (**I**) and (**E**). The states are sketched in Figure 4.2(a), it is considered that the mass flux flows out of state **I** and into state **E**. These states represent the upstream and downstream conditions of the flow.
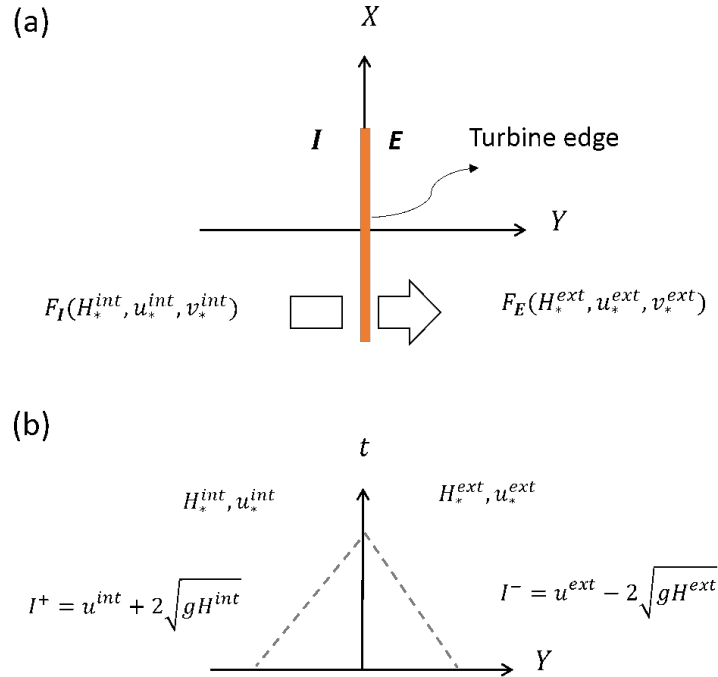
Fig. 4.2: Analytical description of the line momentum sink, used to represent marine turbines in a discontinuous Galerkin model (a). Characteristic lines (b).

The line momentum sink is solved by simulating the discontinuities produced in the velocity and elevation fields as a consequence of the momentum extraction. This is accomplished by computing flow properties at both states. The flow properties are properly represented by the fluid mass flux, defined as the time rate of fluid mass that crosses a given surface. The momentum extracted by the turbine requires the recalculation of mass flux out of the state **I**, prescribed by $F_{\mathbf{I}}(H_*^{int}, u_*^{int}, v_*^{int})$, and into the state **E**, defined as $F_{\mathbf{E}}(H_*^{ext}, u_*^{ext}, v_*^{ext})$ (Draper, 2011). The values H, u, v, represent the total depth of the water column and the depth-average normal velocity and tangential velocity in the state **I** (int) and **E** (ext). In particular, $H_*^{int}, u_*^{int}, H_*^{ext}, u_*^{ext}$ represent the solution of a one-dimensional local Riemann problem. The Riemann problem consists of computing a discontinuity, which initially separates two arbitrary states (Khan, 2010). Consequently, the Riemann solution indicates the mass flux through the discontinuity and therefore, the shock propagation.

The calculation of the internal and external fluxes, $F_{\mathbf{I}}$ and $F_{\mathbf{E}}$, requires specification of altered normal velocities (u_*^{int}, u_*^{ext}) and total depths (H_*^{ext}, H_*^{int}) at the interface, where the discontinuity line is imposed (Serhadlioglu, 2014). The solution to these quantities are obtained from the Riemann characteristic invariants and the relative water drop across the array (given by Equation 4.18). The characteristic invariants correspond to the characteristic lines in a sub-critical flow at the discontinuity (Draper, 2011), see Equations 4.30a and 4.30b. The characteristic lines (I^+ and I^-) at the interface where the Riemann problem is solved are illustrated in Figure 4.2(b).

$$I^+ = u^{int} + 2\sqrt{gH^{int}} \tag{4.30a}$$

$$I^- = u^{ext} - 2\sqrt{gH^{ext}} \tag{4.30b}$$

The four equations that solve the four unknowns $H_*^{int}, u_*^{int}, H_*^{ext}, u_*^{ext}$ and therefore

solves the Riemann problem are (Draper, 2011; Serhadlioglu, 2014):

$$u^{int} + 2\sqrt{gH^{int}} = u_*^{int} + 2\sqrt{gH_*^{int}} \tag{4.31a}$$

$$u^{ext} - 2\sqrt{gH^{ext}} = u_*^{ext} - 2\sqrt{gH_*^{ext}} \tag{4.31b}$$

$$H_*^{int}u_*^{int} = H_*^{ext}u_*^{ext} \tag{4.31c}$$

$$\frac{\Delta H^*}{H_*^{int}} = \frac{H_*^{int} - H_*^{ext}}{H_*^{int}} = \Theta(Fr, B, \alpha_4) \tag{4.31d}$$

where $H^{int}, u^{int}, H^{ext}, u^{ext}$ are obtained by interpolating the discrete solution of the governing equations (Draper *et al.*, 2010). Assuming that the flow remains sub-critical at the turbine, Equations 4.31a, 4.31b, and 4.31c indicate the conditions that the characteristic invariants should meet. Equation 4.31d indicates the condition that the relative change across the array should satisfy. This condition corresponds to the solution of the cubic polynomial Θ (Equation 4.18), derived by the LMAD-OCH theory. The blockage ratio B, Froude number Fr and H_*^{int} are defined relative to the depth and velocity at the external estate (or upstream conditions); the wake velocity parameter α_4 is specified as an initial value. The system of Equations is solved numerically using the Newton-Raphson iterative method. The result is the determination of flux out of the state **I** ($F_{\mathbf{I}}(H_*^{int}, u_*^{int})$) and into the state **E** ($F_{\mathbf{E}}(H_*^{ext}, u_*^{ext})$).

A drawback of the line sink of the momentum is the condition on the relative head drop across the array due to the momentum extracted. This constraint limits the free-surface and makes the analysis of the tidal-stream less realistic. In addition, the mass fluxes and solution of the Riemann problem are calculated per each finite volume mesh used to define the array of turbines. This is an expensive method in computational terms (Shyue, 1998). RVF simulations present high computational cost as their solution requires long computational time or large computational resources (Liang *et al.*, 2006; Kvočka *et al.*, 2015).

4.3.2 Momentum Sink Approach

The momentum sink approach simulates energy captured by the turbine, by including a sink term in the momentum equations. This approach has been widely used to represent arrays of turbine (Sun *et al.*, 2008; Ahmadian *et al.*, 2012a; Ahmadian and Falconer, 2012; Fallon *et al.*, 2014; Nash *et al.*, 2014, 2015; Phoenix, 2017; Plew and Stevens, 2013; Ramos *et al.*, 2013; Sheng *et al.*, 2012; Neill *et al.*, 2012). The sink term method accounts for the momentum extracted by the axial component of the turbine's thrust force. The thrust force computation is based on a thrust force coefficient that describes the device performance. Study of marine turbine performance indicates the significance of turbine configurations on the magnitudes of C_T and C_P. Factors that determine turbine configurations are: hub angle, pitch angle, and tip speed ratio (Bahaj *et al.*, 2007). Additionally, the ambient turbulent intensity influence C_T and C_P by affecting bypass flow and down-stream wake flows (Nishino and Willden, 2012a; Mycek *et al.*, 2014).

Traditionally, the thrust and power coefficients have been assumed to be constant. This approach was justified analytically by the Lanchester-Betz-Joukowsky limit (Burton *et al.*, 2001; van Kuik, 2007). This limit was deduced for an ideal scenario that resembled wind turbine operating conditions, and its derivation provided the theory to design and operate wind turbines (Ragheb and Ragheb, 2011; Huleihil and Mazor, 2012). It indicates that at most, 59% of the upstream kinetic flux (passing through the actuator disc area) can be extracted by a disc and converted into mechanical energy. This optimal performance is associated with C_T=0.9 and C_P=0.59. Furthermore, experiments performed on $1/30^{th}$ scale horizontal axis marine turbine in a laboratory (Myers and Bahaj, 2007), in a cavitation tunnel, a towing tank (Bahaj *et al.*, 2007), and a flume tank (Gaurier *et al.*, 2013) report values for the power and thrust coefficients in the range: $0.4 < C_P < 0.45$ and, $0.78 < C_T < 0.88$.

To perform tidal-stream resource assessment, many far-field hydrodynamic models have

approximated the thrust coefficient as a constant value in the range: $0.8 < C_T < 1.0$ (Ahmadian and Falconer, 2012; Ahmadian *et al.*, 2012b; O'Brien, 2013; Fallon *et al.*, 2014).

A novel contribution of this thesis is an extension of the thrust force already implemented in ADI-M; a brief description of the turbine simulation procedure already introduced in the model is presented. The two-dimensional representation of a thrust force $\vec{F_T}$ exerted by a turbine on a tidal-stream and computed by ADI-M is presented schematically in Figure 4.3. It is assumed that the turbine plane is perpendicular to the thrust force exerted on the flow, consequently, the turbine axis is parallel to the incident current (Fallon, 2012).
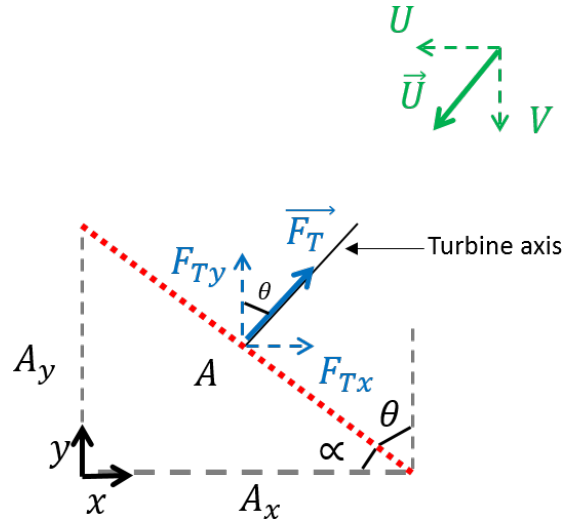
Fig. 4.3: Two-dimensional representation of the thrust force ($\vec{F_T}$) exerted by the turbine to the incident tidal-stream with velocity $\vec{U}$.

Calculation of the thrust force $\vec{F_T}$ (defined as Equation 3.6) is based on the upstream velocity $\vec{U}(U, V)$ located at the same grid cell as the array. This location is justified by the coarse spatial resolution of depth-average models when simulating regional scales. As a result, it is assumed that the velocity within the grid cell is representative of the

upstream flow velocity. This is particularly true for relatively small blockage ratios.

The area of a turbine A used in the sink term calculations corresponds to the cumulative area of the cluster of turbines allocated per grid cell. The turbine cumulative area per grid cell has two components associated with the $x-$ and $y-$directions: A_x and A_y. These components indicate the projected area of the turbine based on the direction of the flow. Computation of the sink term depends on the contribution of each component. These contributions are based on the percentage of the turbine area facing the flow at 90°. Calculation of the turbine area components requires the angle, θ, that the turbine axis makes with an axis parallel to the y-direction (see Figure 4.3). As the axis of the turbine is parallel to the incident current, θ is obtained from the incident angle that the current (U, V) makes with the turbine plane (Equation 4.32). Also, it is necessary to determine the angle, α, that the turbine plane makes with the horizontal axis (Equation 4.33). Turbine area components in the $x-$ and $y-$direction are calculated based on angle α (Fallon, 2012; O'Brien, 2013) (Equation 4.34).

$$\theta = arctan\frac{|U|}{|V|} \tag{4.32}$$

$$\alpha = \frac{\pi}{2} - \theta \tag{4.33}$$

$$A_x = Acos\alpha \qquad \& \qquad A_y = Asin\alpha \tag{4.34}$$

The thrust force implemented in ADI-M is given by Equation 4.35. The thrust force is a function of the turbine area A, the thrust coefficient C_T and the depth-average velocity $\vec{U}$. The thrust coefficient is considered constant and its magnitude varies within the range $0.8 < C_T < 1.0$ (Ahmadian and Falconer, 2012; Ahmadian et $al.$, 2012b; O'Brien, 2013; Fallon et $al.$, 2014).

$$\mathbf{T} = \frac{1}{2}\rho A C_T \vec{U}^2 \tag{4.35}$$

The thrust force acts as a sink term independently of the tidal regime.

Numerically, the sink term corresponds to the thrust force per unit-grid and per unit-mass. The $\vec{F_T}$ components in the $x-$ and $y-$direction are obtained based on the angle

θ that the thrust force makes with a line parallel to the y-direction. Therefore, the components of the thrust force introduced as sink terms in the momentum equations and solved by ADI-M are indicated by:

$$F_{Tx} = \frac{\mathbf{T}}{\Delta x \Delta y}|sin\theta| = \frac{1}{\Delta x \Delta y}\frac{1}{2}\rho A_x C_T U^2 \qquad (4.36)$$
$$F_{Ty} = \frac{\mathbf{T}}{\Delta x \Delta y}|cos\theta| = \frac{1}{\Delta x \Delta y}\frac{1}{2}\rho A_y C_T V^2$$

The turbine's thrust force implemented in ADI-M (Equations 4.36) incorporates the inter-turbine effect of individual turbines, and the direction of the flow on the thrust force calculation. A smaller inter-turbine spacing implies a denser cluster of turbines within grid-cells and consequently a larger effect on flows.

Nevertheless, this methodology does not consider turbine operating conditions such as the blockage ratio and the wake induction factor in the simulation of the energy captured by the turbine. The possibility of including these parameters in the simulation of the thrust force, enables the computation of other parameters such as the water drop across the array and the turbine efficiency. The estimation of η and Δh, provide the metrics to assess the tidal-stream resource. In the following section, the turbine representation method developed in this thesis is presented. This method considers the turbine operating conditions in the computation of the momentum extracted by the turbines.

4.4   Turbine Representation based on the Momentum Sink Method and LMAD-OCH Theory

Herein, an alternative method is proposed to numerically represent marine turbines in depth-average models. The method simulates the energy capture by a turbine array considering the turbine's operating conditions (TOC) within a flow, whose surface is unconstrained. This is accomplished by implementing the LMAD-OCH theory

within the momentum sink approach. The method proposed here will be referred to as *momentum sink-TOC* and provides the possibility of representing marine turbine arrays in more realistic scenarios. This method was implemented in two numerical schemes which separately solve (i) SSF and (ii) RVF. In this way, it was possible to investigate the role of these numerical schemes in simulating spatial gradients of water depth and velocity due to power extraction. According to the numerical implementation of the LMAD-OCH theory through the line sink of momentum, turbine power extraction produces strong spatial gradients in water depth and velocity, which can be considered as discontinuities. The simulation of flows subject to such strong spatial gradients requires a model that solves RVF. Historically, SSF schemes have been developed to assess tidal-stream energy; however recently, models have begun to include RVF solution. One of the objectives of this research is to determine if the complexity of an RVF scheme is necessary to accurately assess tidal-stream resources.

The momentum sink-TOC method computes the energy captured by the turbine, considering that the momentum lost by the stream is proportional to the thrust force exerted by the turbine on the flow. The thrust force calculation (Equation 4.7) includes changes produced in the turbine bypass and core flows due to power extraction. These changes are functions of the turbine's operating conditions prescribed by the blockage ratio and the wake induction factor. Computation of the thrust force requires specification of the following terms: (1) turbine blockage ratio per grid cell, (2) upstream velocity, (3) and thrust coefficient. The specification of these terms is described in the following sections.

4.4.1   Blockage Ratio

In both numerical models, the thrust force applied on the incident current corresponds to the resultant thrust produced by a cluster of turbines allocated per grid cell. As a result, a blockage ratio that accounts for the area of individual turbines within a

grid is necessary. The blockage ratio B, implemented in depth-average models, corresponds to the ratio of the cumulative turbine area per cell-grid (A) over the grid-cell cross-section area ($H\Delta X$). The blockage ratio per grid cell B is defined by Equation 4.37. The cumulative turbine area per cell-grid is obtained by summing up the area of the N individual turbines (A_t) contained in the grid. The number of turbines (N) depends on the inter-turbine spacing (ITS) and the grid-cell size ($\Delta X\ \Delta Y$). This expression is defined by Equation 4.38.

$$\mathbf{B} = \frac{|A|}{H\Delta X} = \frac{NA_t}{H\Delta X} \tag{4.37}$$

$$N = \frac{\Delta X\ \Delta Y}{ITS^2} \tag{4.38}$$

To obtain optimum performance of the device, it is considered that the incident direction of the current is normal to the turbine plane (Ahmadian *et al.*, 2012b; Fallon *et al.*, 2014)

4.4.2 Upstream Velocity

To reduce the effect of a turbine array on the upstream velocity u, the location of upstream velocity was changed from within the grid cell to the neighbouring upstream grid-cell. The new location considers that the grid-cell size is of the order of the turbine wake length. The recovery of mean axial velocities to about 80% - 98% occurs within 10d-40d downstream (Stallard *et al.*, 2013; Nash *et al.*, 2015); in the case of a 16 m diameter turbine the wake extends 160-640 m. In such a situation, the neighbouring cell satisfactorily approximates the upstream conditions of the flow.

The upstream position alternates from one side of the array to the other according to the tidal flow direction, and satisfies the condition presented in Equation **??**.

4.4.3   Thrust Force Coefficient

Calculation of non-constant thrust force coefficient (Equation 4.8) requires specification of the bypass coefficient β_4 and the wake induction factor α_4. These parameters describe the effect of the turbine's thrust on the flow through the intensification of the bypass velocity and the reduction of the velocity passing through the turbine. The parameter α_4 is considered to be an input value of the model. On the other hand, the bypass coefficient corresponds to the physical admissible solution of the quartic polynomial defined in Equation 4.16; β_4 solution describes sub-critical bypass flows (Whelan *et al.*, 2009; Draper *et al.*, 2010). The coefficients of the polynomial require the upstream Froude number, the blockage ratio, and the wake induction factor.

The coefficients of Equation 4.16 are real; therefore, the roots of the quartic polynomial were obtained with an Eigenvalue method (Press *et al.*, 1992). The approach consists of the construction of an upper Hessenberg matrix, whose eigenvalues are the desired roots. The solution procedure can be described as a two-phase approach: on phase 1, an upper Hessenberg matrix is constructed; on phase 2, the matrix is balanced and the eigenvalues of the matrix are calculated with a QR algorithm with shifts. In the case of the polynomial given by Equation 4.16, the β_4 admissible solutions corresponds to real eigenvalues or roots that describe a sub-critical bypass flow. A more detailed description of the Eigenvalue method is presented in Appendix A.2.

4.4.4   Tidal-Stream Resource Assessment Implementation

This research proposes a method to simulate arrays of marine turbines considering the operating conditions of a device within a free-surface flow, and also a procedure to perform tidal-stream resource assessment. The strategy developed to incorporate the momentum sink-TOC method and quantify the resource is described in Figure 4.4. The strategy comprises three steps: (1) momentum sink computation, (2) momen-

tum sink implementation into the hydrodynamic calculations, and (3) energy resource assessment.
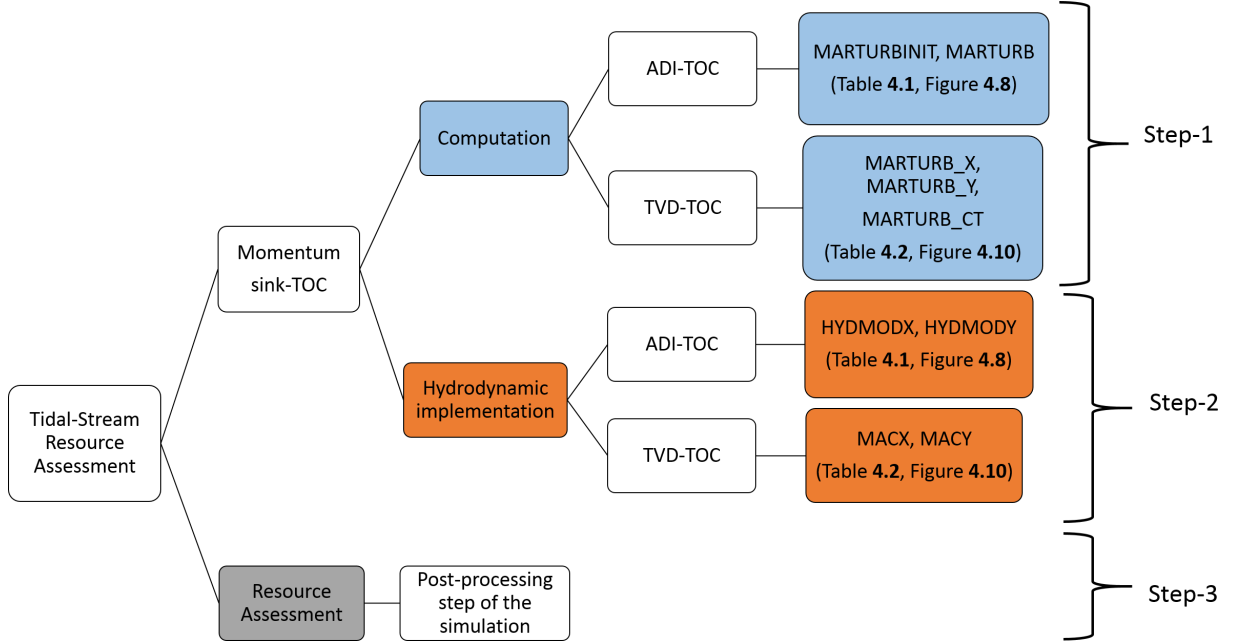
Fig. 4.4: The strategy used to implement the momentum sink-TOC method and assess the tidal-stream resource consists of three steps.

Due to the different solution procedures of the models steps 1-2 are introduced in a different way in ADI-TOC and TVD-TOC. The details of the modification to the codes are outlined in Sections 4.5 and 4.6, respectively. Additionally, the improvements made to the codes are presented in Appendix A.3. The detailed description of steps involved in the strategy presented in Figure 4.4 follows.

Step-1 relates to the calculation terms required to compute the momentum sink-TOC; these are detailed in Figure 4.5. The momentum sink-TOC computation is performed in grid-cells selected to simulate a cluster of turbines and satisfy a prescribed depth ($h > 20$ m). The terms used to compute the momentum sink-TOC are divided into three blocks:

(A1) Calculation of the turbine area components (A_x and A_y) and the blockage ratio
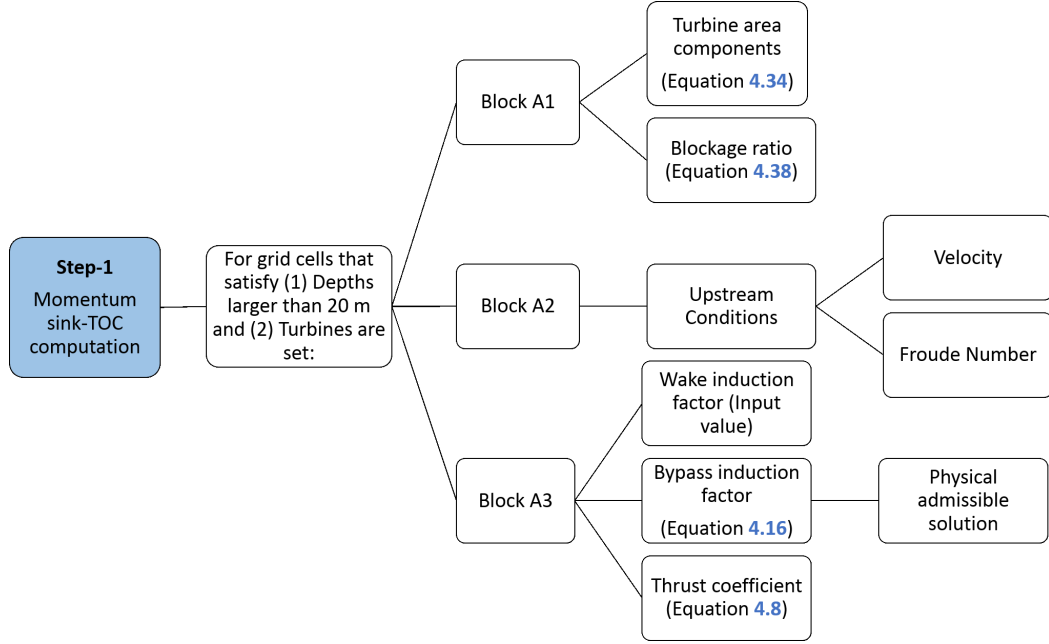
Fig. 4.5: Procedure followed for step-1: Momentum sink-TOC computation.

per grid-cell B.

(A2) Estimation of flow upstream condition prescribed by the velocity and upstream Froude number.

(A3) Identification of the wake induction factor α_4, calculation of the bypass coefficient β_4, which in turn requires the identification of the physical admissible root of the quartic polynomial, and computation of the thrust force coefficient.

Parameters required to define the blockage ratio (turbine diameter and inter-turbine spacing), and the wake induction factor are input values provided by the user.

Step-2 describes the procedure followed to incorporate the momentum sink-TOC into the hydrodynamic calculations of the models; the procedure is detailed in Figure 4.6. The momentum sink term was implemented into the X and Y component of the momentum equations. The parameters required for the specification of the sink term were calculated in step-1, and these parameters are: turbine area component, upstream velocity component, thrust force coefficient, and the specification of the sign-
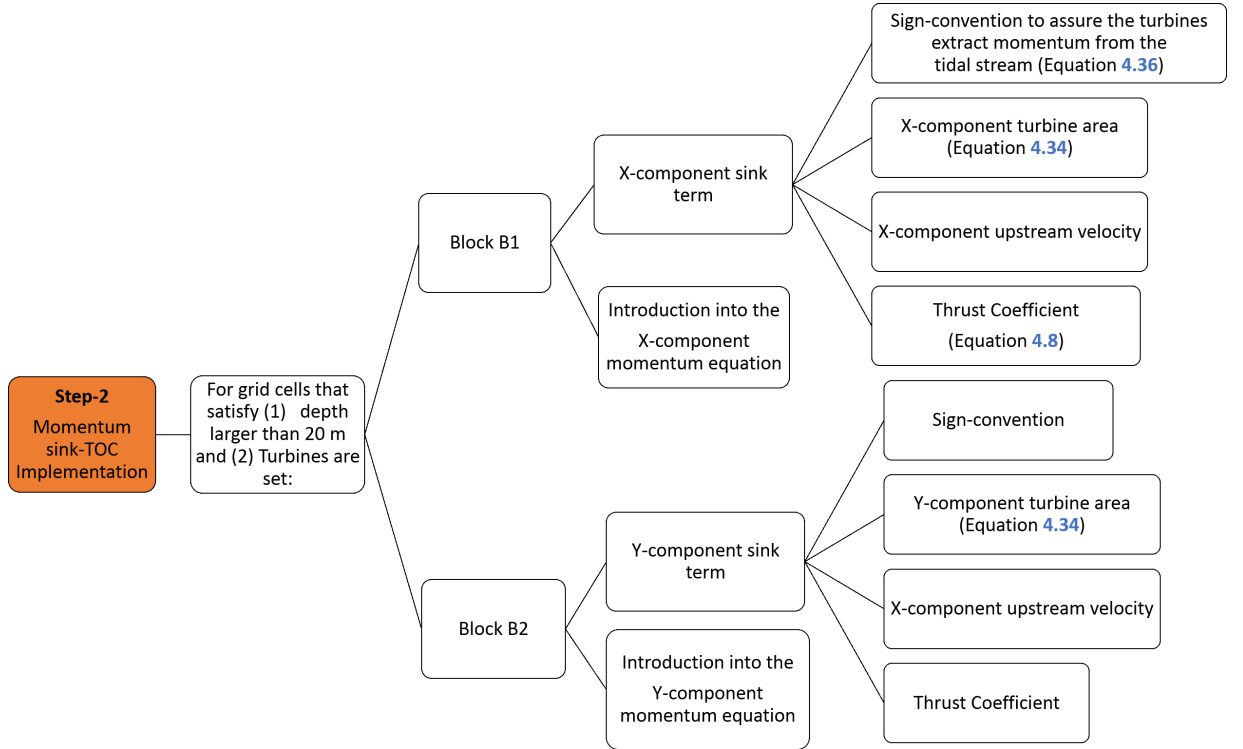
Fig. 4.6: Procedure followed for step-2: Momentum sink-TOC implementation into the hydrodynamic calculations.

convention, which assures the energy capture independently of the tidal regime.

Step-3 describes the procedure followed to perform tidal-stream resource assessment and it is illustrated in Figure 4.7. This is a post-processing simulation step, which is split into four blocks:

(C1) Reading of the model outputs, these values are used to define metrics to quantify the resource.

(C2) Turbine velocity coefficient α_2 calculation, used to calculate the power coefficient and the power removed by the turbine P.

(C3) Head drop across the array estimation Δh, obtained from the depth differences between the upstream and downstream location of the array. This parameter is used to calculate the total power P_T removed and subsequent power metrics.
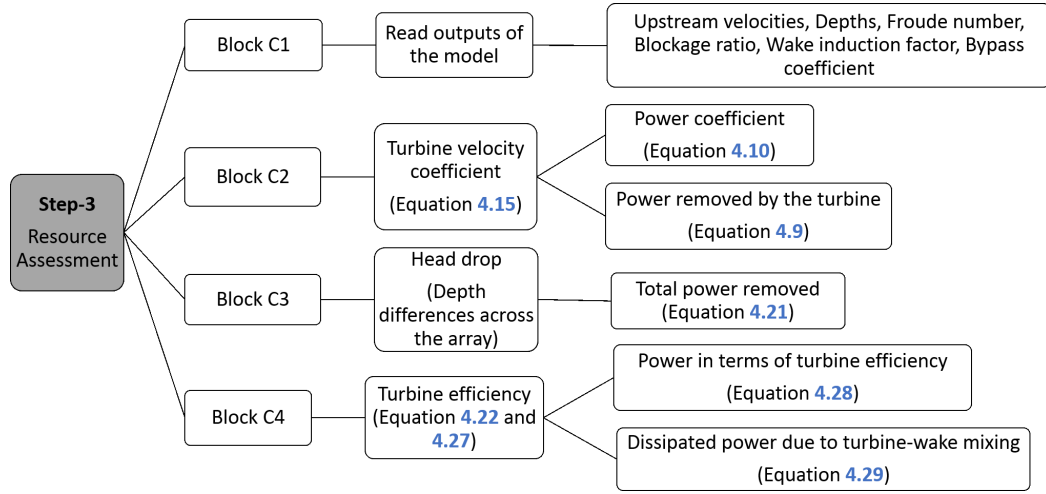
Fig. 4.7: Procedure followed for step-3: Assessment of the resource.

(C4) Turbine efficiency η calculation, which is used to estimate the available power for electricity generation P_* and the dissipated power due to turbine wake mixing P_W.

An example of the Matlab code used to evaluate the resource for step-3 is presented in Appendix A.4. Due to the different solution procedures of the models the momentum sink-TOC implementation differs; the methodologies followed by ADI-TOC and TVD-TOC to compute the energy captured by the turbines is presented below.

4.5 ADI-TOC Model

ADI-TOC model solves for SSF and numerically incorporates the LMAD-OCH theory through the momentum sink-TOC implementation. Also, this version of the model was reformatted to FORTRAN-90. This model is an extended version of the ADI-M scheme introduced in Section 3.5.1. ADI-TOC approximates the solution of the discretised version of the governing equations for tidal power extraction in a channel derived in Section 3.3.1. These equations correspond to the continuity Equation (Eq. 3.1), and momentum Equations (Eqs. 3.4 and 3.5).

The solution procedure of the model is sketched in Figure 4.8. The hydrodynamic calculations are performed in the subroutines highlighted in orange. Meanwhile, the momentum extracted method is computed in the subroutines highlighted in blue. The incorporation of the momentum extraction method required modification of the subroutines involved in the thrust force calculation: MARTURBINIT and MARTURB, and hydrodynamics computation.

The blockage ratio is calculated as an initial condition in the subroutine MARTURBINIT. Later, the components of the turbine area per grid cell A_x and A_y, the upstream velocities, the Froude number, the bypass coefficient β_4, and the thrust force coefficient are calculated every half step in the subroutine MARTURB. The thrust force exerted by the turbines on the flow is part of the hydrodynamic calculations performed in HYDMODX and HYDMODY for the $X-$ and $Y-$ direction, respectively. Descriptions of the main subroutines of ADI-TOC model are presented in Table 4.1.

Fig. 4.8: Flow-chart of the solution procedure of ADI-TOC model.

4.6   TVD-TOC Model

TVD-TOC model solves for RVF and numerically incorporates the LMAD-OCH theory via the momentum sink-TOC. TVD-TOC is executed in parallel mode and 34 threads were used to execute the model. This model is an extended version of the scheme TVD-M introduced in Section 3.5.2. TVD-TOC approximates the solution of the discretised version of the conservative form of the governing equations for tidal power extraction in a channel derived in Section 3.3.2. The model solves the two one-dimensional hyperbolic equations (Equations 3.15 and 3.16) obtained after applying

Description	Subroutines
Reads open boundary data.	BOUND
Reads computational domain.	FIELD
Establishes the integration sections.	FIND
Reads water depths.	DEPTH
Initialises depths, elevations, concentrations and Chezy values.	INITL
Assigns forcing (hydrodynamic data) at the open boundary.	HYDBND
Solves hydrodynamics in x-direction.	HYDMODX
Recalculates water depths.	SIDEH
Checks for flooding and drying of grid-cells.	FLDRY
Solves hydrodynamics in y-direction.	HYDMODY
Calculates (Recalculates) Chezy value for bottom roughness computation.	CHEZY
Calculates (Recalculate) eddy viscosities.	EDDY
Calculates turbine area, blockage ratio and identifies the grid-cells where the momentum sink will be calculated.	MARTURBINIT
Calculates the parameters used in the marine turbine momentum sink calculation: components of the turbine area per grid cell, upstream velocity, upstream Froude number, bypass factor, wake induction factor and thrust coefficient.	MARTURB

Table 4.1: Description of the main subroutines of the ADI-TOC model. The subroutines modified to incorporate the LMAD-OCH theory are highlighted in green.

the operator splitting technique. Discretisation of the governing equations is presented in Appendix A.1.

The model has a modular architecture, which is presented schematically in Figure 4.9. The model is constituted by modules (blue-fill), where each module acts as a package that contains functions and subroutines (green-fill). The use of modules allow the splitting of a numerical code between multiple files. Brief descriptions of the modules, and corresponding subroutines, used by TVD-TOC are given in Table 4.2. The hydrodynamic calculations require boundary conditions (defined in BOUNDARY) and bottom roughness (specified in ROUGHNESS). The solution of the flow in the domain is performed with the MacCormack scheme (specified in MACCORMACK), where the advection terms of the momentum equation are solved separately (in ADVECTION).
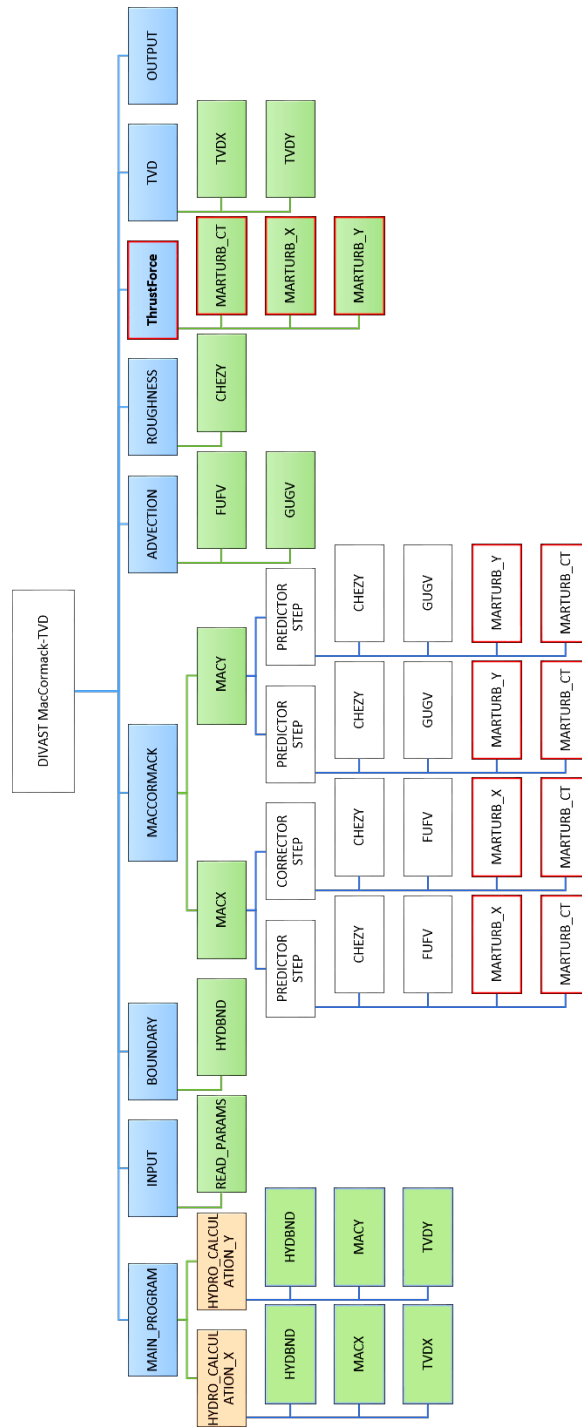
Fig. 4.9: Structure of the TVD-TOC model.

If the flow presents a strong spatial gradient, the Total Variation Diminishing scheme is triggered.

Description	Module	Subroutines
Refers to all the modules of the program. The hydrodynamic calculations in the x- and y-direction start here.	MAIN_PROGRAM	• HYDRO_CALCULATION_X • HYDRO_CALCULATION_Y
Reads input data: control parameters, time series, boundary conditions, domain description and initial conditions.	INPUT	• READ_PARAMS • READ_TIME_SERIES • READ_BOUNDARY • READ_MONIT • READ_DOMAIN • READ_INITIAL
Assigns forcing (hydrodynamic data) at the open boundary conditions.	BOUNDARY	• HYDBND
Refers to the standard MacCormack scheme in the x- and y- direction.	MACCORMACK	• MACX • MACY
Calculates the advection terms in the x- and y-direction.	ADVECTION	• FUFV • GUGV
Calculates (Recalculates) Chezy value for bottom roughness computation	ROUGHNESS	• CHEZY
Calculates the Total Variation Diminishing (TVD) term in the x- and y- direction.	TVD	• TVDX • TVDY
Specifies data for output files.	OUTPUT	• OUTPUT_MONITORING_POINTS • OUTPUT_TERMINAL_INFO • OUTPUT_ELEV_DEP_VEL_FR • OUTPUT_MAX_ELEV_DEP_VEL_FR
Calculates turbine area, blockage ratio and identify the grid-cells where the momentum sink will be calculated.	THRUSTFORCE	• MARTURB_Y • MARTURB_X
Calculates the parameters used in the marine turbine momentum sink calculation: components of the turbine area per grid cell, upstream velocity, upstream Froude number, bypass factor, wake induction factor and thrust coefficient.		• MARTURB_CT

Table 4.2: Description of the main subroutines of the TVD-TOC model. The subroutines modified to incorporate the LMAD-OCH are highlighted in green.

The modular character of TVD-M suggested the incorporation of the turbine-array momentum extraction computation as a module. THRUSTFORCE is the module incorporated in this thesis to calculate B (Equation 4.37) and C_T. The module is highlighted in red in Figure 4.9. The THRUSTFORCE module contains three subroutines. MARTURB-X and MARTURB-Y, calculate the turbine area components A_x and A_y

per grid cell, and the blockage ratio; MARTURB-CT calculates the upstream veloc-ity, the upstream Froude number, solves the β_4 quartic polynomial, and calculates the thrust force coefficient.

Due to the parallel nature of the model, the upstream conditions calculation were introduced via a parallel loop. As the OpenMP interface allows one to parallelise individual sections of the code, the computation of the quartic polynomial roots as a serial calculation was included in the subroutine MARTURB-CT.

The solution procedure of the model is shown in Figure 4.10. The hydrody-namic calculations are performed in the subroutines highlighted in orange. Meanwhile, the momentum extracted method is computed in the subroutines highlighted in blue. The MARTURB-X, MARTURB-Y, and MARTURB-CT subroutines are called by the MACCORMACK module (highlighted in orange) where the hydrodynamic calcula-tions take place and the sink term is computed. The MACCORMACK module uses a two-stage scheme to solve the hydrodynamic calculations: firstly, in the X-direction (MACX subroutine), and secondly, in Y-direction (MACY subroutine). Each 1D prob-lem requires a predictor and a corrector step to obtain the solution. As a result, the MACCORMACK module calls the subroutines of the THRUSTFORCE module 4 times (highlighted in blue). The first time step for the predictor step, and the second time for the corrector step in the x-direction (MACX subroutine); and twice more for the y-direction (MACY subroutine).

In the case of TVD-TOC, the upstream velocity used in the thrust force (Equation 4.36) is computed on MACCORMACK, prior to the calculation. If strong gradients of the flow occur, the TVD subroutines are used (TVDX and TVDY).
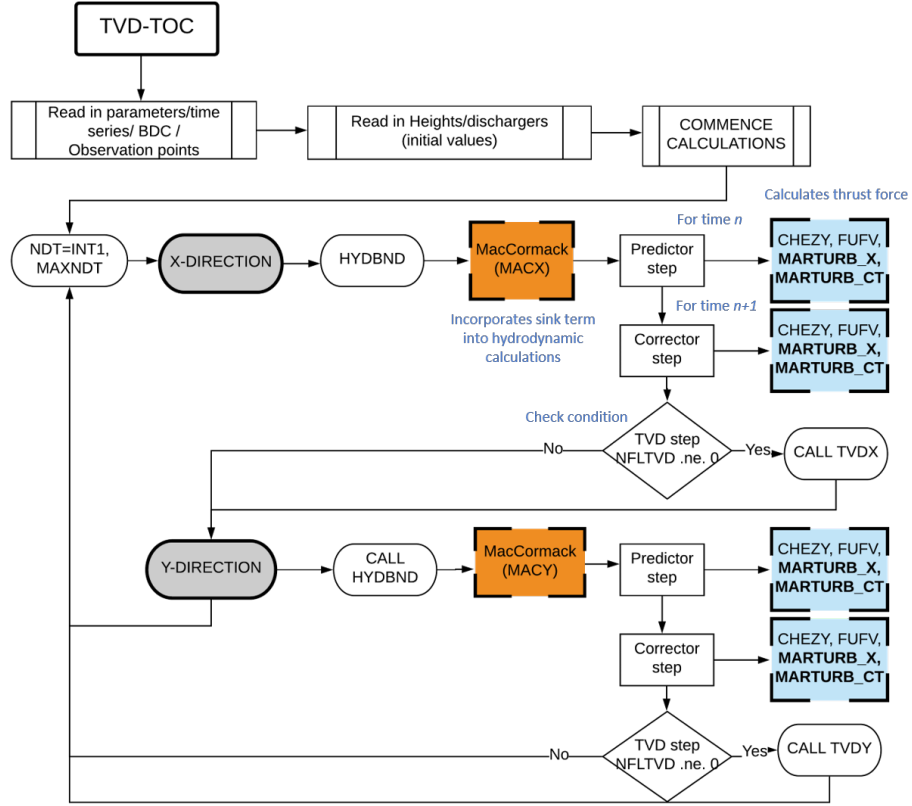
Fig. 4.10: Flow-chart of the solution procedure of TVD-TOC model.

4.7 Summary

This chapter describes details of the LMAD-OCH theory. This theory provides the basis of approximating turbine near-field flow and relates the operating conditions of the turbine to the momentum sink calculation. Additionally, the LMAD-OCH theory provides further information relevant to the tidal-stream resource assessment such as: the turbine efficiency, the identification of the available power, and the total power extracted.

Two current numerical approaches used to represent marine turbines in depth-average models were reviewed: (i) line sink of momentum and (ii) momentum sink. As a result, an improved method to numerically represent marine turbines energy capture was developed. This method is referred to as momentum sink-TOC and it implements

numerically the LMAD-OCH theory through the momentum sink approach within a free-surface flow. Additionally, a procedure to perform tidal-stream resource assessment was proposed.

The strategy followed to incorporate the momentum sink-TOC and assess the resource consists of three steps. The first step corresponds to the calculation of parameters required to simulate the momentum extracted by the turbine array. These parameters are: the turbine blockage ratio per grid cell, the upstream velocity, and the thrust force coefficient. The second step refers to the procedure used to incorporate the momentum sink in the hydrodynamic calculations of the models. The thrust force simulated is a function of the thrust force coefficient $C_T(\alpha_4, \beta_4)$, which in turn depends on the specification of the wake-induction factor and the bypass flow coefficient. The final step refers to the tidal-resource assessment, which was calculated as a post-processing step of the simulations. Relevant metrics calculated for the resource evaluation are identified as: power removed by the turbine, head drop across the array, total power extracted by the turbine, turbine efficiency, power available for electrical generation, and power dissipated by the turbine wake mixing.

The numerical representation of marine turbines developed in this thesis was introduced in a scheme that solves SSF (ADI-TOC), and a scheme that solves RVF (TVD-TOC). Modifications of the solution procedure of the models to incorporate the new representation of the marine turbines were described.

A necessary step is to validate the momentum sink-TOC method and evaluate the accuracy of the parameters used to assess the resource. This procedure is presented in Chapter 5.

Chapter 5

Validation and Comparison of the Models

5.1 Introduction

In this chapter the strategy used to perform tidal-stream resource assessment introduced in Chapter 4 and implemented into a scheme that solves SSF (ADI-TOC model), and a scheme that solves RVF (TVD-TOC) is benchmarked against analytical values of the LMAD-OCH theory, and published results.

Section 5.2 presents the evaluation of the computation of the parameters that describe the changes in the flow produced by power extraction within the turbine near-field extent. These parameters describe intensification of the turbine bypass flow (β_4), the velocity reduction prior to crossing the turbine (α_2), and the relative head drop $\Delta h/h$. The power coefficient and the turbine efficiency were used to evaluate the computation of these parameters by the two numerical schemes. This analysis required the research of different turbine operating conditions. Section 5.3 presents the evaluation of the numerical implementation of marine turbines and associated momentum sink. This evaluation is performed by analysing the relationship between maximum power

extraction and flow rate reduction in a tidal channel that connects two large basins. This analysis considered the study of a set of increasing values of the turbine blockage ratio.

Finally, Section 5.4 presents a comparison of the computational resources used by the scheme that solves SSF (ADI-TOC model), and RVF (TVD-TOC).

5.2 Turbine's Near Extent Flow Parametrisation

To quantify how accurately the ADI-TOC and the TVD-TOC models compute the parametrisation proposed by the LMAD-OCH theory, the power coefficient and turbine efficiency for small Froude numbers were evaluated. These parameters were calculated for a range of turbine operating conditions, and for two different upstream conditions of flow.

The α_4 coefficient is an indicator of turbine porosity. This property indicates the rate of reduction presented by the core-flow velocity at the turbine, with respect to upstream velocity (Draper, 2011; Johnson *et al.*, 2014). Plausible values of the wake induction factor are within the range of $0 < \alpha_4 < 1.0$. A turbine with low porosity ($\alpha_4 \longrightarrow 0$) exerts a larger force on the fluid, where little fluid passes through the turbine and consequently, the flow presents a high reduction at the turbine. Conversely, a turbine with high porosity ($\alpha_4 \longrightarrow 1$) exerts a smaller force on the fluid, the velocity of the flow passing through the disc is high, and the velocity reduction is lower. The optimum α_4 coefficient depends on the turbine arrangement and the surrounding coastal areas (Draper, 2011). In the case of channels, optimum α_4 depends on the natural dynamic balance of the site (Adcock *et al.*, 2013). If the channel's natural dynamic balance varies over the spring-neap cycle, as in the case of the Pentland Firth (Draper *et al.*, 2014a), α_4 is likely to change over the spring-neap cycle.

To evaluate the accuracy of the power coefficient and turbine efficiency computed

by the models, three scenarios were analysed (Table 5.1). These scenarios study the influence of the blockage ratios (B) and Froude numbers (F_r) for variations of the wake induction factor $0 < \alpha_4 < 1.0$. The range of α_4 was discretised into twelve values. The blockage ratio was elected to represent a small ($B = 0.2$) and a large ($B = 0.4$) obstruction of the tidal-stream. The Froude number was chosen to represent both low ($F_r = 0.1$) and high ($F_r = 0.3$) states of sub-critical flow. These values of F_r describe the conditions of the flow in the middle of the channel when no power extraction is performed.

Scenario	B	α_4	F_r
1	0.2	$0 < \alpha_4 < 1$	0.1
2	0.4	$0 < \alpha_4 < 1$	0.1
3	0.2	$0 < \alpha_4 < 1$	0.3

Table 5.1: Scenarios used to verify the parametrisation of the turbine near-field region performed by the models.

The simulation of the scenarios described in Table 5.1 provided the bypass coefficient β_4 and the wake induction factor α_4 necessary to compute the turbine velocity coefficient α_2. This parameter indicates the velocity reduction of the core-flow prior to crossing the turbine, and it shows the inter-relation that exists between flow velocities across and around the turbine, given by the rate of bypass-flow intensification (β_4) and the rate of the downstream core-flow reduction (α_4). The α_2 coefficient and relative head drop $\Delta h/h$ were obtained in the post-processing step of the simulation. The calculation of these two parameters enable the estimation of the power coefficient and turbine efficiency. The scenarios presented in Table 5.1 were simulated in a simple channel configuration. Specifications of the domain used during the simulations are given in the following section.

5.2.1 Simple Channel

A simple channel $C0$ was developed to test the parametrisation of the turbine near-field flow by the models. The domain under study is an idealised channel with an aspect ratio of $W/L = 0.44$, where width $(W) \approx 4$ km and length $(L) \approx 9$ km (Figure 5.1). The channel's aspect ratio was elected to be consistent with reported values in the literature (Draper *et al.*, 2010). A small size domain is used to reduce simulation running time.

For open boundary conditions, the channel was forced with a standing wave with semi-diurnal frequency M_2 on the western boundary (Equation 5.1). The amplitude of the forcing was introduced as a ramped-up wave over two M_2 tidal periods $(2T_{M_2})$ (Equation 5.2) based on Draper (2011).

$$\zeta = A(t) \cos(\omega t) \cos(kx) \tag{5.1}$$

$$A(t) = A\left(-2\left(\frac{t}{2T_{M_2}}\right)^3 + 3\left(\frac{t}{2T_{M_2}}\right)^2\right), t < 2T_{M_2} \tag{5.2}$$

The gradual introduction of the forcing $A(t)$ removed the initial numerical noise in the simulation and helped reach steady state flow faster. At the eastern boundary, water elevation was set to constant and velocity was set to zero. At the walls, the boundary satisfies the no-slip condition. The water depth is relatively shallow and constant at 40 m = 2.5 d, where $d = 16$ m is the turbine diameter. A constant bottom friction, defined as a function of the drag coefficient, was implemented (C_d=0.0025), where $C_e = \sqrt{g/C_d}$ is equivalent to $C_e = 62.6$, which represents a minor bottom drag.

The experiments performed in the simple channel configuration and specifications of the spatial and temporal resolution of the models are outlined in Table 5.2. The explicit method used by TVD-TOC model to approximate the solution of the governing equations limits the time step Δt. Meanwhile, the implicit method used by ADI-TOC model allows a larger Δt than the shock-capturing model.

The consistent boundary conditions and forcing implementation between the models were assured by obtaining consistent hydrodynamic conditions at the natural state. This state refers to a null energy extraction by marine turbines.
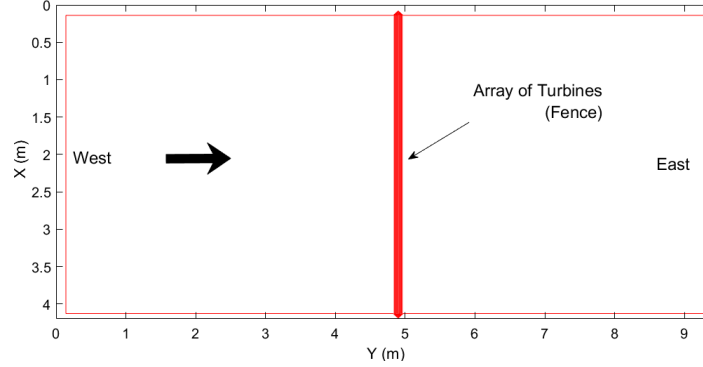
Fig. 5.1: Plan view of the simple channel domain $C0$.

The array studied corresponds to turbines distributed in a single row, which fully covers the channel cross-section. This configuration will be referred to as a tidal fence. The array was deployed in the middle of the channel (Figure 5.1). The simulations started from quiescent initial conditions and a steady periodic flow was reached after the second tidal period. The simulation time was 50 hrs., equivalent to four M_2 tidal periods ($4\ T_{M_2}$).

The results obtained from the models are described in the following section.

5.2.2   Validation of the Turbine Near-field Flow Parametrisation Computation

The power coefficient and turbine efficiency were used as indicators to evaluate how correctly the ADI-TOC and TVD-TOC models compute the parameters, that describe the changes in the flow at the turbine near-field extent. These values were computed for three scenarios as specified in Table 5.2. Additionally, these results provide information about the effect of the blockage ratio and the Froude number on the calculation of C_P

			Fence Configuration					
Model	Scenario	B	α_4	F_r	ΔX (m)	Δt (sec)	TIS (m)	RD
ADI-TOC	1	0.2	$0 < \alpha_4 < 1$	0.1	70	6	41.95	2.62
	2	0.4	$0 < \alpha_4 < 1$	0.1	70	6	29.66	1.85
	3	0.2	$0 < \alpha_4 < 1$	0.3	70	6	41.95	2.62
TVD-TOC	1	0.2	$0 < \alpha_4 < 1$	0.1	70	1.5	41.95	2.62
	2	0.4	$0 < \alpha_4 < 1$	0.1	70	1.5	29.66	1.85
	3	0.2	$0 < \alpha_4 < 1$	0.3	70	1.5	41.95	2.62

Table 5.2: ADI-TOC and TVD-TOC initial parameters specification. Spatial resolution (ΔX), temporal resolution (Δt), Turbine inter-spacing (TIS), and corresponding rotor distance RD.

and η.
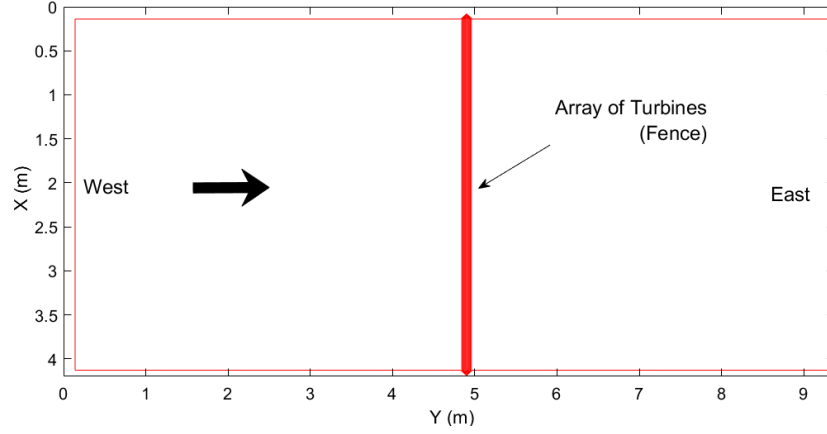
The variation of the blockage ratio for a flow with a low Froude number $F_r = 0.1$ (scenarios 1 and 2 in Table 5.2) produces the C_P and η solutions presented in Figure 5.2. Three solutions were compared: the LMAD-OCH analytical solution (Houlsby et al., 2008; Draper et al., 2010), and two numerical solutions obtained from ADI-TOC and TVD-TOC.

A common feature between the small (Figure 5.2(a)) and large (Figure 5.2(b)) blockage ratio analysis is the existence of a wake induction factor that maximises the magnitude of C_P: $\alpha_4 \simeq 1/3$. In addition, the power coefficient magnitude is subject to the blockage
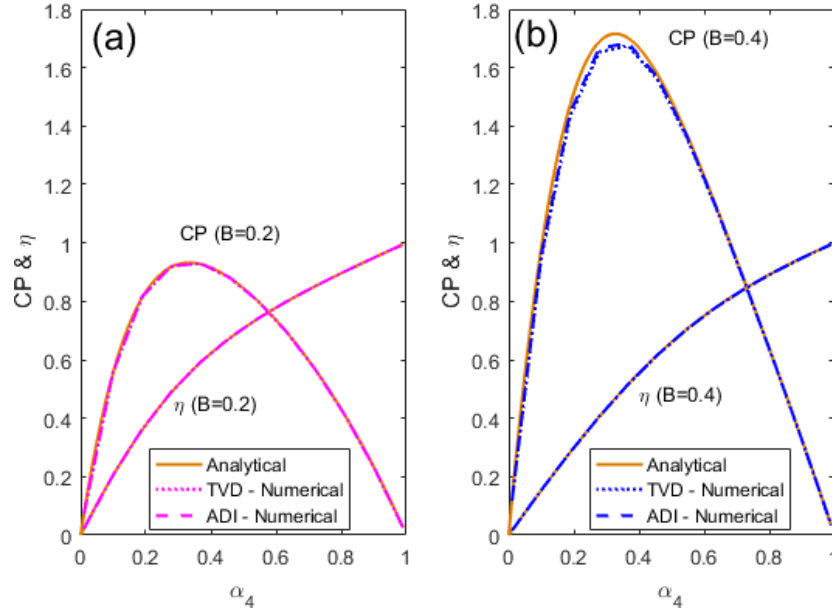
Fig. 5.2: Effect of small (a) and large (b) blockage ratio on the power coefficient and efficiency for wake induction factor $0 < \alpha_4 < 1.0$ and $F_r = 0.1$.

ratio, and higher C_P's values are related to larger B. This is illustrated in Figure 5.2(a), which reports smaller C_P magnitudes for $B = 0.2$ than $B = 0.4$. On the other hand, the turbine efficiencies present slightly larger magnitudes for smaller blockage ratios $(B = 0.2)$ than $B = 0.4$.

Figure 5.2 also indicates that the ADI-TOC and TVD-TOC numerical solutions of C_P and η are consistent for the two scenarios studied. These solutions agree with the analytical solution for the small blockage ratio $(B = 0.2)$, however, they slightly deteriorate when the blockage ratio increases $(B = 0.4)$.

The variation of the Froude number for a small blockage ratio $B = 0.2$ (scenarios 1 and 3 in Table 5.2) produce the C_P and η solutions presented in Figures 5.3(a) and 5.3(b). The increase of the Froude number does not seem to significantly change the α_4 coefficient associated with the maximum value of C_P, or the efficiency of the turbine. Nevertheless, slightly larger magnitudes of C_P are found for the flow with a $F_r = 0.3$. Figure 5.3 indicates that both models satisfactorily represent the power coefficient and
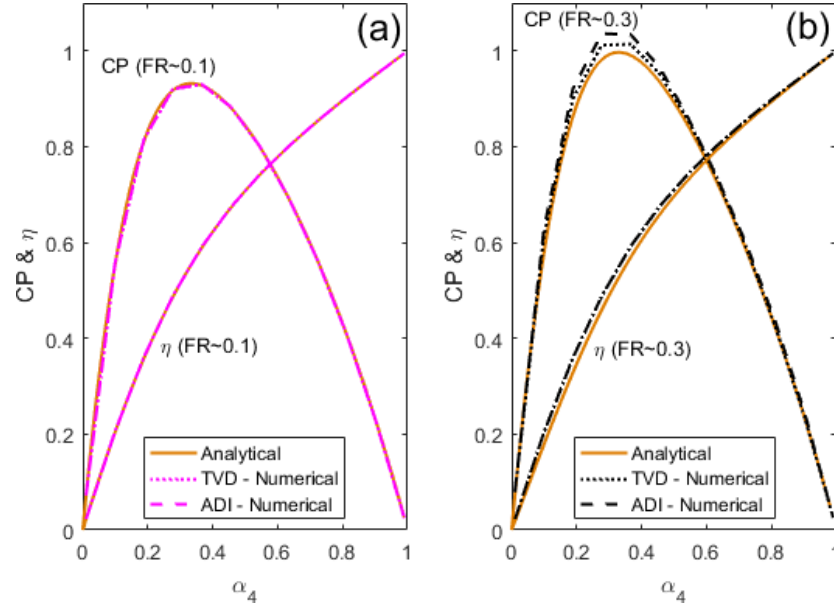
Fig. 5.3: Effect of low (a) and high (b) Froude number on the power coefficient and efficiency for the wake induction factor $0 < \alpha_4 < 1.0$ and fence with B=0.2.

efficiency situation for $0 < \alpha_4 < 1.0$ for $F_r = 0.1$ and $F_r = 0.3$. Although, in the case of large Froude number, TVD-TOC model shows a slightly better agreement with the analytical result.

Summarising, ADI-TOC and TVD-TOC numerical schemes solve the parameters that describe the changes in the flow produced by power extraction at the turbine near-field extent (bypass flow, core flow, and water depth) satisfactorily. The match is particularly good for small blockage ratios and small Froude numbers.

The Froude numbers used for this analysis describes realistic natural conditions within a tidal channel (Draper *et al.*, 2010). The blockage ratios elected, represent plausible limits for tidal energy harvesting. However, it is worth noticing that an idealised turbine configuration was used to benchmark the numerical results with the analytical theory.

5.3   Maximum Power Extraction

The maximum power extracted in a tidal channel is calculated to evaluate the numerical implementation of the marine turbines and the associated momentum sink in ADI-TOC and TVD-TOC. The power removed by the turbine P was derived in Section 4.2.1. For this test, P was calculated based on a thrust force simulated for blockage ratios in the following range $0 < B \leq 0.8$. The nine scenarios investigated are presented in Table 5.3. The blockage ratio $B = 0$ indicates the natural state i.e. no marine turbines deployed and no power extracted. Meanwhile, $B = 0.8$ indicates that the accumulated area of turbines per grid cell covers 80% of the grid cell area. The increase of B implies a reduction of the inter-turbine spacing ITS. This length can be represented in terms of the rotor distance RD $(RD = ITS/d)$, where d is the turbine (rotor) diameter. In this thesis, a turbine with diameter $d = 16m$ is assumed. From Equation 4.38 it is possible to estimate the number of turbines per grid cell N. The number of turbines contained per grid are shown in Table 5.3.

Fence Configuration				
Scenario	B	ITS (m)	RD	N
0	0	-	-	0
1	0.1	86.83	5.43	3
2	0.2	61.40	3.84	6
3	0.3	50.13	3.13	9
4	0.4	43.42	2.71	12
5	0.5	38.83	2.43	15
6	0.6	35.45	2.22	18
7	0.7	32.82	2.05	21
8	0.8	30.70	1.92	24

Table 5.3: Scenarios used to evaluate the momentum sink computed by ADI-TOC and TVD-TOC.

The scenarios evaluated in Table 5.3 were simulated within a tidal channel domain. For the natural state scenario, a sub-critical flow, which reports a small Froude number $(F_r = 0.11)$ in the middle of the channel was obtained and it was used as the initial

scenario. In the case of energy extraction scenarios, an optimal value of the wake induction factor of α_4=1/3 was used. The set-up of the tidal channel domain is specified in the next section.

5.3.1 Tidal Channel

Fig. 5.4: Shannon estuary, Ireland (a) and Cape Cod Canal, Massachusetts, USA (b), GoogleEarth.

Potential locations for testing and deploying of turbine arrays are semi-narrow channels with easy access and shallow water depths. This is the case of the Shannon estuary in Ireland with 1.8 km width (Figure 5.4(a)) and the Cape Cod Canal in Massachusetts USA with 220 m width (Figure 5.4(b)). In order to study the turbine array performance in semi-narrow channels, a domain that resembles the cross-section of the Shannon estuary is studied.

The extent of a regional model depends on the dynamics of the particular region being modelled. Potential coastal sites can be categorised into tidal channels (with or without sub channels), coastal headland, tidal channel formed by an island and oscillating bays surrounded by the continental shelf (Draper, 2011; Adcock *et al.*, 2015). However, a necessary condition in any scenario is the use of a large enough domain so the boundaries have a minimal effect on the array of turbines.

In the particular case of a tidal channel connected to two adjoining seas, the

regional numerical model should include a large fraction of the water bodies on either side of the channel. If the turbines produce a reduction of the flow in the channel, the elevation changes in the boundary conditions are negligible (Adcock *et al.*, 2015). Therefore, if a fixed elevation boundary is implemented in the model, the flow rate change produced by the tidal energy harvesting should be minor.
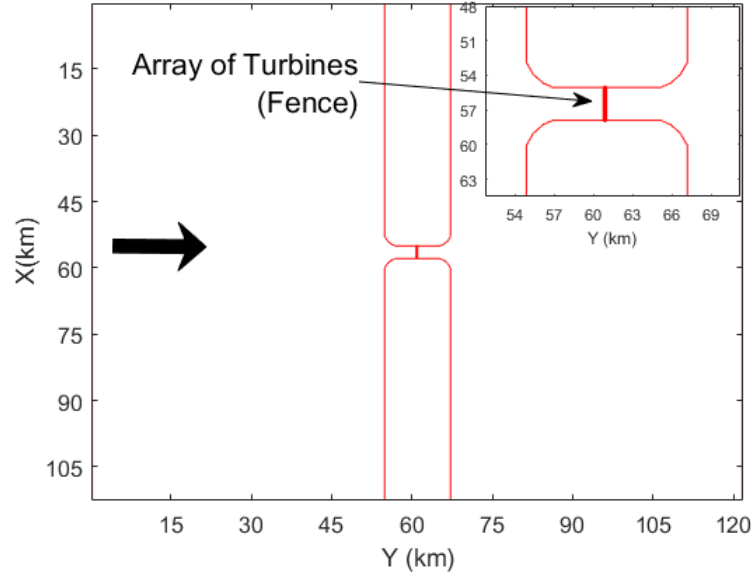
Fig. 5.5: Tidal channel with a constant cross-section that connects two large basins. The zoom out of the channel (upper-right location) shows the array of turbines deployed.

The tidal channel domain under study has a constant cross-sectional area and it is shown in Figure 5.5. The channel is relatively narrow and long, and characterised by an aspect ratio $W/L = 0.25$; it is approximately 12 km long and 3 km wide. The channel connects two large basins, where the extension of the basins is 4.5 times the length of the channel. The domain size is large enough to ensure that boundary conditions do not influence power extraction dynamics. The boundary conditions, bottom friction, depth, initial conditions and simulation time are consistent with the set-up described in section 5.2.1. However, the tidal channel configuration uses a coarser spatial resolution

114

($\Delta X = 150$ m) in both ADI-TOC and TVD-TOC models. Larger time steps were tested to reduce the computing simulation time of the tidal channel domain. The semi-implicit character of ADI-TOC allowed a relatively large time step (Δt=12 s). However, the explicit scheme used by TVD-TOC did not tolerate time steps larger than 1.50 s, their testing produced non-physical instabilities in the flow; consequently Δt=1.50 s was used.

In terms of the simulation time, $4T_{M_2}$ were simulated as in the case of the simple channel domain. This time length was selected because the flow conditions reached at the eighth M_2 tidal cycle are consistent with conditions reported at the fourth tidal cycle. This observation is illustrated in Figures 5.6(a) and 5.6(b), where time series of the stream-wise components of the velocity magnitude ($|V|$) obtained from the fourth (continuous-line) and eighth (dash-line) tidal periods are presented. The time series correspond to scenarios with $B = 0.1$, 0.4, and 0.7 obtained with both models ADI-TOC and TVD-TOC. The figure shows consistency of the $|V|$ velocity simulated by both models for increasing blockage ratios and for the two periods length computed. Note that the smaller time step used in TVD-TOC produces a time series with a larger number of data than ADI-TOC. Additionally, Figure 5.6 shows that the maximum velocity magnitude occurs earlier when the blockage ratio increases, and larger power extractions are simulated. The anticipation of the phase velocity of the current due to power extraction increase has been reported by Draper (2011). It is worth noticing that power and flow rate calculations to be presented in the following section refer to values averaged over a tidal period. Therefore, the phase anticipation reported by the currents with increasing B does not influence the results to be presented.

The experiments performed in the tidal channel domain and the specification of the spatial and temporal resolution of the model are given in Table 5.4. The experiments of maximum power extraction considered an array of turbines distributed in a single row that fully extends across the channel cross-section, which is deployed in the middle
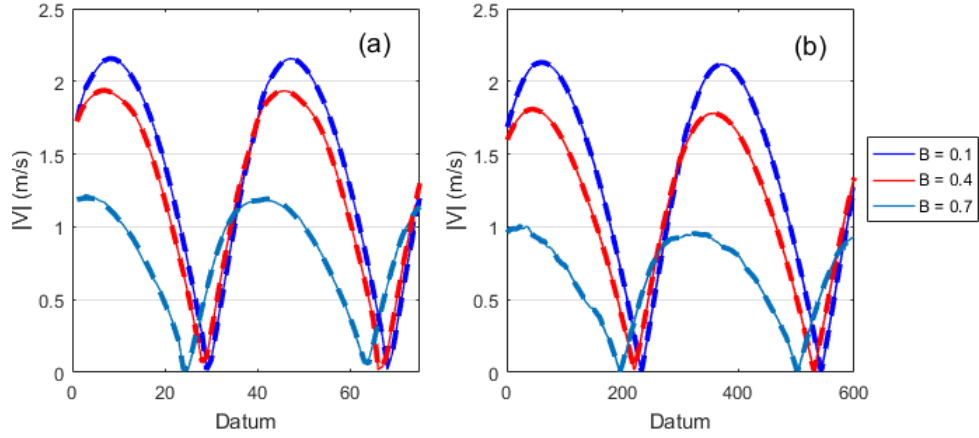
Fig. 5.6: Time series of the stream-wise component of the velocity magnitude at the middle of the channel obtained from ADI-TOC (a) and TVD-TOC (b).

of the narrow channel (Figure 5.5). The fence configuration was selected because it satisfies the requirements of the LMAD-OCH theory (described in Section 4.2). The results obtained with ADI-TOC and TVD-TOC are reported in the next section.

Fence Configuration						
Model	Scenarios	B	α_4	F_r	ΔX (m)	Δt (sec)
ADI-TOC	9	$0 \leq B \leq 0.8$	$\alpha_4 = 1/3$	0.11	150	12
TVD-TOC	9	$0 \leq B \leq 0.8$	$\alpha_4 = 1/3$	0.11	150	1.5

Table 5.4: ADI-TOC and TVD-TOC initial parameters specification. Spatial resolution (ΔX) and temporal resolution (Δt).

5.3.2 Power Extraction and Flow Rate Reduction

The maximum power extracted was computed using both ADI-TOC and TVD-TOC models to benchmark the simulation of the momentum sink extraction by turbines based on their operating conditions. The nine scenarios studied with each model are specified in Table 5.4. These scenarios provide information of the blockage ratio effect on the power removed by the turbine P and the flow rate reduction Q presented in the

channel. A consistent natural-state scenario was computed with both ADI-TOC and TVD-TOC in which a tidal-stream with $F_r = 0.11$ in the middle of the channel was simulated. The snapshots of contour velocity obtained with the models at $t = 38.75$ hrs. (time close to the maximum velocity), during a natural-state scenario, and within a semi-narrow tidal channel are presented in Figures 5.7(a) and 5.7(b). The comparison of the ADI-TOC and TVD-TOC velocity field indicates different velocity solutions when the flow approaches the entrance $(Y/L = 0)$ and exit $(Y/L = 1)$ of the channel. Nevertheless, the models simulated a tidal-stream with consistent velocities in the middle of the channel $(Y/L = 0.5)$; at this location, a fence of turbines was deployed (Figure 5.5). To reduce the influence of the entrance (exit) of the channel, the length of the channel is long $(L=12$ km$)$.
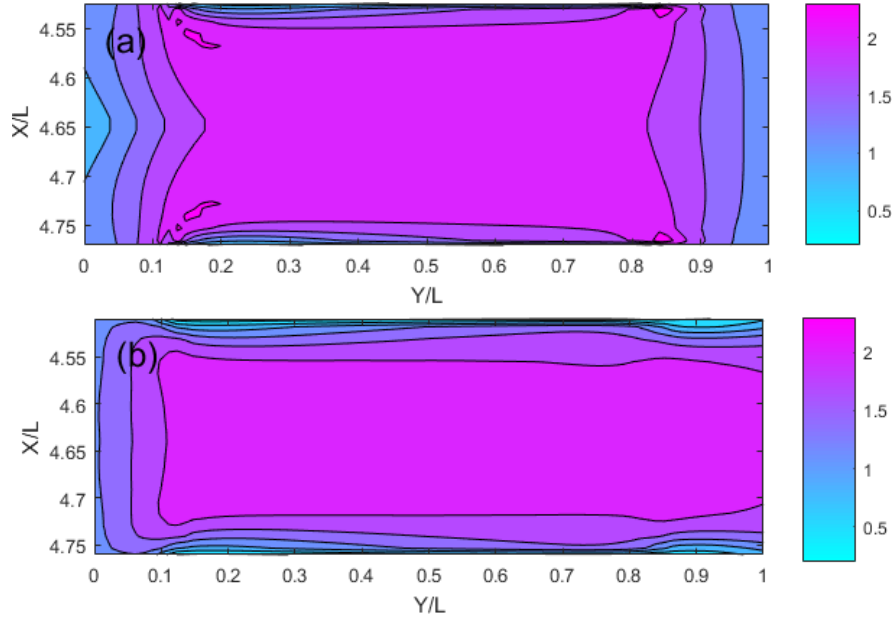
Fig. 5.7: Tidal channel plan view and snapshots of the velocity at natural state obtained with: ADI-TOC (a) and TVD-TOC (b).

The results from the nine scenarios (presented in Table 5.4) were normalised to the maximum value of the power removed and the maximum flow rate, respectively. These results were compared with the analytical estimation of maximum power extracted

reported by Sutherland *et al.* (2007). They considered that the power extracted by an array of turbines (that cover the entire cross section of the channel) could be treated as quasi-steady and studied analytically. The tidal fence implementation favours the simulation of a quasi-steady flow because: (1) it allows a constant tidal flux along the tidal channel, and (2) enables a height difference between the ends of the channel which remains constant with power extraction increase. Indicating that power extraction with a fence configuration only affects turbine near field flow. These criteria were met by the models. For an uniform power extraction across the channel, described by the tidal fence, the normalised power extracted is described by the following equation:

$$\frac{P}{P_{max}} = \left(\frac{3^{3/2}}{2}\right)\left(\frac{Q}{Q_{max}}\right)\left[1 - \left(\frac{Q}{Q_{max}}\right)^2\right] \tag{5.3}$$

where P_{max} corresponds to maximum power extracted obtained by Garrett and Cummins (2005), and Q_{max} is the maximum flow rate at the natural-state. The normalised powers and the associated normalised flow rates obtained with TVD-TOC and ADI-TOC are presented in Figure 5.8. The variation of the blockage ratio produces a trend consistent with the analytical solution reported by Garrett and Cummins (2005) and Sutherland *et al.* (2007), and described by Equation 5.3. The trend indicates: (i) a maximum flow rate and null power extraction at natural-state, (ii) the existence of an optimal blockage ratio that extracts a maximum power P_{MP}, and (iii) the reduction of power extraction for subsequent blockage ratio increases due to flow choking.

Figure 5.8 indicates that analytical maximum power extraction is responsible for a rather strong flow reduction with respect to the natural-state ($\sim 40\%$). A similar reduction is reported by the models; however, the models report a different blockage ratio for maximum power extracted. In the case of TVD-TOC, P_{MP} correspond to $B = 0.6$, meanwhile ADI-TOC reports $B = 0.7$.

The smaller blockage ratio required by TVD-TOC to reach maximum power agrees with Test 3 reported by Draper *et al.* (2010). The test describes a channel with drag
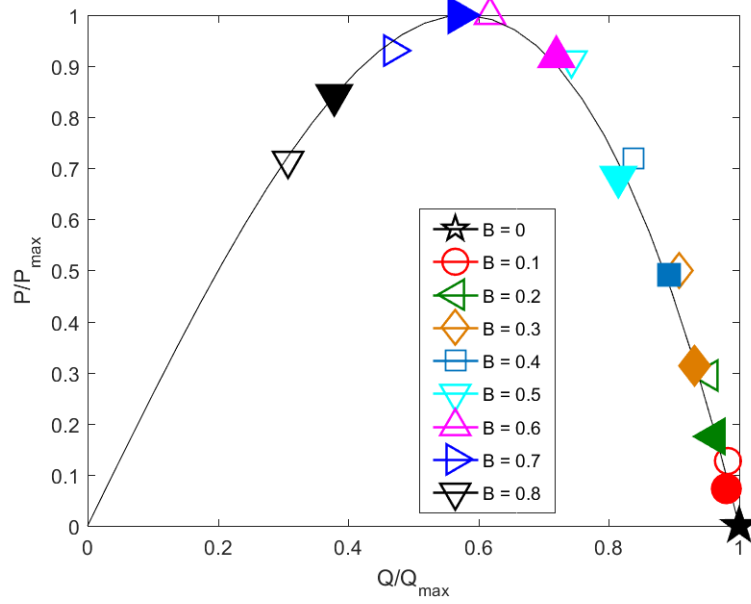
Fig. 5.8: Normalised maximum power removed by the turbines against normalised maximum flow rate for B increasing values. TVD-TOC (unfilled-markers), ADI-TOC (filled-markers), and analytical solution (continuous-line) reported by Garrett and Cummins (2005) and Sutherland *et al.* (2007) .

coefficient C_d =0.0105 ($\sim C_e$=30.5) and Froude number F_r =0.104; these parameters describe a smooth flow over a semi-rough surface. These conditions are similar to the channel reported in this thesis, which is characterised by the drag coefficient C_d=0.0025 ($\sim C_e$=62.6) and Froude number F_r =0.11. The channel simulated in this thesis presents a smoother surface than Test 3; nevertheless, Draper *et al.* (2010) reports that smooth surfaces such as C_d= 0.00105 ($\sim C_e$=96.65) also present a blockage ratio $B = 0.6$ associated with maximum power extracted. On the other hand, rougher surfaces such as C_d=0.035 ($\sim C_e$=16.7) require a smaller blockage ratio ($B = 0.5$) to obtain P_{MP}. The consistency between the results obtained with TVD-TOC and Test 3 suggest that TVD-TOC computes a more accurate power extraction and flow rate reduction than ADI-TOC.

In addition, the use of lower blockage ratios to reach maximum power has been reported

with advection-dominated flows (Draper, 2011; Draper *et al.*, 2010). These types of flows are not completely balanced by the bed friction drag and, consequently, experience important flow advection. Semi-narrow channels such as the study case in this thesis ($W/L =$ 0.25) are inclined to present flows with such characteristics.

The flow rate reduction simulated by the models is also an indicator of the accuracy of the solution procedure implemented by ADI-TOC and TVD-TOC. The analytical solution of Sutherland *et al.* (2007) indicates that maximum power extracted can be reached with an optimal blockage ratio, which in turn is associated with approximately a 40% flow rate reduction. Therefore, if the blockage ratio required to reach P_{MP} is small, the flow reduction occurs at a faster rate. This situation is observed for TVD-TOC results in Figure 5.8. Conversely, if the blockage ratio required to reach P_{MP} is large, then flow reduction take places at a slower flow rate. This is the case for ADI-TOC. As the TVD-TOC model better simulates power extraction and flow rate reduction than the ADI-TOC, the larger blockage ratio reported by ADI-TOC ($B = 0.7$) indicates that the scheme that solves SSF underestimates the flow rate reduction produced by power extraction.

The different velocity reduction simulated by the models is illustrated in Figure 5.6. It is observed that increasing values of the blockage ratio are related to velocity decreases, due to the flow rate reduction produced by power extraction. The velocity reduction rate presented by ADI-TOC is smaller than TVD-TOC. This result is consistent with flow rate reduction underestimation reported by ADI-TOC.

The next analysis is a comparison of model performance in terms of computational requirements. This is accomplished in the next section.

5.4   ADI-TOC and TVD-TOC Numerical Performance

It is important to evaluate the performance of the numerical schemes in terms of computational cost besides evaluating the accuracy of the solution obtained with the models. Schemes that solve RVF typically require higher computational cost than schemes that solve SSF (Liang *et al.*, 2006); this condition makes RVF solution schemes less attractive for practical studies. It is worth mentioning that the shock-capturing method used in this thesis is an efficient TVD-MacCormack scheme (Liang *et al.*, 2006, 2007), which has been further optimised by introducing parallel processing on multiple CPU cores using shared memory (Whittaker, 2014; Kvočka, 2017).

The computational performance of both ADI-TOC and TVD-TOC were evaluated in terms of the execution times against the domain size. In addition, two scenarios were considered: turbines thrust omission (NoT), and turbine thrust inclusion (T). Five domain sizes were considered, on each domain the two scenarios just described were simulated. In total, eighteen experiments were performed (see Table 5.5), nine with ADI-TOC and nine more with TVD-TOC. The simulation time of each experiment was 50 hrs.

The temporal resolution used in the models satisfies the Courant condition. However, due to the explicit nature of the TVD-TOC scheme, a smaller time step was implemented in the simulations ($\Delta t = 1.50s$). Conversely, the semi-implicit character of the ADI-TOC scheme allowed a larger time step ($\Delta t = 12.0s$). In terms of the spatial resolution, a consistent grid size $\Delta X = 150$ m was used.

The domain size was calculated as the multiplication of the maximum number of grids in the $X-$ and $Y-$ directions ($I_{max} \times J_{max}$), the scenarios evaluated are presented in Table 5.5. In the particular case of the larger domain (1642×1703), the scenarios that simulate the turbine thrust were not performed due to the large computational

requirement and the lack of new information.

Model	Domain	Size $(I_{max} \times J_{max})$	NoT	T	$\Delta t(sec)$	$\Delta X(m)$
ADI-TOC	1	60×134	Y	Y	12.0	150
	2	22×812	Y	Y	12.0	150
	3	22×1703	Y	Y	12.0	150
	4	751×812	Y	Y	12.0	150
	5	1642×1703	Y	-	12.0	150
TVD-TOC	1	60×134	Y	Y	1.50	150
	2	22×812	Y	Y	1.50	150
	3	22×1703	Y	Y	1.50	150
	4	751×812	Y	Y	1.50	150
	5	1642×1703	Y	-	1.50	150

Table 5.5: Experiments performed to evaluate the computational performance of ADI-TOC and TVD-TOC.

The execution times of the experiments performed by the models were completed considering the following definitions. In the case of ADI-TOC, a serial model (i.e. the program runs in a single CPU), the execution time of 50 hrs. simulation is given by the CPU-time. On the other hand, TVD-TOC, a parallel model (i.e. the tasks are shared and performed simultaneously on multiple CPU cores), the execution time is given by the system clock. However, if we consider the *time* used by all the processors used in the parallel computation, the cumulative time is given by the CPU-time of TVD-TOC. The comparison of the execution times obtained with ADI-TOC and TVD-TOC are presented in Figure 5.9.

In general, it is found that the execution time increases with the size of the domain. In terms of the inclusion (T) and omission (NoT) of turbines, TVD-TOC presents similar execution times for both scenarios. Meanwhile, ADI-TOC reports a slight increase in execution times when turbines are incorporated.

The comparison of the elapsed time required to perform a 50 hrs. simulation indicates that ADI-TOC simulations are performed faster (Figure 5.9-pentagram) than TVD-TOC for small domain sizes (Figure 5.9-circle). If the domain size increases,
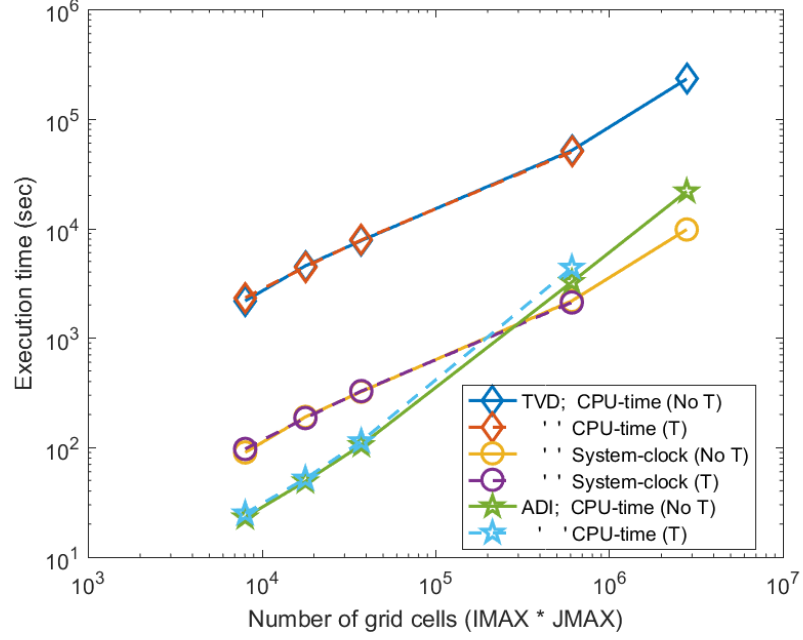
Fig. 5.9: Execution time for ADI-TOC (pentagram) and TVD-TOC for two conditions: turbines omission (continuous line) and inclusion (dash line).

TVD-TOC performs faster simulations that ADI-TOC. Nevertheless, if the cumulative time used by all of the CPU cores is considered (Figure 5.9-diamond), then TVD-TOC requires a larger execution time than ADI-TOC for any experiment evaluated. This indicates that despite the optimisations incorporated to TVD-TOC, this scheme reports higher computational cost than ADI-TOC. In addition, the execution of TVD-TOC requires a high-performance computing system.

5.5   Discussion and Conclusion

In this chapter, the methods developed in this thesis to simulate momentum sink extracted by the turbine based on the operating conditions of marine turbines were assessed and validated. The method was implemented in two depth-average hydrodynamic models: ADI-TOC scheme which simulates SSF, and TVD-TOC scheme which

simulates RVF. The array of turbines selected for the validation tests consisted of marine turbines placed in a tidal fence across a channel.

The power coefficient and the turbine-efficiency were calculated in a simple channel to benchmark the capacity of ADI-TOC and TVD-TOC models to compute the turbine near-field flow parametrisation. Plausible values of wake induction factor were explored $(0 < \alpha_4 < 1.0)$, and this range represents conditions of the turbine with high porosity $\alpha_4 \to 1.0$, and low porosity $\alpha_4 \to 0.0$. The wake induction factor variation was studied as a function of two factors: blockage ratio and Froude number. The comparison of the numerical values with analytical results indicates consistent results with Houlsby *et al.* (2008), particularly for small blockage ratios and small Froude numbers. The similarity of the results indicate that the models are able to compute the parameters α_2, β_4 and $\Delta h/h$ correctly; and that the models are able to incorporate the physical characteristics of turbines given by B and α_4.

The maximum power extracted was analysed to evaluate the numerical implementation of the marine turbines and the associated energy capture simulation. The variations of the blockage ratio $0 < B \leq 0.8$ indicate that ADI-TOC and TVD-TOC numerical schemes computed trends of power extraction and associated flow rate reductions, which are consistent with the analytical solution of Garrett and Cummins (2005) and Sutherland *et al.* (2007). The trends indicate that a continued increase of the blockage ratio leads to a maximum power extraction, after which further increases of B results in a smaller power extraction due to chocking of the flow. The blockage ratio associated with maximum power extraction reported by TVD-TOC and ADI-TOC are $B = 0.6$ and $B = 0.7$, respectively. The smaller blockage ratio required by TVD-TOC to reach maximum power agrees with observations reported by (Draper *et al.*, 2010). Additionally, the lower blockage ratio reported by TVD-TOC is also consistent with the type of flow expected in narrow channels: advection-dominated flow. These findings suggest that TVD-TOC reports a more accurate flow reduction and power

extraction than ADI-TOC. As a consequence, it is found that the ADI-TOC scheme underestimates the velocity reduction due to power extraction.

A comparison between the computational requirements of ADI-TOC model and TVD-TOC model was based on an assessment of execution times. Aspects such as the domain size and the marine energy extraction procedure (and omission) were considered. The time-elapse of the numerical simulation tends to be smaller in TVD-TOC than ADI-TOC if the domain size is large. However, if the parallel computing procedure of TVD-TOC scheme is considered and the total time used by the processors is taken into account, then the TVD-TOC model reports higher computational cost than ADI-TOC. This observation is independent of the domain-size and the energy extraction procedure (and omission).

An investigation into a better understanding of head loss across turbine arrays computed by the above models is presented in Chapter 6.

Chapter 6

Tidal-Stream Resource Assessment in a Tidal Channel

6.1 Introduction

In the previous chapter, it was shown that the ADI-TOC and TVD-TOC models are able to simulate the momentum extracted by an array of turbines undertaking the operating conditions of the turbine. This is possible due to the implementation of the momentum sink-TOC method.

Hereafter, the methods developed to simulate turbines, together with the procedure proposed in this thesis to assess tidal-stream energy, are compared to the original formulation used in ADI-M, and to a conventional methodology used to evaluate the resource. Comparisons of both methodologies are presented in Section 6.2. In Section 6.3 a more realistic turbine array configuration is introduced: the partial-fence, in addition, a new set of blockage ratios is defined. In Section 6.4, effects of power extraction on hydrodynamics are investigated in terms of wake induction factors, turbine array configurations, and blockage ratios.

Finally, in Section 6.5, the performance of partial-fence, and fence configurations,

for more realistic blockage ratios are evaluated and compared. The numerical results obtained from the ADI-TOC and TVD-TOC schemes are benchmarked against solutions that consider the head drop across an array as the solution of the cubic polynomial reported by LMAD-OCH theory.

6.2   C-CTE and C-TOC Methodology Comparison

To consider advantages of calculating the energy captured by an array in terms of the LMAD-OCH theory, this section compares tidal energy assessments obtained from the original formulation used in ADI-M, with the evaluation derived from the methodology proposed in this thesis.

The original formulation used by ADI-M to compute the marine turbine's energy capture is based on a pre-defined constant thrust coefficient. In addition, the conventional strategy used to estimate the resource relies on a pre-defined constant power coefficient. The formulation and strategy used by ADI-M to assess tidal energy are referred to as C-CTE methodology; this is outlined in Figure 6.1.
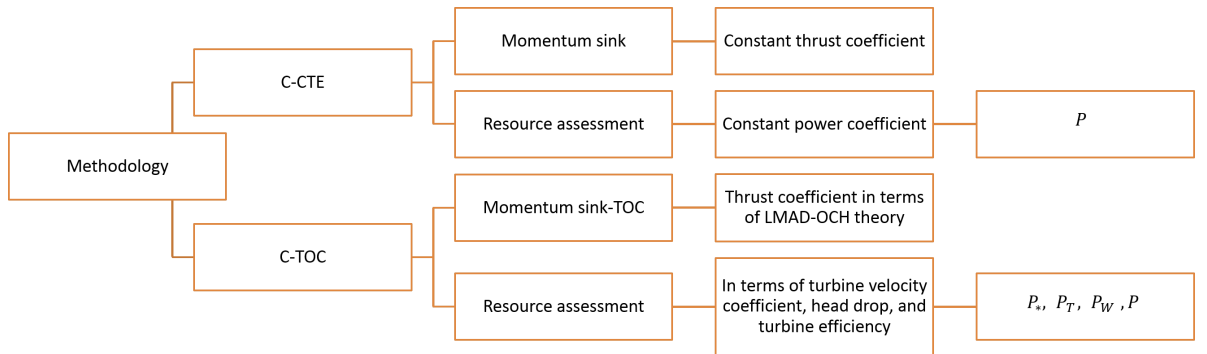
Fig. 6.1: General description of methodologies C-CTE and C-TOC.

This methodology has been implemented in far-field hydrodynamic models to perform tidal-stream resource assessment (Ahmadian and Falconer, 2012; Ahmadian *et al.*,

2012b; O'Brien, 2013; Fallon *et al.*, 2014).

Thrust and power coefficients depend on factors that determine the turbine configuration such as hub angle, pitch angle, and tip speed ratio (Bahaj *et al.*, 2007). The magnitude of the coefficients has been identified analytically for wind-turbines scenarios (Burton *et al.*, 2001; van Kuik, 2007), and experimentally for marine turbines in the laboratory (Myers and Bahaj, 2007; Bahaj *et al.*, 2007; Gaurier *et al.*, 2013). The C-CTE methodology has been used to study the role of the inter-turbine spacing of the turbine array on energy output and on the environment (Hartnett *et al.*, 2012; Fallon *et al.*, 2014). Typical values of the thrust coefficient used in depth-average simulations are $0.8 < C_T < 1.0$. However, C_T can be adjusted to better represent the power extraction and changes in velocities. Phoenix (2017) proposed the identification of C_T based on a turbine efficiency of 40%. This value of C_T depends on the spatial resolution and depth used in the simulation; for a simulation with grid size ΔX=16 m and 50 m depth, Phoenix (2017) reports C_T=1.30. To evaluate the C-CTE methodology, the following constant values of the thrust and power coefficients were implemented: C_T^{CTE} =1 and C_P^{CTE}=0.35. This methodology was implemented in both models: TVD-TOC and ADI-TOC; the scenarios evaluated with C-CTE are presented in Table 6.1.

Fence Configuration							
Model	Scenarios	Methodology	B	α_4	F_r	ΔX (m)	Δt (sec)
ADI-TOC	9	C-TOC	$0 \leq B \leq 0.8$	$\alpha_4 = 1/3$	0.11	150	12
	9	C-CTE	$0 \leq B \leq 0.8$		0.11	150	12
TVD-TOC	9	C-TOC	$0 \leq B \leq 0.8$	$\alpha_4 = 1/3$	0.11	150	1.5
	9	C-CTE	$0 \leq B \leq 0.8$		0.11	150	1.5

Table 6.1: ADI-TOC and TVD-TOC initial parameters specification for the evaluation of C-TOC and C-CTE methodology. Spatial resolution (ΔX) and temporal resolution (Δt).

The results from the C-CTE methodology are compared with C-TOC. The C-

TOC methodology applies the LMAD-OCH theory (Houlsby *et al.*, 2008) through the momentum sink-TOC. This enables the parametrisation of the changes produced in the flow, a consequence of the momentum extracted at the turbine near-field region. As a result, it is possible to relate the operating conditions of a turbine to the momentum sink through the calculation of the thrust coefficient at every time-step. Additionally, the evaluation of the resource by the C-TOC methodology considers the turbine velocity coefficient, head drop, and turbine efficiency. These parameters enable the calculation of power metrics useful to estimate tidal-stream resources. The C-TOC methodology is outlined in Figure 6.1.

According to the momentum sink-TOC method, simulations of the thrust and power coefficients require the specification of B and the turbine-wake induction factor α_4. The magnitude of α_4 depends on the turbine arrangement and the surrounding coastal areas (Draper, 2011). Similarly, the C-TOC methodology was implemented in TVD-TOC and ADI-TOC schemes, the scenarios evaluated with this approach are presented in Table 6.1.

The domain size and the turbine array configuration were chosen to perform the comparison of C-CTE and C-TOC methodologies, and consists of a tidal channel which connects two larger basins (Figure 5.5). The set-up of this domain was introduced in Section 5.3.1, where it describes a channel with non-varying cross-sectional area and constant depth. Turbines are distributed in a single row that fully covers the channel cross-section and they are deployed in the middle of the channel.

The determination of α_4 required for the C-TOC methodology is described in the following section.

6.2.1   Wake Induction Factor for a Fence Turbine Array

The calculation of the sink term requires the specification of parameters such as the wake induction factor α_4. To determine the optimal α_4 for fence configuration, the effect of the parameter variation ($0 < \alpha_4 < 1.0$) was evaluated. Twelve scenarios were studied, and they are presented in Table 6.2. These experiments considered a constant blockage ratio $B = 0.2$. In addition, the flow state in the middle of the channel in the natural-state was characterised by F_r=0.11.

Turbine Wake Induction Factor			
Scenarios	B	F_r	α_4
0	0	0.11	-
1	0.2		0.01
2	"		0.1
3	"		0.18
4	"		0.27
5	"		0.36
6	"		0.45
7	"		0.54
8	"		0.63
9	"		0.72
10	"		0.81
11	"		0.90
12	"		0.99

Table 6.2: Scenarios evaluated with a fence configuration to select the optimal wake induction factor α_4. These scenarios were evaluated in both ADI-TOC and TVD-TOC models.

An optimal α_4 to be implemented in the C-TOC methodology maximises the power coefficient. Figure 6.2 presents the time-average of the thrust and power coefficients obtained from the variation of wake induction factor for a range of plausible values $0 < \alpha_4 < 1.0$. These results were obtained with both the ADI-TOC and TVD-TOC schemes. Figure 6.2 indicates that the models report consistent results. Indicating that the solution obtained from the models for the turbine velocity coefficient α_2, and the bypass induction factor β_4 are similar.

Additionally, the maximum power coefficient falls within the range $0.28 < \alpha_4 < 0.46$. The value chosen for the wake induction factor is $\alpha_4 = 1/3$. The identification
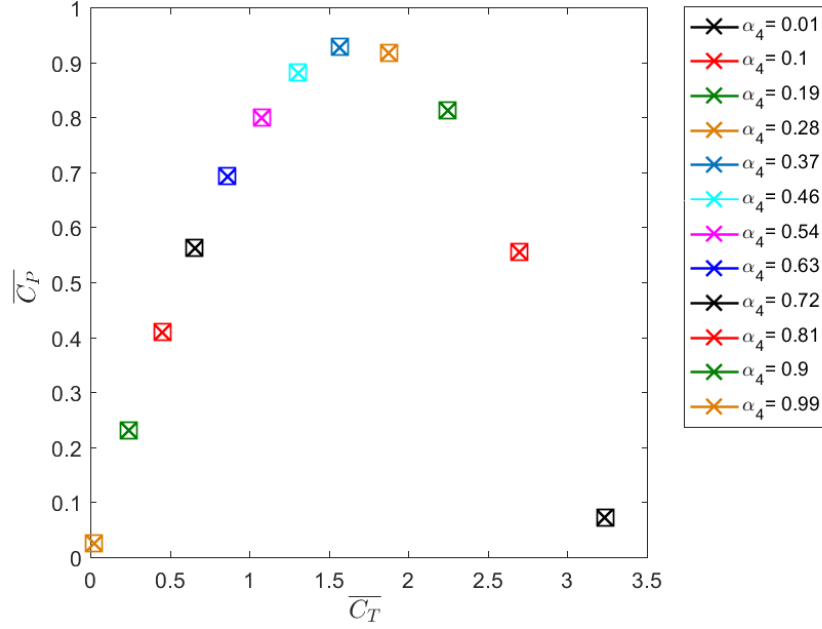
Fig. 6.2: Thrust and power coefficients obtained from the variation of wake induction factor, ADI-TOC (x-marker) and TVD-TOC (square marker).

of α_4 enables the calculation of the thrust coefficient $C_T^{TOC}(\beta_4, \alpha_4)$, and the power coefficient $C_P^{TOC}(\alpha_2, C_T)$ to be implemented into the C-TOC methodology.

6.2.2 Thrust and Power Coefficients

An initial step in tidal-stream resource assessment is the determination of both C_T and C_P. In this section, the comparison between the thrust and power coefficient obtained with C-CTE and C-TOC methodologies are presented. C-CTE uses pre-defined values of thrust and power: $C_T^{CTE} = 1$ and $C_P^{CTE} = 0.35$, and in this section the calculation of the thrust and power coefficient to be used in the C-TOC methodology is presented.

The calculation of the thrust and power coefficient based on the LMAD-OCH theory requires characterisation of turbine operating conditions. This information is provided by the wake induction factor and blockage ratio. Considering a situation

close to optimal power extraction conditions (by setting $\alpha_4 = 1/3$) and evaluating nine blockage ratios scenarios $0 \leq B \leq 0.8$ (Table 6.1), it is possible to determine C_T^{TOC} given by Equation 4.8, and the power coefficient C_P^{TOC} defined by Equation 4.10. At a natural-state ($B = 0$), the tidal-stream is characterised by F_r=0.11 in the middle of the channel. However, the deployment of turbines and an increase in blockage ratio will affect the upstream conditions, described by the Froude number, and in turn, will augment the turbine bypass flow, characterised by the bypass factor β_4 (Equation 4.16). As a result, each blockage ratio used will produce different flow conditions at the turbine near-field extent. In turn, these new conditions will produce particular values of thrust and power coefficients.

The values obtained for C_T^{TOC} and C_P^{TOC} are presented in Figure 6.3; where time-averaged values over the last tidal cycle for the thrust and power coefficients obtained by varying B are shown. It is observed that the coefficients obtained for ADI-TOC and TVD-TOC are similar for small blockage ratios, but they begin to diverge for large values of B. Furthermore, large values of B produce a higher increase rate of C_T^{TOC} and C_P^{TOC}. Note that a nearly linear relationship between thrust and power coefficient is presented.

Figure 6.3 indicates that the blockage ratio increases lead to larger magnitudes of the thrust and power coefficients. In this way, the maximum value of the power coefficient corresponds to the largest blockage ratio tested (B =0.8). Nevertheless, large blockage ratios are not necessarily related to the generation of more electrical power. This point was observed in Section 5.3 and will be further discussed in future sections.

In the case of the C-CTE methodology, pre-defined values of thrust and power coefficients are invariant with respect to blockage ratio. However, it is worth noticing that the momentum sink computed in C-CTE undertakes the inter-turbine spacing variation in the calculation via the turbine area specification. The next step of a C-CTE and C-TOC comparison was the identification of the momentum extracted effects
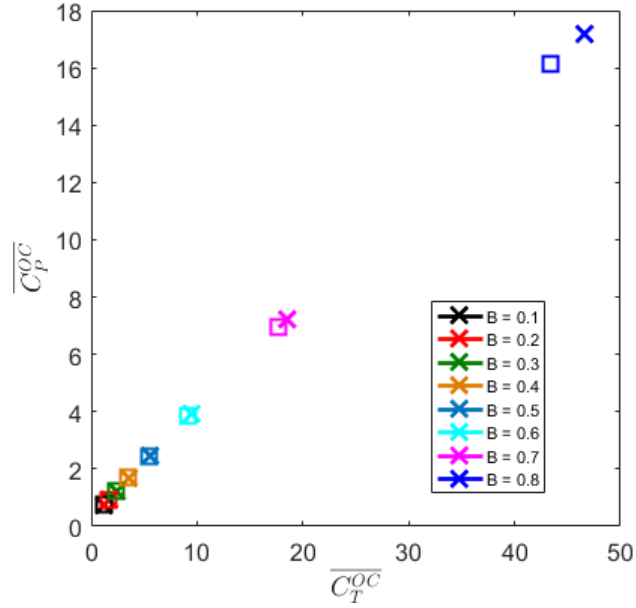
Fig. 6.3: Thrust and power coefficients computed with C-TOC methodology for increasing values of B, ADI-TOC (x-marker) and TVD-TOC (square-marker).

on the upstream conditions.

6.2.3 Upstream Velocity

Momentum sink calculations depend on the upstream velocity vector of the tidal-stream ($\overrightarrow{U}(U,V)$). The computation of energy captured by the turbine was defined in Section 4.3.2. For convenience, the components of the thrust force introduced as sink terms in the momentum equations solved by the models (Equation 4.36) are presented again:

$$F_{Tx} = \frac{1}{\Delta x \Delta y} \frac{1}{2} \rho A_x C_T U^2$$
$$F_{Ty} = \frac{1}{\Delta x \Delta y} \frac{1}{2} \rho A_y C_T V^2$$

The fence configuration assumes that upstream conditions (axial-velocity and water depth) are uniform upstream across the channel of the fence. In the case of C-TOC, the upstream velocity is located at one grid-cell upstream of the fence (Section 4.4.2). The

energy captured by the turbine array was estimated for nine blockage ratio scenarios introduced in Table 5.3. For each scenario, the time-dependent C_T^{TOC} was estimated and used in the computation of the sink term. To identify the magnitude of C_T^{TOC}, the time-average value of the last tidal cycle was calculated. The values obtained for ADI-TOC and TVD-TOC schemes are presented in Table 6.3.

C_T^{TOC}								
Model/B	0.1	0.2	0.3	0.4	0.5	0.6	0.7	0.8
ADI-TOC	1.2	1.7	2.4	3.6	5.6	9.5	18.5	46.6
TVD-TOC	1.2	1.7	2.4	3.5	5.5	9.2	17.7	43.4

Table 6.3: Time-average thrust coefficients obtained with C-TOC methodology for $0.1 \leq B \leq 0.8$.

The effect of momentum extraction on the axial-component of the upstream velocity obtained with ADI-TOC and TVD-TOC are presented in Figures 6.4(a) and 6.4(c), respectively. The visualisation of time series indicates a velocity reduction with respect to blockage ratio increase. The velocity decrease at $B =$0.8 with respect to the natural-state reported by TVD-TOC is 70%; meanwhile, ADI-TOC reports 63%. The smaller velocity reduction simulated by ADI-TOC was reported in Section 5.3, where it was found that ADI-TOC underestimates the velocity decrease due to power extraction. It is worth noticing that the velocity time series obtained from ADI-TOC and TVD-TOC present small fluctuations for $B \geq$0.7. Large blockage ratios imply a stronger bypass flow and a substantial decrease of the upstream velocity and flow rate. Under these circumstances, the flow is susceptible to becoming critical (Draper *et al.*, 2010). The small fluctuations presented for $B \geq$0.7 can be associated with the flow transition regime from subcritical to critical flow. Additionally, the red dash line at time 38.75 hrs. indicates a situation close to maximum velocity, this time was used for the snapshots presented in following sections.

In the case of C-CTE methodology, the upstream velocity location coincides with
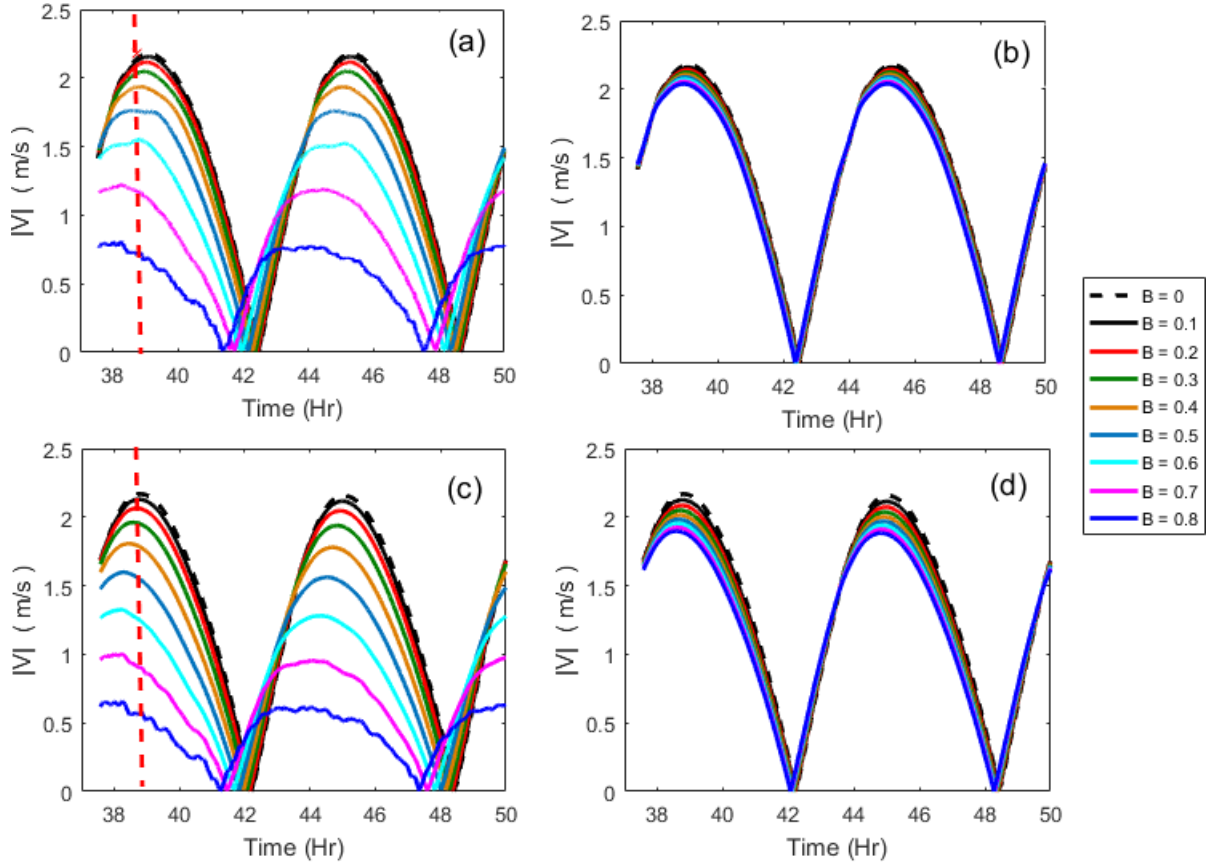
Fig. 6.4: Time series of the axial component of velocity (V). Results obtained from ADI-TOC for C-TOC (a) and C-CTE methodology (b). Results obtained from TVD-TOC for C-TOC (c) and C-CTE methodology (d).

the turbine array location (Fallon, 2012). The momentum extracted was calculated considering C_T^{CTE} and the inter-turbine spacing associated with $0 \leq B \leq 0.8$. The axial components of the upstream velocity obtained from the implementation of C-CTE in ADI-TOC and TVD-TOC scheme are shown in Figures 6.4(b) and 6.4(d), respectively. The time series reflects a reduction of the velocity with blockage ratio increase. However, the magnitude of reduction is smaller than the results reported by C-TOC. The velocity reduction presented at $B = 0.8$, with respect to the natural-state, reported by ADI-TOC is 6%, while TVD-TOC indicates 12%. The larger velocity rate reduction reported by TVD-TOC for C-TOC and C-CTE strategy than ADI-TOC is

consistent with findings reported in Section 5.3.

The larger velocity reduction obtained with C-TOC strategy can be related to the larger momentum extraction due to the large magnitudes of thrust coefficient derived (see Table 6.3). These magnitudes are larger than C_T^{CTE}, even for B=0.1.

Based on the C-TOC methodology, it is possible to differentiate between the power available for electrical generation and total power extracted. This power analysis requires the calculation of the head drop produced by momentum extraction. The estimation of the head drop across an array is performed in the following section.

6.2.4   Head Drop Across an Array

The momentum extracted by a turbine array produces a pressure change across the array evident in water depth change (dh). The head drop in the tidal-stream due to power extraction indicates that the turbine extracts potential energy from the tidal-stream rather than kinetic energy (Draper, 2011).

The head drops produced by the energy capture simulated with C-TOC and C-CTE, were calculated. Each methodology was applied to eight scenarios of $0.1 \leq B \leq 0.8$.

The application of C-TOC leads to the head drop estimation shown in Figure 6.5(a). The mean head drop was obtained from ADI-TOC and TVD-TOC schemes, and these solutions are compared to the head drops found analytically by solving the cubic polynomial derived by Houlsby *et al.* (2008) (Equation 4.18). The solution of the polynomial depends on the upstream Froude number, blockage ratio, and the thrust coefficient. The analytical solutions were calculated with the Fr, B, and C_T^{TOC}, obtained from the nine scenarios simulated with TVD-TOC model, as this scheme better simulates the power extraction and the flow reduction than ADI-TOC. In this way, the Δh solutions indicate the head drop expected according to the upstream conditions of flow and operating conditions of the turbine.

Figure 6.5(a) shows that the blockage ratio increase is linked to larger head drops.

This trend is presented in both models; however, for small B, TVD-TOC tends to overestimate the head drop; meanwhile, ADI-TOC is more consistent with the analytical solution. On the other hand, for large blockage ratios, both schemes slightly under-estimate Δh, but TVD-TOC presents a more accurate description.
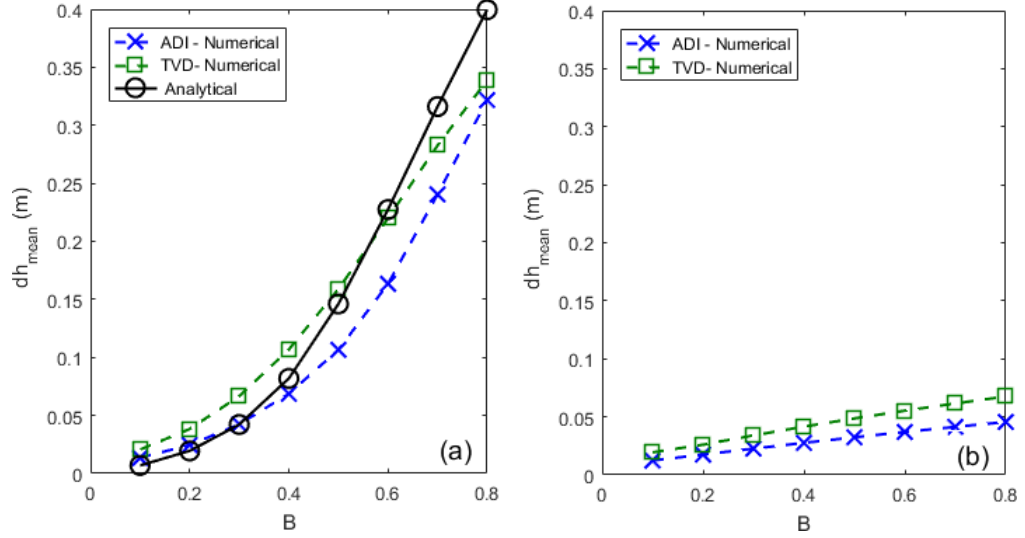
Fig. 6.5: Mean head drop across an array: C-TOC methodology (a) and C-CTE methodology (b).

The implementation of C-CTE produces the head drops shown in Figure 6.5(b). Blockage ratio increase also leads to larger head drops; however, the magnitude of Δh is significantly smaller than the results obtained with C-TOC methodology. Likewise, C-TOC, the head drops calculated with TVD-TOC scheme are higher than ADI-TOC.

A conclusion similar to the upstream velocity section can be reached for the head drop analysis: the smaller thrust force produced by implementing C-CTE methodology indicates that a smaller Δh is expected, as less momentum is removed, and consequently, a smaller pressure change takes place across the array. After calculating the head drops, it is possible to estimate turbine efficiencies; this is performed in the following section.

6.2.5 Turbine Efficiency

An advantage of LMAD-OCH theory is the ability to calculate turbine efficiency. This parameter indicates turbine performance and corresponds to the ratio of power removed by the turbine (P) to the total power extracted from the tidal-stream ($P + P_W$). The solution for tidal-streams with a small Froude number depends solely on the turbine velocity coefficient α_2 and the relative head drop across the turbine array $\Delta h/h$. This expression of turbine efficiency is given by Equation 4.27:

$$\eta \approx \alpha_2 \left(1 - \frac{1}{2} \frac{\Delta h}{h} \right)$$

The relative water depth change used in the η calculation was obtained numerically (as the depth differences across the array), and analytically (as the solution of the cubic polynomial derived by Houlsby et $al.$ (2008)). Turbine efficiency was calculated with the small Froude and general Froude number equations, as both solutions were consistent only values calculated with Equation 4.27 are reported.
Turbine efficiencies calculated for the fence configuration are presented in Figure 6.6. The results correspond to the time-average of the last tidal cycle, and they were obtained from the variation of the blockage ratio $0.1 \leq B \leq 0.8$.

Figure 6.6(a) indicates consistent results between the analytical and numerical solution of the efficiency for the B range analysed. Additionally, the solutions obtained with ADI-TOC and TVD-TOC are very similar; TVD-TOC tends to present slightly larger efficiencies than ADI-TOC. Considering a situation of optimum power extraction (by considering $\alpha_4 = 1/3$), the variation of B indicates that the efficiency decreases with blockage ratio increase. Consequently, large efficiencies found for small B, such as ~ 0.6 for $B < 0.2$, drop to almost half if the blockage ratio is large, such as $B = 0.8$.

Conversely, Figure 6.6(b) reports the relationship between turbine efficiency and thrust coefficient. This figure reports the numerical values obtained with ADI-TOC and TVD-TOC only. It is found that the relationship between η and time-averaged thrust
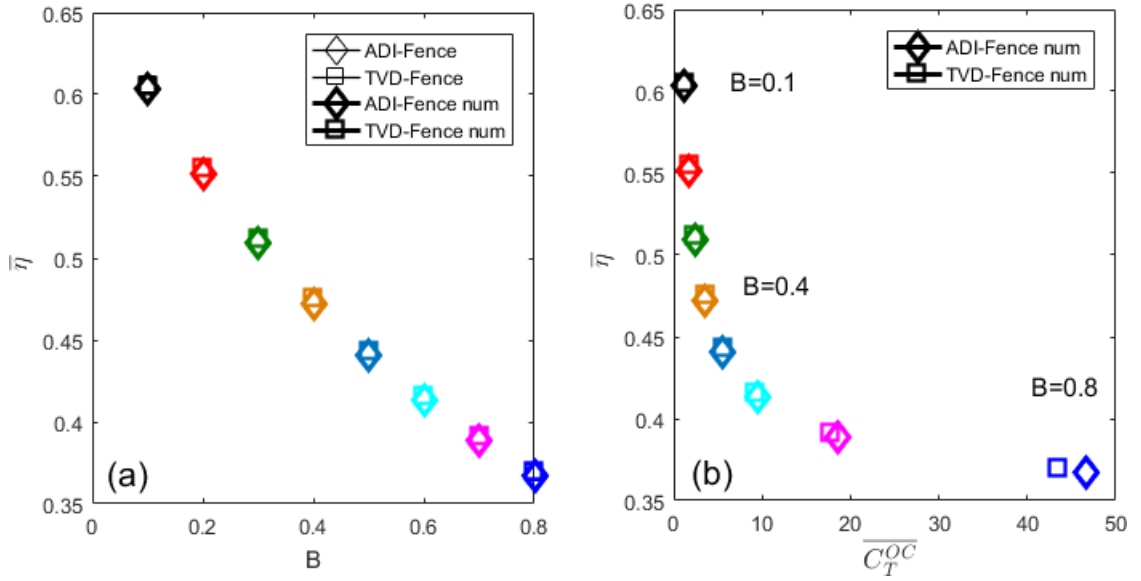
Fig. 6.6: Turbine efficiency for a fence configuration plotted against increasing values of blockage ratio (a) and thrust coefficient (b). Numerical (bold-markers) and analytical solutions (light-markers).

.

coefficient is similar between the models, except at large blockage ratios where ADI-TOC and TVD-TOC solutions for C_T^{TOC} diverge. It is worth mentioning that a fence configuration with $B > 0.5$ is not a feasible solution, due to practical and environmental reasons; nevertheless, these scenarios are presented to include in the analysis limit cases. Figure 6.6(b) indicates that turbine efficiency decrease is associated with the augmentation of the thrust coefficient. The C_T increment is related to an increase in the thrust force, which for large blockage ratios is associated with higher power dissipation and less available power. This point will be further discussed in Sections 6.2.6 and 6.5.5. Note, the efficiency drop is more rapid at a relatively small B, rather than higher blockage ratios. A similar trend was reported by Vogel *et al.* (2013).

Summarising, the higher values of turbine efficiency associated with relative low B indicate that a larger fraction of the total power extracted is available for power generation. However, the smaller drop in turbine efficiency found at large blockage

ratios suggests the ability to extract a large amount of power for electricity generation, maintaining a relatively high turbine efficiency (Draper, 2011). At high blockage ratios, a greater flow passes through the closely spaced turbines within the array. This is because the reduced inter-turbine spacing limits the flow diversion around the turbine. As a result, the shear generated by the core and bypass flow is smaller and generates lower mixing losses (Vogel et al., 2013). Nevertheless, total power extracted with high blockage ratios is restricted by the effects produced on the flow dynamics due to the high level of resistance introduced by the turbine on the flow, and by power lost in the mixing processes. In the following section, an analysis of power extracted by a turbine is presented.

6.2.6   Power Analysis

By obtaining the head drop and turbine efficiency the C-TOC methodology enable the calculation of further power metrics. In addition to the power removed by the turbine P in terms of cubic velocity (derived in Section 4.2.1):

$$P = \frac{1}{2}\rho V^3 A C_P^{TOC}$$

is possible to calculate the (i) total power extracted by the turbine $P + P_W$ (derived in Section 4.2.2):

$$P_T = P + P_W = \rho g u b h \Delta h \left(1 - Fr^2 \frac{1 - \Delta h/2h}{(1 - \Delta h/h)^2} \right)$$

(ii) power dissipated by turbine wake mixing P_W and (iii) power available in terms of turbine efficiency P_*. In the case of C-CTE methodology, the power analysis is restricted to the power removed by the turbine:

$$P = \frac{1}{2}\rho V^3 A C_P^{CTE}$$

where C_P^{CTE} indicates the power coefficient calculated with C-CTE methodology. In this test, the pre-defined value of power coefficient used is C_P^{CTE}=0.35.
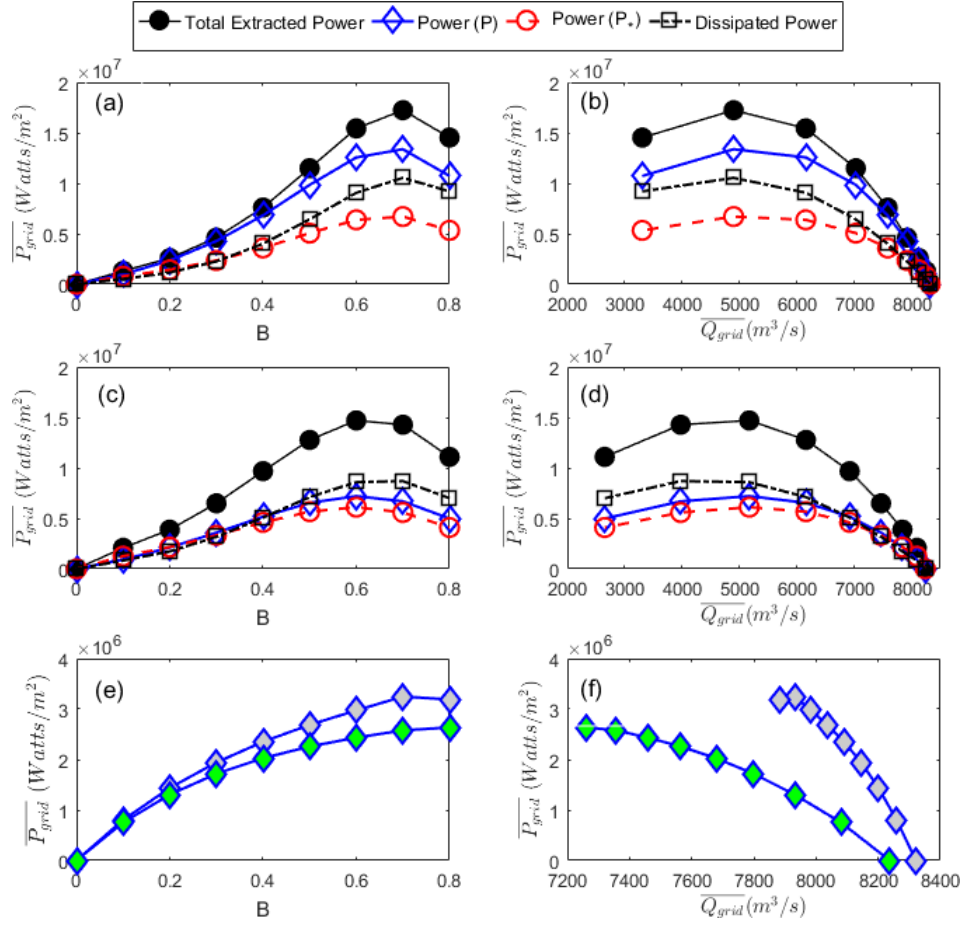
Fig. 6.7: C-TOC methodology and ADI-TOC (a and b). C-TOC methodology and TVD-TOC (c and d). C-CTE methodology and ADI-TOC (e and f; grey filling). C-CTE methodology and TVD-TOC (e and f; green filling).

Power metrics obtained with C-TOC and C-CTE methodology are presented graphically in Figure 6.7. The implementation of C-TOC enables the calculation of several metrics in addition to the power removed by the turbine P; such as P_T, P_*, and P_W. Note values reported herein correspond to the temporal average per grid cell. The results obtained with ADI-TOC are presented in Figures 6.7(a) and 6.7(b). The figures show that blockage ratio increase leads to maximum values of the power metrics analysed at B =0.7. The largest magnitude is reported by P_T (17.2 MW), followed by P (13.4 MW), P_W (10.5 MW), and finally P_* (6.7 MW). These results indicate

141

that blockage ratio increase leads to large power available for electricity generation P_*, but large B also dissipated an important amount of power (P_W). On the other hand, the metric P provides a description of the resource closer to the total power removed P_T, suggesting that this metric overestimates the power that can be used for electrical energy generation. In terms of the flow rate, Figure 6.7(b) shows the time-average flow rate per grid cell. This indicates that large blockage ratios reduce the flow rate considerably, as the flow has to pass through heavily packed turbine configurations. In the case of maximum power metrics, the flow rate decreases from $8.3E3$ m^3/s at natural-state to $4.9E3$ m^3/s. Therefore, at $B = 0.7$ the flow rate reduces by 40%.

The results obtained with C-TOC methodology and TVD-TOC are presented in Figures 6.7(c) and 6.7(d). The figures show a similar trend to ADI-TOC, but this time blockage ratio associated with the maximum values of the power metrics analysed occurs at $B = 0.6$, except for P_W which reaches its maximum value at $B = 0.7$. In addition, the magnitudes reported by TVD-TOC are smaller than ADI-TOC. The largest magnitude reported by TVD-TOC is given by P_T (14.7 MW), followed by P_W (8.7 MW), P (7.2 MW), and finally P_* (6.1 MW).

Regarding flow rates, Figure 6.7(d) indicates that flow rate decreases in a similar way to ADI-TOC, however, blockage ratios larger than $B > 0.6$ produced a larger flow rate reduction than ADI-TOC. The results obtained from the implementation of C-TOC methodology in TVD-TOC and ADI-TOC indicates the following: larger magnitudes of P_T, P, P_W, and P_* are reported by ADI-TOC. However, this is expected as this scheme tends to underestimate the velocity reduction produced by power extraction. Nevertheless, it is worth noting that power in terms of efficiency P_* reported by ADI-TOC and TVD-TOC are similar. Further, TVD-TOC generates similar magnitudes of power removed by the turbine P and power P_*. This indicates that P calculated with TVD-TOC provides a more accurate description of power available for electrical energy generation. This result is expected as the shock-capturing model better simulates the

velocity reduction produced by power extraction than ADI-TOC.

The metrics of power calculated with C-CTE are presented in Figures 6.7(e) and 6.7(f). The results obtained with ADI-TOC (grey-filling) and TVD-TOC (green-filling) indicate that power removed by the turbine P is one order of magnitude smaller than P obtained with C-TOC methodology; consequently, the flow rate reduction is also substantially smaller. As expected, ADI-TOC generates larger magnitudes of P and smaller flow rate reductions than TVD-TOC. The smaller P and Q reported by C-CTE methodology indicates that the inter-turbine spacing in addition to a pre-defined power coefficient is not able to correctly represent the momentum extracted by the turbine.

The next stage was the implementation of C-TOC to a more realistic configuration, a partial fence. In the following section, only results obtained with the C-TOC methodology are reported; consequently, the terms C_T^{TOC}, and C_P^{TOC} are omitted and only C_T and C_P are referred to.

6.3 Partial-Fence Configuration Modelling

The method developed in this thesis to represent marine turbines in depth-average hydrodynamics models is implemented in a turbine configuration closer to real-world scenarios. This method simulates the momentum sink extracted by the turbine, considering the operating conditions of the marine turbine. This was accomplished by implementing the linear momentum actuator disk in an open channel flow theory. Additionally, this method has been adopted into the two numerical schemes: one that solves SSF, and the other that simulates RVF.

The LMAD-OCH theory has been used to study partial-fence performance near a coastal headland (Draper *et al.*, 2013a), and in the Anglesey Skerries region, UK (Serhadlıoğlu *et al.*, 2013). Additionally, this array configuration was used in laboratory scale experiments to study momentum lost by porous discs in a channel and a

headland (Draper *et al.*, 2013b). The methodology developed in this thesis to study the fence configuration is used to simulate the partial-fence scenario. In contrast to the line sink of momentum method, implementation of the sink term methodology allows computations of energy captured by the turbines at the edges of a partial-fence without particular specifications. This is possible because ADI-TOC and TVD-TOC do not present numerical singularities at these locations of a partial-fence.

The deployment of a partial-fence produces a laterally unbounded flow, because the energy extraction occurs only in a partial section of the channel. The flow that passes through the array, the array-core flow, will experience a momentum loss and will present a reduced velocity downstream the array. On the other hand, the flows that bypass the array will experience their intensification. The mixing of the downstream array-core flow with the array-bypass flow generates an array-wake mixing region. The performance of a long partial-fence, that is constituted by regular spacing devices, can be studied over the near field region L_v length (see Section 4.2), and the far field region extent L_h; where $L_h > L_v$ (Draper *et al.*, 2010). LMAD-OCH theory can be used to study the near field region L_v. In this way, it is possible to determine the momentum extracted by the turbines within the fence, because the flow structure within the L_v length is expected to be similar to the bounded flow (Draper *et al.*, 2010, 2013a; Serhadlıoğlu *et al.*, 2013). Consequently, the theory can be used to study the performance of individual turbines within the partial-fence. However, the LMAD-OCH theory cannot provide information about the power extraction within the far-field region. At this length scale, the array-wake mixing is presented, and the assumptions of upstream uniform flow and quasi-steady flow are difficult to satisfy. This indicate that LMAD-OCH theory only considers the turbine-wake mixing between the turbine-core flow and turbine-bypass flow (Nishino and Willden, 2013b).

The partial-fence configuration studied in this thesis was incorporated in a tidal channel with uniform depth and a constant cross-section, which connects two large

basins (Figure 5.5). The large domain-size used in the simulation of a partial-fence enables the development and dissipation of array-wakes. The domain represents a semi-narrow channel with aspect ratio $W/L = 0.25$, where $L =$12150 m length and $W =$3000 m width. The set-up of the domain is specified in Section 5.3.1. The motivation for this geometry is to study tidal dynamic conditions similar to the Shannon estuary and sites where tidal-stream turbines will be tested, such as the Cape Cod Canal, Massachusetts, USA.

The partial-fence was deployed in the middle of the channel ($Y/L = 1/2$), covering 40% of a channel cross-section; the length of the array is 1200 m and it is presented in Figure 6.8. The array was defined over eight grid-cells, where each grid-cell contains a cluster of turbines. The diameter of an individual turbine was 16 m and the number of devices per grid-cell depends on the inter-turbine spacing used. Figure 6.8 shows the effect of a
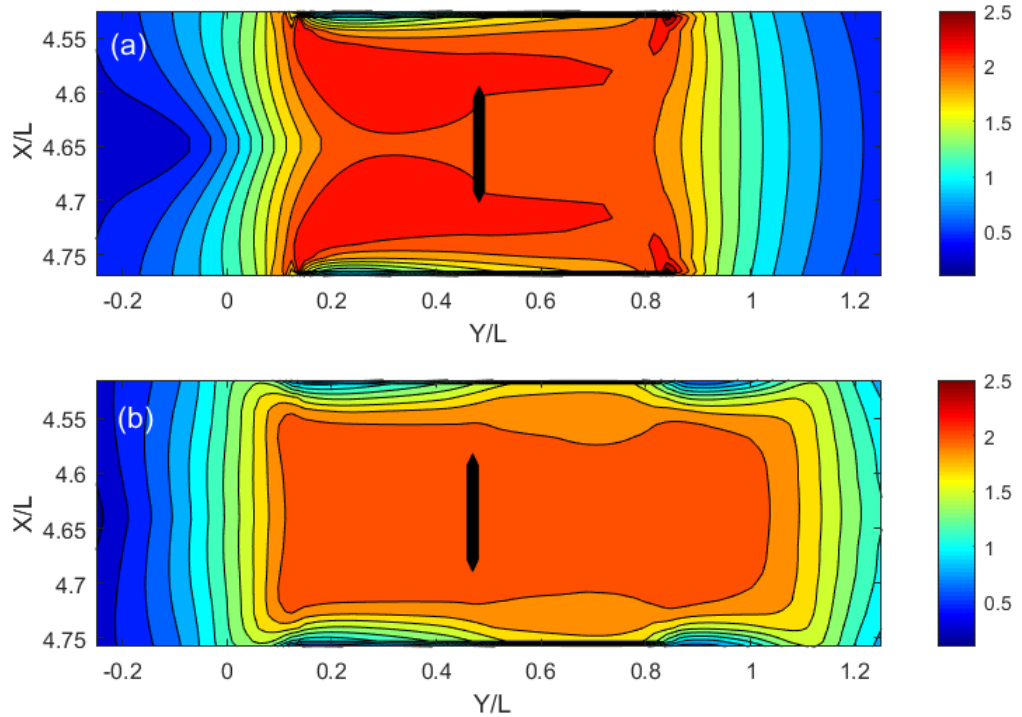
Fig. 6.8: Tidal channel plan view and snapshots of the velocity for a partial-fence configuration with B=0.1, obtained with ADI-TOC (a) and TVD-TOC (b).

partial-fence turbine configuration on the flow field simulated with ADI-TOC (Figure 6.8(a)) and TVD-TOC (Figure 6.8(b)) at time t=38.75 hrs. The blockage ratio of the turbines within the array is B =0.1. The impact of the low blockage ratio on the tidal-stream is simulated differently by the models. The ADI-TOC scheme generates array-bypass flows with higher intensity than TVD-TOC, reaching $\sim$2.5 m/s. On the other hand, TVD-TOC presents a uniform velocity upstream and downstream the array; in addition, the stream simulated by the RVF solver generates smaller magnitudes $\sim$2.0 m/s. A more detailed analysis of blockage ratio influence of a partial-fence simulated by the numerical schemes is given in Sections 6.4 and 6.5.2. The partial coverage of a channel cross-section by the new turbine configuration, in addition to the inter-turbine spacing, suggest that further specifications of blockage ratio are required to accurately define partial-fences. These refinements are described in the following section.

6.3.1   Blockage Ratio

To define partial-fence configurations more accurately, arrays can be subjected to further blockage ratios specifications. The study of a partial-fence as the coupling of the turbine-scale with the array-scale introduced the definition of the local (B_l), array (B_a), and global (B_g) blockage ratios (Nishino and Willden, 2012b). The thrust force calculation in the models is based on the contribution of the turbine cluster area per grid cell, and not on the individual simulation of a turbine. The local (Bl_{grid}), array (Ba_{grid}) and global (Bg_{grid}) blockage ratio has been re-defined in terms of the grid-cell; where it satisfies: $Bg_{grid} = Bl_{grid}Ba_{grid}$. These new definitions are consistent with blockage ratios proposed by Nishino and Willden (2012b).

The array blockage ratio, as a function of the grid cell, refers to the ratio of the representative array area to the channel cross-sectional area.

$$Ba_{grid} = \frac{N_c \Delta X}{W} \tag{6.1}$$

where N_c stands for the number of cell-grids that constitute the partial-fence, W indicates the channel width and ΔX is the spatial resolution of the grid-cell. The local blockage ratio per grid cell refers to the ratio of accumulated turbine area per grid-cell to cell-grid area:

$$Bl_{grid} = \frac{N_g A_t}{H \Delta X} \tag{6.2}$$

where N_g indicates the number of turbines per grid-cell, A_t refers to an individual turbine area of diameter d ($A_t = \pi d^2 / 4$) and H is the mean water depth. Finally, the global blockage ratio, as a function of the grid cell, (Equation 6.3) refers to the ratio of the total turbine area in the array to the channel cross-sectional area.

$$Bg_{grid} = \frac{N_c N_g A_t}{HW} \tag{6.3}$$

The following relations were obtained to corroborate the consistency of the blockage ratios as a function of the grid cell used in this thesis with Nishino and Willden (2012b) procedure. The expressions used in this thesis correspond to the left-hand side of Equations 6.4, the terms used by Nishino and Willden (2012b) to define the blockage ratios as a function of individual devices are on the right-hand side:

$$\frac{\Delta X}{N_g} = d + s \tag{6.4}$$

$$N_c N_g = n$$

$$N_c \Delta X = n(d + s)$$

According to Nishino and Willden (2012b), $d + s$ indicates the inter-centre turbine distance, where d and s refer to turbine diameter and turbine spacing. The total number of turbines in the partial-fence is given by n.

The scenarios studied in this thesis with partial-fences are presented in Table 6.4. The local-, array-, and global-blockage ratio per grid cell used in each scenario, as well as the total number of turbines that constitute the partial-fence, are specified in Table.

Partial-fence Configuration						
Scenario	Bl_{grid}	Ba_{grid}	Bg_{grid}	ITS (m)	RD	N_{pf}
0	0	0	0	-	-	0
1	0.05	0.40	0.02	122.61	7.66	12
2	0.10	0.40	0.04	86.77	5.42	24
3	0.15	0.40	0.06	70.86	4.43	36
4	0.20	0.40	0.08	61.38	3.84	48
5	0.25	0.40	0.10	54.90	3.43	60
6	0.30	0.40	0.12	50.12	3.13	72
7	0.35	0.40	0.14	46.40	2.90	84
8	0.40	0.40	0.16	43.41	2.71	96

Table 6.4: Local blockage ratio per grid-cell (Bl_{grid}), array blockage ratio (Ba_{grid}), global blockage ratio (Bg_{grid}), inter-turbine spacing (ITS), rotor distance (RD), and estimated number of individual turbines within a partial-fence (N_{pf})

The range of blockage ratios considered in Table 6.4 falls into the scope of partial-fence numerical simulations performed with 3D RANS: $0.0785 < B_l < 0.3142$, $0.25 < B_a < 1$, and $B_g = 0.0785$ (Perez-Campos and Nishino, 2015); $0.196 < B_l < 0.357$ and $B_g = 0.039$ (Nishino and Willden, 2013b). The partial-fences studied with depth-average models and the line sink of momentum method were studied in wider channels in order to resemble conditions of tidal-streams close to coastal headlands. In those cases, the ratios between the array-width and channel width are $B_a = 0.1$ and 0.06 (Draper *et al.*, 2013a), and $B_a = 0.20$ (Draper *et al.*, 2013b). Nevertheless, the local blockage ratios analysed in these studies fall into the range reported here.

In the analysis presented in subsequent sections variations of the local blockage ratio per grid cell is considered; as Bl_{grid} is equivalent to B in the fence setting, the parameter Bl_{grid} will be referred to as B.

6.4 Hydrodynamic Effects of Power Extraction

In the absence of turbine deployment, the tidal currents within a channel ($0 < X < L$) experience velocity increases and head drop due to the geometrical constraints of the

channel. However, marine energy extraction will further affect channel hydrodynamics. This effect is studied in this thesis by considering three aspects: wake induction factor (α_4), blockage ratio (B), and turbine array configuration (fence and partial-fence). The six scenarios discussed in the following sections are presented in Table 6.5. For fence configurations, two scenarios are considered: increase in the blockage ratio of an array, which operates at optimal power extraction conditions, and variations of wake induction factor for specific blockage ratios. In the case of partial-fence scenarios, the variation of blockage ratio is analysed only. The effect of increasing values of wake induction factor on the tidal-stream are studied by considering a tidal fence only; this configuration satisfactorily shows influences of α_4 on flows.

Hydrodynamic Effects							
Model	Configuration	Scenario	B	α_4	F_r	ΔX (m)	Δt (sec)
ADI-TOC	Fence	1	$0 \leq B \leq 0.8$	$\alpha_4 = 1/3$	0.11	150	12
		2	B=0.2	$0 < \alpha_4 < 1$	0.10	150	12
	Partial-Fence	3	$0 \leq B \leq 0.8$	$\alpha_4 = 1/3$	0.11	150	12
TVD-TOC	Fence	4	$0 \leq B \leq 0.8$	$\alpha_4 = 1/3$	0.11	150	1.5
		5	B=0.2	$0 < \alpha_4 < 1$	0.11	150	1.5
	Partial-Fence	6	$0 \leq B \leq 0.8$	$\alpha_4 = 1/3$	0.11	150	1.5

Table 6.5: ADI-TOC and TVD-TOC initial parameters specification for the scenarios used to evaluate the hydrodynamic effects of both configurations: fence and partial-fence.

6.4.1 Wake Induction Factor Influence on the Tidal-Stream

The wake induction factor, α_4, is an indicator of turbine porosity. The influence of this parameter on the power coefficient and turbine efficiency was reviewed in Sections 5.2 and 6.2.1. It was found that a specific α_4 leads to optimal power extraction. To better understand the hydrodynamic implications of α_4, a fence turbine configuration with a local blockage ratio of $B = 0.2$ was used to evaluate variations of wake

induction factor within a plausible range of $0 < \alpha_4 < 1$. The cases analysed correspond to scenarios 2 and 5 of Table 6.5. The flow at natural-state in the middle of the channel is characterised by F_r =0.10 for ADI-TOC, and F_r =0.11 for TVD-TOC. To appreciate effects of α_4 variations on tidal-streams, stream-wise profiles of the water elevation (ζ) and Y-component of the velocity (V) were analysed. The profiles correspond to the transect-line that passes along the channel's centreline. This transect is shown in Figure 6.9(e).

To compare the hydrodynamic effects of α_4 simulated by ADI-TOC and TVD-TOC, the profiles obtained from both models at t=38.75 hrs were normalised to the maximum value of the profile with the largest magnitude within a specific length. In this way, the different flow conditions (defined by F_r) simulated at natural-state by the models are overcome, and so it is possible to compare the influences of wake induction factor on tidal-streams.

In relation to water elevations, the profile of the largest magnitude is given by α_4 as it tends to zero ($\alpha_4 \rightarrow 0$), and this parameter is associated with low porosity, where the value selected was $\alpha_4 = 0.01$. The elevation profiles analysed were normalised to the maximum value of $\alpha_4 = 0.01$ profile within the length $-0.3 < Y/L < 1.3$, and this value is denoted by ζ_*. Figure 6.9 shows the elevation profiles normalised by ζ_* obtained for two cases: turbine omission and power extraction with $\alpha_4 = 0.01$. The mean water depth corresponds to ζ/ζ_*=0.

Results obtained with ADI-TOC (Figures 6.9(a) and 6.9(b)) and TVD-TOC (Figures 6.9(c) and 6.9(d)) are presented. The normalised profiles are presented within the lengths $-0.3 < Y/L < 1.3$ and -1000 m $< Y <$ 1000 m. Their extent is specified in the plan view of the domain in Figure 6.9(e). The $-0.3 < Y/L < 1.3$ length is represented by a dotted-line. The -1000 m $< Y <$ 1000 m length is denoted by a square dash-line. This length is also specified by vertical lines in Figures 6.9(a)(c).

The $-0.3 < Y/L < 1.3$ extent shows (i) high tide on the left basin, (ii) head drop

produced by the geometrical constraints of the channel, (iiii) water depth decreases below the mean water depth near the channel's exit, and in the case of power extraction, (iv) depth discontinuity at the location where the tidal fence is situated ($Y/L = 0.5$). These features are presented in the simulations obtained from both models.
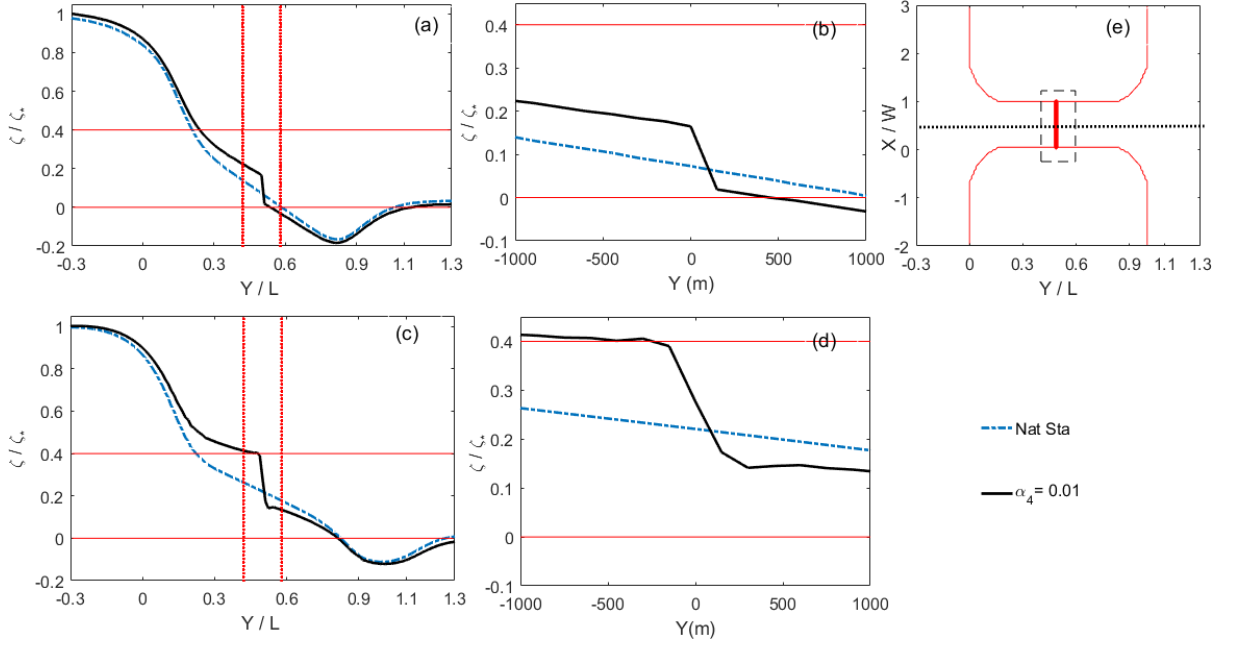
Fig. 6.9: Normalised water elevation profiles along the channel centreline obtained with ADI-TOC (a)(b) and TVD-TOC (c)(d).

Regarding the head drop below mean water (Δh_e), this depends on the channel geometry. This head drop is associated with exit separation effects (Garrett and Cummins, 2005), and it is more pronounced in channels with advection-dominated flows (Draper, 2011). The simulation of this type of flow has been identified in the tidal channel under study in Section 5.3.2. The head loss is of the order of $(\Delta|\vec{U}|)^2/2g$ over the region where the cross-section changes from constant to expanded at the channel's end (Garrett and Cummins, 2005). The magnitude $\Delta|\vec{U}|$ is the difference in the instantaneous velocity magnitude between the channel's opening and the uniform section within the channel (Draper, 2011). To accurately estimate the dynamical balance of

the tidal channel at the natural state, Garrett and Cummins (2005); Sutherland *et al.* (2007) suggest the calculation of the phase lag of the current behind the maximum elevation difference in the channel. If the phase lag decreases from 90°, the flow within the channel is balanced between the pressure gradient and acceleration terms. Therefore, there is a small effect of background friction and head loss due to exit separation (Garrett and Cummins, 2005). On the other hand, if the phase lag tends to zero, the pressure gradient forcing is balanced by friction together with separation effects, producing a quasi-steady flow. The phase lags obtained with the models used in this study are 25° (TVD-TOC) and 36.5^o (ADI-TOC), and they indicate that the channel produces a flow between the two limits. This means the flow is subject to advection, but still closer to the quasi-steady state (Sutherland *et al.*, 2007), and also subject to exit separation effects.

Note that at natural state the elevation solutions obtained from the models are different. ADI-TOC generates a larger head drop due to exit separation effects Δh_e located before the channel's exit, while TVD-TOC generates Δh_e at the exit of the channel. Additionally, the phase lag reported by the models indicates channel exit effects are more important in TVD-TOC than ADI-TOC. The semi-narrow channel under study presents a velocity increase at channel exit at t=38.75 hrs as a consequence of the pressure gradient generated along the channel and the head drop Δh_e. The velocity spatial gradient near the channel exit is expected to be better solved by TVD-TOC due to the shock-capturing effect, so Δh_e should be better represented by TVD-TOC.

The influence of the location of Δh_e in the natural state profiles simulated by the models is illustrated within the -1000 m $< Y <$ 1000 m extent. Here, the fence is situated at $Y = 0$. In ADI-TOC (Figure 6.9(b)), the proximity of Δh_e to the middle of the channel ($Y = 0$) produces a depth drop near this location. In the case of TVD-TOC (Figure 6.9(d)), the closeness of Δh_e to the exit of the channel and therefore,

away from the middle, implies a reduced influence of Δh_e on the water elevation at $Y = 0$.

Normalised elevation profiles for selected values of α_4 within the -1000 m $< Y <$ 1000 m extent, and obtained with ADI-TOC and TVD-TOC are presented in Figures 6.10(a) and 6.10(c), respectively. Large values of wake induction factor $(\alpha_4 \rightarrow 1.0)$ present a profile similar to the natural-condition state. This small change in elevations is consistent with a turbine with high porosity, which allows large flow rate through the turbine and presents little losses by turbine wake mixing. Conversely, small values of the parameter $(\alpha_4 \rightarrow 0)$ indicate a more pronounced water elevation discontinuity at the location of the fence. These results are consistent with a turbine with low porosity tending to block flow.
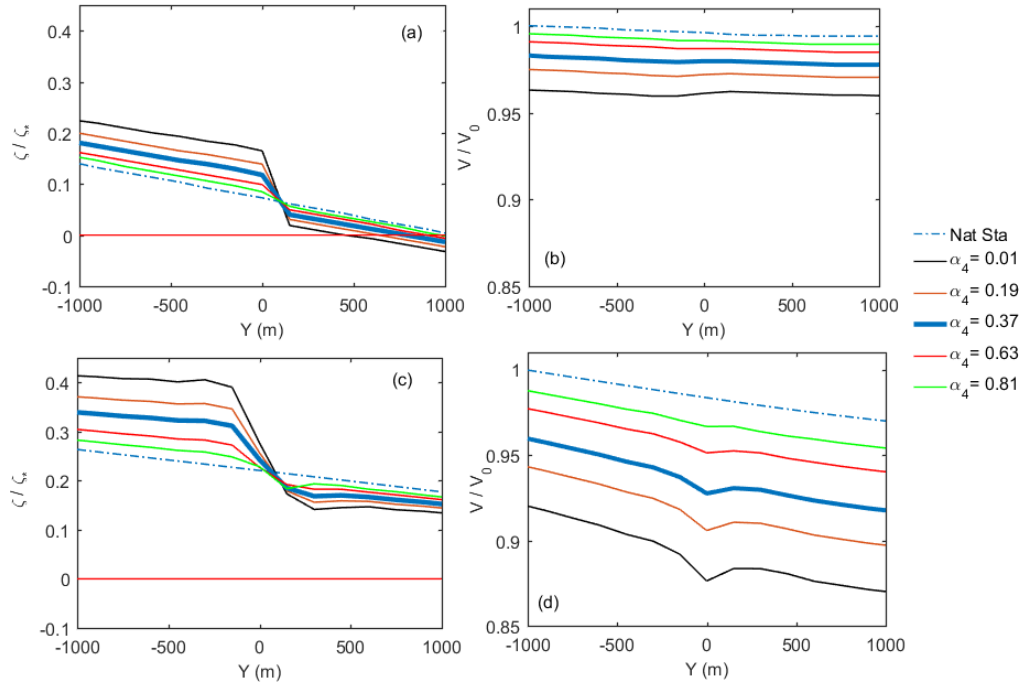
Fig. 6.10: Selected values of normalised water elevation profiles and Y- component of the velocity along the channel centreline obtained with ADI-TOC (a)(b) and TVD-TOC (c)(d).

In the case of the velocity, the profiles obtained for increasing values of wake in-

duction factor, were normalised to the maximum value of the natural-state velocity profile within the -1000 m $< Y <$ 1000 m length, and this value is denoted by V_0. The solutions obtained with ADI-TOC and TVD-TOC, along the channel centre, are presented in Figures 6.10(b) and 6.10(d), respectively. The profiles with stronger velocity reduction correspond to the $\alpha_4 \to 0$ scenario, and this velocity decrease is associated with larger dissipation by wake mixing. While profiles for $\alpha_4 \to 1.0$ resemble the natural state scenario.

The situation that leads to optimum power extraction, $\alpha_4 \approx 1/3$, is represented by a thick-blue line in Figure 6.10. This value of α_4 produces a medium change on the velocity and elevation profiles, suggesting that the maximisation of power extraction is linked to the reduction of power dissipation by turbine wake mixing.

A comparison of the water depth profiles obtained with both schemes (Figures 6.10(a) and 6.10(c)), shows that ADI-TOC simulates a smaller head drop across the tidal fence than TVD-TOC. The comparison of the velocity profiles (Figures 6.10(b) and 6.10(d)) indicates that the simulation of the velocity reduction associated with turbine wake mixing (via the simulation of $\alpha_4 \to 1.0$) is smaller in ADI-TOC than TVD-TOC. Additionally, the rapidly varying flow scheme generates a more pronounced velocity discontinuity at the array location.

ADI-TOC's performance is consistent with previous findings, and the scheme correctly simulates the head drop across the tidal fence, especially for small blockage ratios, as Section 6.2.4 indicates, but it under-represents velocity reduction. Conversely, TVD-TOC tends to over estimate the head drop across the tidal fence, however, it correctly simulates velocity decrease.

6.4.2 Turbine Array Configuration and Blockage Ratio Influences

Turbine configuration determines the effects power extraction has on tidal-streams. However, the degree of impact depends on the blockage ratio of the turbines within the array. In the case of a fence deployment, as the array covers completely the cross-section of the channel and the flow is bounded by the walls of the channel, the impact of power extraction occurs uniformly across the channel. Conversely, the deployment of a partial-fence implies the existence of an unbounded flow, which only experiences energy extraction in a limited section of the channel cross-section. To account for the hydrodynamic changes produced by the turbine configuration, the blockage ratio range $0 \leq B \leq 0.8$ was evaluated for both a fence and a partial-fence. The cases evaluated correspond to scenarios 1, 3, 4, and 6 of Table 6.5. These scenarios consider a flow characterised by F_r=0.11 in the middle of the channel at natural-state.

The effects of increased B on velocity and elevation fields are assessed using time snapshots and stream-wise profiles at flood tide (t =38.75 hrs). In the case of the velocity field, the effect of a large blockage ratio (B=0.6) in fence and partial-fence configurations are presented in Figure 6.11. The tidal-stream flows from left to right. The deployment of the fence is observed in Figure 6.11(a) for ADI-TOC, and in Figure 6.11(b) for TVD-TOC. Both models report that power extraction via the tidal fence produces similar velocity reductions across the channel. However, downstream of the fence, the stream presents a uniform velocity within about 4000 m.

A comparison of results obtained via the models show that power extraction with a tidal fence simulated with ADI-TOC, reduces the flows' velocity within the channel from the natural state value to approximately 1.5 m/s; while TVD-TOC shows a further reduction to 1.3 m/s. The smaller velocity decrease reported by ADI-TOC is consistent with the incapability of the scheme to simulate velocity reductions accurately. In the case of TVD-TOC, the downstream velocity is more influenced by the channel's exit

than ADI-TOC is. The response of TVD-TOC is consistent with the increase of velocity produced by the exit separation effects reported in Section 6.4.1.
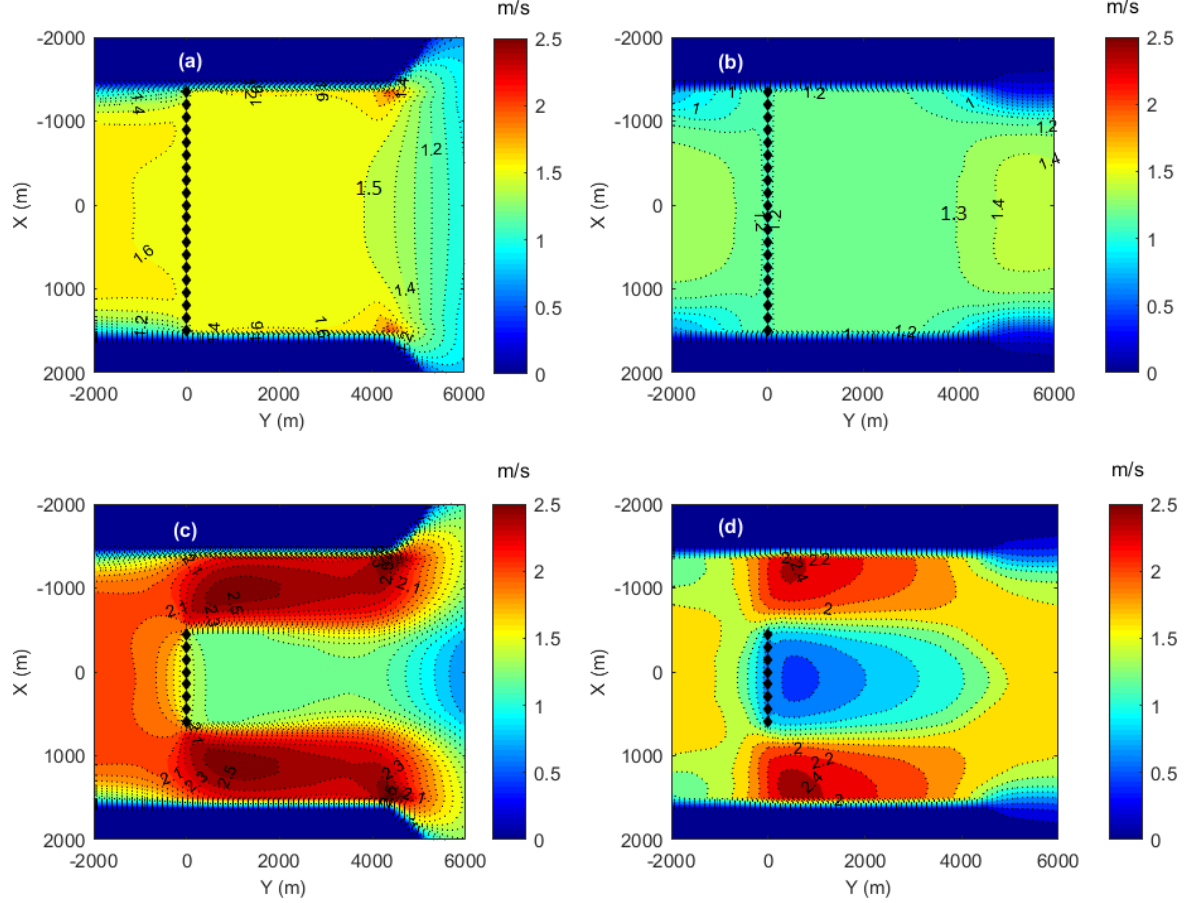
Fig. 6.11: Plan view of velocity contours within the tidal channel. Fence and partial-fence configuration with B=0.6 simulated with ADI-TOC (a)(c), and with TVD-TOC (b)(d).

The impact of smaller blockage ratios on the tidal-stream is reported with stream-wise profiles of the Y- component of the velocity (V) and the water elevation ζ at t=38.75 hrs. These profiles correspond to transect-line that passes along the channel's centre (Figure 6.10(e)). Results obtained from ADI-TOC correspond to Figures 6.12(a) and 6.12(b), and results from TVD-TOC are presented in Figures 6.12(c) and 6.12(d). The velocity stream-wise profile obtained with the fence configuration for $B = 0.6$

shows an almost uniform decrease of the velocity along the channel within the -1000 m $< Y <$ 1000 m length. This behaviour is also found for smaller blockage ratios. In the case of B =0.1, the profile is close to the natural-state conditions. In term of the elevation, ADI-TOC (Figure 6.12(a)) and TVD-TOC (Figure 6.12(c)) show profiles which indicate an increase of the head drop across the fence when larger blockage ratios are implemented.

The comparison of the profiles obtained between the models indicates that elevation profile at the natural-state simulated by ADI-TOC is lower than TVD-TOC. For the power extraction scenario, velocity profiles simulated by TVD-TOC present a stronger reduction than ADI-TOC. Additionally, TVD-TOC simulates a larger Δh than ADI-TOC. These findings are consistent with the solutions reported by the models for α_4 variation (Section 6.4.1).

In the case of a partial-fence turbine configuration, the velocity field simulated with ADI-TOC and TVD-TOC are presented in Figures 6.11(c) and 6.11(d), respectively. Both models indicate that power extraction with a partial-fence favours the existence of two regions: array-bypass flow and array-wake flow. These regions describe the velocity intensification when bypassing the array, and the significant velocity diminution downstream of the array. Note that the partial-fence produces a velocity reduction in the upstream flow, just before passing through the array. This feature illustrates the influence of a partial-fence on the free flow as reported by (Vogel *et al.*, 2013; Perez-Campos and Nishino, 2015).

The comparison between the models indicates that the magnitude of the array-bypass flow simulated with ADI-TOC is larger in extent and slightly larger in magnitude than TVD-TOC. Also, the array-bypass flow obtained with ADI-TOC has a stronger influence on the velocity at the partial-fence edges than TVD-TOC. Regarding the array-wake, a larger velocity reduction is reported by the rapidly varying scheme within the array-wake than ADI-TOC. Despite this, the array-wake simulated by TVD-
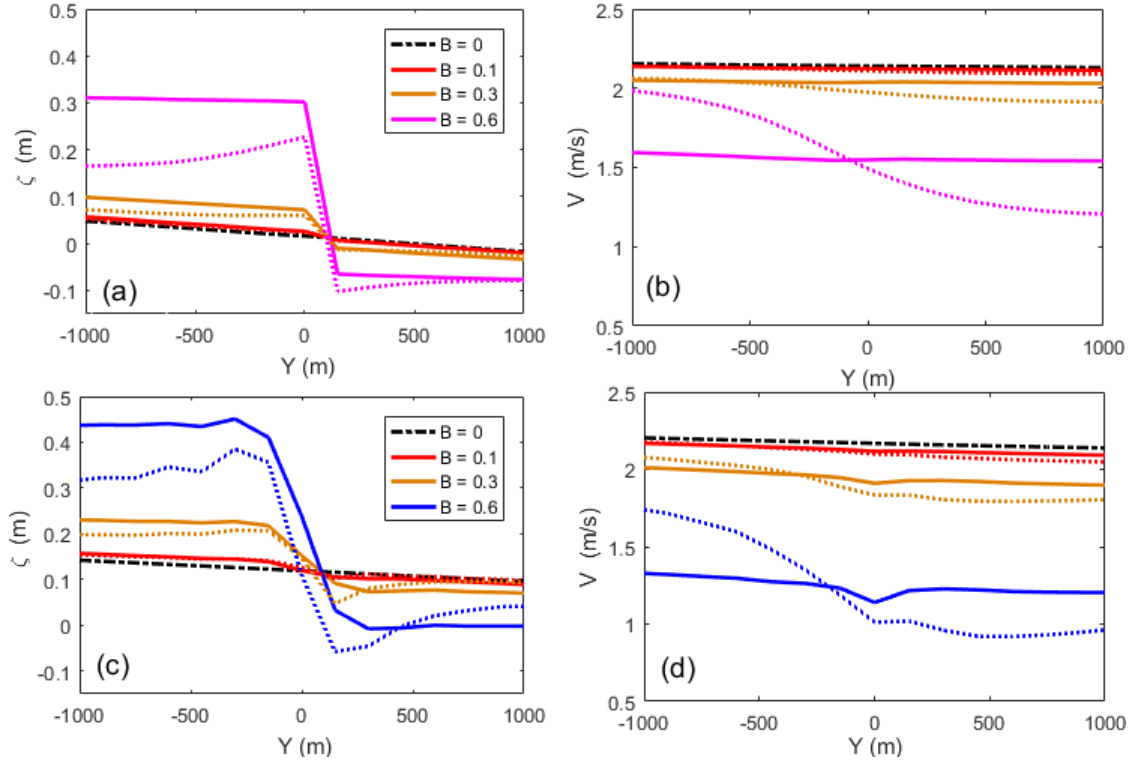
Fig. 6.12: Stream-wise profile of the water elevation ζ and Y- component of the velocity, along the channel centreline, for a fence (continuous-line) and partial-fence (dash-line) configuration obtained with ADI-TOC (a and b) and TVD-TOC (c and d).

TOC recovers to an upstream magnitude within 6000 m. Recovery over this distance does not occur in ADI-TOC. Note the array-wake reported in the simulations imply a situation where the individual turbines' wake has merged. Therefore, the array-wake requires a longer distance to recover than an individual turbine's wake (Nash and Phoenix, 2017). Research has been carried out to identify the distance required for turbine's wake to merge, however, the author is not aware of array-wake extension reported in the literature.

The strong velocity reduction reported downstream of a partial-fence is evident in the stream-wise velocity profile presented in Figure 6.12(b)(d) for ADI-TOC and TVD-TOC. Both models report a profile with larger magnitude upstream of the array than downstream. The magnitude of the difference increased when a larger B was used. In

terms of elevations, ADI-TOC (Figure 6.12(a)) and TVD-TOC (Figure 6.12(c)) show that the partial-fence presents a larger downstream depth reduction than the fence (the magnitude of the head drop is analysed in Section 6.5.3). This drop is associated with the velocity reduction produced by the array-wake generation.

Summarising, the blockage ratio has a stronger effect on the velocity and elevation profile than the variation in wake induction factor (α_4) for a given blockage ratio. By introducing an uniform thrust force on the flow, the fence configuration produces uniform effects of power extraction on the core- and bypass-flow at the turbine scale i.e. at the near-field region extent (Houlsby *et al.*, 2008; Draper *et al.*, 2010). Conversely, if the partial-fence is long enough, the power extraction simulation demonstrates the existence of another scale (larger and slower than the turbine scale), referred to as the array-scale (Nishino and Willden, 2012b).

6.5   Resource Assessment within Realistic Blockage Ratio Range

Maximum power extraction depends on the dynamic balance of the channel (Draper *et al.*, 2010), turbine efficiency, and turbine spacing reflected in the blockage ratio. Additionally, maximum power extraction is associated with high blockage ratios (Draper *et al.*, 2010) and significant flow rate reduction (Sutherland *et al.*, 2007), due to the blocking effect produced by the reduction of the turbines lateral spacing. However, large thrust turbines are not practical for realistic designs (Adcock *et al.*, 2015), and they could also significantly influence tidal hydrodynamics, and mixing and transport processes of the potential site. These effects would occur at the local scale (turbine scale), and at the regional scale ($10^1 - 10^6$ m) (Adcock *et al.*, 2015). Within the local scale, the small lateral spacing (associated with large blockage ratios) favours turbine wake merging and bypass flow acceleration (Nash and Phoenix, 2017). This alteration

of flow around turbines increases turbulence downstream of the fence, affecting tidal hydrodynamics (Adcock *et al.*, 2015). Within the regional scale, large arrays could produce substantial changes in current velocities, sediment transport, flushing times, and other geochemical processes (Adcock *et al.*, 2015; Bonar *et al.*, 2015; Nash and Phoenix, 2017). In the case of a large array, the reduction of tidal range and delay in high and low tides were reported to be more significant for small lateral turbine spacing (Fallon *et al.*, 2014).

As a result of this evidence, the evaluation of tidal-stream resource is performed within realistic blockage ratios ($0 < B \leq 0.4$). First, the procedure used to assess the tidal-streams is used to evaluate the performance of partial-fences; this implies the calculation of the optimal wake induction factor, the thrust coefficient, the power coefficient, and the turbine efficiency. To understand the influences of partial-fence on upstream velocities and head drops, results obtained with this configuration are compared to a tidal fence and to analytical solutions derived from the LMAD-CH theory. Later, metrics used to quantify the power: P, P_*, P_T, and P_W are calculated for both turbine configurations. Additionally, these metrics are estimated using the head drop deduced by the LMAD-OCH theory. The solutions obtained are compared to the estimations obtained from the models. Finally, the results are summarised and discussed, and conclusions derived from this Chapter are presented.

6.5.1 Partial-Fence Optimal Wake Induction Factor and C_T & C_P Calculation

To determine the optimal wake induction factor a the partial-fence configuration, plausible values of wake induction factors were analysed for $B = 0.2$, in a similar way to a fence scenario (Table 6.2). Initial parameter specifications for the scenarios simulated are presented in Table 6.6. To determine the value of α_4 that leads to significant power extraction, total power extracted P_T, power removed by the turbine P, and available

power P_*, these metrics were calculated with the partial-fence configuration. The numerical head drop, defined as the head drop across the array obtained from the depth differences obtained with the models, was used to compute the power metrics mentioned previously.

Partial-Fence Configuration						
Model	Scenario	B	α_4	Δt (sec)	TIS (m)	RD
ADI-TOC	1	0.2	$0 < \alpha_4 < 1$	12	61.40	3.84
TVD-TOC	2	0.2	$0 < \alpha_4 < 1$	1.5	61.40	3.84

Table 6.6: ADI-TOC and TVD-TOC initial parameters specification. Temporal resolution (Δt), Turbine inter-spacing (TIS), and corresponding rotor distance RD. Spatial resolution $\Delta X = 150$ was used in both schemes.

The metrics generated by ADI-TOC (Figure 6.13(a)), and TVD-TOC (Figure 6.13(b)) correspond to the time-averaged of the last tidal cycle, and the average over the array i.e. the metrics obtained at each grid that constitute the partial-fence averaged to obtain a value representative of the array.

Figure 6.13 shows the metrics obtained for increasing values of wake induction factor $0 < \alpha_4 < 1.0$, $B = 0.2$, and $F_r = 0.11$. For values $\alpha_4 \longrightarrow 0$, maximum values of total power extracted were obtained, but nil power is available for electricity generation. The other limit, $\alpha_4 \longrightarrow 1$, indicates that P_T is small, but again no power is available to the turbine. Maximum values of P and P_* are observed in the range $0.30 < \alpha_4 < 0.5$.

The variation of power within the range $0 < \alpha_4 < 1.0$ is consistent with the variation between the power coefficient and α_4 reported by Draper (2011), except at $\alpha_4 \approx 1.0$. Based on the LMAD-OCH theory, the analytical calculation of the total power extracted becomes zero as $\alpha_4 \longrightarrow 1.0$, indicating that the downstream velocity reduction due to turbine wake mixing decreases to negligible values. As a result, the power extraction and head drop decrease until reaching the situation $\alpha_4 = 1.0$, where no power is extracted and no head drop is presented.
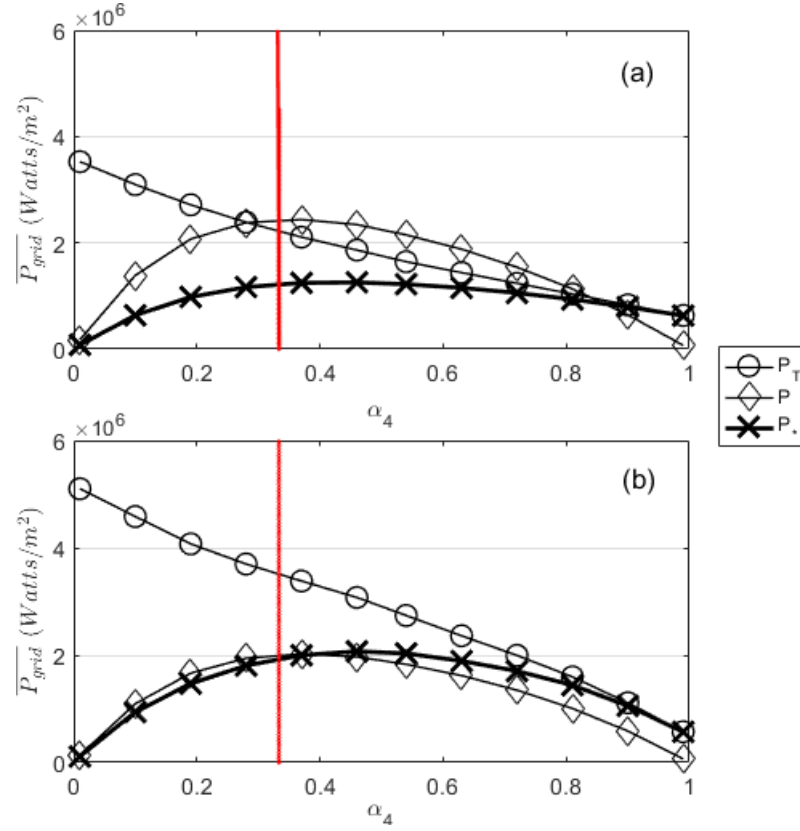
Fig. 6.13: Partial-fence P_T, P, and P_* metrics obtained from ADI-TOC (a) and TVD-TOC (b). Red-line indicates $\alpha_4 = 1/3$.

The solutions reported in this thesis show an important decrease of the head drop as expected; however, at $\alpha_4 = 0.99$ the relative change of the head drop is different from zero ($\Delta h/h \neq 0$). Consequently, for $\alpha_4 \approx 1.0$ the models indicate an important reduction of the total and available power, but different from zero as Figure 6.13 indicates. It is worth mentioning that the partial-fence scenario with high porosity turbines ($\alpha_4 \longrightarrow 1$) is not an attractive option for power extraction due to the low power extraction potential. Nevertheless, this scenario is presented because it shows the differences between the analytical and numerical solutions.

Comparing results from ADI-TOC (Figure 6.13(a)) and TVD-TOC (Figure 6.13(b)), it is shown that TVD-TOC generates higher total power extracted and available power

P_* than ADI-TOC. Note, the power removed by the turbine P simulated with this scheme is similar to P_*. Meanwhile, ADI-TOC tends to over-estimate P, but under-estimates P_* and P_T.

The higher magnitudes of P_T reported by TVD-TOC are explained by the larger head drop simulated by the scheme for $B = 0.2$ in comparison with ADI-TOC; the analysis of the head drop for a partial-fence is reported in Section 6.5.3, and it is found that TVD-TOC simulates a more accurate head drop than ADI-TOC. In terms of P_*, the higher values obtained with TVD-TOC are justified by the linear dependence of P_* on the total power extracted; therefore, larger magnitudes of P_T obtained with TVD-TOC imply larger values of P_*. The expected consistency between P and P_* is better represented by TVD-TOC.

Maximum values of power removed by turbines and available power P_* are observed within the range $0.30 < \alpha_4 < 0.5$. This range is consistent with optimal wake induction factors for partial-fence configurations reported by (Serhadlıoğlu *et al.*, 2013). To evaluate the performance of turbine configurations (fence versus partial-fence) $\alpha_4 = 1/3$ is used to be consistent with the operating conditions set for a tidal fence. In this way, the capacity of the models to simulate unbounded flows generated by the partial-fence is evaluated. Note that $\alpha_4 = 1/3$ still represents a condition close to optimal power extraction; however, a maximum performance could be obtained with $\alpha_4 \approx 0.45$.

A constant value of the wake induction factor was used during a tidal cycle, but a slightly better performance could be obtained if a variable wake velocity coefficient was taken into account (Serhadlıoğlu *et al.*, 2013). The identification of α_4 enables the calculation of thrust and power coefficients. These coefficients are functions of the upstream conditions through the Froude number, which in turn depends on the tidal regime, consequently C_T and C_P are modulated by the tidal cycle. The thrust and power coefficients for the last tidal cycle simulated are presented in Figure 6.14.

In the case of a partial-fence, values of C_T (Figure 6.14(a)) and C_P (Figure 6.14(c))
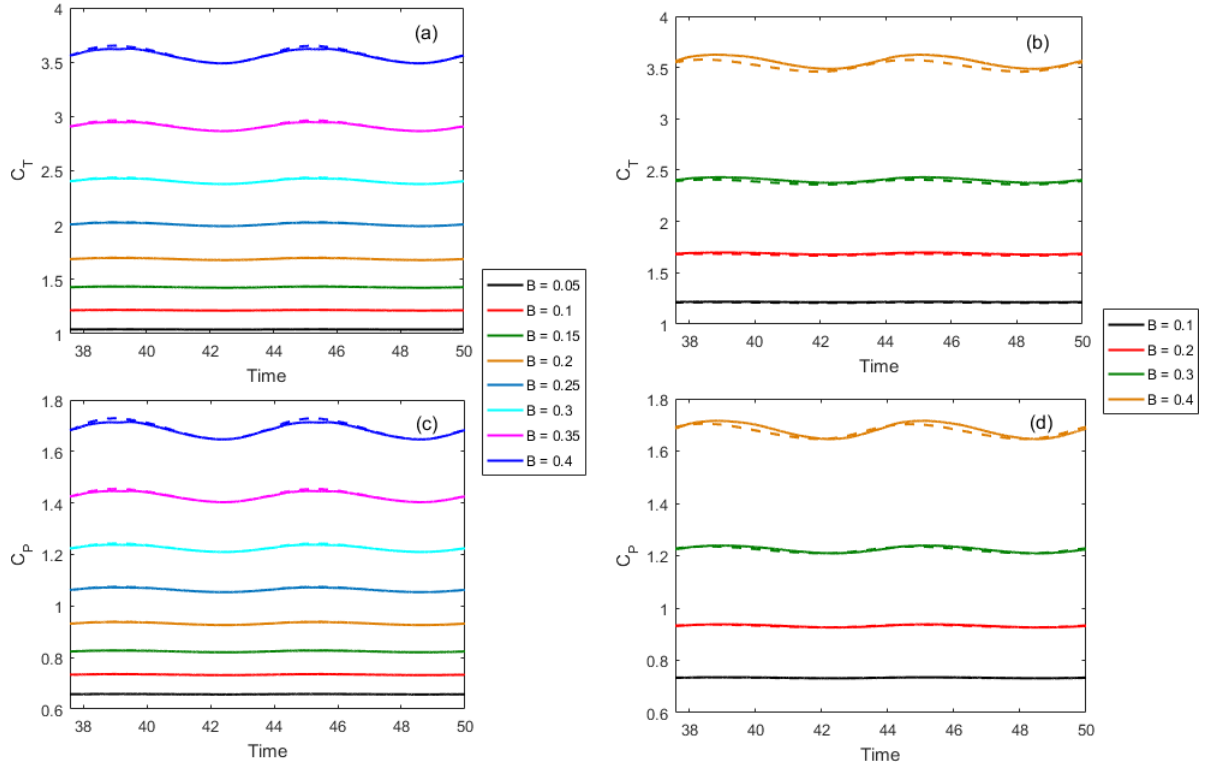
Fig. 6.14: Time-series of the thrust and power coefficient. ADI-TOC partial-fence solutions from a middle-cell (continuous-line) and an edge-cell (dash-line) (a and c). Fence solutions obtained from ADI-TOC (continuous-line) and TVD-TOC (dash-line) (b and d).

taken from the middle of the array are compared with values taken from the edge of a partial-fence. The models report slightly larger values of the coefficients in cells at the array edges. As TVD-TOC solutions are similar to ADI-TOC, the results from the rapidly varying flow are not presented. Conversely, Heathcote *et al.* (2016) identified slightly smaller thrust coefficient at the edges of a partial-fence constituted by four devices in a wide channel with a high blockage ratio ($B = 0.393$). However, the subtle differences found between the edge- and the middle-cell suggest that the thrust and power coefficient may be considered as constant along the partial-fence.

Regarding the fence configuration, the C_T solutions obtained from TVD-TOC and ADI-TOC are presented in Figure 6.14(b). Meanwhile, the C_P solution obtained with

the models is reported in Figure 6.14(d). The time-series obtained with TVD-TOC tends to present slightly smaller magnitudes than ADI-TOC, possibly because of the larger velocity reduction reported in the TVD-TOC model. Nevertheless, the solutions obtained with both schemes are consistent. Additionally, the fence and the partial-fence configuration report similar magnitudes of C_P and C_T time series.

6.5.2 Upstream Velocities for a Partial-Fence and a Fence

Modification of upstream conditions due to energy extraction are studied to better understand the power extraction estimations of a partial-fence. The upstream conditions at the partial-fence are compared to the fence configuration. In this way, the role of the bounded-flow and the unbounded-flow are analysed. The scenarios evaluated and the parameters specification of the models are presented in Table 6.7.

Small Blockage Ratios					
Model	Configuration	Scenario	B	α_4	Δt (sec)
ADI-TOC	Fence	1	$0 \leq B \leq 0.4$	$\alpha_4 = 1/3$	12
	Partial-Fence	2	$0 \leq B \leq 0.4$	$\alpha_4 = 1/3$	12
TVD-TOC	Fence	3	$0 \leq B \leq 0.4$	$\alpha_4 = 1/3$	1.5
	Partial-Fence	4	$0 \leq B \leq 0.4$	$\alpha_4 = 1/3$	1.5

Table 6.7: ADI-TOC and TVD-TOC initial parameters specification for the analysis of small blockage ratios with a fence and a partial-fence configuration.

To identify the effects of a partial-fence on the upstream velocities, the time-averaged Y-component of velocity was calculated at each grid cell that constitutes the array. Velocities obtained for increasing values of blockage ratio computed with ADI-TOC (Figure 6.15(a)), and TVD-TOC (Figure 6.15(b)) are presented.
The figures indicate that upstream velocities along the fence tend to be uniform for small blockage ratios ($B \leq 0.15$), but further increases in B generates a different behaviour between the grid-cells located in the middle and on the edges. Large values

of B produces larger velocity decreases in the middle of the array, meanwhile the edges exhibit smaller velocity reduction.

A comparison of results obtained with the models shows that the upstream velocities obtained from ADI-TOC present smaller reductions with increasing B than TVD-TOC. In addition, for small B, velocities simulated with ADI-TOC at the edges of a partial-fence show slightly enhance magnitudes. This suggests that the faster array-bypass flow computed with the ADI-TOC scheme is influencing velocities at the partial-fence edges.

To compare upstream velocities generated by both configurations, time-averaged velocities obtained from the partial-fence were averaged over the grids that constitute the array. In the case of the fence, as the upstream conditions are uniform along the array, a middle grid-cell was elected. The time-averaged and array-averaged velocity V from both configurations were calculated, and the results obtained from ADI-TOC are presented in Figure 6.15(c); the results obtained from TVD-TOC are shown in Figure 6.15(d). The figures show that velocity reduction rates reported by ADI-TOC, for both configurations, are smaller than TVD-TOC rates. This result is consistent with findings reported in Section 5.3 which indicates that ADI-TOC underestimates velocity reductions due to power extraction. Additionally, velocity reductions simulated by ADI-TOC for the partial-fence are smaller than for the fence; meanwhile, TVD-TOC reports the opposite. To understand the larger velocity reductions reported by TVD-TOC for the partial-fence, the flow rate was evaluated.

Time-averaged and array-averaged flow rates were calculated for the partial-fence and the fence with both ADI-TOC (Figure 6.15(e)), and TVD-TOC (Figure 6.15(f)). The figures show that the array-averaged flow rates decrease for ADI-TOC for the partial-fence are smaller than the fence. Conversely, TVD-TOC indicates a smaller flow rate reduction for bounded flows than unbounded flows.

The partial-fence is expected to generate smaller velocity reductions than a fence
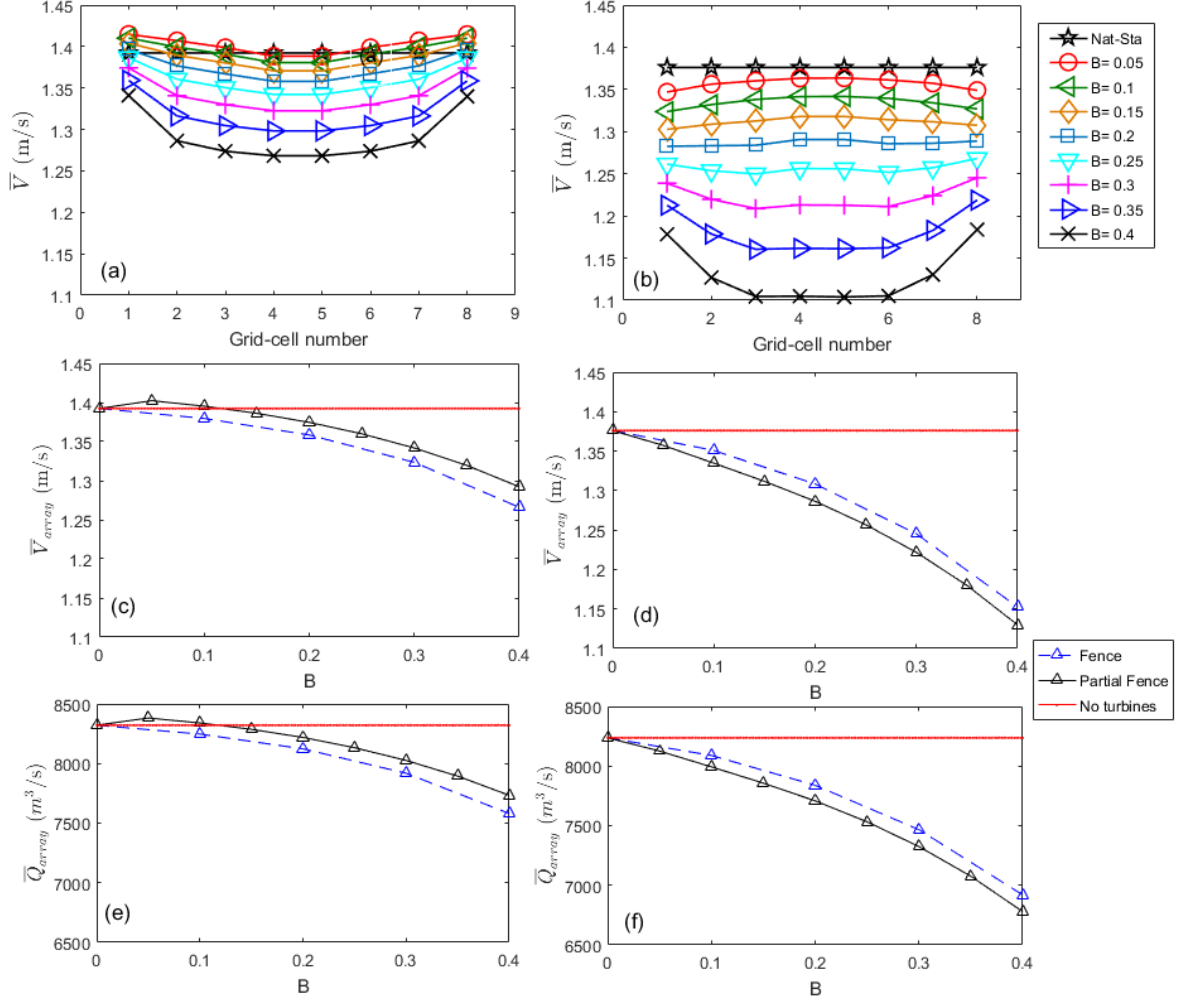
Fig. 6.15: Blockage ratio effect on a partial-fence upstream velocities, ADI-TOC (a), and TVD-TOC (b). Array-averaged for fence and partial-fence configurations obtained from ADI-TOC (c and e), and TVD-TOC (d and f).

with increasing blockage ratio. A larger thrust force would enhance flow diversion around the partial-fence, resulting in a smaller mass flux passing through the turbine array (Serhadlıoğlu *et al.*, 2013; Draper *et al.*, 2013a). Despite the fact that the ADI-TOC model has a tendency to under-estimate velocities reductions, the scheme shows smaller flow rate reductions for the partial-fence configuration as expected. Conversely,

TVD-TOC shows correct slightly larger velocities reductions with the partial-fence than the fence for $B \geq 0.6$ (Figure 6.16). This suggests that for large blockage ratios, the flow rate obtained by the scheme for the partial-fence is better computed.
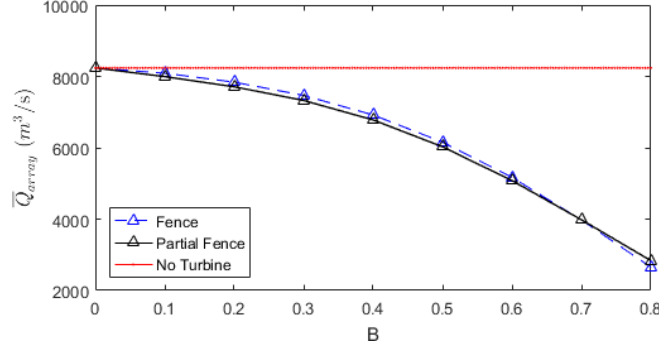
Fig. 6.16: Blockage ratio effect on flow rate obtained from TVD-TOC

The inaccuracy of TVD-TOC to report correct flow rates with the partial-fence for $B \leq 0.5$ could be related to the solution procedure used by the model, to compute the strong velocity spatial gradient generated near the partial-fence. The TVD-TOC scheme introduces non-linear artificial dissipation terms to prevent the creation of spurious numerical oscillations; features likely to be generated at regions with strong spatial gradients (Kvocka, 2015). Consequently, the slightly larger velocity reduction in the partial-fence reported by TVD-TOC could be related to an excess of artificial dissipation.

6.5.3 Head Drops Across a Partial-Fence and a Fence

Estimation of turbine-efficiency requires calculation of head drop across an array. This parameter was calculated for a partial-fence considering both the analytical and numerical solutions. As the TVD-TOC scheme simulates flow field velocities reductions and power extraction better than ADI-TOC for a fence scenario, the analytical solution was calculated with Fr, B, and C_T obtained from the TVD-TOC model simulations. Meanwhile, numerical solutions correspond to head drops obtained from depth

differences of the array upstream and downstream locations.

The head drop analytical solution obtained for increasing B was calculated for both fence (Figure 6.17(a)) and partial-fence configurations (Figure 6.17(b)). These scenarios were described in Table 6.7. In the case of the fence, the flow conditions produced by energy extraction with bounded flow scenario suggests that a single cell is representative of the head drop across an array, therefore, a single value from the middle of the fence is presented. The numerical solution of the head drop across the fence obtained from ADI-TOC and TVD-TOC are presented in Figure 6.17(a). It is found that increasing blockage ratios corresponds to larger head drops. In addition, it is observed that the ADI-TOC solution for a fence scenario is more consistent with the analytical solution than TVD-TOC. This result suggests that when power extraction is taken from bounded flows, where the dissipation effects are mainly due to the turbine-wake, the head drop can be estimated quite accurately with a SSF solution scheme.

In the case of a partial-fence, the energy extraction occurs along a limited section of the cross-channel, indicating that array-bypass flows could influence the properties of the flow at the edges of a partial-fence. However, the LMAD-OCH theory is a 1D theoretical model, which assumes symmetrical conditions in the flow (Houlsby *et al.*, 2008). Consequently, the head drop derived by the theory is uniform along the partial-fence. Additionally, the numerical implementation of the LMAD-OCH theory with the discontinous Galerkin model has also considered a uniform head drop along the partial-fence (Serhadlioglu, 2014).

The analytical solutions obtained for a partial-fence configuration are shown in Figure 6.17(b). It is shown that uniform solutions of the head drop are obtained along the partial-fence; additionally, the increasing of B leads to larger head drops. Note that the head drops reported for a partial-fence present larger magnitudes than the fence.

Conversely, simulations of a partial-fence performed with TVD-TOC (Figure 6.17(c))
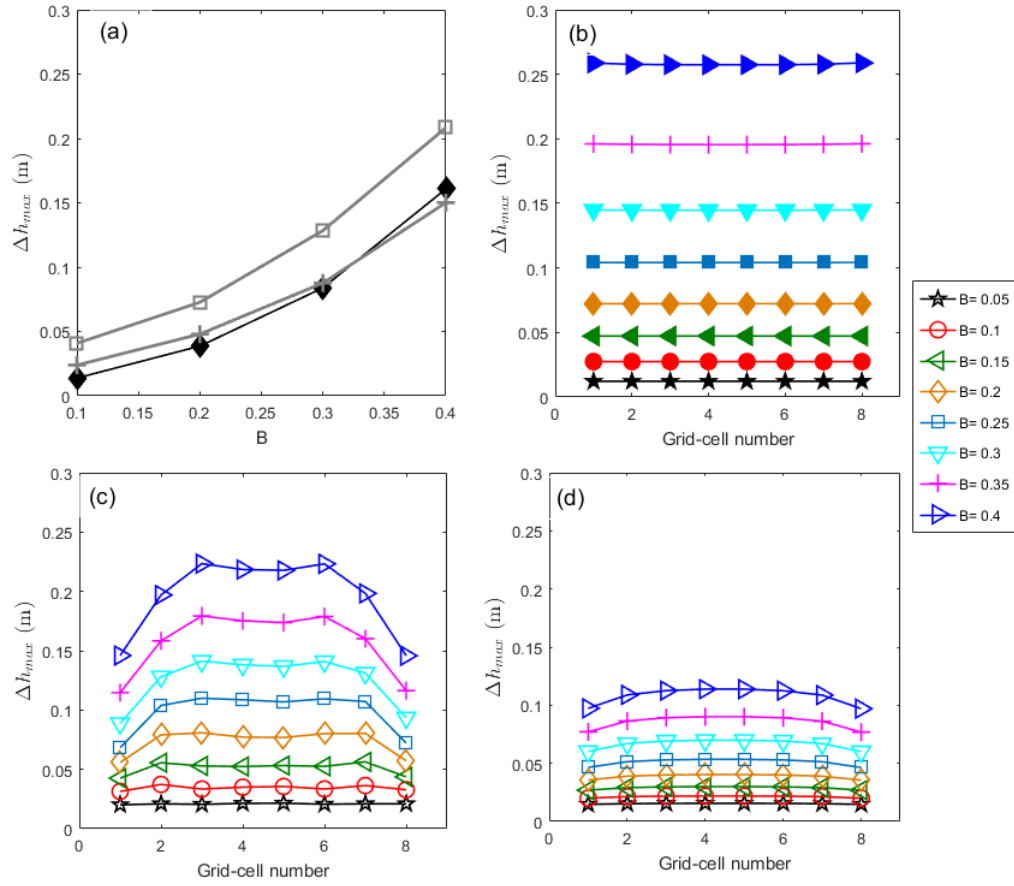
Fig. 6.17: Maximum head drops across a fence (a); analytical (filled makers) and numerical solutions ADI-TOC (x-marker) and TVD-TOC (square-marker). Maximum head drop across a partial-fence; analytical (b) and numerical solutions TVD-TOC (c) and ADI-TOC (d).

and ADI-TOC (Figure 6.17(d)) indicate non-uniform head drops along the turbine configuration for large B. The numerical solutions presented in the figure correspond to maximum head drop reported per grid cell. Within the partial-fence, maximum values of head drop are found in the middle cells, while smaller depth change are exhibited towards the edge of an array.

The comparison of the numerical solutions obtained from TVD-TOC and ADI-TOC for a partial-fence indicate that the TVD-TOC scheme simulates a head drop larger than ADI-TOC. The depth change across the middle-cells of the array obtained from
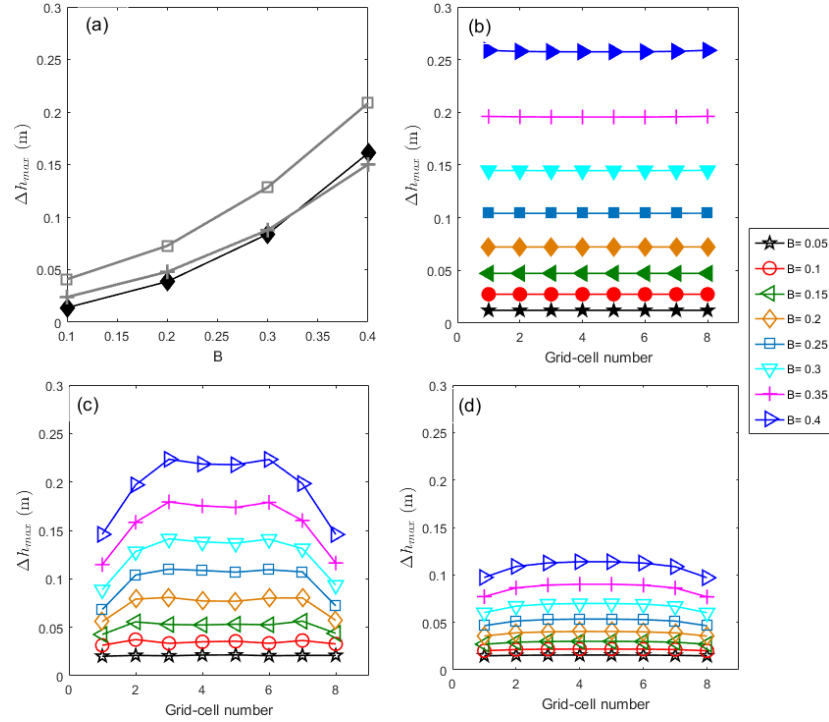
Fig. 6.18

TVD-TOC is closer to the analytical solution for small B. However, for $B \geq 0.30$, the magnitude of the head drop reported by TVD-TOC becomes smaller than the analytical solution.

Summarising, the consistency between the analytical and numerical solutions for the head drop across the fence indicates that the models correctly simulate head drops for bounded flow conditions. The ADI-TOC scheme presents a particularly good agreement. Conversely, the head drop across the partial-fence calculated with the models is non-uniform, as the analytical theory suggests. In the case of small blockage ratios, the head drop computed in the middle-cells with the TVD-TOC model is closer to the analytical solution than ADI-TOC is. Despite the similarity of the TVD-TOC numerical solution and the analytical solution, the agreement decreases for large B. The TVD-TOC model is able to provide reasonable insight into the effect of small blockage ratios on the head drop across the partial-fence. In addition, the results provide evidence of

171

the influence of the bypass flow on the head drop at the edges of a partial-fence.

6.5.4   Turbine Efficiency for a Partial-Fence

The calculation of head drop across a partial-fence allows estimation of turbine efficiency. The turbine efficiency is determined for increasing blockage ratios ($0 \leq B \leq 0.4$) and compared with results from the fence configuration. The initial parameters specification of the scenarios evaluated are presented in Table 6.7.

Analytical and numerical solutions of the turbine efficiency for flows characterised by small Froude numbers were calculated for a partial-fence. As the solutions were found to be consistent, only the numerical solutions are reported. These solutions are functions of the head drop obtained by both ADI-TOC and TVD-TOC. The turbine efficiencies calculated for a partial-fence and a fence turbine configuration are presented in Figures 6.19(a) and 6.19(b), respectively. The figures show the time-averaged and the array-averaged of the turbine efficiency obtained from ADI-TOC and TVD-TOC schemes for increasing B. These values were plotted against the time-averaged, array-averaged thrust coefficients.

The turbine efficiency obtained for a partial-fence (Figure 6.19(a)), suggests a gradual efficiency reduction with increasing blockage ratio and thrust coefficient. The maximum turbine efficiency found is $\overline{\eta}_{array} = 0.63$ for $B =0.05$ and $\overline{C_{T}}_{array} =1.0$; this value of efficiency reduces to $\overline{\eta}_{array} = 0.47$ for $B =0.4$ and $\overline{C_{T}}_{array} =3.5$. The reduction of turbine-efficiency with increasing blockage ratio is expected, as more energy is lost during turbine-wake mixing (Serhadlioglu, 2014).

The comparison of the ADI-TOC and TVD-TOC solutions for a partial-fence shows consistent results, although TVD-TOC presents slightly higher efficiency values. Furthermore, the comparison of the solutions obtained for a partial-fence against the fence configuration (Figure 6.19(b)) shows a high degree of similarity. Values of the turbine efficiency calculated for both configurations are presented in Table 6.8. The
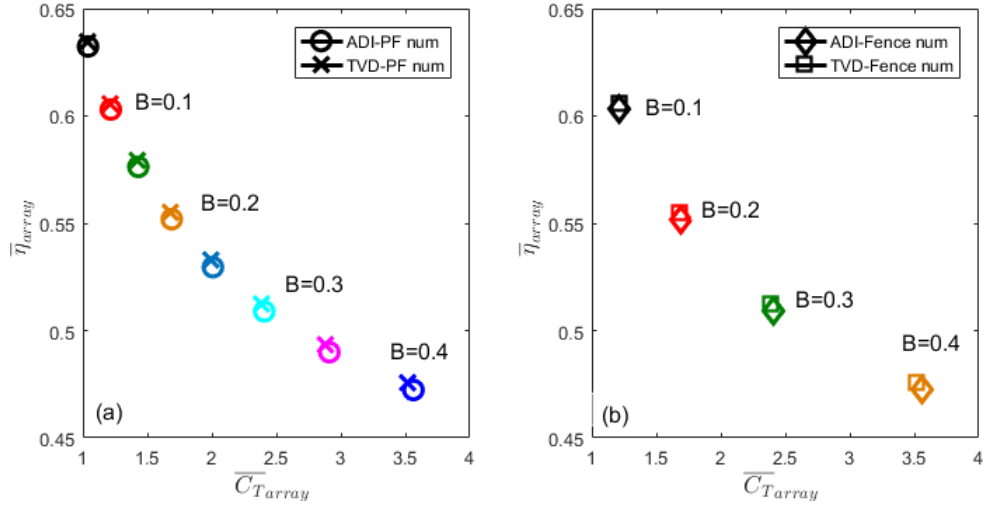
Fig. 6.19: Turbine efficiency and thrust coefficient for partial-fence (a) and fence (b) configurations obtained from ADI-TOC and TVD-TOC.

similar turbine efficiency results obtained from both configurations suggest that this partial-fence is long enough to resemble conditions similar to a fence in the near-field region. Nevertheless, it is worth mentioning that the turbine efficiency calculated for a partial-fence configuration does not capture the power dissipated by the array-wake mixing.

The LMAD-OCH theory is based on the assumption of steady flow, in the case of the partial fence, this consideration does not hold in tidal-streams. The LMAD-OCH theory assumes that the mixing of flow behind the devices takes place only within the turbine far-wake region (Nishino and Willden, 2013b). This is the region where the turbine-wake dissipates by turbulent mixing between the turbine-core flow and turbine-bypass flow (Nash and Phoenix, 2017). Therefore, LMAD-OCH theory is not suitable to provide information on the array-wake mixing region (Vogel et al., 2013).

	Turbine Efficiency			
B	Partial-Fence		Fence	
	ADI-TOC	TVD-TOC	ADI-TOC	TVD-TOC
0.1	0.6	0.61	0.6	0.61
0.2	0.55	0.56	0.55	0.56
0.3	0.51	0.51	0.51	0.51
0.4	0.47	0.48	0.47	0.48

Table 6.8: Numerical solution of time-averaged and array-averaged turbine efficiency for a partial-fence and a fence turbine array. Solutions obtained from TVD-TOC and ADI-TOC for increasing B.

6.5.5   Comparison between Fence and Partial-fence Configurations

To perform power analysis of a partial-fence the head drop across an array is required to calculate the total power extracted by the turbine. Additionally, turbine efficiency is used to estimated power availability P_* for electrical generation and power dissipation by turbine wake mixing.

To compare analytical solutions derived from the LMAD-OCH theory with numerical solutions obtained from TVD-TOC and ADI-TOC, the power metrics were calculated following two approaches. The first approach solves the metrics using the analytical solution of the head drop across an array. As the TVD-TOC scheme simulates head drop across a partial-fence better than ADI-TOC, the parameters required for solving the polynomial (Fr, B, and C_T) were obtained from the TVD-TOC model simulations. The second approach solves the metrics using the head drop obtained from both models. This corresponds to the water depth differences between the upstream and downstream location of the array. Additionally, to compare the performance of a partial-fence with a fence, numerical and analytical solutions of power metrics were obtained for both configurations.

The total power extracted estimated using the analytical and numerical calcula-

tions of the head drops are presented in Figure 6.20. The figures show the time-averaged and array-averaged P_T per grid cell for increasing blockage ratios. The analytical solutions for the fence and partial-fence configurations, (Figure 6.20(a)) are compared to the solutions obtained from TVD-TOC (Figure 6.20(b)) and ADI-TOC (Figure 6.20(c)).
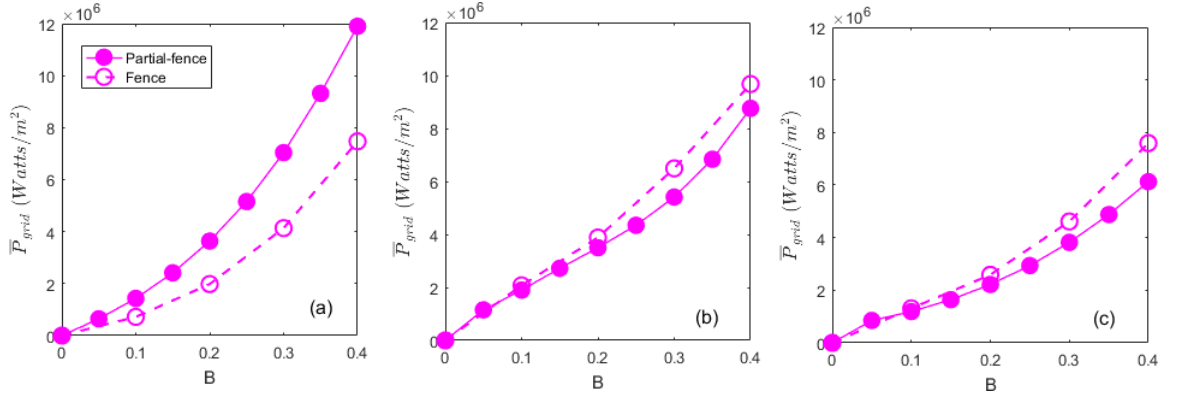
Fig. 6.20: P_T for a fence (dash-line) and partial-fence (continuous-line) scenario. Analytical solutions (a), and solutions from TVD-TOC (b) and ADI-TOC (c).

The analytical solution of the total power extracted predicts increasing of P_T with increasing blockage ratio. In addition, the solution for a partial-fence configuration presents higher magnitudes than the fence configuration. However, the numerical solutions reports the opposite i.e. smaller magnitudes of P_T were found for partial-fence configurations. As P_T is a function of the head drop, its magnitude depends on the analytical and numerical head drop (Δh) obtained in Section 6.5.3.

Regarding a partial-fence, it was found that the analytical solutions of the head drop for increasing B were larger than the fence configuration. However, the numerical solutions of Δh for a partial-fence reported by the models were smaller than the fence. This occurred because the partial-fence presented reduced head-drops at the edges of the array. Therefore, the P_T solutions reported for a partial-fence by Figure 6.20 are consistent with the Δh solutions found. Note that the partial-fence analytical solutions omit the head drop reduction at the partial-fence edges and present larger

head drops than the analytical scenario reported for a fence. These features contribute to the large differences presented between the analytical and numerical solutions of the partial-fence.

Regarding the fence configuration, the head drop obtained from the models were consistent with the analytical solution; but, the TVD-TOC scheme tended to overestimate the Δh (Section 6.5.3). These trends are evident in the P_T solutions reported for the fence. Therefore, the ADI-TOC solution is consistent with the analytical solution of P_T for the fence configuration, but the TVD-TOC tends to overestimate it.

Summarising, the P_T solution comparison of the models suggest that ADI-TOC solves the total power extracted for the fence configuration better than TVD-TOC. However, the TVD-TOC solution for P_T of a partial-fence is closer to the analytical solution, suggesting that this scheme provides a more accurate P_T solution for a partial-fence than ADI-TOC.

The power available for electricity generation calculated with the analytical and numerical calculation of the head drop are presented in Figure 6.21. The time-averaged and array-averaged of P_* for increasing blockage ratios are reported. The analytical solutions for the fence and partial-fence configuration (Figure 6.21(a)) are compared to the solution obtained from TVD-TOC (Figure 6.21(b)) and ADI-TOC (Figure 6.21(c)).

The analytical solutions of P_* generate higher magnitudes for a partial-fence than the fence configuration. Meanwhile the numerical solution shows higher P_* for the fence configuration. The metric P_* depends on the turbine-efficiency (η) and the head drop. As the η solutions obtained with the models are similar, the head drop across an array explains the P_* solutions.

In terms of a fence configuration, the available power found with ADI-TOC is closer to the analytical solution; because the Δh numerical solution of ADI-TOC is consistent with the fence Δh analytical solution. Conversely, P_* obtained from TVD-TOC
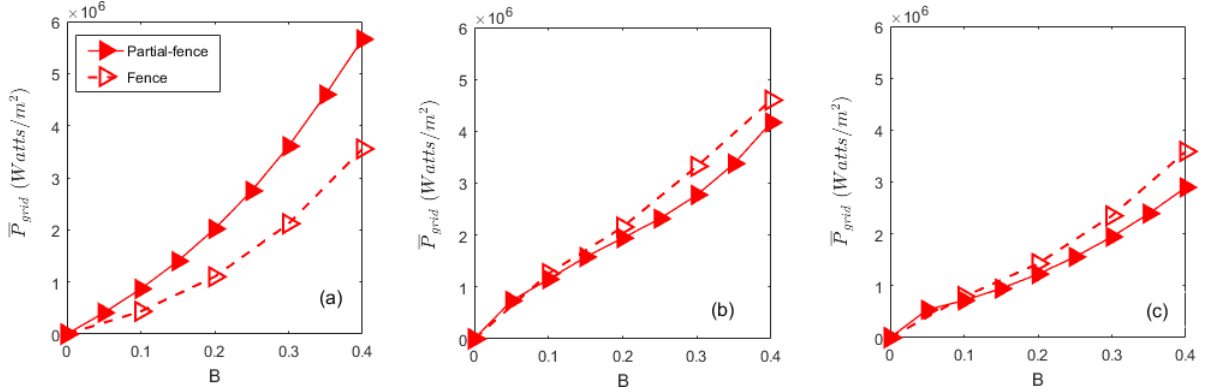
Fig. 6.21: Power removed by the turbine in terms of the efficiency P_* for a fence (dash-line) and partial-fence (continuous-line) scenario. Analytical solutions (a), and solutions from TVD-TOC (b) and ADI-TOC (c).

is closer to the analytical solution reported for a partial-fence. However, TVD-TOC underestimates the analytical solution of P_* because the numerical solution generated by the model for the head drop also underestimates the analytical head drop obtained for a partial-fence.

Power P removed by the turbines in terms of cubic velocity is shown in Figure 6.22. The time-averaged and array-averaged of P for increasing blockage ratios are presented. Solutions for a fence and partial-fence configuration were obtained from TVD-TOC (Figure 6.22(a)) and ADI-TOC (Figure 6.22(b)).

The solutions of P shows slightly higher magnitudes for the fence than partial-fence configuration. TVD-TOC shows a similar trend, but ADI-TOC generates slightly larger magnitudes of P for a partial-fence. Nevertheless, P presents similar magnitudes for the fence and partial-fence turbine configuration. This consistency suggests that for the range $0 \leq B \leq 0.4$, the upstream velocity is not strongly influence by the two turbine configurations evaluated, when a common wake induction factor is used ($\alpha_4 = 1/3$). Recall, similar consistency in velocities between both configurations was found in Sections 6.5.2 and 6.4.2.
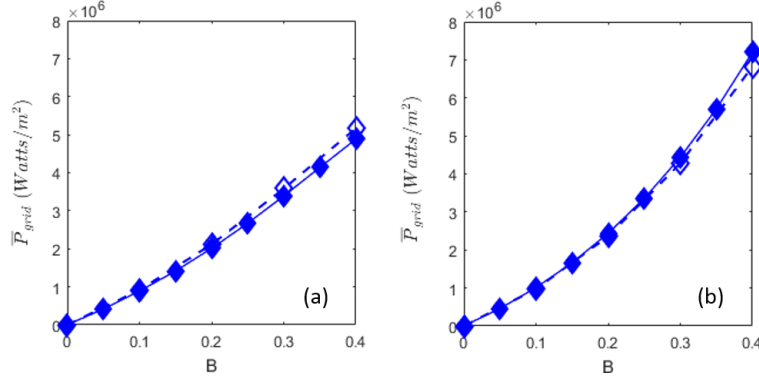
Fig. 6.22: Power removed by the turbine P for a fence (dash-line) and partial-fence (continuous-line) scenario. Solutions from TVD-TOC (a) and ADI-TOC (b).

A comparison of P values obtained from the models indicates that TVD-TOC presents smaller magnitudes than ADI-TOC. As P depends on the cube of the stream velocity and since ADI-TOC under predicts the velocity reductions, larger magnitudes of P are generated by the ADI-TOC scheme.

Power dissipated by turbine wake mixing P_W is presented in Figure 6.23. The time-averaged and array-averaged of P_W for increasing blockage ratios is presented. The analytical solutions for the fence and partial-fence configurations (Figure 6.23(a)) are compared with the solutions from TVD-TOC (Figure 6.23(b)) and ADI-TOC (Figure 6.23(c)).

The analytical solutions of P_W shows higher magnitudes for a partial-fence than a fence configuration. However, the numerical solutions indicates slightly larger magnitudes for the fence. P_W depends on the turbine efficiency and the total power extracted, which in turn is strongly dependent on the head drop across an array. This dependency indicates that P_W solutions are explained by head drop values.
The comparison of P_W computed by the models indicates that TVD-TOC presents larger magnitudes than ADI-TOC. However, the ADI-TOC P_W solution for the fence configuration is more consistent with the P_W analytical solution. In the case of a
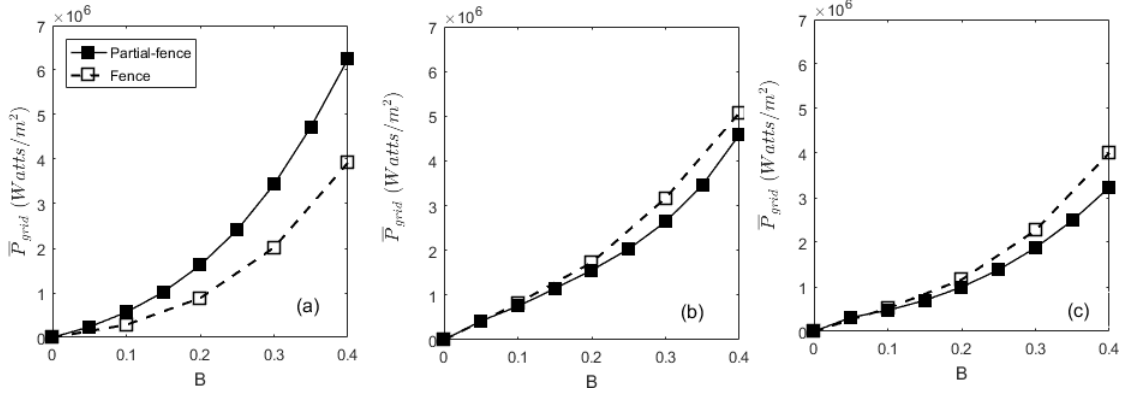
Fig. 6.23: Power dissipated per turbine-wake P_W for a fence (dash-line) and partial-fence (continuous-line) scenario. Analytical solutions (a), and solutions from TVD-TOC (b) and ADI-TOC (c).

partial-fence, TVD-TOC generates P_W values closer to the analytical solution.

Summarising, a power analysis was performed for two scenarios: a fence and a partial-fence turbine configurations. The analysis compared analytical solutions of the metrics: P_T, P, P_*, and P_W with numerical solutions obtained from TVD-TOC and ADI-TOC.

6.6   Summary and Discussion

6.6.1   Summary

In this chapter, two methodologies used to estimate power potential of a channel are compared. The array of turbines considered consist of a single row that fully covers the cross section of a channel for a fence. This fence configuration was deployed in the middle of a channel which connects two large basins. The effect of a set of increasing blockage ratios ($0 < B \leq 0.8$) was investigated on various parameters. The first methodology (C-CTE) refers to the use of plausible constant values of the thrust and power coefficient; this was the original methodology used to perform tidal assessment. The second methodology (C-TOC) corresponds to the methodology developed in this

thesis. This approach uses LMAD-OCH to relate operating conditions of the turbine (blockage ratio and wake induction factor) to perturbations in water depth and velocity produced by tidal-energy extraction. These perturbations are considered to occur within the turbine near-field. The C-TOC methodology enables the calculation of thrust coefficients as a function of turbine bypass factor (β_4) and wake induction factor (α_4); also this allows the calculation of power coefficients as a function of turbine velocity coefficient, (α_2). These methodologies were tested in both ADI-TOC and TVD-TOC numerical models.

Also in this chapter, a methodology developed in this thesis was used to study the performance of a long partial-fence turbine array. The partial-fence configuration required the definition of local-, array- and global-blockage ratios. The values used in the simulations were within the scope of scenarios being studied with models that solve RVF and with 3D simulations. Far-field hydrodynamic effects produced by power extraction were then evaluated. This was achieved by analysing the impacts of wake induction factors, and the effects of blockage ratio increases on two turbine configurations: a fence and a partial-fence.

Finally, the analysis was restricted to realistic blockage ratios ($0 < B \leq 0.4$). The optimum wake induction factor for a partial-fence configuration was identified. Then influences of fence and partial-fence configurations on upstream velocities, head drops across the array, and turbine-efficiencies were evaluated. A power analysis was performed with ADI-TOC and TVD-TOC models. This consisted of calculating and comparing metrics for both turbine configurations: total power extracted, power removed in terms of the efficiency, power dissipated by turbine wake mixing, and power removed by the turbine. These metrics were calculated with both analytical and numerical solutions of head drops.

6.6.2 Discussion and Conclusion

The numerical implementation of the LMAD-OCH theory provides a broader picture of the tidal resource than the use of constant values of thrust and power coefficients. The inclusion of turbine operating conditions in analysis of the turbine near-field flow region enables the parametrisation of changes due to power extraction at turbine-scale level. Consequently, it is possible to estimate turbine efficiencies, which in turn allows the definition of the total power extracted, the available power for electricity generation, and the power dissipated by wake mixing. In addition, for a fence configuration performed for conditions of optimal power extraction ($\alpha_4 = 1/3$), the testing of increasing values of blockage ratios indicates that TVD-TOC and ADI-TOC schemes report consistent values of available power P_*. However, the other metrics of the power analysis (P, P_T, and P_W) are better simulated by the shock-capturing model because the ADI-TOC scheme underestimates the velocity reduction produced by power extraction.

The performance of a partial-fence was studied using the methodology developed in this thesis. By introducing numerically energy captured by a turbine as a sink term in the momentum equations, it was possible to simulate the elevation and velocity discontinuities produced by the energy extraction along the partial-fence. The simulation of this configuration did not present spurious solutions at the turbine array edges. The implementation of a momentum sink term method enabled the specification of grid-cells, where the momentum was extracted without disturbing the solution of the flow surrounding. Additionally, the method developed in this thesis related directly to elevation and velocity discontinuities computed due to the turbines thrust force.

To examine and quantify the disturbance caused by turbine arrays to the local hydrodynamics, this thesis considered changes in the M_2 tidal constituent. Hydrodynamic changes produced by the testing of increasing values of wake induction factor has not been previously reported in the literature. However, the analytical solutions obtained for the power coefficient and the turbine-efficiency as a function of α_4 (presented

in Section 5.2.2 and reported by (Draper, 2011)), indicate that the flow behaviour reported is reasonable. The effect of the fence and partial-fence turbine configuration on the velocity and elevation are intensified with increasing values of B. In the case of a partial-fence new features arise these are: array-bypass flow and array-wake mixing; these have an impact on the downstream flow regime.

Performance evaluations of the fence and partial-fence turbine configurations, for realistic blockage ratios ($0 < B \leq 0.4$), for close to optimal power extraction conditions ($\alpha_4 = 1/3$) were carried out and compared. It was found that ADI-TOC and TVD-TOC simulate head drop across a fence correctly, and the ADI-TOC scheme presents a particularly good agreement. In the case of the partial-fence, it was found that the flow conditions along the partial-fence are non-uniform, contrary to the partial-fence specifications tested with the line momentum sink method (Serhadlioglu, 2014). The non uniformity is evident in the array upstream velocity ($\overline{V}$), and water elevation change across an array (Δh_{max}). The ADI-TOC and TVD-TOC models report that at the partial-fence middle cells, the head drop tends to behave as the fence configuration but, towards the edges Δh was influenced by the bypass flow and presented a reduced magnitude. The head drop across the partial-fence is better simulated by the TVD-TOC scheme. A consistent behaviour with the head drop was found for the upstream velocity along the fence, for $B > 0.25$, the models report a smaller velocity decrease towards the edges of a partial-fence. Velocity reductions at the outermost turbine location are expected (Draper, 2011) and have been reported in 3D RANS simulations (Nishino and Willden, 2013b).

The non-uniform conditions of the flow at the partial-fence indicate the existence of locations where extractable power will be larger within the array. A similar situation is reported for a partial-fence deployed near a headland (Draper *et al.*, 2013a), where more power was removed from the southern end (or the northern end), depending on whether the blockage ratio led to prior maximum extraction (or beyond the maximum

power extraction).

In terms of flow rates, a partial-fence simulated with ADI-TOC shows smaller velocities reductions than the fence with a larger B. This result is expected because the thrust force would intensify flow diversion around the fence, resulting in smaller mass flux passing through the turbine array (Serhadlıoğlu *et al.*, 2013; Draper *et al.*, 2013a). Conversely, TVD-TOC presents a slightly larger flow rate reduction for a partial-fence for $B \leq 0.6$, possibly as a side effect of the total variation diminishing scheme implementation.

Finally, a power analysis of the fence and partial-fence configurations was performed. The turbines within the arrays are considered to perform at conditions close to optimum power extraction. In the case of the fence configuration, the total power extracted, available power (P_*), and dissipated power are correctly solved by the two schemes. ADI-TOC generates better results in this analysis. The better performance of ADI-TOC for the fence scenario is due to the fact that ADI-TOC correctly solves the head drop across the fence, and the calculation of the metrics: P_T, P_*, and P_W rely on the head drop estimation.

In the case of a partial-fence, the total power extracted, available power and dissipated power are more satisfactorily solved by the TVD-TOC scheme. This is because the head drop across this array is more accurately solved by TVD-TOC. However, TVD-TOC tends to underestimate these metrics because Δh simulated in the partial-fence presents a significant reduction towards the edges of the array.

Regarding power removed by the turbine, P, this metric is more accurately solved by TVD-TOC for the two configurations evaluated. Conversely, ADI-TOC overestimated P because this scheme under-represents the velocity reduction produced by power extraction.

The similar results in η, C_P, and C_T obtained from both ADI-TOC and TVD-TOC for both configurations suggests that the partial-fence length is large enough

to resemble conditions similar of a fence in the near-field region. In addition, the solution consistency of η, C_P and C_T is somewhat expected as both configurations perform resource assessment as functions of turbine near-field or turbine-scale solutions. Consequently, the power extraction and resultant power dissipation by turbine-wake mixing are restricted to the near-field region.

To provide a context to the solutions obtained from ADI-TOC and TVD-TOC, the C_P and C_T solutions obtained from the models for increasing values of $0 < \alpha_4 < 1.0$ are compared with the most updated and accepted analytical models to study partial-fences: (i) LMAD-OCH and (ii) Two-scale. The C_P and C_T solutions obtained from ADI-TOC and TVD-TOC schemes for fence and partial-fence are presented in Figure 6.24. The fence presents a $B = 0.2$; the partial-fence additionally presents $Ba_{grid} = 0.4$ and $Bg_{grid} = 0.08$, for both configurations $F_r = 0.11$ was considered. The figure illustrates consistent solutions for fence and partial-fence configurations; additionally, it shows consistency between the numerical solutions and LMAD-OCH theory (Houlsby et al., 2008). A significant research object has been achieved: to improve a numerical approach to perform tidal resource assessment by incorporating relationships between turbine operating conditions, and the changes within the turbine near-field region, in the energy capture calculation.

It is worth noticing that LMAD-OCH analytical solutions are larger than C_T and C_P values obtained from the Two-scale analytical model (Nishino and Willden, 2012b). A two-scale approach has recently become the accepted theoretical model to describe power extraction from unbounded flows (Adcock et al., 2015). This model addresses the partial-fence scenario as the coupling of the turbine- and array-scale in a flow with a rigid lid (Figure 6.24). The Nishino and Willden (2012b) solution generates smaller magnitudes of power and thrust coefficient than LMAD-OCH theory, due to the additional consideration of array-wake mixing in a two-scale approach. Houlsby et al. (2008) on the other hand, considers only the turbine-downstream mixing, which is not
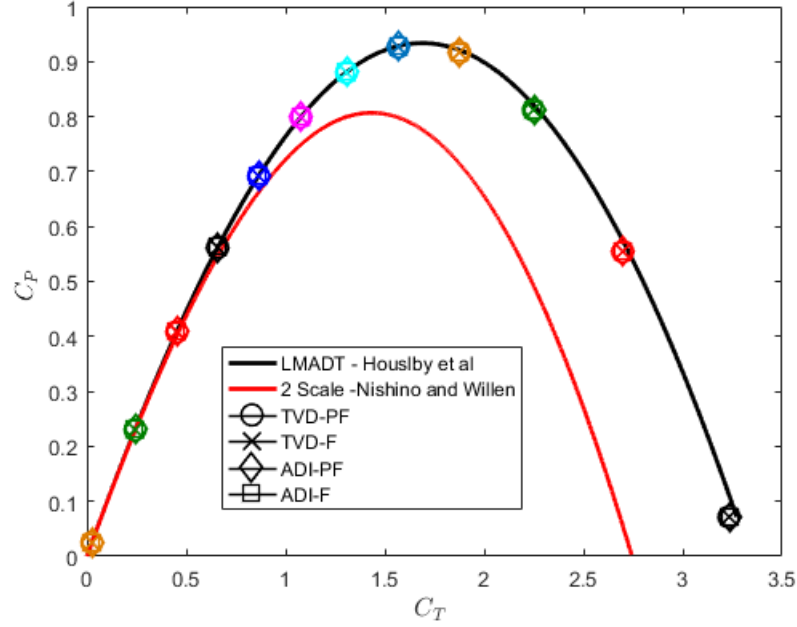
Fig. 6.24: Solutions for fence and partial-fence obtained from TVD-TOC and ADI-TOC. Partial-fence analytical solutions from LMAD-OCH and Two-scale models.

very significant in comparison to the array-wake (Nishino and Willden, 2012b). The two-scale theory introduces the scale separation of the array and turbine-scale to study the unbounded flow. In this way, it is possible to account for flow diversion at the level of individual turbines and around partial-fences (Nishino and Willden, 2012b). This approach provides a deeper understanding of the fundamental flow mechanism involved in the interaction of the flow passing (and bypassing) the turbines, with the flow passing (and bypassing) the array. In addition, the two-scale approximation accounts for the effect of both the local and global blockage ratio of the array. In the case of the rigid lid surface, Nishino and Willden (2012b) report that for optimal turbine spacing conditions, the maximum power coefficient in a single-row of turbines is C_P=0.789 (presented in the Figure 6.24); higher than the Lanchester-Betz limit (0.593). However, attempts to numerically couple the turbine-scale with the array-scale are limited to simulations of turbine arrays (Nishino and Willden, 2013a), which require high- fidelity

turbine scale simulations i.e. this methodology has not been applied to regional scale (Adcock *et al.*, 2015).

The two-scale analytical model was extended to include the effect of the free-surface deformation (Vogel *et al.*, 2016). The changes in the free-surface across an array due to power extraction, evident in the head drop, are intensified with the increase of the flow's Froude number (Draper, 2011). Vogel *et al.* (2016) analysed the variation of the Froude number in an infinitely wide channel, and reported an increase of the maximum power coefficient with the increase of Fr, beyond the rigid-lid estimation. In the particular case of a local blockage ratio $B_L = 0.4$, the consideration of free-surface deformation indicates a maximum power coefficient $C_P = 0.888$, which corresponds to a 10% increased with respect to the rigid-lid approach. However, this model has only been applied theoretically.

Chapter 7

Conclusions and Recommendations

7.1   Introduction

This research implemented the LMAD-OCH theory (Houlsby *et al.*, 2008), in two complex hydrodynamic models that can solve real-world problems to simulate marine turbine configurations and to perform tidal-stream resource assessment.

A method to represent turbine array energy captured by the line momentum sink derived by Draper *et al.* (2010) and Draper (2011) was adapted. This method, referred to as momentum sink-TOC, combines the momentum sink approach developed by Ahmadian *et al.* (2012a), O'Brien (2013), and Fallon *et al.* (2014) with parametrisation of changes produced by power extraction at the turbine near-field region developed by Houlsby *et al.* (2008). The marine turbine representation adapted in this research was used to develop two numerical schemes to simulate turbine array power extraction: a scheme that solves SSF (ADI-TOC) and a scheme that solves RVF (TVD-TOC). The momentum sink-TOC method and the numerical schemes developed were evaluated in an idealized turbine array, and good agreement was found between the numerical predictions and accepted analytical values in a benchmark comparison. Finally, the momentum sink-TOC method and the procedure proposed to assess the resource were

implemented in realistic turbine configuration.

7.2 Summary

The main achievements from this thesis can be categorised into four sections: (i) marine turbine numerical representation, (ii) numerical models developments, (iii) turbine near-field simulations, and (iv) development of tidal-stream resource assessment methodology.

7.2.1 Marine Turbine Numerical Representation

The momentum sink-TOC method was developed in this thesis to numerically simulate energy capture by arrays of marine turbines. This method facilitates the analysis of the far-field effects of power extraction. Calculation of momentum extracted by arrays was incorporated into models as a sink term in the momentum equations of SSF (Equations 3.4 and 3.5), and RVF (Equations 3.14 and 3.13). Momentum sink is included as a function of velocity normal to turbine-array, and inter-turbine spacing of turbines within a grid-cell (Ahmadian and Falconer, 2012; Fallon, 2012; O'Brien, 2013). Furthermore, momentum sink accounts for perturbations in water depth and velocity across a tidal turbine array by including turbine operating conditions in thrust coefficient calculations. The relationship between the momentum sink within shallow water and the physical characteristics of turbines were derived by Houlsby *et al.* (2008). Simulating the perturbation in water depths and velocities across an array using a sink term flow was modelled without constraints on water depth. Flow perturbations across an array are directly associated with momentum loss without the need to set constraints between upstream and downstream conditions as implemented in previous models (Draper *et al.*, 2010; Draper, 2011). The novel numerical representation of the effect of a turbine array on the momentum equation developed in this thesis differs

from previous research for tidal resource assessment by: (i) incorporating the natural constraints of tidal-streams in coastal areas, (ii) including turbine operating conditions into energy capture processes, (iii) considering the turbine near-field changes produced in flows due to power extraction, and (iv) implementing an unconstrained free-surface.

7.2.2 Numerical Models Developments

Energy capture due to marine turbines was introduced as a sink term into the momentum equations. The solution of two systems of governing equations has been approximated numerically. The simulation of SSF required the solution of the two-dimensional shallow water equations (Section 3.3.1); the computation of RVF used the conservative form of the equations (Section 3.3.2). The model ADI-TOC, simulates SSF, which is characterised by low Froude numbers. The model TVD-TOC, solves RVF and consequently can simulate strong gradients of flow.

Energy captured by turbine arrays produces perturbations in water depths and velocities of the flow. Simulation of momentum extracted using the momentum sink-TOC method in finite-difference models has the advantage of computing turbine configurations which partially covers the flow without requiring the specification of additional conditions at the edges of a partial-fence. This is possible because ADI-TOC and TVD-TOC do not present numerical singularities at these locations of an array.

The TVD-TOC scheme is a shock-capturing model that consists of the algebraic combination of first-order and second-order upwind schemes. In regions where strong gradients of flow exist and spurious numerical solutions are likely to appear, the model uses a lower-order scheme to simulate the flow. The use of the TVD-TOC scheme to represent marine turbines with the momentum sink-TOC method constitutes an efficient approach for simulating energy capture in RVF. This is because the TVD-TOC scheme is not required to solve the Riemann problem at each grid where an array of turbines are defined in order to compute the discontinuities produced in the flow due

to power removal. Solving the Riemann problem represents an expensive procedure in computational terms (Shyue, 1998).

TVD-TOC and ADI-TOC schemes are capable of solving perturbations in depths and velocities produced in the flow by array power extraction. Water elevation changes across a fence are well represented by these models i.e increasing blockage ratios are linked to increasing head drops. For fence configurations, the head drop is more accurately represented by the ADI-TOC scheme; meanwhile, for the partial-fence configuration, the head drop is better represented by the TVD-TOC scheme. For both turbine configurations, satisfactory head drops are obtained with the TVD-TOC scheme. This suggests that strong spatial water depth gradients due to energy capture are better solved by the shock-capturing capability.

Another advantage of the ADI-TOC and TVD-TOC schemes reported here is the ability to incorporate the flooding and drying processes into the study. This feature is particularly important for the assessment of more complex, real-world sites, such as estuaries where mudflats can represent a significant percentage of the region.

7.2.3   Turbine Near-Field Simulations

Tidal-stream power extraction considering two turbine configurations were investigated; the first covers completely the cross-section of the channel, a fence; while the second one covers partially the flow, a partial-fence.

In terms of turbine operating conditions, it was shown that an increase in blockage ratio led to a maximum power extraction, after which further increase in B results in smaller power extraction due to the flow choking. The increase of the blockage results in an increase in the thrust force applied to the tidal-stream. As a result, large blockage ratios intensify magnitudes of flow bypassing turbines and reduces the amount of power extracted by the turbines.

The wake induction factor also plays an important role in determining available power

for electrical energy generation. Low wake induction factor indicates high downstream turbine-wake mixing and, consequently, high power loss. On the other hand, a high wake induction factor suggests minimal power extraction. The use of an optimum wake velocity coefficient and a high blockage ratio generates higher power extraction from the stream. In addition, the use of an optimum wake velocity coefficient generates solutions that fall into the subcritical bypass flow. In this way, the bypass factor (from the β_4 quartic polynomial) corresponds to a physically admissible solution.

In the case of partial-fences, the momentum sink-TOC method is used to determine energy capture by turbines due to partial-fences at the near-field scale. This configuration represented the simulation of an unbounded flow. And it is characterised by an array-wake behind the partial-fence, which eventually mixes with the array-bypass tidal-stream. Flow conditions along the partial fence are not uniform as array-bypass flows tend to influence the upstream velocity and water depth at the edges of the array.

The two turbine configurations analysed showed consistent efficiency, power- and thrust-coefficients. The similarity of the results is explained by the use of the same wake-induction factor and the similar upstream conditions in the channel for both configurations.

Regarding turbulence simulation, the use of the LMAD-OCH theory enabled the parametrisation of the turbine-wake mixing within the near-field region. Over the near-field length scale, it is assumed that elevation and velocity perturbations occur. Consequently, flow passing through the fence and partial-fence mixes to and from a smooth vertical profile similar to upstream profiles (Houlsby *et al.*, 2008). This assumption captures vertical flow variations produced by horizontal mixing effects (Adcock *et al.*, 2015). Additionally, the turbulence induced by the bottom friction approach and inviscid flow assumption used in the models to simulate energy dissipation by the turbine-wake mixing correctly represent turbine turbulent mixing (Nishino and Willden, 2012a).

191

7.2.4 Development of Tidal-Stream Resource Assessment Methodology

This thesis assesses upper limits for tidal-stream resource assessment in a semi-narrow tidal channel. The upper limit considered only the M_2 tidal constituent. Resource evaluation additionally allowed the identification of the numerical scheme that performs more accurate, and computationally more affordable, tidal-stream resource assessments.

The power extraction of the available energy resource is evaluated as a post-processing step of the simulation. Simulation of marine turbine power extraction considers the characteristics and arrangement of turbines within a row in the computation of energy captured by turbines. This method directly relates depth and velocity discontinuities produced by turbine power extraction to the computed thrust forces. Contrary to Draper (2011), the head drop across the array used for the tidal-stream resource assessment was obtained from the depth difference between the array upstream and downstream location, which was computed by the newly extended models.

LMAD-OCH theory with a deformable surface and downstream mixing enable the calculation of the turbine efficiency (Houlsby *et al.*, 2008). This parameter indicates the fraction of the total extracted power removed by turbines, which is available for electricity generation. Note that this parameter does not account for power lost by array-wake mixing dissipation. The measure of turbine efficiency provides a distinction between total power extracted, power available for electrical energy generation, and power dissipated by turbine-wake mixing.

This research proposed two numerical models to perform tidal-stream power resource assessment. The assessment identified available power for electricity generation in terms of turbine-efficiency (P_*) and cubic velocity (P), dissipated power by turbine wake mixing, and total power extracted. An initial tidal-stream resource pre-assessment can be performed with the model that simulates SSF: ADI-TOC. This

scheme is computationally cheaper than TVD-TOC scheme, and provides a maximum upper limit to the power extraction. On the other hand, a more accurate assessment and estimation of the upper limit of the power extraction requires the TVD-TOC model. This scheme is able to solve unbounded flows which experience strong spatial gradients, such as the depth and velocity perturbations produced by turbine power extraction.

The methodology proposed in this thesis to simulate marine turbines and assess the tidal-stream resource constitute a strategy that (i) does not constraint the free-surface, and (ii) enables power metrics computations across partial-fences. Considering these properties allows for the analysis of realistic turbine arrangement scenarios.

7.3 Conclusions

The main conclusions and novel developments arising from the research in this thesis are as follows:

- A novel method of representing marine turbines (sink-TOC) was developed. The method used the operating conditions of the turbine, described by the blockage ratio and wake velocity coefficient, in the calculation of energy capture by turbines. Significantly, this method does not constrain the water depth.

- An alternative and computationally less expensive approach to simulate the sharp gradients in water depth and velocity due to power extraction in a rapidly varying flow scheme was developed. The developed approach is a shock-capturing method that combines MacCormack and TVD schemes.

- Depth perturbations due to power extraction were solved by both models ADI-TOC and TVD-TOC. Head drops across a fence are correctly solved by ADI-TOC. Meanwhile, the head drops across a partial-fence are satisfactorily solved

by TVD-TOC. A satisfactory head drop was obtained with TVD-TOC scheme for both configurations, indicating that water depth gradients are better solved by the shock-capturing capability.

- The total power extracted, available power P_*, and dissipated power are correctly approximated by the both ADI-TOC and TVD-TOC schemes. For a tidal fence, model metrics are better computed by the scheme that solves slow and smooth flows, because the head drop across the array simulated by this scheme is more accurate. In the case of the partial-fence, the total power extracted, available power P_*, and dissipated power are better solved by solving a rapidly varying flow solution.

- For unbounded flows, the head drop is better simulated by the RVF scheme. Additionally, at the edges of the partial-fence it is found that array-bypass flows influence upstream conditions of flow passing through an array. In terms of power removed by turbines P, this metric is better solved by an RVF solver as this model correctly represent the flow velocity reduction produced by power extraction.

- Simulation of unbounded flows scenario with sink-TOC method and RVF solver indicate non-uniform conditions along the partial-fence, contrary to one-dimensional LMAD-OCH. This is a relevant contribution of using TVD-TOC to evaluate the resource.

- Comparison of the computational requirements of ADI-TOC and TVD-TOC indicates that TVD-TOC model requires higher computational cost than ADI-TOC independent of the domain-size, and whether an energy extraction procedure is incorporated or omitted.

- The developments in this research more completely resolve hydrodynamic calculations within models that can simulate the real-world environment such as

estuaries, sites where mudflats can represent a significant percentage of the region.

- Resource evaluations performed with both ADI-TOC and TVD-TOC indicate the possibility of omitting shock-capturing capability for initial evaluation of the site. Simpler ADI-TOC type schemes may be used. This is an important finding for preliminary investigating site tidal energy assessments.

7.4   Future Research

7.4.1   Potential Turbines Configurations

The research presented in this thesis can be extended from arrays of turbines deployed as a row (fence or semi-fence) to complex configurations such as farms; taking advantage of larger areas. Potential configurations are double rows of turbines with aligned or staggered arrangements (Adcock *et al.*, 2015). Investigations regarding turbine-array optimal distribution in the farm-layout field indicate that long rows are more efficient than two rows with staggered distribution (Serhadlıoğlu *et al.*, 2013; Draper and Nishino, 2013). However, other researchers show rows with staggered distributions overperform devices allocated in series (Nash *et al.*, 2015; Phoenix, 2017). In addition, the location for the deployment can be selected base on the undisturbed kinetic energy flux (Serhadlıoğlu *et al.*, 2013; Draper *et al.*, 2013a). A more accurate approach for performing this task is the analysis of the velocity ellipse parameters of the tidal currents to determine the primary direction of the tidal current (Phoenix, 2017).

7.4.2 Irish Sites Assessment

The methodology developed in this research could be used to asses an upper limit for the tidal-stream resource assessment of different Irish sites. Locations with viable energy resources are: the North East Coast, the Tuskar Rock and Carnsore Point, the Shannon Estuary, the Strangford lough, and the Ram Race Copeland islands (SEI, 2006; O'Rourke *et al.*, 2010).

Assessment of these locations would provide information about the role of the geometry of the sites, optimum location of the turbine arrays in farm layouts, turbine operating conditions, and also about how energy capture affects tidal systems hydrodynamics.

7.4.3 Viscous Terms

A further recommendation is the inclusion of viscous terms in the governing equations solved by the models. Viscous terms consideration enables (i) studying the influence of boundaries in the flow (Harlow and Welch, 1965) and (ii) analysis of viscous mixing effects in the array-scale wake (Vogel *et al.*, 2013). ADI-TOC model allows the consideration of viscous terms; however, TVD-TOC requires their incorporation.

7.4.4 Two-scale Approach for Partial Fence

In the case of scenarios where the flow is laterally unbounded, i.e. the tidal-stream bypasses the array configuration, a more accurate approach is the two-scale modelling assumption (Adcock *et al.*, 2015). A subsequent step would be to implement the numerical simulation of the turbine-scale and array-scale coupling in the power extraction simulation. In particular, the free-surface analytical model proposed by Vogel *et al.* (2016) could be used as a reference. This model considers that turbine-scale flow and array-scale flow can be analysed as two quasi-inviscid open channel flow

problems. The numerical models reported in this thesis could be expanded to compute the turbine-scale and array-scale couple system and to include a more sophisticated turbulence solution procedure such as the Smagorinsky eddy-viscosity model.

7.4.5   Tidal Turbine Rotor Design

Theoretical and numerical results for tidal energy resource assessment reported in this thesis indicate that turbines performance increases when significant blockage ratios are used. This implies that turbines have to be designed to sustain higher levels of thrust (Heathcote *et al.*, 2016). A following step would be the use of thrust coefficients and blockage ratios documented in this research to design tidal turbine rotors. Inclusion of blockage ratio on the rotor design in an infinitely long fence indicates that higher levels of blockage ratio require the increase of rotor solidity and blade pitch decrease (Schluntz and Willden, 2015). The solidity depends on the blade chord, the number of blades, and rotor radius. It indicates the ratio of blade area to the disc area swept out by the blades.

To design a rotor for a specific thrust coefficient, it is necessary to specify an optimum blade angle of attack, which in turn require to study the blade twist and solidity for a given tip speed ratio (Heathcote *et al.*, 2016). The right identification of the solidity ensures blades do not overlap at the root when blade twist is introduced. The analysis of the solution space of thrust coefficient and tip speed ratio allows the identification of a maximum power coefficient for the rotor. Power coefficient increases with both the tip speed ratio and thrust coefficient; however, solidity increase is restricted by geometric limitations and tip speed ratio is limited by cavitation.

In the case of rotors within partial-fences, the design of the rotor should consider the non-uniform conditions generated along the short fence. The performance of a rotor designed to maximised power coefficient decreases when it is used within a four-turbine fence Heathcote *et al.* (2016). This configuration produced a power coefficient

reduction by approximately one-third of the original value as a result of a larger amount of flow bypassing the turbine.

Bibliography

Adcock, T. A., Draper, S. and Nishino, T. 2015. Tidal power generation - a review of hydrodynamic modelling. *Proceedings of the Institution of Mechanical Engineers, Part A: Journal of Power and Energy* 229(7), pp. 755–771.

Adcock, T. A. A., Draper, S., Houlsby, G. T., Borthwick, A. G. L. and Serhadlioglu, S. 2013. The available power from tidal stream turbines in the Pentland firth. *Proceedings of the Royal Society A: Mathematical, Physical and Engineering Sciences* 469(2157), pp. 20130072–20130072.

Ahmadian, R., Falconer, R. and Bockelmann-Evans, B. 2012a. Far-field modelling of the hydro-environmental impact of tidal stream turbines. *Renewable Energy* 38(1), pp. 107–116.

Ahmadian, R., Falconer, R. and Bockelmann-Evans, B. 2012b. Far-field modelling of the hydro-environmental impact of tidal stream turbines. *Renewable Energy* 38(1), pp. 107–116.

Ahmadian, R. and Falconer, R. A. 2012. Assessment of array shape of tidal stream turbines on hydro-environmental impacts and power output. *Renewable Energy* 44, pp. 318–327.

Arakawa, A. and Lamb, V. 1977. Computational design of the basic dynamical processes of the ucla general circulation model. *Methods in Computational Physics*

17, pp. 173–265. Available at: http://www-pcmdi.llnl.gov/projects/modeldoc/amip/33ucla_fn.html.

Bahaj, A. S., Molland, A. F., Chaplin, J. R. and Batten, W. M. J. 2007. Power and thrust measurements of marine current turbines under various hydrodynamic flow conditions in a cavitation tunnel and a towing tank. *Renewable Energy* 32(3), pp. 407–426.

Bellos, V. and Tsakiris, G. 2016. *Grid coarsening and uncertainty in 2D hydrodynamic modelling*, Taylor & Francis Group, pp. 714–720.

Blanchfield, J., Garrett, C., Wild, P. and Rowe, A. 2008. The extractable power from a channel linking a bay to the open ocean. *Proceedings of the Institution of Mechanical Engineers, Part A: Journal of Power and Energy* 222(3), pp. 289–297.

Blazek, J. 2001. *Computational Fluid Dynamics - Principles and Applications*. Netherlands: Elsevier, first ed.

Blunden, L. S. and Bahaj, A. S. 2006. Tidal energy resource assessment for tidal stream generators. *Proceedings of the Institution of Mechanical Engineers, Part A: Journal of Power and Energy* 221(2), pp. 137–146.

Bonar, P. A. J., Bryden, I. G. and Borthwick, A. G. L. 2015. Social and ecological impacts of marine energy development. *Renewable and Sustainable Energy Reviews* 47, pp. 486–495.

Borthwick, A. G. L. 2016. Marine renewable energy seascape. *Engineering* 2(1), pp. 69–78.

Boye, B. A. 2014. *Integrated Modelling of Hydrodynamic Processes, Faecal Indicator Organisms and Related Parameters with Improved Accuracy using Parallel (GPU) Computing*. Ph.D. thesis, Cardiff University.

BP. 2018. Bp statistical review of world energy. Report, Pureprint, Available at: https://www.bp.com/content/dam/bp/en/corporate/pdf/energy-economics/statistical-review/bp-stats-review-2018-full-report.pdf.

Brown, E., Colling, A., Wright, J. B. J. B., Park, D. and Team., O. U. O. C. 1999. *Waves, Tides and Shallow-Water Processes*. Butterw orth-Heinemann, Oxford: Oxford, Open University, 2nd edition ed. Available at: http://www.sisal.unam.mx/labeco/LAB_ECOLOGIA/OF_files/Waves,%20Tides%20and%20Shallow-Water%20Processes%20(2nd%20Edition).pdf.

Bryden, I. G. and Couch, S. J. 2007. How much energy can be extracted from moving water with a free surface: A question of importance in the field of tidal current energy? *Renewable Energy* 32(11), pp. 1961–1966.

Bryden, I. G., Couch, S. J., Owen, A. and Melville, G. 2007. Tidal current resource assessment. *Proceedings of the Institution of Mechanical Engineers, Part A: Journal of Power and Energy* 221(2), pp. 125–135.

Bryden, I. G., Grinsted, T. and Melville, G. T. 2004. Assessing the potential of a simple tidal channel to deliver useful energy. *Applied Ocean Research* 26(5), pp. 198–204.

Burton, T., Sharpe, D., Jenkins, N. and Bossanyi, E. 2001. *Wind Energy Handbook*. Wiley.

Carnahan, B., Luther, H. A. and Wilkes, J. O. 1969. *Applied numerical methods*. Malabar, Florida: Krieger Publishing Company.

Charlier, R. H. 2003. Sustainable co-generation from the tides: A review. *Renewable and Sustainable Energy Reviews* 7, p. 187–213.

Chung, T. J. 2010. *Computational Fluid Dynamics*. Cambridge: Cambridge University Press, second edition ed.

Coppinger, D. 2016. *Development of a nested 3D hydrodynamic model for tidal turbine impact assessment*. Ph.D. thesis, National University of Ireland, Galway.

Courant, R., Friedrichs, K. and Lewy, H. 1928. On the partial difference equations of mathematical physics. *Mathematische Annalen* (100), p. 20.

Cushman-Roisin, B. and Beckers, J.-M. 2007. *Introduction to Geophysical Fluid Dynamics Physical and Numerical Aspects*. Academic Press.

Denny, E. 2009. The economics of tidal energy. *Energy Policy* 37, p. 1914–1924.

Divett, T., Vennell, R. and Stevens, C. 2013. Optimization of multiple turbine arrays in a channel with tidally reversing flow by numerical modelling with adaptive mesh. *Philos Trans R Soc* A371.

Douglas, C. L., Harrison, G. P. and Chick, J. P. 2008. Life cycle assessment of the Seagen marine current turbine. *Journal of Engineering for the Maritime Environment* Proc. IMechE Part M(222).

Draper, S. 2011. *Tidal Stream Energy Extraction in Coastal Basins*. Ph.D. thesis, St Catherine's College, University of Oxford.

Draper, S., Adcock, T. A. A., Borthwick, A. G. L. and Houlsby, G. T. 2014a. Estimate of the tidal stream power resource of the Pentland firth. *Renewable Energy* 63, pp. 650–657.

Draper, S., Borthwick, A. G. and Houlsby, G. T. 2013a. Energy potential of a tidal fence deployed near a coastal headland. *Philos Trans A Math Phys Eng Sci* 371(1985), p. 20120176.

Draper, S., Houlsby, G. T., Oldfield, M. L. G. and Borthwick, A. G. L. 2010. Modelling tidal energy extraction in a depth-averaged coastal domain. *IET Renewable Power Generation* 4(6), p. 545.

Draper, S. and Nishino, T. 2013. Centred and staggered arrangements of tidal turbines. *Journal of Fluid Mechanics* 739, pp. 72–93.

Draper, S., Nishino, T. and Adcock, T. A. 2014b. Turbine blockage in non-uniform flow. *19th Australasian Fluid Mechanics Conference* p. 4.

Draper, S., Nishino, T., Adcock, T. A. and Houslby, G. T. 2014c. Wind and tidal turbines in uniform flow. *3rd Oxford Tidal Energy Workshop* .

Draper, S., Stallard, T., Stansby, P., Way, S. and Adcock, T. 2013b. Laboratory scale experiments and preliminary modelling to investigate basin scale tidal stream energy extraction. *10th European Wave and Tidal Energy* p. 12. Available at: http://users.ox.ac.uk/~spet1235/890-Scott%20Draper.pdf.

EY. 2013. Rising tide, global trends in the emerging ocean energy market. Report, Available at: https://www.ey.com/Publication/vwLUAssets/EY-Ocean-energy-2013/$FILE/EY-Ocean-energy-2013.pdf.

Falconer, R. 1984. Temperature distributions in tidal flow field. *Journal of environmental engineering* 110(6), pp. 1099–1116.

Falconer, R. and Lin, B. 2001. DIVAST MODEL REFERENCE MANUAL. Report, Cardiff University.

Falconer, R. A. 1993. *An Introduction to Nearly-horizontal flows*, London: Chapman and Hall, chap. 2.

Falconer, R. A. and Asce, M. 1986. Water quality simulation study of a natural harbor. *Journal of Waterway, Port, Coastal and Ocean Engineering* 112, pp. 15–34.

Fallon, D. 2012. *Numerical Modelling of the far-field impacts of tidal turbines*. Master's thesis, National University of Ireland, Galway.

Fallon, D., Hartnett, M., Olbert, A. and Nash, S. 2014. The effects of array configuration on the hydro-environmental impacts of tidal turbines. *Renewable Energy* 64, pp. 10–25.

Foreman, M. G. G. and Henry, R. F. 1989. The harmonic analysis of tidal model time series. *Adv. Water Resources* 12, p. 12.

Fraenkel, P. 2002. Power from marine currents. *Proceedings of the Institution of Mechanical Engineers Part A Journal of Power and Energy* (216(A1)), p. 1–14.

García-Navarro, P., Alcrudo, F. and Savirón, J. 1992. 1-D open-channel flow simulation using TVD-McCormack scheme. *J. Hydraul. Eng.* 118(10), pp. 1359–1372.

Garret, C. and Cummins, P. 2013. Maximum power from a turbine farm in shallow water. *J. Fluid Mech.* (714), p. 634–643.

Garrett, C. and Cummins, P. 2004. Generating power from tidal currents. *Journal of Waterway, port, coastal and ocean engineering* 130, pp. 114–118.

Garrett, C. and Cummins, P. 2005. The power potential of tidal currents in channels. *Proceedings of the Royal Society A: Mathematical, Physical and Engineering Sciences* 461(2060), pp. 2563–2572.

Garrett, C. and Cummins, P. 2007. The efficiency of a turbine in a tidal channel. *Journal of Fluid Mechanics* 588.

Garrett, C. and Cummins, P. 2008. Limits to tidal current power. *Renewable Energy* 33(11), pp. 2485–2490.

Gaurier, B., Davies, P., Deuff, A. and Germain, G. 2013. Flume tank characterization of marine current turbine blade behaviour under current and wave loading. *Renewable Energy* 59, pp. 1–12.

204

Ghidaoui, M. S., Kolyshkin, A. A., Liang, J. H., Chan, F. C., Li, Q. and Xu, K. 2006. Linear and nonlinear analysis of shallow wakes. *J. Fluid Mech.* 548, pp. 309–340.

Godin, G. 1988. *Tides.* Ensenada BC. Mexico: Centro de Investigacion Cientifica y de Educacion Superiour de Ensenada (CICESE).

Gustafsson, B. 2011. *Fundamentals of scientific computing*, vol. 8 of *Texts in Computational Science and Engineering.* Sweden: Springer.

Harlow, F. H. and Welch, J. E. 1965. Numerical calculation of time-dependent viscous incompressible flow of fluid with free surface. *Physics of Fluids* 8(12), pp. 2182–2189.

Harten, A. 1982. High resolution schemes for hyperbolic conservation laws. *Journal of Computational Physics* 135, pp. 260–278.

Hartnett, M., Nash, S., Olbert, A. and O'Brien, N. 2012. Modelling of hydro-environmental impacts from the installation of tidal stream devices in the Shannon estuary. Tech. rep., Department of Civil Engineering, National University of Ireland, Galway.

Heathcote, F., Vogel, C. R. and Willden, R. H. J. 2016. *Design and operation of a 1MW four turbine tidal fence*, Taylor & Francis Group, 6000 Broken Sound Parkway NW, Suite 300, Boca Raton, FL 33487-2742 CRC Press 2016, p. 545–552. Available at: https://doi.org/10.1201/9781315229256-65.

Heavey, S., Leen, S. and McGarry, P. 2017. An efficient and accurate methodology for hydrofoil characterisation and tidal turbine design. In: *Proceedings of the 12th European Wave and Tidal Energy Conference (EWTEC).* p. 10.

Houlsby, G. and Vogel, C. 2017. The power available to tidal turbines in an open channel flow. *Proceedings of the Institution of Civil Engineers, Energy* 170, pp. 12–21.

Houlsby, G. T., Draper, S. and Oldfield, M. L. G. 2008. Application of linear momentum actuator disc theory to open channel flow. Tech. Rep. OUEL2296/08, Oxford Univesity Engineering Laboratory UK.

Huleihil, M. and Mazor, G. 2012. Wind turbine power: The Betz limit and beyond. In: Carriveau, R., ed., *Advances in Wind Power*, Rijeka: IntechOpen, chap. 1. Available at: https://doi.org/10.5772/52580.

IPCC. 2012. *Summary for Policymakers*, Cambridge University Press, Cambridge, U.K. and N.Y., USA., book section SPM.

Johnson, B., Francis, J., Howe, J. and Whitty, J. 2014. Computational actuator disc models for wind and tidal applications. *Journal of Renewable Energy* 2014, pp. 1–10.

Kang, Y.-H., Kwak, D. Y. and Park, K. 2014. Multigrid methods for improving the variational data assimilation in numerical weather prediction. *Tellus* A(66). Available at: http://dx.doi.org/10.3402/tellusa.v66.20217.

Karsten, R. H., McMillan, J. M., Lickley, M. J. and Haynes, R. D. 2008. Assessment of tidal current energy in the Minas Passage, bay of Fundy. *Proceedings of the Institution of Mechanical Engineers, Part A: Journal of Power and Energy* 222(5), pp. 493–507.

Kempener, R. and Neumann, F. 2014. Tidal energy technology brief. Report, International Renewable Energy Agency (IRENA).

Khan, F. A. 2010. *Two-dimensional shock capturing numerical simulation of shallow water flow applied to dam break analysis.* Ph.D. thesis, Loughborough University.

Kiessling, A. 2009. An introduction to parallel programming with OpenMP. Report, The university of Edinburgh.

Kressner, D. 2005. *Numerical Methods for General and Structured Eigenvalue Problems.*, vol. 46 of *Lecture Notes in Computational Science and Engineering.* Netherlands: Springer. Available at: http://www.informatik.uni-trier.de/~ley/pers/hd/k/Kressner:Daniel.

Kundu, P. K. and Cohen, I. M. 2002. *Fluid Mechanics.* USA: Academic Press, second ed.

Kvocka, D. 2015. DIVAST-TVD user manual. Tech. rep., Hydro-environmental Research Centre School of Engineering Cardiff University.

Kvočka, D. 2017. *Modelling elevations, inundation extent and hazard risk for extreme flood events.* Ph.D. thesis, Cardiff University, Available at: http://orca.cf.ac.uk/101761/1/2017KvockaDPhD.pdf.

Kvočka, D., Falconer, R. A. and Bray, M. 2015. Appropriate model use for predicting elevations and inundation extent for extreme flood events. *Natural Hazards* 79(3), pp. 1791–1808.

LeVeque, R. J. 2002. *Finite-volume methods for Hyperbolic Problems.* Cambridge texts in applied mathematics. Cambridge Unicersity Press.

Lewis, A., Estefen, S., Huckerby, W. M., Pontes, T. and Torres-Martinez, J. 2011. *Ocean Energy*, Cambridge University Press, Cambridge, U.K. and N.Y., USA., book section 6, p. 38.

Liang, D., Falconer, R. A. and Lin, B. 2006. Comparison between TVD-MacCormack and ADI-type solvers of the shallow water equations. *Advances in Water Resources* 29(12), pp. 1833–1845.

Liang, D., Lin, B. and Falconer, R. A. 2007. Simulation of rapidly varying flow using

an efficient TVD–Maccormack scheme. *International Journal for Numerical Methods in Fluids* 53(5), pp. 811–826.

Ltd, B. . V. 2005. PHASE II UK TIDAL STREAM ENERGY RESOURCE ASSESS-MENT. Report 107799/D/2200/03.

Mannion, B., McCormack, V., Kennedy, C., Leen, S. B. and Nash, S. 2018. An experimental study of a flow-accelerating hydrokinetic device. *Proceedings of the Institution of Mechanical Engineers, Part A: Journal of Power and Energy* p. 15.

Ming, H. T. and Chu, C. R. 2000. Two-dimensional shallow water flows simulation using TVD-MacCormack scheme. *Journal of Hydraulic Research* 38(2), pp. 123–131.

Mycek, P., Gaurier, B., Germain, G., Pinon, G. and Rivoalen, E. 2014. Experimental study of the turbulence intensity effects on marine current turbines behaviour. Part I: One single turbine. *Renewable Energy* 66, pp. 729–746.

Myers, L. and Bahaj, A. S. 2007. Wake studies of a 1/30th scale horizontal axis marine current turbine. *Ocean Engineering* 34(5-6), pp. 758–762.

Nash, S. 2010. *Development of an efficient dynamically-nested model for tidal hydraulics and solute transport*. Ph.D. thesis, National University of Ireland, Galway.

Nash, S., O'Brien, N., Olbert, A. and Hartnett, M. 2014. Modelling the far field hydro-environmental impacts of tidal farms – A focus on tidal regime, inter-tidal zones and flushing. *Computers & Geosciences* 71, pp. 20–27.

Nash, S., Olbert, A. and Hartnett, M. 2015. Towards a low-cost modelling system for optimising the layout of tidal turbine arrays. *Energies* 8(12), pp. 13521–13539.

Nash, S. and Phoenix, A. 2017. A review of the current understanding of the hydro-environmental impacts of energy removal by tidal turbines. *Renewable and Sustainable Energy Reviews* 80, pp. 648–662.

Neill, S. and Hashemi, M. R. 2018. *Fundamentals of Ocean Renewable Energy. Generating Electricity from the Sea*. United Kingdown: Academic Press. Available at: https://doi.org/10.1016/B978-0-12-810448-4.09994-8.

Neill, S., Jordan, J. R. and Couch, S. J. 2012. Impact of Tidal Energy Converter (TEC) arrays on the dynamics of headland sand banks. *Renew Energy* (37), p. 387–97.

Nishino, T. and Willden, R. H. J. 2012a. Effects of 3-D channel blockage and turbulent wake mixing on the limit of power extraction by tidal turbines. *International Journal of Heat and Fluid Flow* 37, pp. 123–135.

Nishino, T. and Willden, R. H. J. 2012b. The efficiency of an array of tidal turbines partially blocking a wide channel. *Journal of Fluid Mechanics* 708, pp. 596–606.

Nishino, T. and Willden, R. H. J. 2013a. *Energetics of marine turbine arrays – extraction, dissipation and diminution*, [Online].

Nishino, T. and Willden, R. H. J. 2013b. Two-scale dynamics of flow past a partial cross-stream array of tidal turbines. *Journal of Fluid Mechanics* 730, pp. 220–244.

O'Brien, N. 2013. *Development of computationally efficient nested hydrodynamic models*. Ph.D. thesis, National University of Ireland, Galway.

Olbert, A. 2006. *Investigations into turbulence processes in tide-induced flows - scale and numerical modelling*. Ph.D. thesis, National University of Ireland, Galway.

O'Rourke, F., Boyle, F. and Reynolds, A. 2010. Tidal current energy resource assessment in ireland: Current status and future update. *Renewable and Sustainable Energy Reviews* 14(9), pp. 3206–3212.

O'Rourke, F., Boyle, F. and Reynolds, A. 2014. Ireland's tidal energy resource: an assessment of a site in the Bulls Mouth and the Shannon estuary using measured data. *Energy Conversion and Management* 87, pp. 726–734.

Perez-Campos, E. and Nishino, T. 2015. Numerical validation of the two-scale actuator disc theory for marine turbine arrays. *Proceedings of the 11th European Wave and Tidal Energy Conference* p. 8.

Phoenix, A. 2017. *Development of a tidal flow model for optimisation of tidal turbine arrays.* Ph.D. thesis, National University of Ireland, Galway.

Plew, D. and Stevens, C. 2013. Numerical modelling of the effect of turbines on currents in a tidal channel - Tory Channel, New Zealand. *Renew Energy* (57), p. 269–82.

Pozrikidis, C. 2009. *Fluid Dynamics Theory, Computation, and Numerical Simulation.* USA: Springer, second ed.

Press, W., Teukolsky, S., Vetterling, W. and Flannery, B. 1992. *Numerical Recipes in Fortran. The Art of Scientific Computing.* USA: Press Syndicate of the University of Cambridge, second ed.

Ragheb, A. M. and Ragheb, M. 2011. *Wind Turbines Theory - The Betz Equation and Optimal Rotor Tip Speed Ratio*, Croatia: InTech, book section 2.

Ramos, V., Carballo, R., Álvarez, M., Sánchez, M. and Iglesias, G. 2013. Assessment of the impacts of tidal stream energy through high-resolution numerical modeling. *Energy* (61), p. 541–54.

Ravela, S. C. 2010. *Comparison of Shared memory based parallel programming models.* Ph.D. thesis, Blekinge Institute of Technology.

Rodenhuis, G. S. 1994. *Two-dimensional nearly-horizontal flow models*, London: E & FN spon, book section 10.

Rogers, B. D., Borthwick, A. G. L. and Taylor, P. H. 2003. Mathematical balancing of flux gradient and source terms prior to using roe's approximate Riemann solver. *Journal of Computational Physics* 192(2), pp. 422–451.

Rourke, F. O., Boyle, F. and Reynolds, A. 2009. Renewable energy resources and technologies applicable to Ireland. *Renewable and Sustainable Energy Reviews* 13(8), pp. 1975–1984.

Schluntz, J. and Willden, R. H. J. 2015. The effect of blockage on tidal turbine rotor design and performance. *Renewable Energy* 81, pp. 432–441.

SEI. 2006. Tidal & current energy resources in ireland. Report, Sustainable Energy Ireland.

Selin, N. E. 2018. *Tidal power Types & Facts*, [Online]. Available at: https://www.britannica.com/science/tidal-power.

Serhadlioglu, S. 2014. *Tidal Stream Resource Assessment of the Anglesey Skerries and the Bristol Channel*. Ph.D. thesis, University of Oxford.

Serhadlıoğlu, S., Adcock, T. A. A., Houlsby, G. T., Draper, S. and Borthwick, A. G. L. 2013. Tidal stream energy resource assessment of the anglesey skerries. *International Journal of Marine Energy* 3-4, pp. e98–e111.

Sheng, J., Thompson, K., Greenberg, D. and Hill, P. 2012. Assessing the far field effects of tidal power extraction on the bay of Fundy, gulf of Maine and Scotian shelf - final report. Report, Department of Oceanography, Dalhousie University.

Shyue, K.-M. 1998. An efficient shock-capturing algorithm for compressible multicomponent problems. *Journal of Computational Physics* (142), pp. 208–242.

SIMEC. 2018. *Simec atlantis energy — a global sustainable energy company*, [Online]. Available at: https://simecatlantis.com/.

Sleigh, A. 2006. *Solution of the st venant equations / shallow-water equations of open channel flow*, [Online]. Available at: http://www.efm.leeds.ac.uk/CIVE/UChile/part03.pdf.

Sleiti, A. K. 2017. Tidal power technology review with potential applications in Gulf Stream. *Renewable and Sustainable Energy Reviews* 69, p. 435–441.

Stallard, T., Collings, R., Feng, T. and Whelan, J. 2013. Interactions between tidal turbine wakes: experimental study of a group of three-bladed rotors. *Philos Trans A Math Phys Eng Sci* 371(1985), p. 20120159.

Stansby, P. 2006. Limitations of depth-averaged modeling for shallow wakes. *Journal of Hydraulic Engineering* 132(7), pp. 737–740.

Stelling, G. S., Wiersman, A. K. and Willemse, J. B. T. M. 1986. Practical aspects of accurate tidal computations. *Journal of Hydraulic Enginnering* 112(9), pp. 802–816.

Stewart, R. H. 2004. *Introduction To Physical Oceanography.* Department of Oceanography, Texas A&M University, USA: OpenSource. Available at: http://oceanworld.tamu.edu/resources/ocng_textbook/PDF_files/book_PDF_files.htmlhttps://open.umn.edu/opentextbooks/BookDetail.aspx?bookId=20.

Sun, X., Chick, J. P. and Bryden, I. G. 2008. Laboratory-scale simulation of energy extraction from tidal currents. *Renewable Energy* 33(6), pp. 1267–1274.

Sutherland, G., Foreman, M. and Garrett, C. 2007. Tidal current energy assessment for johnstone strait, vancouver island. *Proceedings of the Institution of Mechanical Engineers, Part A: Journal of Power and Energy* 221(2), pp. 147–157.

Thompson, L., Hautala, S. and Kelly, K. 2005. *Tide dynamics*, [Online]. Available at: Thompson/Ocean420/.

Toro, E. F. 2001. *Shock-capturing methods for free-surface shallow flows.* U.K: Wiley.

Toro, E. F. 2009. *Riemann Solvers and Numerical Methods for Fluid Dynamics, a practical introduction.* Springer.

Toro, E. F., Spruce, M. and Speares, W. 1994. Restoration of the contact surface in the hll-riemann solver. *Shock Waves* (4), pp. 25–34.

Trefethen, L. and Bau, D. I. 1997. *Numerical Linear Algebra*. SIAM: Society for Industrial and Applied Mathematics.

Vallis, G. K. 2005. *Atmospheric and Oceanic Fluid Dynamics Fundamentals and Large-Scale Circulation*. Cambridge University Press.

van Kuik, G. A. M. 2007. The Lanchester–Betz–Joukowsky limit. *Wind Energy* 10(3), pp. 289–291.

Versteeg, H. K. and Malalasekera, W. 2007. *An Introduction to Computational Fluid Dynamics*. England: Pearson Prentice Hall, second edition ed. Available at: http://ftp.demec.ufpr.br/disciplinas/TM702/Versteeg_Malalasekera_2ed.pdf.

Vincent, S. and Caltagirone, J.-P. 2001. Numerical modelling of bore propagation and run-up on sloping beaches using a MacCormack TVD scheme. *Journal of Hydraulic Research* 39(1), pp. 41–49.

Vogel, C. R., Houlsby, G. T. and Willden, R. H. J. 2016. Effect of free surface deformation on the extractable power of a finite width turbine array. *Renewable Energy* 88, pp. 317–324.

Vogel, C. R., Willden, R. H. and Houslby, G. T. 2013. *A correction for depth-averaged simulations of tidal turbine arrays*, [Online].

von Arx, W. 1962. *An introduction to physical oceanography*. Earth Science. U.S.A: Addison-Wesley.

Vreugdenhil, C. B. 1994. *Numerical methods for shallow-water flow*, vol. 13 of *Water science and technology library*. The Netherlands: Klumer academic publishers.

Wang, B. 2002. Kelvin waves. *Elsevier Science* p. 7.

Weiyan, T. 1992. *Shallow water hydrodynamics : mathematical theory and numerical solution for a two-dimensional system of shallow water equations.* Elsevier oceanography series ; 55. Beijing, China: Water & Power Press.

Wesseling, P. 2001. *Principles of computational fluid dynamics*, vol. 29 of *Springer series in computational mathematics.* Springer-Verlag Berlin Heidelberg.

Whelan, J., Thomson, M., Graham, J. M. R. and Peiró, J. 2007. *Modelling of free surface proximity and wave induced velocities around a horizontal axis tidal stream turbine*, [Online].

Whelan, J. I., Graham, J. M. R. and Peiró, J. 2009. A free-surface and blockage correction for tidal turbines. *Journal of Fluid Mechanics* 624, p. 281.

Whittaker, P. 2014. *Modelling the Hydrodynamic Drag Force of Flexible RiparianWoodland.* Ph.D. thesis, Cardiff University.

Appendix A

A.1 Governing Equations Discretisation used by TVD-TOC Model

In Section 3.3.2 the conservative form of the governing equations that describe a tidal stream subject to power extraction was deduced. Here, it was found that the governing equations could be re-written as two one-dimensional hyperbolic equations, one for x-direction (Equation 3.15) and another one for y-direction (Equation 3.16). These equations are represented by the following equalities:

$$\frac{\partial X}{\partial t} + \frac{\partial F}{\partial x} = S \tag{A.1}$$

$$\frac{\partial X}{\partial t} + \frac{\partial G}{\partial y} = T \tag{A.2}$$

The solution of Equation A.1 and A.2 is numerically approximated with the explicit MacCormack scheme, which require the use of a Predictor and Corrector step. The Predictor step of Equation A.1 is:

$$X_{i,j}^{\overline{n+1}} = X_{i,j}^{n} - \frac{\Delta t}{\Delta x}\left(F_{i+1,j}^{n} - F_{i,j}^{n}\right) + \Delta t S_{i,j}^{n} \tag{A.3}$$

Meanwhile, the corrector step of A.1 is

$$X_{i,j}^{n+1} = X_{i,j}^{n} - \frac{\Delta t}{\Delta x}\left(F_{i,j}^{\overline{n+1}} - F_{i,j-1}^{\overline{n+1}}\right) + \Delta t S_{i,j}^{\overline{n+1}} \tag{A.4}$$

Where the superscripts are temporal indices and the subscripts are spatial indices; Δx and Δt indicate the time and spatial step. In the current version of the model the finite difference calculation is forward in space for the predictor step and is backward for corrector step. The temporal index $\overline{n+1}$ correspond to the predicted variable and can be denote as p; on the other hand $n+1$ indicates the corrected variable and can be written as c

By substituting the corresponding values of the vectors X, F, and S (given by Equation 3.14) in the predictor step (Equation A.3) the following expression is obtained:

$$
\begin{bmatrix} H_{i,j}^p \\ q_{xi,j}^p \\ q_{yi,j}^p \end{bmatrix} = \begin{bmatrix} H_{i,j}^n \\ q_{xi,j}^n \\ q_{yi,j}^n \end{bmatrix} - \frac{\Delta t}{\Delta x} \begin{bmatrix} q_{xi+1,j}^n - q_{xi,j}^n \\ \frac{\beta(q_{xi+1,j}^n)^2}{H} - \frac{\beta(q_{xi,j}^n)^2}{H} + \frac{g}{2}\left((H_{i+1,j}^n)^2 - (H_{i,j}^n)^2\right) \\ \frac{\beta q_{xi+1,j}^n q_{yi+1,j}^n}{H} - \frac{\beta q_{xi,j}^n q_{yi,j}^n}{H} \end{bmatrix} +
$$

$$
\Delta t \begin{bmatrix} 0 \\ -gH\frac{\partial h_{i,j}^n}{\partial x} - \frac{gq_{xi,j}^n \sqrt{(q_{xi,j}^n)^2+(q_{yi,j}^n)^2}}{H^2C^2} - \frac{A_{xi,j}C_{Ti,j}(q_{xi,j}^n)^2}{2H^2} \\ 0 \end{bmatrix} \quad (A.5)
$$

Therefore, the discretised equations for the predictor step in x-direction are given by:

$$
H_{i,j}^p = H_{i,j}^n - \frac{\Delta t}{\Delta x}\left(q_{xi+1,j}^n - q_{xi,j}^n\right) \quad (A.6)
$$

$$
q_{xi,j}^p = q_{xi,j}^n - \frac{\Delta t}{\Delta x}\left(\frac{\beta}{H}\left((q_{xi+1,j}^n)^2 - (q_{xi,j}^n)^2\right)\right) + \frac{g\Delta t}{2\Delta x}\left((H_{i+1,j}^n)^2 - (H_{i,j}^n)^2\right) +
$$

$$
\Delta t\left(-gH\frac{\partial h_{i,j}^n}{\partial x} - \frac{gq_{xi,j}^n\sqrt{(q_{xi,j}^n)^2+(q_{yi,j}^n)^2}}{H^2C^2} - \frac{A_{xi,j}C_{Ti,j}(q_{xi,j}^n)^2}{2H^2}\right) \quad (A.7)
$$

$$
q_{yi,j}^p = q_{yi,j}^n - \frac{\Delta t}{\Delta x}\left(\frac{\beta}{H}\left(q_{xi+1,j}^n q_{yi+1,j}^n - q_{xi,j}^n q_{yi,j}^n\right)\right) \quad (A.8)
$$

On the other hand the corrector step in x-direction is described by the following equation:

$$
X_{i,j}^c = X_{i,j}^n - \frac{\Delta t}{\Delta x}\left(F_{i,j}^p - F_{i-1,j}^p\right) + \Delta t S_{i,j}^p \quad (A.9)
$$

Appendix A.

The substitution of the corresponding values of the vectors X, F, and S (given by Equation 3.14) in the corrector step (Equation A.9) lead to the following expression:

$$
\begin{bmatrix} H_{i,j}^c \\ q_{xi,j}^c \\ q_{yi,j}^c \end{bmatrix} = \begin{bmatrix} H_{i,j}^n \\ q_{xi,j}^n \\ q_{yi,j}^n \end{bmatrix} - \frac{\Delta t}{\Delta x} \begin{bmatrix} q_{xi,j}^p - q_{xi-1,j}^p \\ \frac{\beta(q_{xi,j}^p)^2}{H} - \frac{\beta(q_{xi-1,j}^p)^2}{H} + \frac{g}{2}\left((H_{i,j}^p)^2 - (H_{i-1,j}^p)^2\right) \\ \frac{\beta q_{xi,j}^p q_{yi,j}^p}{H} - \frac{\beta q_{xi-1,j}^p q_{yi-1,j}^p}{H} \end{bmatrix} +
$$
$$
\Delta t \begin{bmatrix} 0 \\ -gH\frac{\partial h_{i,j}^p}{\partial x} - \frac{gq_{xi,j}^p \sqrt{(q_{xi,j}^p)^2+(q_{yi,j}^p)^2}}{H^2 C^2} - \frac{A_{xi,j}C_{Ti,j}(q_{xi,j}^p)^2}{2H^2} \\ 0 \end{bmatrix} \quad \text{(A.10)}
$$

Consequently, the resultant discretised equations for the corrector step in x-direction are:

$$
H_{i,j}^c = H_{i,j}^n - \frac{\Delta t}{\Delta x}\left(q_{xi,j}^n - q_{xi-1,j}^n\right) \quad \text{(A.11)}
$$

$$
q_{xi,j}^c = q_{xi,j}^n - \frac{\Delta t}{\Delta x}\left(\frac{\beta}{H}\left((q_{xi,j}^p)^2 - (q_{xi-1,j}^p)^2\right)\right) +
$$
$$
\frac{g\Delta t}{2\Delta x}\left((H_{i,j}^p)^2 - (H_{i-1,j}^p)^2\right) +
$$
$$
\Delta t \left(-gH\frac{\partial h_{i,j}^p}{\partial x} - \frac{gq_{xi,j}^p\sqrt{(q_{xi,j}^p)^2 + (q_{yi,j}^p)^2}}{H^2 C^2} - \frac{A_{xi,j}C_{Ti,j}(q_{xi,j}^p)^2}{2H^2}\right) \quad \text{(A.12)}
$$

$$
q_{yi,j}^c = q_{yi,j}^n - \frac{\Delta t}{\Delta x}\left(\frac{\beta}{H}\left(q_{xi,j}^p q_{yi,j}^p - q_{xi-1,j}^p q_{yi-1,j}^p\right)\right) \quad \text{(A.13)}
$$

The final solutions at the next time level $(n+1)$ in x-direction have the following form:

$$
H_{i,j}^n = \frac{1}{2}\left(H_{i,j}^p + H_{i,j}^c\right) \quad \text{(A.14)}
$$

$$
q_{xi,j}^n = \frac{1}{2}\left(q_{xi,j}^p + q_{xi,j}^c\right) \quad \text{(A.15)}
$$

$$
q_{yi,j}^n = \frac{1}{2}\left(q_{yi,j}^p + q_{yi,j}^c\right) \quad \text{(A.16)}
$$

A similar procedure is followed to solve the one-dimensional hyperbolic equation for y-direction.

A.2 Eigenvalue Method

The eigenvalue method was implemented numerically with the subroutine zrhqr reported by Press *et al.* (1992) and obtained from `http://iri.columbia.edu/~ines/` `Naren/FortranNumericalRecepies/`. The solution procedure of zrhqr can be described as a two-phase approach (see Figure A.1). On phase 1, an upper Hessenberg matrix is constructed. Later on, phase 2 zrhqr uses the subroutines balanc and hqr to balance the matrix and calculate the eigenvalues of the matrix with the QR algorithm with shifts.
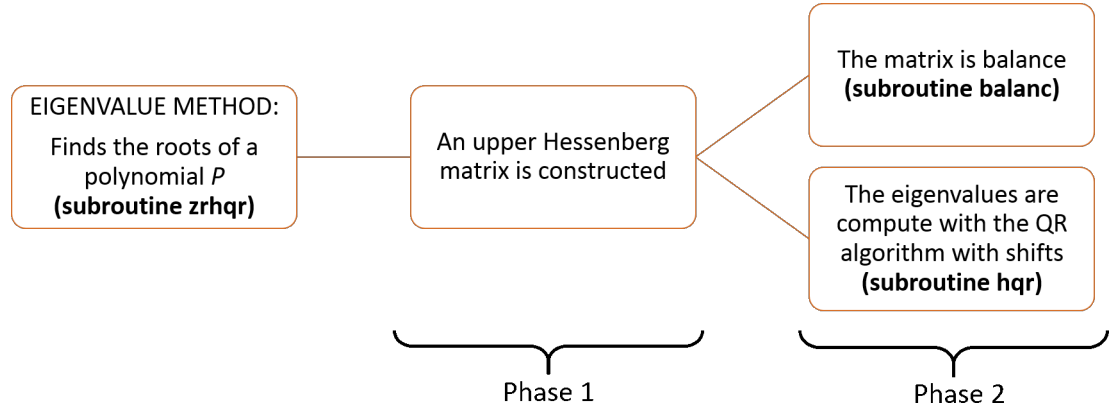
Fig. A.1: Numerical implementation of the Eigenvalue method. The subroutine zrhqr proceeds in two phases: Phase 1 requires zrhqr and Phase 2 uses subroutines balanc and hqr.

The description of the method and the tasks performed by the subroutines follows. Finding the roots of polynomial $G(\lambda)$ with real coefficients a_i and degree m where $1 \leq i \leq m+1$ expressed as:

$$G(\lambda) = \sum_{i=1}^{m+1} a_i \lambda^{i-1} \tag{A.17}$$

is equivalent to finding the eigenvalues (λ) of the following characteristic polynomial:

$$G(\lambda) = det\left[\mathbf{M} - \lambda\mathbf{I}\right] \tag{A.18}$$

where M is the companion $m \times m$ matrix given by Equation A.19 (Press *et al.*, 1992) and I is the $m \times m$ identity matrix. The eigenvalues of M are the roots of G and these eigenvalues are obtained by solving the determinant of $[\mathbf{M} - \lambda\mathbf{I}]$.

$$M = \begin{bmatrix} -\frac{a_m}{a_{m+1}} & -\frac{a_m-1}{a_{m+1}} & \cdots & -\frac{a_2}{a_{m+1}} & -\frac{a_1}{a_{m+1}} \\ 1 & 0 & \cdots & 0 & 0 \\ 0 & 1 & \cdots & 0 & 0 \\ \vdots & & \ddots & & \vdots \\ 0 & 0 & \cdots & 1 & 0 \end{bmatrix} \tag{A.19}$$

In the case of higher order polynomials, the computation of the eigenvalues requires an iterative method that converges to the solution. The method implemented in this thesis proceeds in two phases: Firsts, the matrix M is reduced to an upper Hessenberg matrix H; second, H is balanced and the QR algorithm with shifts is used to perform the iterative process that causes H to converge to a triangular matrix T. The eigenvalues of the triangular matrix are the values on the diagonal. The two phases are described in Figure A.2.
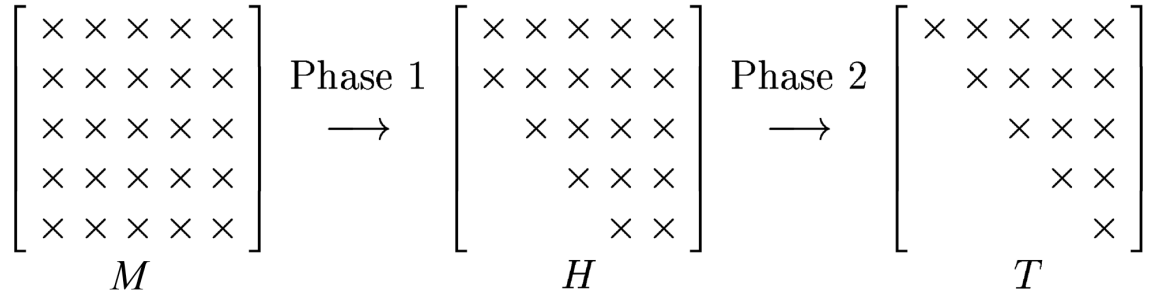
Fig. A.2: Description of the two phases involved in the Eigenvalue method: Phase 1 reduces matrix M to an upper Hessenberg matrix (H) and Phase 2 convergence to a triangular matrix (T), taken from Trefethen and Bau (1997). Copyright ©1997 Society for Industrial and Applied Mathematics. Reprinted with permission. All rights reserved.

The H matrix has zeros everywhere below the diagonal except for the first sub-diagonal row. H is obtained by applying orthogonal similarity transformations based on House-

holder matrices to the matrix M (Kressner, 2005). The use of H speeds up the convergence of QR algorithm with shifts (Trefethen and Bau, 1997).

At phase 2, H is replaced by a balance matrix. The balancing procedure reduces the sensitivity of the eigenvalues to rounding errors during the execution of the QR with shifts algorithm (Press *et al.*, 1992). This technique uses similarity transformations to make corresponding rows and columns of the matrix have comparable norms. In this way, the overall norm of the matrix is reduced, but the eigenvalues are unchanged. Balancing the matrix can improve substantially the accuracy of the eigenvalues computed. The subroutine balanc performs the balancing procedure.

The final step of phase 2 is the implementation of the QR algorithm with shifts. The introduction of shifts k (i.e. $H \rightarrow H - kI$) at each step speeds up the convergence of the QR algorithm, the s-step of the algorithm is (Press *et al.*, 1992):

$$Q_s \cdot (H_s - k_s I) = R_s \tag{A.20}$$

where Q is orthogonal (i.e. $Q^T = Q^{-1}$) and R is an upper triangular matrix. The following step is given by:

$$H_{s+1} = R_s \cdot Q_s^T + k_s I = Q_s \cdot H_s \cdot Q_s^T \tag{A.21}$$

as $s \rightarrow \infty$, H_s converges to a form where the eigenvalues are isolated on the diagonal of a triangular matrix or become eigenvalues of a 2X2 submatrix on the diagonal (Press *et al.*, 1992; Kressner, 2005). The subroutine hqr performs the QR algorithm with shifts.

A.3   Momentum Sink-TOC

Main subroutines used for the numerical implementation of momentum sink-TOC method in ADI-TOC and TVD-TOC. Modifications made to the subroutines are high-

lighted in yellow and green colour.

A.3.1 ADI-TOC

MARTURBINIT

```
SUBROUTINE MARTURBINIT(IMAX,JMAX,TURBDIAM,CONPI,TURBSPA,TURBCORR,  DELX,B_OC,TURBAREA)
        INCLUDE  'HARBOUR.CMN'
        INTEGER  HFIX


        HFIX = 40.0
! DENSITY OF TURBINES  IN THE MODEL    (TF/(DX*DY))
        TURBNUM=1./(TURBSPA**INT2)
! CUMULATIVE AREA OF T: TO BE USED IN THE TFORCE CALCULATION IN THE MODEL
        TURBAREA=TURBNUM*((TURBDIAM**INT2)*CONPI)/4.


DO  I=1,IMAX
DO  J=1,JMAX
IF  ((IWET(I,J).EQ.7).AND.(HX(I,J).GE.20))THEN
! TURBINE-AREA AND B-GRID:   TO BE USED IN THE POWER CALCULATION POST-PROCESSING
! (DX**2) -  COMPENSATES THE TURBINE AREA DEFINITION USED (PER GRID CELL, AS THE THRUST
! FORCE IS DONE PER GRID CELL   TF/(DX*DY))
!.................................
        TURBAREA_F = TURBAREA*(DELX**2)
        B_OC = (TURBAREA/(HFIX*DELX))*(DELX**2)


! SINGLE TURBINE LOCATION
!.................................
        ITURB_LOC = 376
        JTURB_LOC = 406


IF  ((I.EQ.ITURB_LOC).AND.(J.EQ.JTURB_LOC)) THEN
        WRITE(1024,'(8F16.6)') TURBSPA,  DELX,  TURBDIAM,  HX(I,J),  B_OC,  TURBAREA_F
END IF
        TURBDRAG(I,J)=TURBCORR
ELSE
        TURBDRAG(I,J)=0.
END IF
END DO
END DO
```

RETURN

CLOSE(1024) ! TURBINE AREA FEATURES

END

MARTURB

SUBROUTINE MARTURB(IMAX,JMAX,TURBAREA,CONPI,TURBDEN,TURBCORR,ALFA4OC,DELX,&

NDT, HFDT, B_OC)

INCLUDE 'HARBOUR.CMN'

INTEGER HFIX, ITURB_LOC, JTURB_LOC, JLOC2, JLOC3, i_dumb, i_dumb2

REAL GRAV

!EXTRA–VARIABLES

HFIX = 40.0

GRAV=9.80665

! DEFINE PARAMETERS FOR OPEN CHANNEL THEORY

!..

! REFERENCE TURBINE LOCATION

        ITURB_LOC=376

        JTURB_LOC = 406

! BEFORE FENCE(BF)/AFTER FENCE (AF) LOCATIONS

!..

!BF FOR V>0

        JLOC2=JTURB_LOC–1

! AF FOR V<0

        JLOC3=JTURB_LOC+1

N =2*NDT–1

TIMESC = REAL(N)*HFDT

TIMEHR=TIMESC/3600.0

DO I=1,IMAX

DO J=1,JMAX

IF ((IWET(I,J).EQ.7).AND.(HX(I,J).GE.20.))THEN

        UMAG=ABS(UM(I,J))

        VMAG=ABS(VM(I,J))

IF(VMAG.EQ.0.)THEN

        THETA(I,J)=(conpi/2.)

ELSE

!CALCULATE THETA AND ALPHA;

!IT IS ASSUMED TURBINE IS ORIENTATED NORMAL TO FLOW

        THETA(I,J)=(ATAN(UMAG/(VMAG)))

        ALPHA(I,J)=((CONPI/2.)–THETA(I,J))

```
END IF


!CALCULATE PROJECTED AREA OF TURBINE IN X AND Y DIRECTION
        TURBARX(I,J)=TURBAREA*cos(ALPHA(I,J))
        TURBARY(I,J)=TURBAREA*sin(ALPHA(I,J))
IF (TURBARX(I,J).LT.0.)THEN
        TURBARX(I,J)=0.
END IF
IF (TURBARY(I,J).LT.0.)THEN
        TURBARY(I,J)=0.
END IF
! UP-STREAM VELOCITY
!................................
        VM(I,J) = VM(I,JLOC2)
        UM(I,J) = UM(I,JLOC2)
IF (VM(I,J).GT.0) THEN
        VM(I,J) = VM(I,JLOC2)
        UM(I,J) = UM(I,JLOC2)
        HX_OC = HX(I,JLOC2)+EU(I,JLOC2)
IF (VM(I,J).LT.0.02) THEN
        VM = 0.02
END IF
ELSE
        VM(I,J) = VM(I,JLOC3)
        UM(I,J) = UM(I,JLOC3)
        HX_OC = HX(I,JLOC3)+EU(I,JLOC3)
END IF


! FR
!................................
        FR_OC = VM(I,J)/SQRT(HFIX*GRAV)


!BETA4 CALCULATION
!................................
        A4C = (FR_OC**2.0)/2.0                 !B4^4
        A3C = 2.0*ALFA4OC*(FR_OC**2.0)         !B4^3
        A2C =  -2.0 + 2.0*B_OC - (FR_OC**2.0) !B4^2
        A1C = -4.0*ALFA4OC - 2.0*ALFA4OC*FR_OC**2.0  + 4.0   !B4 COEFFICIENT
A0C = (FR_OC**2.0)/2.0 + 4.0*ALFA4OC - 2.0*B_OC*(ALFA4OC**2.0)  - 2.0 !CTE COEFFICIENT


!acoef - VECTOR CONTAINING THE QUARTIC POLYNOMIAL COEFFICIENTS
```

Appendix A.

```fortran
!A0C + A1C*B4 + A2C*B4^2 + A3C*B4^3 + A4C*B4^4
        acoef = (/ A0C, A1C, A2C, A3C, A4C /)


! ROOT CALCULATION STARTS WHEN THE FORCING IS FULLY IMPLEMENTED AND
! THE COEFFICIENTS ARE NOT LONGER ZERO.
        IF (TIMEHR.GT.2*12.42)THEN


!CT CALCULATION FOR TIMEHR > 24.84 HRS
!................................
!         !mm - M POLYNOMIAL DEGRE (4)
!          !rtr - OUTPUT  VECTOR FOR REAL ROOTS
!          !rti - OUTPUT  VECTOR FOR COMPLEX ROOTS
!           WRITE(*,*) 'ROOT REAL 3',rtr(3)
        CALL zrhqr(acoef,mm,rtr,rti)
        BETA4 = rtr(3)
        CT_OC(I,J) = (BETA4**2.0)-(ALFA4OC**2.0)
ELSE
!CT CALCULATION FOR TIMEHR < 24.84 HRS
        CT_OC(I,J) = 1.0
END IF !2*TM2  CONDITION


ELSE
        TURBDRAG(I,J)=0.0
        CT_OC(I,J) = 0.0
END IF   !IWET=7 CONDITION
```

The following section of the code find polynomial's roots by constructing an upper Hessenberg matrix whose eigenvalues are the desired roots.

```fortran
!————————————————————————————————
      SUBROUTINE zrhqr(acoef,mm,rtr,rti)
!————————————————————————————————
REAL acoef(mm+1),rtr(mm),rti(mm)
PARAMETER (MAXM=50)
INTEGER j,k
REAL hess(MAXM,MAXM),xr,xi

if (mm.gt.MAXM.or.acoef(mm+1).eq.0.) then
        write(*,*) 'bad args in zrhqr'
endif

do 12 k=1,mm                      !Construct the matrix
```

224

Appendix A.

```
          hess(1,k)=-acoef(mm+1-k)/acoef(mm+1)
do 11 j=2,mm
          hess(j,k)=0.
11        continue
          if (k.ne.mm) hess(k+1,k)=1.
12     continue
!_____
!    USES balanc,hqr
call balanc(hess,mm,MAXM)
call hqr(hess,mm,MAXM,rtr,rti) !Find its eigenvalues
!_____
do 14 j=2,mm              !Sort roots by their real partis by straight insertion
          xr=rtr(j)
          xi=rti(j)
do 13 k=j-1,1,-1
          if(rtr(k).le.xr)goto 1
          rtr(k+1)=rtr(k)
          rti(k+1)=rti(k)
13        continue
          k=0
1      rtr(k+1)=xr
          rti(k+1)=xi
14     continue
          return
END
!_____
       SUBROUTINE balanc(acoef,n,np)
!_____
INTEGER n,np
REAL acoef(np,np),RADIX,SQRDX
PARAMETER (RADIX=2.,SQRDX=RADIX**2)
INTEGER i,j,last
REAL c,f,g,r,s

1      continue
          last=1
do 14 i=1,n                      !Calculate row and column norms
          c=0.
          r=0.
do 11 j=1,n
          if(j.ne.i)then
```

```fortran
        c=c+abs(acoef(j,i))
        r=r+abs(acoef(i,j))
        endif
11        continue
        if(c.ne.0..and.r.ne.0.)then   !If both are nonzero
        g=r/RADIX
        f=1.
        s=c+r
2         if(c.lt.g)then       !Find the integer power of the machine radix that
!                             comes closest to balancing the matrix
        f=f*RADIX
        c=c*SQRDX
        goto 2
        endif

        g=r*RADIX
3    if(c.gt.g)then
        f=f/RADIX
        c=c/SQRDX
        goto 3
        endif
        if((c+r)/f.lt.0.95*s)then
        last=0
        g=1./f
        do 12 j=1,n              !Apply similarity transformation
        acoef(i,j)=acoef(i,j)*g
12          continue
        do 13 j=1,n
        acoef(j,i)=acoef(j,i)*f
13          continue
        endif
        endif
14        continue
        if(last.eq.0)goto 1
        return
END
!_____
SUBROUTINE hqr(acoef,n,np,wr,wi)
!_____
INTEGER n,np
REAL acoef(np,np),wi(np),wr(np)
```

226

Appendix A.

```fortran
INTEGER i,its,j,k,l,m,nn
REAL anorm,p,q,r,s,t,u,v,w,x,y,z

anorm=0.                    !compute matrix norm for possible use in locating single
                            !small subdiagonal element
do 12 i=1,n
do 11 j=max(i-1,1),n
        anorm=anorm+abs(acoef(i,j))
11      continue
12    continue
        nn=n
        t=0.                        !Gets changed only by an exceptional shift
1       if(nn.ge.1)then         !Begin search for next eigenvalue
        its=0
2       do 13 l=nn,2,-1     !Begin iteration: look for single small subdiagonal element
        s=abs(acoef(l-1,l-1))+abs(acoef(l,l))
        if(s.eq.0.)s=anorm
        if(abs(acoef(l,l-1))+s.eq.s)goto 3
13      continue
        l=1
3       x=acoef(nn,nn)
        if(l.eq.nn)then                         !One root found
        wr(nn)=x+t
        wi(nn)=0.
        nn=nn-1
else
        y=acoef(nn-1,nn-1)
        w=acoef(nn,nn-1)*acoef(nn-1,nn)
if(l.eq.nn-1)then                       !Two roots found ...
        p=0.5*(y-x)
        q=p**2+w
        z=sqrt(abs(q))
        x=x+t
if(q.ge.0.)then                     !... a real pair
        z=p+sign(z,p)
        wr(nn)=x+z
        wr(nn-1)=wr(nn)
if(z.ne.0.)wr(nn)=x-w/z
        wi(nn)=0.
        wi(nn-1)=0.
else                                !... a complex pair
```

```
        wr(nn)=x+p
        wr(nn−1)=wr(nn)
        wi(nn)=z
        wi(nn−1)=−z
endif
        nn=nn−2
else                                      !No roots found. Continue iteration

if(its.eq.30) then
        write(*,*) 'too many iterations in hqr'
endif

if(its.eq.10.or.its.eq.20)then        !Form exceptional shift
        t=t+x
do 14 i=1,nn
        acoef(i,i)=acoef(i,i)−x
14          continue
        s=abs(acoef(nn,nn−1))+abs(acoef(nn−1,nn−2))
        x=0.75*s
        y=x
        w=−0.4375*s**2
endif
        its=its+1
do 15 m=nn−2,l,−1     !Form shift and then look for 2 consecutive
        z=acoef(m,m)        !small subdiagonal elements
        r=x−z
        s=y−z
        p=(r*s−w)/acoef(m+1,m)+acoef(m,m+1)
        q=acoef(m+1,m+1)−z−r−s
        r=acoef(m+2,m+1)
        s=abs(p)+abs(q)+abs(r)                !Scale to prevent overflow or underflow
        p=p/s
        q=q/s
        r=r/s
if(m.eq.l)goto 4
        u=abs(acoef(m,m−1))*(abs(q)+abs(r))
        v=abs(p)*(abs(acoef(m−1,m−1))+abs(z)+abs(acoef(m+1,m+1)))
if(u+v.eq.v)goto 4
15          continue
4           do 16 i=m+2,nn
        acoef(i,i−2)=0.
```

Appendix A.

```fortran
      if (i.ne.m+2) acoef(i,i-3)=0.
16          continue
do 19 k=m,nn-1                        ! Double QR step on rows 1 to nn and columns m to nn
          if(k.ne.m)then
          p=acoef(k,k-1)                    ! Begin setup of householder vector
          q=acoef(k+1,k-1)
          r=0.
          if(k.ne.nn-1)r=acoef(k+2,k-1)
          x=abs(p)+abs(q)+abs(r)
          if(x.ne.0.)then
          p=p/x                             !Scale to prevent overflow or underflow
          q=q/x
          r=r/x
          endif
          endif
          s=sign(sqrt(p**2+q**2+r**2),p)
          if(s.ne.0.)then
          if(k.eq.m)then
          if(l.ne.m)acoef(k,k-1)=-acoef(k,k-1)
          else
          acoef(k,k-1)=-s*x
          endif

          p=p+s
          x=p/s
          y=q/s
          z=r/s
          q=q/p
          r=r/p
do 17 j=k,nn                          !Row modification
          p=acoef(k,j)+q*acoef(k+1,j)
if(k.ne.nn-1)then
          p=p+r*acoef(k+2,j)
          acoef(k+2,j)=acoef(k+2,j)-p*z
endif
          acoef(k+1,j)=acoef(k+1,j)-p*y
          acoef(k,j)=acoef(k,j)-p*x
17          continue
do 18 i=l,min(nn,k+3)                 !Column modification
          p=x*acoef(i,k)+y*acoef(i,k+1)
          if(k.ne.nn-1)then
```

229

```
        p=p+z*acoef(i,k+2)
        acoef(i,k+2)=acoef(i,k+2)-p*r
        endif
        acoef(i,k+1)=acoef(i,k+1)-p*q
        acoef(i,k)=acoef(i,k)-p
18              continue
        endif
19          continue
goto 2                              !... for next iteration on current eigenvalue
        endif
        endif
goto 1                              !... for next eigenvalue
        endif
return
END
```

HYDMODX (HYDMODY)

The following section of the code indicate the instruction used to incorporate the sink term in the hydrodynamic calculations. Similar modifications were introduced in HYDMODY.

```
SUBROUTINE HYDMODX(IMAX,JMAX,JEND,C1,D1,D2,D3,D4,D5,D2BETA,D3CORI, &
D3WINC,ADVCON,NADVIT,NUMOUT,HOAT,RUFLEN,NFLWIN, &
WINVX,RTWINY,RTWINX)
INCLUDE 'HARBOUR.CMN'
DIMENSION P(IDIM),Q(IDIM),R(IDIM),S(IDIM)

!        COMMENCE CALCULATIONS OF HYDRODYNAMIC MODEL IN X-DIRECTION
!        MARINE TURBINE CALCULATIONS
!..........................................
VELMAG=ABS(UM(IBM1,J))
D3MARTURB=(D3*TURBDRAG(IBM1,J)*TURBARX(IBM1,J)* &
CT_OC(IBM1,J)*VELMAG)/(4.0)

BIBM1=QXL(IBM1,J)-D2BETA*(DUUHDX+DUVHDY)+D3CORI*QYMAV &
        -D4BDFR*QXL(IBM1,J)-D3MARTURB*UM(IBM1,J) &
        +WSTRESS-D1DPC*(EL(IB,J) &
        -EL(IBM1,J))+D5*EDDVAL*(UMR-TWO*UMC+UML)
TEMP1=ONE+D4BDFR+(D3MARTURB/DPC)
```

230

A.3.2   TVD-TOC

The implementation of momentum sink-TOC method in TVD-TOC was done via THRUSTFORCE module.

THRUSTFORCE MODULE

```fortran
MODULE ThrustForce
IMPLICIT NONE
REAL, DIMENSION(:,:), ALLOCATABLE :: CT, Ax, Ay
CONTAINS
!==================================================
! TURBINE AREA X- COMPONENT
!==================================================
SUBROUTINE MARTURB_X(IMAX, JMAX, IWET,IACT, QX, QY, DP, TURBDIAM, TURBSPA)
IMPLICIT NONE

!INPUT VARIABLES
INTEGER, INTENT(IN):: IMAX, JMAX
REAL, INTENT(IN):: TURBDIAM, TURBSPA
LOGICAL, DIMENSION(IMAX, JMAX), INTENT(IN) :: IWET,IACT
REAL, DIMENSION(IMAX, JMAX), INTENT(IN) :: DP, QX, QY

!LOCAL VARIABLES
INTEGER:: I,J
REAL :: U, V, UMAG, VMAG, THETA, ALPHA, TURBNUM, TURBAREA
REAL, PARAMETER :: CONPI = 4.0 * ATAN(1.0)

TURBNUM = 1.0/(TURBSPA**2.0)
TURBAREA = TURBNUM * ((TURBDIAM**2.00) * CONPI)/4.0

! CALCULATE Ax
!................................
!$OMP PARALLEL DO PRIVATE(I, J, U, V)
DO J = 2, JMAX-1
DO I = 1, IMAX

IF (IWET(I,J).EQ.7) THEN
        U = QX(I,J) / DP(I,J)
        V = QY(I,J) / DP(I,J)
```

```fortran
        UMAG = ABS(U)
        VMAG = ABS(V)
! ASSUMING TURBINE'S ORIENTATION IS NORMAL TO THE FLOW (PI/2 = 90^o)
! THETA [RADIANS]: ANGLE THAT THE CURRENT MAKES WITH THE HORIZONTAL (Horizontal =0.0)
! ALPHA [RADIAS]: ANGLE OF THE TURBINE WITH THE HORIZONTAL (PI/2 = 90^o - THETA)
IF (VMAG.EQ.0) THEN
        THETA = CONPI/2.0
ELSE
        THETA = ATAN(UMAG/VMAG)
        ALPHA = CONPI/2.0 - THETA
END IF
        Ax(I,J)=TURBAREA*COS(ALPHA)
IF (Ax(I,J).LT.0.0) THEN
        Ax(I,J)=0.0
END IF

IF (I.EQ.30)THEN
        WRITE(501,'(9F15.6)') Ax(I,J), TURBAREA, ALPHA, THETA, UMAG, VMAG
END     IF
ELSE
Ax(I,J)=0.0
END IF

END DO
END DO
!$OMP END PARALLEL DO
END SUBROUTINE MARTURB_X


!======================================================
! TURBINE AREA Y-COMPONENT
!======================================================
SUBROUTINE MARTURB_Y(IMAX, JMAX, IWET,IACT, QX, QY, DP, TURBDIAM, TURBSPA )
IMPLICIT NONE
!INPUT VARIABLES
INTEGER, INTENT(IN):: IMAX, JMAX
REAL, INTENT(IN):: TURBDIAM, TURBSPA
LOGICAL, DIMENSION(IMAX, JMAX), INTENT(IN) :: IWET,IACT
REAL, DIMENSION(IMAX, JMAX), INTENT(IN) :: DP, QX, QY

!LOCAL VARIABLES
INTEGER:: I,J
```

Appendix A.

```fortran
REAL :: U, V, UMAG, VMAG, THETA, ALPHA, TURBNUM, TURBAREA
REAL, PARAMETER :: CONPI = 4.0 * ATAN(1.0)


TURBNUM = 1.0/(TURBSPA**2.0)
TURBAREA = TURBNUM * ((TURBDIAM**2.00) * CONPI)/4.0


! CALCULATE Ay
!................................
!$OMP PARALLEL DO PRIVATE(I, J, U, V)
DO J = 2, JMAX-1
DO I = 1, IMAX

IF (IWET(I,J).EQ.7) THEN
        U = QX(I,J) / DP(I,J)
        V = QY(I,J) / DP(I,J)
        UMAG = ABS(U)
        VMAG = ABS(V)
IF (VMAG.EQ.0) THEN
        THETA = CONPI/2.0
ELSE
        THETA = ATAN(UMAG/VMAG)
        ALPHA = CONPI/2.0 - THETA
END IF
        Ay(I,J) = TURBAREA*SIN(ALPHA)
IF (Ay(I,J).LT.0.0) THEN
        Ay(I,J)=0.0
END IF


IF (I.EQ.30)THEN
        WRITE(502,'(9F15.6)') Ay(I,J), TURBAREA, ALPHA, THETA, UMAG, VMAG
END     IF
ELSE
        Ay(I,J)=0.0
END IF


END DO
END DO
!$OMP END PARALLEL DO
END SUBROUTINE MARTURB_Y

!=====================================================
```

233

Appendix A.

```
! CT- COEFFICIENT CALCULATION
!=====================================================================
SUBROUTINE MARTURB_CT(IMAX, JMAX, IWET,IACT,DP, QX, QY, TURBDIAM, TURBSPA, ALFA4_OC, &
 DX,  TIME,  FR_OC,  BETA4, ALFA4,  TURBAREA_2,  DEPTH, BLOCKAGE, ILOC, J_TLOC, JLOC, &
  JLOC3)
IMPLICIT NONE

!INPUT VARIABLES
INTEGER, INTENT(IN):: IMAX, JMAX
REAL, INTENT(IN):: TURBDIAM, TURBSPA, ALFA4_OC,  DX, TIME
LOGICAL, DIMENSION(IMAX, JMAX), INTENT(IN) :: IWET,IACT
REAL, DIMENSION(IMAX, JMAX), INTENT(IN) :: DP, QX, QY

!LOCAL VARIABLES
INTEGER:: I, J
INTEGER, PARAMETER::m=4          !Polinomial Degree
REAL:: BLOCKAGE, TURBAREA, TURBAREA_2, TURBNUM, TURBNUM_2, DEPTH, BETA4, ALFA4, A4C, &
&               A3C, A2C, A1C, A0C, a(m+1),rtr(m), rti(m), FR_OC,U_OC, V_OC,   FR_US, &
&         GRAV, ILOC, JLOC, TWO_TP_SEC, J_TLOC_U, J_TLOC_D, J_TLOC,   &
&          U_DF, V_DF, U_UF, V_UF, JLOC3, V_OC_up, V_OC_down, FR_OC_up, FR_OC_down, &
 FR_OC_2, H_OC
REAL, PARAMETER :: CONPI = 4.0 * ATAN(1.0)

! TURBINE-AREA AND B-GRID
TURBNUM = 1.0/(TURBSPA**2.0)
! TO BE USED IN THE TFORCE CALCULATION IN THE MODEL
TURBAREA = TURBNUM * ((TURBDIAM**2.00) * CONPI)/4.0
! TO BE USED IN THE POWER CALCULATION POST-PROCESSING
TURBAREA_2 = TURBAREA*(DX**2)

! (DX**2) - COMPENSATE THE TURBINE AREA DEFINITION USED
!(PER GRID CELL, AS THE TRUSTH FORCE IS DONE PER GRID CELL TF/(DX*DY))
BLOCKAGE = (TURBAREA/(DEPTH*DX))*(DX**2)

! VARIABLES THAT MAY REQUIRE UPDATE
! UPSTREAM CONDITIONS - LOCATION
        ILOC =30
        J_TLOC=70
        JLOC=J_TLOC-1
        JLOC3 = J_TLOC+1
        DEPTH=40.00
```

Appendix A.

```
        GRAV=9.80665
! ALFA4
        LFA4=ALFA4_OC
! TIME CONDITION
        TWO_TP_SEC=89424


IF(TIME.GT.TWO_TP_SEC) THEN
! CALCULATE FR
!$OMP PARALLEL DO PRIVATE(I, J, U_OC, V_OC)
DO J = 2, JMAX-1
DO I = 1, IMAX

! AT TURBINES ARRAY
IF (IWET(I,J).EQ.7) THEN
!.................................
! Up-stream velocity
!.................................
        U_OC = QX(I,JLOC) / DP(I,JLOC)
        V_OC = QY(I,JLOC) / DP(I,JLOC)
        H_OC = DP(I,JLOC)
IF (V_OC.GT.0) THEN
        U_OC = QX(I,JLOC) / DP(I,JLOC)
        V_OC = QY(I,JLOC) / DP(I,JLOC)
        H_OC = DP(I,JLOC)
IF (V_OC.LT.0.02) THEN
        V_OC = 0.02
END IF
ELSE
        U_OC = QX(I,JLOC3) / DP(I,JLOC3)
        V_OC = QY(I,JLOC3) / DP(I,JLOC3)
        H_OC = DP(I,JLOC3)
END IF

! FROUDE NUMBER UPSTREAM
        FR_OC_2 = ABS(V_OC)/SQRT(H_OC*GRAV)
        FR_OC = (V_OC)/SQRT(DEPTH*GRAV)
        A4C = (FR_OC**2)/2         !B4^4 COEFFICIENT
        A3C = 2*ALFA4*FR_OC**2        !B4^3 COEFFICIENT
        A2C = -2 + 2*BLOCKAGE - FR_OC**2    !B4^2 COEFFICIENT
        A1C = -4*ALFA4 - 2*ALFA4*FR_OC**2  + 4    !B4 COEFFICIENT
        A0C = (FR_OC**2)/2 + 4*ALFA4 - 2*BLOCKAGE*ALFA4**2  - 2   !CTE COEFFICIENT
```

```
        a = (/A0C, A1C, A2C, A3C, A4C/)          ! Coefficients
! !BETA4 CALCULATION − Solve the eigenvalue system
!mm − M POLYNOMIAL DEGRE (4)
! rtr − OUTPUT  VECTOR FOR REAL ROOTS
! rti − OUTPUT  VECTOR FOR COMPLEX ROOTS
        CALL zrhqr(a,m, rtr , rti )
        BETA4 = rtr (3)
!!CALCULATE CT−THURST COEFFICIENT
        CT( I ,J)=BETA4∗∗2 − ALFA4∗∗2
ELSE
        CT( I ,J)=0.0
END IF    !IWET=7 CONDITION
END DO
END DO
!$OMP END PARALLEL DO
ELSE
        CT( I ,J)=0.0
END IF !2∗TM2  CONDITION
END SUBROUTINE MARTURB_CT
```

The following step is the polynomial's root calculation. The procedure used is similar to the the section of the code highlighted in green in Section A.3.1

```
END MODULE ThrustForce
```

MACX (MACY)

The following section of the code highlight in yellow the modifications made in MACCORMACK module, particularly in the predictor step of MACX subroutine. Similar modifications were introduced in the MACX's corrector step and MACY's predictor and corrector step.

```
   SUBROUTINE MACX( IMAX, JMAX, NFLCHZ, NFLTURB, PRESET, DPMIN, PRESES, SSLOPE, DT,&
&  DX, ANGLAT, BETA,      IWET, IALL, IACT, VARCHZ, QM, H, ETL, QXL, QYL, ETU, QXU,&
&  QYU, TURBDIAM, TURBSPA, ALFA4_OC, TIME, FR_OC, BETA4, ALFA4, TURBAREA_2, DEPTH,&
& BLOCKAGE, ILOC, J_TLOC, JLOC, JLOC3)
IMPLICIT NONE
```

Appendix A.

```
!MAIN VARIABLES
INTEGER, INTENT(IN) :: IMAX, JMAX, NFLCHZ, NFLTURB
REAL, INTENT(IN) :: PRESET, DPMIN, PRESES, SSLOPE, DT, DX, ANGLAT, BETA, TURBDIAM, &
& TURBSPA, ALFA4_OC, TIME
LOGICAL, DIMENSION(IMAX,JMAX), INTENT(IN) :: IWET, IALL
REAL, DIMENSION(IMAX,JMAX), INTENT(IN) :: VARCHZ, QM, H
REAL, DIMENSION(IMAX,JMAX), INTENT(INOUT) :: QXL, QYL, ETL
LOGICAL, DIMENSION(IMAX,JMAX), INTENT(INOUT) :: IACT
REAL, DIMENSION(IMAX,JMAX), INTENT(OUT) :: ETU, QXU, QYU
REAL :: FR_OC, BETA4, ALFA4, TURBAREA_2, DEPTH, BLOCKAGE, ILOC, J_TLOC, JLOC, JLOC3,&
& U_OC, V_OC, H_OC

!LOCAL VARIABLES
INTEGER :: I, IM1, IP1, J
REAL :: TTMP, DTDX, HDT, HDTDXG, DTDXBETA, DTG, DTCORI, DET, QYTMP, ETTMP

!ALLOCATE ARRAYS
ALLOCATE( CHZ(IMAX,JMAX), DP(IMAX,JMAX), FX(IMAX,JMAX), FY(IMAX,JMAX), ETM(IMAX,JMAX), &
QXM(IMAX,JMAX), QYM(IMAX,JMAX), CT(IMAX,JMAX), Ax(IMAX,JMAX) )
!DERIVED VALUES
DTDX = DT / DX
HDT = 0.5 * DT
HDTDXG = 0.5 * DTDX * 9.81
DTDXBETA = DTDX * BETA
DTG = DT * 9.81
DTCORI = DT * 3.1415926 * SIN(ANGLAT * 3.1415926 / 180.0) / 21600.0
DET = SSLOPE * DX
!TURBINE J-LOCATION
        ILOC = 376
        J_TLOC= 406
! UPSTREAM CONDITIONS - LOCATION
        JLOC=J_TLOC-1
        JLOC3 = J_TLOC+1


! ————————————————————————————————————————————————————
!    RESET MAIN VARIABLES
! ————————————————————————————————————————————————————
!$OMP PARALLEL
!$OMP DO PRIVATE(I, J)
DO J = 1, JMAX
DO I = 1, IMAX
IF( IALL(I,J) ) THEN
```

237

Appendix A.

```
!RESET VALUES
ETL(I,J) = ETU(I,J)
QXL(I,J) = QXU(I,J)
QYL(I,J) = QYU(I,J)
!DRYING CHECK
DP(I,J) = H(I,J) + ETL(I,J)
IF ( DP(I,J) .GT. PRESET ) THEN
IACT(I,J) = .TRUE.
ELSE
IACT(I,J) = .FALSE.
QXL(I,J) = 0.0
QYL(I,J) = 0.0
END IF
END IF
END DO
END DO
!$OMP END DO


!$OMP DO PRIVATE(I,  J)
DO J = 1, JMAX
DO I = 2, IMAX-1
!THE VELOCITY AT WET/DRY INTERFACE SHOULD BE 0
IF ( IWET(I,J) .AND. IACT(I,J) ) THEN
IF ( (.NOT.IACT(I-1,J)) .OR. (.NOT.IACT(I+1,J)) ) THEN
QXL(I,J) = 0.0
END IF
END IF
END DO
END DO
!$OMP END DO
!$OMP END PARALLEL


!CALCULATE CHEZY VALUE
CALL CHEZY( IMAX, JMAX, IACT, QXL, QYL, VARCHZ, NFLCHZ )


!CALCULATE X-DIRECTION ADVECTION TERMS
CALL FUFV( IMAX, JMAX, IACT, QXL, QYL, DP )
!CALCULATE TURBINE AREA X-DIRECTION AND THRUST COEFFIENT
CALL MARTURB_X(IMAX, JMAX, IWET,IACT, QXL, QYL, DP, TURBDIAM, TURBSPA)

CALL MARTURB_CT(IMAX, JMAX, IWET,IACT,DP, QXL, QYL, TURBDIAM, TURBSPA, ALFA4_OC, DX, TIME, &
```

238

```
& FR_OC,   BETA4, ALFA4,   TURBAREA_2,   DEPTH,   BLOCKAGE, ILOC, J_TLOC, JLOC, JLOC3)
! ———————————————————————————————————————————————————————
!   PREDICTOR STEP
! ———————————————————————————————————————————————————————
!$OMP PARALLEL
!$OMP DO PRIVATE(I, J, IP1, IM1, TTMP) SCHEDULE(DYNAMIC, 10)
DO J = 2, JMAX − 1
DO I = 2, IMAX − 1
IF ( IWET(I,J) ) THEN

!CONTINUITY EQUATION − X DIRECTION
IP1 = I + 1
ETM(I,J) = ETL(I,J) + HDT * QM(I,J) − DTDX * (QXL(IP1,J) − QXL(I,J))

IF ( IACT(I,J) ) THEN
IM1 = I − 1
!ACTIVE POINTS
IF ( IACT(IP1,J) .AND. IACT(IM1,J) )  THEN
!ADVECTIVE ACCELERATION − X DIRECTION
        QXM(I,J) = QXL(I,J) − DTDXBETA * (FX(IP1,J) − FX(I,J)) + DTCORI * QYL(I,J)
!PRESSURE GRADIENT (WATER SLOPE) − X DIRECTION
        TTMP = ETL(IP1,J) − ETL(I,J)
IF ( (DP(I,J).LT.PRESES .OR. DP(IP1,J).LT.PRESES) .AND. ABS(TTMP).GT.DET ) THEN
        QXM(I,J) = QXM(I,J) − HDTDXG * (DP(I,J) + DP(IP1,J)) * SIGN(DET,TTMP)
ELSE
        QXM(I,J) = QXM(I,J) − HDTDXG * (DP(I,J) + DP(IP1,J)) * TTMP
END IF
!BED FRICTION − X DIRECTION
        TTMP = DTG * SQRT(QXL(I,J)**2 + QYL(I,J)**2) / (DP(I,J) * CHZ(I,J))**2
IF (TTMP .LT. 0.3) THEN
!EXPLICIT SCHEME FOR BED FRICTION TERM
        QXM(I,J) = QXM(I,J) − TTMP * QXL(I,J)
ELSE
!SEMI−IMPLICIT SCHEME FOR BED FRICTION TERM
        QXM(I,J) = QXM(I,J) / (1.0 + TTMP)
END IF
IF (NFLTURB .NE. 0) THEN
!THRUST FORCE, PREDICTOR STEP,   X−DIRECTION

!! UPSTREAM CONDITIONS
IF  (IWET(I,J).EQ.7) THEN
        U_OC = QXL(I,JLOC) / DP(I,JLOC)
```

```
      H_OC = DP(I,JLOC)
IF (U_OC.GT.0) THEN
      U_OC = QXL(I,JLOC) / DP(I,JLOC)
      H_OC = DP(I,JLOC)
IF (U_OC.LT.0.02) THEN
      U_OC = 0.02
END IF
ELSE
      U_OC = QXL(I,JLOC3) / DP(I,JLOC3)
      H_OC = DP(I,JLOC3)
END IF
      TTMP=HDT*(ABS(U_OC)*(U_OC))*Ax(I,J)
      QXM(I,J) = QXM(I,J) - TTMP*CT(I,J)
END IF ! IWET=7 COND
END IF   ! NFLTURB COND
 ELSE
      QXM(I,J) = 0.0
END IF   !        ACTIVE POINTS
!ADVECTIVE ACCELERATION - Y DIRECTION
      QYM(I,J) = QYL(I,J) - DTDXBETA * (FY(IP1,J) - FY(I,J))
ELSE
!INACTIVE POINTS
      QXM(I,J) = QXL(I,J)
      QYM(I,J) = QYL(I,J)
END IF
END IF
END DO
END DO
!$OMP END DO
```

A.4   Resource Assessment

Tidal-stream resource assessment was calculated as a post-processing simulation step. To read the outputs of a single simulation and calculate metrics required for the assessment a MATLAB code was used, it was denoted as Turb-MATvar.m Later, results from multiple simulations were compared with COM-Turb-MATvar.m file. Both files were adjusted for the wake induction factor and blockage ratio evaluation, and for the

fence and partial-fence analysis. The following files show the general procedure used to assess the resource simulated with ADI-TOC and TVD-TOC. For practical reasons the figures plotting is omitted.

A.4.1 Turb-MATvar.m

```
clear all; close all; clc
tic
%% LOCATION
        path ='XX\';
        ext = '.png';
% % Monitoring points
%.........................................................................
        I_CSTA = [ 376 376 376 376 376 376 376 376 376 376 376];
        J_CSTA = [1    2   406 811 812  405 396 407 416 367 447 ];
% Stations number
        numfiles_ts = length(J_CSTA);
% Boundary
        j_bd1 =[1 2]; j_bd2 =[4 5];
% Middle channel (Turbine array location)
        js3 = 3;
% upstream    (Before Fence)
        j_up_1C =6;           j_up_10C =7;
% Entrance chhanel/ UC1 /  UC2
        j_sts_Bfence = [ 10 7 6];
% downstream    (After Fence)
        j_d_1C =8;      j_d_10C =9;
% Exit chhanel/ UC1 /  UC2
        j_sts_Afence = [8 9 11];
rho = 1026;    %Water density.(kg/m^3)
g = 9.81;         %(m/s^2)


%% EXTRACTING DOMAIN  VARIABLES
        path_file = 'XX\';
        file = 'VAR_DOMAIN_FENCE';
        fname = fullfile(path_file, file); parameters = load(fname);
% turbine location (single cell)
        jturb = parameters.jturb_loc;
        iturb = parameters.iturb_loc_sc;
```

Appendix A.

```matlab
% fence  i- location
        ifence = parameters.fence;
% transect
        jvector = parameters.minVal_1j:parameters.maxVal_1j;
        jvector_2 = jvector(2:end-1);
% Transect plot
        ifence_tran = ifence(10);
% Domain size
        imax = parameters.maxVal_1i;
        jmax =parameters.maxVal_1j;
        DELX=parameters.DX;
% J-location; Entrance/ Exit channel
        j_ch_ent = parameters.minLan_1j;
        j_ch_exit = parameters.maxLan_1j;
        j_ch_cell_length = parameters.L_CELL;
% meters
        L_meters = parameters.parameters.L;
        W_meters = parameters.parameters.W;


%% TURBINE FEATURES
        SS= dlmread('OC_TURBINE_FEATURES.DAT','',1,0);
        TURBSPA = SS(1); %m
        DELX = SS(2); %m
        TURBDIAM = SS(3);
        HFIX = SS(4); %m
        B = SS(5); %B_OC
        TURBAREA_F = SS(6);%1/m * m^2
        bh_term = TURBAREA_F/B;
        rho = 1026;    %Water density.(kg/m^3)
        h = HFIX;
        g = 9.81;          %(m/s^2)


%% DISCRETE TIME
        discrete_time=  [ 38.700   38.750    38.800]; %(HR)
        numfiles = length(discrete_time);
% Snapshot time (Vmax time)
        tdis = 2;
%% FLOW FIELD
numfiles_2 = tdis; % snapshot file to be plot
for k =1
    myfilename = sprintf('%s%c%s', 'SHANNON1','A'-1+k,'.HYD'); %order A->Z
```

242

```matlab
        M = dlmread(myfilename,'',3,0);
        ii = M(:,1);
        jj = M(:,2);
        [row,colm]=size(ii);
end
%  Arrays declaration
            um = ones(row,numfiles_2);
            vm = ones(row,numfiles_2);
             ele = ones(row,numfiles_2);


%  Arrays fillin up
for  k = 1: numfiles_2;
        myfilename = sprintf('%s%c%s', 'SHANNON1','A'-1+k,'.HYD'); %order A->Z
        M = dlmread(myfilename,'',3,0);
        um(:,k) = M(:,3);
        vm(:,k) = M(:,4);
        ele(:,k) = M(:,5);
end
[col,row]=size(vm(:,1));


% Reshaping
% Need MaxX, MaxY to resize as matrices for fore viewing
            Maxjj=max(max(jj));            Maxii = max(max(ii));
            jj = reshape(jj, Maxjj,[]);    ii = reshape(ii, Maxjj,[]);
            jj = jj(:,1);    ii = ii(1,:);
% mts
            iim=ii*DELX; jjm=jj*DELX;
for  NFRAMES = tdis
        um_2 = reshape(um(:,NFRAMES), Maxjj, []);
        vm_2 = reshape(vm(:,NFRAMES), Maxjj, []);
        ele_2 = reshape(ele(:,NFRAMES), Maxjj, []);
        % % % normalizing VM-snapshot
        % %       vm_max_r = max(vm_2); %max rows
        % %       vm_max_c = max(vm_max_r); %max columns
        % %     vm_2n = vm_2./vm_max_c;


        % omitting normalization at the moment
        um_2n = um_2;
        vm_2n = vm_2;
        ele_2n = ele_2;
```

243

Appendix A.

```
% Contour of vm velocity component, spaced equally at 20 increment between
% maximum and minimum.
maxvm = max( vm_2n );                    minvm = min( vm_2n );
Mmaxvm=(max(maxvm));                     Mminvm = (min(minvm));


maxele = max( ele_2n );                  minele = min( ele_2n );
Mmaxele=(max(maxvm));                    Mminele = (min(minvm));


max_um = max( um_2n );                   min_um = min( um_2n );
Mmax_um=(max(max_um));                   Mmin_um = (min(min_um));


 zinc =(Mmaxvm − Mminvm) /20;        zlevels = Mminvm : zinc : Mmaxvm;


 zinc_ele =(Mmaxele − Mminele) /20;      zlevels_ele = Mminele : zinc_ele : Mmaxele;


 zinc_um =( Mmax_um − Mmin_um) /20;      zlevels_um = Mmin_um : zinc_um : Mmax_um;
end



% % I , J −>I2 , J2 FOR SNAPSHOT PLOT
        [Im,Jm]=meshgrid( iim , jjm );
        Im_L = Im/L_meters ; % normalize with respect to "L"
        Jm_L = Jm/L_meters ;

%% TRANSECT
        um_transect =um_2 ( : , ifence_tran );
        vm_transect =vm_2 ( : , ifence_tran );
        ele_transect =ele_2 ( : , ifence_tran );
% % J −>J2
        %  j2 = jj − jturb ;     % Turbine location is the NEW origin
        j2 = jj − j_ch_ent ;    % Channel entrance is the NEW origin
        j2_m = j2 ∗ DELX;         % meters
        j2_m_L = j2_m/L_meters ;
% Array location
        jturb_vector  = jturb∗ones (1 ,length( ifence ));
        jturb_vector_mL=jturb_vector ∗(DELX/ L_meters );
        ifence_mL =ifence ∗(DELX/ L_meters );


%% TIME SERIES
for k=1
    myfilename=sprintf( '%s%c%s ', 'SHANNON1' , 'A'−1+k , '.VEL') %order A−>Z
```

244

```
    M = dlmread(myfilename,'',6,0);
    ts_TIME = M(:,1);
end


for k=1 : numfiles_ts    % counter for total number of files
    myfilename=sprintf('%s%c%s', 'SHANNON1','A'-1+k,'.VEL');
    M = dlmread(myfilename,'',6,0);
    ts_UX(:,k)   = M(:,2);
    ts_UY(:,k) = M(:,3);
    ts_UMAG(:,k) = M(:,4);
    ts_ELE(:,k) = M(:,5);
end


%% LAST  TYDAL CYLE    (MONITORING POINTS)
% initial time (t0) and indice (ind0)
        t0 = ts_TIME(end)-12.42;
        benchmark = (ts_TIME(2)-ts_TIME(1));
        ind0=find(abs(ts_TIME-t0)<=benchmark);
%indice choosen
        iind0= ind0(1) ;


% Parameters   in  the  last  tidal  cycle
%..................................................
% middle channel
        UY_DIR_s = ts_UY(iind0:end, js3);
        ELE_s = ts_ELE(iind0:end,  js3);
        ts_TIME_s=ts_TIME(iind0:end);
%Vmax
        Vmax_st3 = max(UY_DIR_s);
%indice
        benchmarck =5.5556e-07;
        vind2=find(abs(UY_DIR_s-Vmax_st3)<=benchmarck);
        vind=vind2(1);
%H
        heta0_vmax= ELE_s(vind) ;
%time
        TIME_choosen = ts_TIME_s(vind);
% Time in tidal cycles
        TIMETM2_s =ts_TIME_s./12.42;
        TIME_choosen_M2 = TIME_choosen./12.42;
% Water drop data
```

```
          UY_d_s_1C = ts_UY(iind0:end, j_d_1C);        ELE_d_s_1C = ts_ELE(iind0:end, j_d_1C);
          UY_up_s_1C = ts_UY(iind0:end, j_up_1C);      ELE_up_s_1C = ts_ELE(iind0:end, j_up_1C);
          dh_data_1C= abs(ELE_up_s_1C - ELE_d_s_1C);


%% OCH- PARAMETERS
% NC-cell number counter
% PFL- partial fence length(number of cells)
PFL = 1; %fence


for NC=1:PFL;
    myfilename=sprintf('%s%c%s', 'CELL','1'-1+NC,'_OC_PARAMETERS.DAT');
    M = dlmread(myfilename,'',2,0);
    TIMEHR = M(:,2);
    ALFA4 = M(1,6); %As ALFA4=cte
    [row,colm]=size(TIMEHR);
end


%Arrays declaration
    VM_OC = ones(row,PFL);
    FR = ones(row,PFL);
    CT_OC = ones(row,PFL);
    BETA4 = ones(row,PFL);
    HX_OC = ones(row,PFL);
%  Arrays fillin up
for NC=1;
    myfilename=sprintf('%s%c%s', 'CELL','1'-1+NC,'_OC_PARAMETERS.DAT');
    M = dlmread(myfilename,'',2,0);
            VM_OC(:,NC) = M(:,3);
            FR(:,NC) = M(:,5);
            FR_S = FR.^2; % FR^2
            CT_OC(:,NC) = M(:,7);
            BETA4(:,NC) = M(:,8);
            HX_OC(:,NC) = M(:,9);
    %% ALFA2
            a_alfa2 = ALFA4.*(BETA4(:,NC) -1);
            b_alfa2 = (BETA4(:,NC) - ALFA4)*B;
            c_alfa2 = 1 -((FR_S(:,NC).*(BETA4(:,NC) +1))* 1/2);
            d_alfa2 = a_alfa2./b_alfa2;
            ALFA2(:,NC)   = d_alfa2.*c_alfa2;
    %%  CP
            CP_OC(:,NC) = ALFA2(:,NC).*CT_OC(:,NC);
```

Appendix A.

```matlab
%% LAST  TYDAL  CYLE
% initial time (t0) and indice (ind0)
        t0 = TIMEHR(end)−12.42;
        benchmark = (TIMEHR(2)−TIMEHR(1));
        ind0=find(abs(TIMEHR−t0)<=benchmark);
%indice choosen
        iind0= ind0(2) ;
% Parameters  in the last tidal cycle
%...........................................................................
        VM_OC_s(:,NC)=(VM_OC(iind0:end,NC));
        VM_OC_s = abs(VM_OC_s);
        HX_OC_s(:,NC)=(HX_OC(iind0:end,NC));
        CP_s(:,NC)=(CP_OC(iind0:end,NC));
        CT_s(:,NC)=(CT_OC(iind0:end,NC));
        FR_s(:,NC)=(FR(iind0:end,NC));
        ALFA2_s(:,NC)=(ALFA2(iind0:end,NC));
        BETA4_s(:,NC)=(BETA4(iind0:end,NC));
        TIMEHR_s=(TIMEHR(iind0:end));
%Vmax
        Vmax = max(abs(VM_OC_s));
%indice
        benchmarck =5.5556e−07;
        vind2=find(abs(VM_OC_s(:,NC)−Vmax(:,NC))<=benchmarck);
        vind=vind2(1);
%H
        heta0_vmax(:,NC)= HX_OC_s(vind,NC);
%time
        TIME_choosen = TIMEHR_s(vind);
%CP for Vmax
        CP_vmax(:,NC)= CP_s(vind,NC);
%CT for Vmax
        CT_vmax(:,NC)= CT_s(vind,NC);
end


%%   POWER AND FLOW RATE
% Max Power
        P_OC_max= 0.5*rho*(Vmax.^3)*TURBAREA_F*CP_vmax;
% Power time series
        P_OC_ts = 0.5*rho*(VM_OC_s.^3)*TURBAREA_F.*CP_s;
% Max Flow rate
        Q0_max = (heta0_vmax*DELX)* Vmax;
```

Appendix A.

```matlab
% Flow rate time series
        Q0_ts = (HX_OC_s*DELX).* VM_OC_s;


%% ANALYTICAL WATER DROP
a1 =   ones(size(CT_s))*1/2;
b1 = - ones(size(CT_s))*3/2;
c1 =  CT_s*B;
c11= c1.*FR_s.^2;
c2 =  1 - FR_s.^2 + (c11./2);
d2 = - c11./2;


%  dh/h root calculation (matlab)
for scase = 1:length(a1);
    % Polynomial
    p_dhh = [a1(scase) b1(scase) c2(scase) d2(scase)];
    %Roots .....................................
    r_dhh = roots(p_dhh);
    rg_real = (r_dhh);


    % function
    fp_2 = @(x)    p_dhh(1)*x.^3 + p_dhh(2)*x.^2 + p_dhh(3)*x  + p_dhh(4);
    % fzero method (Brent)
    for i = 1:length(rg_real)
        rs_fzero(i) = fzero(fp_2,rg_real(i));
    end
    r_dhh_final =rs_fzero;
    % Saving roots
    r1_dhh(scase) = r_dhh_final(1);
    r2_dhh(scase) = r_dhh_final(2);
    r3_dhh(scase) = r_dhh_final(3);
end
%% dh/h
        dh_h = r3_dhh;
%% dh
        dh_1 = r1_dhh*HFIX;
        dh_2 = r2_dhh*HFIX;
        dh_3 = r3_dhh*HFIX;
        dh = dh_3;


% size dh-NUMERICAL
        [nc_ana nr_ana] = size(dh) ;
```

```
                [nc_num nr_um] = size(dh_data_1C) ;
                factor_rs = nr_ana/nc_num;
                rfactor_rs = round(factor_rs) ;
% VEL–OC
                VEL_UPS_abs_rs = VM_OC_s(1:rfactor_rs:end,1)    ;
% ALFA2
                ALFA2_rs = ALFA2_s(1:rfactor_rs:end,1)    ;
% FR
                FR_rs = FR_s(1:rfactor_rs:end,1)    ;


%% dh —— NUMERICAL
                dh_num = dh_data_1C(1:end-1);
%% dh/h —— NUMERICAL
                dh_h_num=abs(dh_num/HFIX);
%%  EFFICIENCY
for n = 1: length(dh_h);
    eta_1(n) = ALFA2_s(n)*(((1 - (dh_h(n))*(1/2))  - FR_s(n)^2*(1 - dh_h(n))^-1)/(1- FR_s(n)^2*...
        (1 - (dh_h(n))*(1/2)) * (1 - dh_h(n))^-2));
    eta_2(n) = ALFA2_s(n)*(1 - dh_h(n)*(1/2));
end


%%   EFFICIENCY   NUMERICAL
for n = 1: length(dh_num);
    eta_1_num(n) = ALFA2_rs(n)*(((1 - (dh_h_num(n))*(1/2))  - FR_rs(n)^2*...
        (1 - dh_h_num(n))^-1)/(1- FR_rs(n)^2*(1 - (dh_h_num(n))*(1/2)) * (1 - dh_h_num(n))^-2));
    eta_2_num(n) = ALFA2_rs(n)*(1 - dh_h_num(n)*(1/2));
end


%% TOTAL POWER EXTRACTED
for n = 1: length(dh_h);
    PPW(n) = g*rho*VM_OC_s(n)*(bh_term)*dh(n)*(1 - FR_s(n)^2*...
        ((1-(dh_h(n))*(1/2))/(1-(dh_h(n)))^2));
end


%% TOTAL POWER EXTRACTED NUMERICAL
for n = 1: length(dh_num);
    PPW_num(n) = g*rho*VEL_UPS_abs_rs(n)*(bh_term)*dh_num(n)*(1 - FR_rs(n)^2*...
        ((1-(dh_h_num(n))*(1/2))/(1-(dh_h_num(n)))^2));
end


%% POWER AVAILABLE
```

Appendix A.

```matlab
for n = 1: length(dh_h);
    Pa_1(n) = eta_1(n) * PPW(n);
    Pa_2(n) = eta_2(n) * PPW(n);
end

%% POWER AVAILABLE NUMERICAL
for n = 1: length(dh_num);
    Pa_1_num(n) = eta_1_num(n) * PPW_num(n);
    Pa_2_num(n) = eta_2_num(n) * PPW_num(n);
end

%% POWER DISSIPATED
Pdisi = PPW - Pa_1;
Pdisi_2 = PPW - Pa_2;

%% POWER DISSIPATED NUMERICAL
Pdisi_num = PPW_num - Pa_1_num;
Pdisi_2_num = PPW_num - Pa_2_num;

%%  MEAN VALUES
% Time average per grid cell;
% ANALYTICAL
        dh_h_mean = mean(abs(dh_h));
        dh_mean = mean(abs(dh));
        eta_1_mean=mean(abs(eta_1));
        eta_2_mean=mean(abs(eta_2));
        PPW_mean=mean(abs(PPW));
        Pa_1_mean=mean(abs(Pa_1));
        Pa_2_mean=mean(abs(Pa_2));
        Pdisi_mean=mean(abs(Pdisi));
        Pdisi_2_mean=mean(abs(Pdisi_2));
% NUMERICAL
        dh_h_num_mean = mean(abs(dh_h_num));
        dh_num_mean = mean(abs(dh_num));
        eta_1_num_mean=mean(abs(eta_1_num));
        eta_2_num_mean=mean(abs(eta_2_num));
        PPW_num_mean=mean(abs(PPW_num));
        Pa_1_num_mean=mean(abs(Pa_1_num));
        Pa_2_num_mean=mean(abs(Pa_2_num));
        Pdisi_1_num_mean=mean(abs(Pdisi_num));
        Pdisi_2_num_mean=mean(abs(Pdisi_2_num));
```

250

```
%% SAVING WORKSPACE
    path_com ='XX\';
    name ='1C_CONF_E9';              %Experiment 09
    save([path_com name '.mat'])     %For P's comparison different B's
    disp('Time_Elapse_(min)')             %Time elapse
    toc/(60)
```

A.4.2   COM-Turb-MATvar.m

```
clc; clear all; close all;
%% LOCATION
          path ='XX\';
          ext = '.png';
%% EXTRACTING DOMAIN  VARIABLES
          path_file = 'XX\';
          file = 'VAR_DOMAIN_FENCE';
          fname = fullfile(path_file,file);
          parameters = load(fname);
% Variables
          jturb = parameters.jturb_loc;
          ifence = parameters.fence;
% picking up a cell wich is representative of the fence situtation
          len = length(ifence); len_2 = round(len/2);
          iturb = ifence(len_2);
          NC =1.0; %Fence
%transect
          jvector = parameters.minVal_1j:parameters.maxVal_1j;
          jvector_2 = jvector(1:end-1);
%transect length
          jini = parameters.minVal_1j;
          jmax = parameters.maxVal_1j;
% channel lenght (j direction)
          ch_ini_j = parameters.minLan_1j;
          ch_end_j = parameters.maxLan_1j;
%% DATA
nexp = 9 ;           %number of experiments
mydata = cell(1, nexp);
for k=1:nexp;
    myfilename=sprintf('1C_CONF_E%d.mat',k); %order 0->nexp
    mydata{k}=importdata(myfilename);
end
```

```
        FE01 = mydata{1,1}; % -> B=0.0
        FE02 = mydata{1,2}; %Experiment 02 -> B=0.1
        FE03 = mydata{1,3}; %Experiment 03 -> B=0.2
        FE04 = mydata{1,4}; %Experiment 04 -> B=0.3
        FE05 = mydata{1,5}; %Experiment 05 -> B=0.4
        FE06 = mydata{1,6}; %Experiment 06 -> B=0.5
        FE07 = mydata{1,7}; %Experiment 07 -> B=0.6
        FE08 = mydata{1,8}; %Experiment 08 -> B=0.7
        FE09 = mydata{1,9};
% variables
        discrete_time = FE01.discrete_time; %(HR)
        HFIX = FE01.depth;
        DELX= FE02.DELX;
        TIMETM2_s = FE02.TIMETM2_s;
        TIME_s = TIMETM2_s*12.42;
        NC = FE02.NC;
%% NATURAL STATE
        ts_TIME_s = FE01.ts_TIME_s;
        ts_TIME = FE01.ts_TIME;
        UY_DIR_s_NTS=FE01.UY_DIR_s;
        UY_DIR_s_NTS= abs(UY_DIR_s_NTS);
        UY_DIR_s_NTS_mean=mean(UY_DIR_s_NTS);
        ELE_s_NTS = FE01.ELE_s;
        UY_NTS = FE01.ts_UY;
        ELE_NTS = FE01.ts_ELE;
        Q0_ts_NTS = FE01.Q0_ts;
        H = ELE_s_NTS + HFIX;
        FR_NTS = FE01.FR_ts_s;
% Channel cross section width
        W_CELL = FE01.W_CELL;
% Maximum velocity in the tidal cycle
        T_Uy_01 = [ FE01.Vmax_st3,  FE02.Vmax, FE03.Vmax, FE04.Vmax, FE05.Vmax,...
            FE06.Vmax, FE07.Vmax, FE08.Vmax, FE09.Vmax];
        T_heta_vmax = [ FE01.heta0_vmax,  FE02.heta0_vmax, FE03.heta0_vmax,...
            FE04.heta0_vmax, FE05.heta0_vmax,FE06.heta0_vmax, FE07.heta0_vmax,...
            FE08.heta0_vmax, FE09.heta0_vmax];
%%    VM & ELE

%% VM & ELE - BD
% j_bd1 =[1  2];
        j_bd1= FE03.j_bd1;
```

Appendix A.

```matlab
% j_bd2  =[4  5];
        j_bd2= FE03.j_bd2;
% VEL
station = j_bd1(1);
T_BD1_VEL_CELL1 = [ FE01.ts_UY(:,station),  FE02.ts_UY(:,station), FE03.ts_UY(:,station),...
    FE04.ts_UY(:,station), FE05.ts_UY(:,station),...
    FE06.ts_UY(:,station), FE07.ts_UY(:,station), FE08.ts_UY(:,station), FE09.ts_UY(:,station)];
station = j_bd1(2);
T_BD1_VEL_CELL2 = [ FE01.ts_UY(:,station),  FE02.ts_UY(:,station), FE03.ts_UY(:,station),...
    FE04.ts_UY(:,station), FE05.ts_UY(:,station),...
    FE06.ts_UY(:,station), FE07.ts_UY(:,station), FE08.ts_UY(:,station), FE09.ts_UY(:,station)];
station = j_bd2(1);
T_BD1_VEL_CELL3 = [ FE01.ts_UY(:,station),  FE02.ts_UY(:,station), FE03.ts_UY(:,station),...
    FE04.ts_UY(:,station), FE05.ts_UY(:,station),...
    FE06.ts_UY(:,station), FE07.ts_UY(:,station), FE08.ts_UY(:,station), FE09.ts_UY(:,station)];
station = j_bd2(2);
T_BD1_VEL_CELL4 = [ FE01.ts_UY(:,station),  FE02.ts_UY(:,station), FE03.ts_UY(:,station),...
    FE04.ts_UY(:,station), FE05.ts_UY(:,station),...
    FE06.ts_UY(:,station), FE07.ts_UY(:,station), FE08.ts_UY(:,station), FE09.ts_UY(:,station)];

% ELE
station = j_bd1(1);
T_BD1_EL_CELL1 = [ FE01.ts_ELE(:,station),  FE02.ts_ELE(:,station), FE03.ts_ELE(:,station),...
 FE04.ts_ELE(:,station), FE05.ts_ELE(:,station),...
 FE06.ts_ELE(:,station), FE07.ts_ELE(:,station), FE08.ts_ELE(:,station), FE09.ts_ELE(:,station)];
station = j_bd1(2);
T_BD1_EL_CELL2 = [ FE01.ts_ELE(:,station),  FE02.ts_ELE(:,station), FE03.ts_ELE(:,station),...
 FE04.ts_ELE(:,station), FE05.ts_ELE(:,station),...
 FE06.ts_ELE(:,station), FE07.ts_ELE(:,station), FE08.ts_ELE(:,station), FE09.ts_ELE(:,station)];
station = j_bd2(1);
T_BD1_EL_CELL3 = [ FE01.ts_ELE(:,station),  FE02.ts_ELE(:,station), FE03.ts_ELE(:,station),...
 FE04.ts_ELE(:,station), FE05.ts_ELE(:,station),...
 FE06.ts_ELE(:,station), FE07.ts_ELE(:,station), FE08.ts_ELE(:,station), FE09.ts_ELE(:,station)];
station = j_bd2(2);
T_BD1_EL_CELL4 = [ FE01.ts_ELE(:,station),  FE02.ts_ELE(:,station), FE03.ts_ELE(:,station),...
 FE04.ts_ELE(:,station), FE05.ts_ELE(:,station),...
 FE06.ts_ELE(:,station), FE07.ts_ELE(:,station), FE08.ts_ELE(:,station), FE09.ts_ELE(:,station)];

%%  OCH
%% VM and FR upstream
    n=1;
```

```
    T_VM_OC = [FE02.VM_OC_s(1:n:end,1), FE03.VM_OC_s(1:n:end,1), FE04.VM_OC_s(1:n:end,1), ...
        FE05.VM_OC_s(1:n:end,1), FE06.VM_OC_s(1:n:end,1), FE07.VM_OC_s(1:n:end,1),...
        FE08.VM_OC_s(1:n:end,1), FE09.VM_OC_s(1:n:end,1)];
    T_VM_OC_mean=mean(abs(T_VM_OC));
    TIME = FE02.TIMEHR_s(1:n:end);


%% B
        T_Bt = [  FE01.B, FE02.B, FE03.B, FE04.B, FE05.B,...
            FE06.B, FE07.B, FE08.B, FE09.B];


%% COEFFICIENTS
% I,J LOCATION UPSTREAM
        NumCellUps =1.0;
        J_LOC_UP = jturb−NumCellUps;
% time series discretization
        n=1;%100;%200;
    T_CT_01 = [ FE02.CT_s(1:n:end,1), FE03.CT_s(1:n:end,1), FE04.CT_s(1:n:end,1),...
        FE05.CT_s(1:n:end,1),FE06.CT_s(1:n:end,1), FE07.CT_s(1:n:end,1),...
        FE08.CT_s(1:n:end,1),FE09.CT_s(1:n:end,1)];
    T_CT_mean=mean(T_CT_01);


    T_CP_01 = [ FE02.CP_s(1:n:end,1), FE03.CP_s(1:n:end,1), FE04.CP_s(1:n:end,1),...
        FE05.CP_s(1:n:end,1),FE06.CP_s(1:n:end,1), FE07.CP_s(1:n:end,1),...
        FE08.CP_s(1:n:end,1),   FE09.CP_s(1:n:end,1)];
    T_CP_mean=mean(T_CP_01);


    T_FR_01 = [FE02.FR_s(1:n:end,1), FE03.FR_s(1:n:end,1), FE04.FR_s(1:n:end,1),...
        FE05.FR_s(1:n:end,1),FE06.FR_s(1:n:end,1), FE07.FR_s(1:n:end,1),...
        FE08.FR_s(1:n:end,1), FE09.FR_s(1:n:end,1)];


    T_BETA4_01 = [FE02.BETA4_s(1:n:end,1), FE03.BETA4_s(1:n:end,1), FE04.BETA4_s(1:n:end,1),...
        FE05.BETA4_s(1:n:end,1), FE06.BETA4_s(1:n:end,1), FE07.BETA4_s(1:n:end,1),...
        FE08.BETA4_s(1:n:end,1), FE09.BETA4_s(1:n:end,1)];
%% Water drop
% Analytical − dh
%...........................
        dh_analytical_ts = [FE02.dh; FE03.dh; FE04.dh; FE05.dh;...
            FE06.dh; FE07.dh; FE08.dh; FE09.dh];
% Trasnpuesta
        dh_analytical_ts_trans = dh_analytical_ts ';
%| dh_{max}|
```

254

```
        dh_analytical_max = max( dh_analytical_ts_trans );
%| dh_{mean}|
        dh_analytical_mean =mean( dh_analytical_ts_trans );


% dh − from the model
%.......................................
        dh_data_ts_1C = [FE02.dh_data_1C, FE03.dh_data_1C, FE04.dh_data_1C ,...
            FE05.dh_data_1C ,FE06.dh_data_1C ,FE07.dh_data_1C, FE08.dh_data_1C ,...
            FE09.dh_data_1C ];
%| dh |
        dh_data_abs_1C = abs( dh_data_ts_1C );
%| dh_{max}|
        dh_data_abs_max_1C = max( dh_data_abs_1C );
%| dh_{mean}|
        dh_data_mean_1C =mean( dh_data_abs_1C );


%%  Pmax and Qmax
%% Numerical P
% P − time series
        T_P_ts = [ FE02.P_OC_ts, FE03.P_OC_ts, FE04.P_OC_ts, FE05.P_OC_ts ,...
            FE06.P_OC_ts, FE07.P_OC_ts, FE08.P_OC_ts, FE09.P_OC_ts ];
        T_P_ts_mean_0 = mean( T_P_ts );
        T_P_ts_mean =[0, T_P_ts_mean_0 ]; % NTS inclusion
% Cumulative (Power) from the Array for given B;
        T_P_ts_mean_sumfence = T_P_ts_mean*W_CELL;
% P−max each case and normalization
        T_P_vmax = [   FE01.P_OC_max, FE02.P_OC_max, FE03.P_OC_max, FE04.P_OC_max ,...
            FE05.P_OC_max ,FE06.P_OC_max, FE07.P_OC_max, FE08.P_OC_max, FE09.P_OC_max ];
%% Numerical Q
        T_Q_vmax = [FE01.Q0_max,   FE02.Q0_max, FE03.Q0_max, FE04.Q0_max, FE05.Q0_max ,...
            FE06.Q0_max, FE07.Q0_max, FE08.Q0_max, FE09.Q0_max ];
        Q0_NST =mean(FE01.Q0_ts );
        Q_ts = [ FE02.Q0_ts, FE03.Q0_ts, FE04.Q0_ts, FE05.Q0_ts ,...
            FE06.Q0_ts ,FE07.Q0_ts, FE08.Q0_ts, FE09.Q0_ts ];
        Q_ts_mean = mean( Q_ts )              ;
        Q0_ts_mean =[Q0_NST, Q_ts_mean ];
% Cumulative (Q) from the Array for given B;     sum of  the values
% obtained from the temporal average per grid cell.
        T_Q_ts_mean_sumfence = Q0_ts_mean*W_CELL;
%% Analytical P−max
% P_SU07 = gamma * rho * g * a * Qmax;
```

Appendix A.

```
%...............................................................
% (a) is the amplitude of the sinusoidal height difference between the ends of the channel,
% (Qmax) is the maximum volume flux in the natural tidal regime.
% variables
g = 9.81;        % (m/s)
rho = 1025;        % (kg/m3)
gamma = 0.20;


%% Efficiency
    eta_1_mean = [FE02.eta_1_mean, FE03.eta_1_mean, FE04.eta_1_mean, ...
        FE05.eta_1_mean, FE06.eta_1_mean, FE07.eta_1_mean, FE08.eta_1_mean,...
        FE09.eta_1_mean];
%% Efficiency  NUMERICAL
    T_eta_1_NUM_mean = [FE02.eta_1_num_mean, FE03.eta_1_num_mean, FE04.eta_1_num_mean, ...
        FE05.eta_1_num_mean, FE06.eta_1_num_mean, FE07.eta_1_num_mean, FE08.eta_1_num_mean,...
        FE09.eta_1_num_mean];
%% Efficiency -2
    eta_2_mean = [FE02.eta_2_mean, FE03.eta_2_mean, FE04.eta_2_mean, ...
        FE05.eta_2_mean, FE06.eta_2_mean, FE07.eta_2_mean, FE08.eta_2_mean,...
        FE09.eta_2_mean];
%% Efficiency -2  NUMERICAL
    T_eta_2_NUM_mean = [FE02.eta_2_num_mean, FE03.eta_2_num_mean, FE04.eta_2_num_mean, ...
        FE05.eta_2_num_mean, FE06.eta_2_num_mean, FE07.eta_2_num_mean, FE08.eta_2_num_mean,...
        FE09.eta_2_num_mean];


%% P+PW
    PPW_mean = [0 FE02.PPW_mean, FE03.PPW_mean, FE04.PPW_mean, ...
        FE05.PPW_mean, FE06.PPW_mean, FE07.PPW_mean, FE08.PPW_mean,...
        FE09.PPW_mean];
% Cumulative (Power) from the Array for given B;
        T_PPW_ts_mean_sumfence = PPW_mean*W_CELL;


%% P+PW  - NUMERICAL
        PPW_NUM_mean = [0.0 FE02.PPW_num_mean, FE03.PPW_num_mean, FE04.PPW_num_mean, ...
            FE05.PPW_num_mean, FE06.PPW_num_mean, FE07.PPW_num_mean, FE08.PPW_num_mean,...
            FE09.PPW_num_mean];
% Cumulative (Power) from the Array for given B;
        T_PPW_ts_mean_sumfence_NUM = PPW_NUM_mean*W_CELL;


%% Pa
        Pa_1_mean = [0, FE02.Pa_1_mean, FE03.Pa_1_mean, FE04.Pa_1_mean, FE05.Pa_1_mean,...
```

Appendix A.

FE06.Pa_1_mean, FE07.Pa_1_mean, FE08.Pa_1_mean, FE09.Pa_1_mean];
% Cumulative (Power) from the Array for given B;
    T_Pa1_ts_mean_sumfence=Pa_1_mean*W_CELL;

    Pa_2_mean = [0, FE02.Pa_2_mean, FE03.Pa_2_mean, FE04.Pa_2_mean, FE05.Pa_2_mean,...
        FE06.Pa_2_mean, FE07.Pa_2_mean, FE08.Pa_2_mean, FE09.Pa_2_mean];
% Cumulative (Power) from the Array for given B;
    T_Pa2_ts_mean_sumfence=Pa_2_mean*W_CELL;

%% Pa ——   NUMERICAL
    Pa_1_NUM_mean = [0.0, FE02.Pa_1_num_mean, FE03.Pa_1_num_mean, FE04.Pa_1_num_mean,...
        FE05.Pa_1_num_mean, FE06.Pa_1_num_mean, ...
        FE07.Pa_1_num_mean, FE08.Pa_1_num_mean, FE09.Pa_1_num_mean];
% Cumulative (Power) from the Array for given B;
    T_Pa1_ts_mean_sumfence_NUM=Pa_1_NUM_mean*W_CELL;

    Pa_2_NUM_mean = [0.0, FE02.Pa_2_num_mean, FE03.Pa_2_num_mean, FE04.Pa_2_num_mean,...
        FE05.Pa_2_num_mean, FE06.Pa_2_num_mean, ...
        FE07.Pa_2_num_mean, FE08.Pa_2_num_mean, FE09.Pa_2_num_mean];
% Cumulative (Power) from the Array for given B;
    T_Pa2_ts_mean_sumfence_NUM=Pa_2_NUM_mean*W_CELL;

%% Dissipated P
    Pdisi_mean = [0, FE02.Pdisi_mean, FE03.Pdisi_mean, FE04.Pdisi_mean, FE05.Pdisi_mean,...
        FE06.Pdisi_mean , FE07.Pdisi_mean , FE08.Pdisi_mean , FE09.Pdisi_mean];
% Cumulative (Power) from the Array for given B;
    T_Pw1_ts_mean_sumfence = Pdisi_mean*W_CELL;

    Pdisi_2_mean = [0, FE02.Pdisi_2_mean, FE03.Pdisi_2_mean, FE04.Pdisi_2_mean,...
        FE05.Pdisi_2_mean, FE06.Pdisi_2_mean , FE07.Pdisi_2_mean , FE08.Pdisi_2_mean,...
        FE09.Pdisi_2_mean];
% Cumulative (Power) from the Array for given B;
    T_Pw2_ts_mean_sumfence = Pdisi_2_mean*W_CELL;

%% Dissipated P —— NUMERICAL
    Pdisi2_NUM_mean = [0.0, FE02.Pdisi_2_num_mean, FE03.Pdisi_2_num_mean,...
        FE04.Pdisi_2_num_mean , FE05.Pdisi_2_num_mean ,...
        FE06.Pdisi_2_num_mean , FE07.Pdisi_2_num_mean ,...
        FE08.Pdisi_2_num_mean , FE09.Pdisi_2_num_mean];

% Cumulative (Power) from the Array for given B;

```
        T_Pw1_ts_mean_sumfence_NUM = Pdisi2_NUM_mean*W_CELL;


%%    Pnorm  vs  Qnorm
%% Numerical  Pnorm  and  Qnorm
% % Max − values
% Maximum  Transport
        T_Q_01_MAX=max(T_Q_vmax);
        T_Qnorm_01 = T_Q_vmax./T_Q_01_MAX;
% Maximum  Power
        T_P_01_MAX=max(T_P_vmax);
        T_Pnorm_01 = T_P_vmax./T_P_01_MAX;


%% Analytical  solution  (GC15;  Sutherland  Eq)
% Flow  rate − Max − values
        Q = T_Q_vmax;  Qmax =max(Q);
 % Q−max − Max − values
        Q_2 =linspace(1.0,max(Q),30);        Qmax_2 =max(Q_2);
% EQ2 − GC05;
        s1_2   = ((3^(3/2))/2) * (Q_2./Qmax_2);
        s2_2 = 1 − (Q_2./Qmax_2).^2;
        PPmax_S07_2 = s1_2.*s2_2;
        QQmax_S07_2 = Q_2./Qmax_2;


%%  SAVING  WORKSPACE
name ='EXP268_Fence_Brange_adi';
save([path name '.mat']) %FOR P's  comparison  at  different  B's
```

A.5   Grid Structures

ADI-M and TVD-M use a different grid structure to compute and store the variables. Using the notation introduced by Arakawa and Lamb (1977) ADI-M uses a staggered Arakawa C-grid and TVD-M uses a non-staggered A-grid (Figure A.3). ADI-M computes and storages water elevation at the centre of the cell (denoted by Θ); meantime, discharges are discretised on the x and y direction as uH and vH, respectively (Falconer and Lin, 2001; Nash, 2010) as Figure A.3(a) indicates. Contrary, TVD-M implemented a cell-centered, non-staggered computational grid (Liang et al., 2006; Bellos and Tsakiris, 2016). This procedure indicates that all the variables are stored and
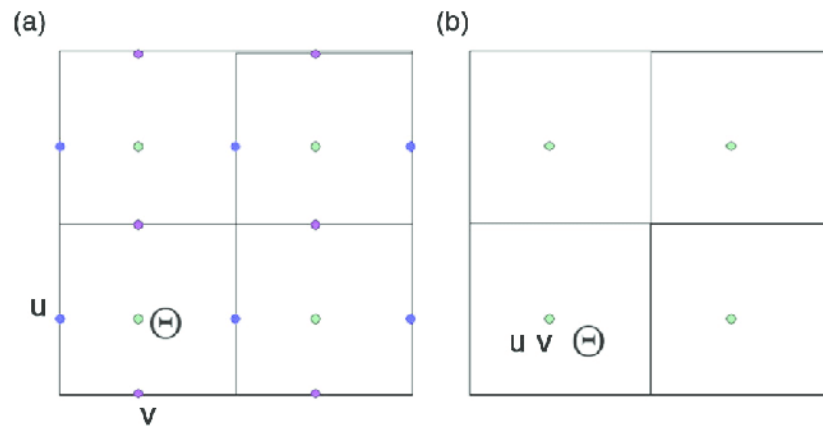
Fig. A.3: Staggered grid (a), non-staggered grid (b). Figure taken from Kang *et al.* (2014).

computed at the center of the grid as Figure A.3(b) indicates.